



A University of Sussex DPhil thesis

Available online via Sussex Research Online:

<http://sro.sussex.ac.uk/>

This thesis is protected by copyright which belongs to the author.

This thesis cannot be reproduced or quoted extensively from without first obtaining permission in writing from the Author

The content must not be changed in any way or sold commercially in any format or medium without the formal permission of the Author

When referring to this work, full bibliographic details including the author, title, awarding institution and date of the thesis must be given

Please visit Sussex Research Online for more information and further details

A numerical approach to studying cell dynamics



Uduak Zenas George

Department of Mathematics

University of Sussex

A thesis submitted for the degree of

Doctor of Philosophy

September, 2011

Declaration

WORK NOT SUBMITTED ELSEWHERE FOR EXAMINATION

I hereby declare that this thesis has not been submitted in whole or in part to this or any other University for the award of a degree.

Uduak Zenas George

A numerical approach to studying cell dynamics

Uduak Zenas George

Submitted for the degree of Doctor of Philosophy

University of Sussex, August 2011

Abstract

The focus of this thesis is to propose and implement a highly efficient numerical method to study cell dynamics. Three key phases are covered: mathematical modelling, linear stability analytical theory and numerical simulations using the moving grid finite element method. This aim is to study cell deformation and cell movement by considering both the mechanical and biochemical properties of the cortical network of actin filaments and its concentration. These deformations are assumed to be a result of the cortical actin dynamics through its interaction with a protein known as myosin II in the cell cytoskeleton.

The mathematical model that we consider is a continuum model that couples the mechanics of the network of actin filaments with its bio-chemical dynamics. Numerical treatment of the model is carried out using the moving grid finite element method. By assuming slow deformations of the cell boundary, we verify the numerical simulation results using linear stability theory close to bifurcation points. Far from bifurcation points, we show that the model is able to describe the deformation of cells as a function of the contractile tonicity of the complex formed by the association of actin filaments with the myosin II motor proteins. Our results show complex cell deformations and cell movements such as cell expansion, contraction, translation and protrusions in accordance with experimental observations.

The migratory behaviour of cells plays a crucial role in many biological events such as immune response, wound healing, development of tissues, embryogenesis, inflammation and the formation of tumours.

Acknowledgements

I would like to thank my supervisor Dr Anotida Madzvamuse for his supervision and patience throughout this project. His kind and excellent support led to the successful completion of this project. I would also like to thank Dr Angelique Stephanou whose previous work we extended in this project for her advice and support. I am grateful to Akwa Ibom State University of Technology for funding my study and the Department of Mathematics, University of Sussex for engaging me as an Associate tutor during my study in the department.

I would like to thank my external examiner, Dr Kevin Painter for his kind suggestions and corrections to this thesis. I would like to acknowledge Dr Peter Giesl for helpful suggestions and advise during my annual reviews. I would like to thank Oonagh Caunter, Louise Winters, Gemma Farrell and other staff of the departmental office for their support throughout my study. My thanks also goes to Tom Armour for making available all the software and computing tools that were used in this project. I am grateful to Dr Pryer and Dr Venkataraman. I am also thankful to the Maths postgraduate students for all the chats and fun especially my office mates Shatha and Leila.

Special thanks goes to my lovely husband Dr Zenas George and our son Akwaeno-Abasi for their enormous support, kindness, love and patience during this study.

I am very grateful to my parents David and Jessey Ekpo for their enormous support and advice throughout my education.

Dedication

I would like to dedicate this thesis to God Almighty for his guidance and mercies to me and my family.

Contents

Contents	1
List of Figures	4
List of Tables	11
Nomenclature	12
1 Introduction	13
1.1 General overview	13
1.1.1 Outline of the thesis	16
1.2 Notation and mathematical preliminaries	17
1.2.1 Notation	17
1.2.2 Some mathematical formulae	17
1.2.3 Spaces and norms	18
1.2.4 Reynolds transport theorem	19
1.2.5 Method of Frobenius	19
1.2.6 Bessel's equation	20
1.2.7 Modified Bessel's equation	22
2 Biological overview of cell movement	23
2.1 Introduction	23
2.2 Description of an eukaryotic cell	24
2.2.1 Overview	24
2.2.2 The cell cytoskeleton	24
2.3 Dynamics of actin filaments	29
2.3.1 Molecular mechanism of actin nucleation	31
2.3.2 Actin depolymerisation enhancing proteins	33
2.3.3 Actin binding and cross-linking proteins	34
2.4 Cell movement	35
2.4.1 Mechanism of cell movement	36
2.5 Project motivation	40

3	Mathematical description of cell movement	42
3.1	Introduction	42
3.2	General overview of the cytomechanical model	44
3.3	Derivation of the model equations	45
3.3.1	Reaction-diffusion equation for actin biochemical dynamics on a continuously deforming cell domain	45
3.3.2	Force balance mechanical equation for actin dynamics	47
3.3.3	The cytomechanical model	52
3.4	Selection of parameter values	53
3.4.1	Determination of dimensional parameter values	53
3.4.2	Nondimensionalisation and non-dimensional parameter values	54
3.5	Linear stability analysis on a fixed unit disc	55
3.6	Eigenfunctions on a unit disk	59
3.6.1	Laplace operator in polar coordinates	59
3.6.2	Neumann Laplacian on a disk	60
3.7	Mode selection and the dispersion relation	65
3.7.1	Isolation of a finite range of unstable wavenumbers	66
3.7.2	Parameter space	68
3.8	Summary	72
4	A moving grid finite element method for cell movement	73
4.1	Introduction	73
4.2	Basic concept of the moving grid finite element method	75
4.3	Derivation of the weak formulation	75
4.3.1	Weak formulation of the force balance equation	76
4.3.2	Weak formulation of the reaction-diffusion equation	80
4.3.3	Weak formulation of the coupled problem	82
4.3.4	Finite-dimensional subspaces	82
4.4	Finite element discretization of the model	83
4.4.1	Semi-discrete model of the force balance equation	86
4.4.2	Semi-discrete model of the reaction-diffusion equation	88
4.4.3	Fully discrete scheme of the coupled problem	88
4.5	Computation of the evolution of the domain	89
4.5.1	Numerical computations	90
4.6	Numerical implementation of the moving grid finite element method	90
4.6.1	Mesh generation	91
4.6.2	Computation of the unit normal	92
4.6.3	Evaluation of the global matrices and force vectors	94
4.7	Summary	99

5	Numerical simulation of cell movement	101
5.1	Introduction	101
5.2	Validating numerical results close to bifurcation points	102
5.2.1	Excitation of the eigenmode $w_{1,1}$	102
5.2.2	Excitation of the eigenmode: $-w_{0,2}$	102
5.3	Validating numerical results far from bifurcation points	104
5.3.1	Excitation of mixed modes	105
5.3.2	Excitation of higher modes	105
5.4	Numerical simulations of cell dynamics far away from bifurcation points .	106
5.4.1	Cell deformation for the case where the eigenmode $w_{1,1}$ is excited	107
5.4.2	Cell deformation for higher and mixed modes	108
5.5	Numerical investigation of the dynamics of parameter space $(\tilde{\psi}, \tilde{p})$	109
5.6	Numerical simulation on a realistic cell	111
5.7	Qualitative comparison with experimental observations I	111
5.8	Qualitative comparison with experimental observations II	112
5.9	Limitation of the model	112
5.10	Numerical experiments	124
5.11	Summary	125
6	Conclusions and future work	127
6.1	Conclusion	127
6.2	Future work	129
	References	131
A	Stability analysis	143
A.1	Stability analysis of the reaction-diffusion equation	143
B	Weak form and wellposedness	147

List of Figures

2.1	A schematic showing a cell with its three main components.	25
2.2	A schematic representation of the components of the cell showing the cytoskeletal filaments and some organelles.	25
2.3	A schematic description of actin polymerisation and de-polymerisation kinetics. (a) is an illustration of actin polymerisation and de-polymerisation. (b) is an illustration of cell membrane protrusion in response to a stimulant. G-actin molecules rapidly diffuse towards the side closer to the stimulant and polymerises into F-actin. The force generated by the polymerisation causes the membrane to protrude towards the source of the stimulant.	28
2.4	An illustration of a crawling cell with three areas enlarged to show the arrangement of actin filaments. Actin filaments are shown in red, the arrowheads are pointing towards the plus end (Alberts et al. 2002).	30
2.5	Schematic description of the activity of Arp2/3 complex and formins during actin nucleation in cells. Arp2/3 complex and formins initiate the production of new actin filaments via polymerisation of monomeric actin. Arp2/3 initiates the production of branched filaments while formins are dimers and are attached to the growing ends of actin filaments. Formin act by encouraging the growth of single filaments necessary for formation of actin bundles.	32
2.6	Schematic representation of the process of actin nucleation in cells. Nucleation promoting factors such as WASP and Scar/WAVE activates Arp2/3 complex to nucleate a branch. The growing ends of the filament branch grows until it is capped by capping proteins and pushes out the membrane as it grows thereby creating a lamellipodia.	33
2.7	Actin-thymosin complex is sterically prevented from binding to the plus end an actin filament (Alberts et al. 2002).	34
2.8	Schematic representation of the two modes of migration in eukaryotic cells.	36
2.9	A schematic illustration of the three stages of mesenchymal mode of cell migration.	37

2.10	A schematic illustration of the initiation of blebs. They are formed either by the rupture of the cortex or by membrane detachment. In a , a local or global pressure resulting from a local or global contractile activity of actomyosin complex can detach the membrane from the cortex thereby initiating a bleb. In b , a local rupture of the cortex initiates a bleb. In both cases expansion of the bleb is caused by an intracellular hydrostatic pressure generated by the effect of the contractile stress on the cytosol. . . .	39
3.1	Function $\sigma(a)$ describing the actomyosin network contractility. The contractility first increases in a parabolic way with the actin density until a critical density of actin is reached, after which the contractility begins to decrease exponentially.	50
3.2	A graphical and pictorial description of the variation of the function $p(a)$ on a typical cell.	51
3.3	A plot of $\sigma'(1)$ against \tilde{a}_{sat} with $\tilde{\psi} = 1.0$	58
3.4	A plot showing the derivative of Bessel's function J'_m for $m = 0, 1, 2, 3$	63
3.5	A surface plot of the vibration mode $w_{1,1}(r, \theta) = J_1(j'_{1,1}r) \cos \theta$ which corresponds to the lowest non-zero wavenumber $k_{1,1}^2$ on a unit disk. . . .	65
3.6	We present in (a) a plot of $b(k^2) < 0$ when $k_{1,1}^2 = 3.38994$ is the only excitable wavenumber. In (b) we show its corresponding dispersion relation $\text{Re } \lambda := \max(\text{Re } \lambda)$. In both cases $\delta(l) = 1$	67
3.7	We present in (a) a plot of $b(k^2) < 0$ when the first 2 non-zero wavenumbers $k_{1,1}^2 = 3.38994$ and $k_{2,1}^2 = 9.32838$ are the only excitable wavenumbers. In (b) we show the corresponding dispersion relation $\text{Re } \lambda := \max(\text{Re } \lambda)$. In both cases $\delta(l) = 1$	68
3.8	Surface plots of selected eigenmodes for some bands of wavenumbers displayed in Table 3.5.	69

- 3.9 We present in (a) parameter space plot of the pressure coefficient \tilde{p} against the contractile tonicity $\tilde{\psi}$ showing the regions where instability exist for $\delta(l) = 1$. The ash area (H) signifies the region of Hopf instability with a dispersion relation that isolates $k_{1,1}^2$ as the only unstable non-zero wavenumber. The region (dark blue) preceding that of Hopf instability represents the region where the uniform steady state is always stable for all wavenumbers k^2 . Immediately after the Hopf instability region we have a purple region (OS1) where an oscillatory instability exists for $k_{1,1}^2$. The green region is a Turing instability region and has a dispersion relation that isolates $k_{1,1}^2$ as the only unstable non-zero wavenumber. In the purple region (OS2) an oscillatory instability exists for $k_{2,1}^2$. The light blue region is also a Turing instability region and has a dispersion relation that isolates the first two non-zero wavenumbers. And in (b) and (c) we show how the variation of \tilde{p} results in a transition from an oscillatory instability to a Turing instability for $\tilde{\psi} = 38.24$. In (b) $\delta(l) = 1$ and (c) $\delta(l) = 0$. . . 71
- 4.1 A description of a typical element S of the triangulation $\mathcal{T}_{h,t}$ 83
- 4.2 An illustration of the technique of global refinement with node projection. Refinement edge midpoints denoted by \circ are projected to the surface $g(x,y) = x^2 + y^2 - 1 = 0$ and are added to the nodes of the mesh denoted by \bullet . (a) shows the macro triangulation and the surface $g(x,y) = 0$ in dash line. (b), (c) and (d) show the refinement edge midpoints \circ , the projection of the refinement edge midpoints to the line $g(x,y) = 0$ and the mesh after one global refinement of the macro triangulation respectively. This technique eventually produces an affine mesh for linear finite element discretisation of Ω_t after a few global refinements. 92
- 4.3 Affine mesh for linear finite element discretisation of Ω_0 : (a), (b) and (c) show the grid after two, three and four global refinements of the macro triangulation respectively. Successive refinement with nodal projection produces a better approximation of the boundary $g(x,y) = x^2 + y^2 - 1 = 0$. 92
- 4.4 (a) is a cross-section of a polygonal circle showing the outward pointing unit vector normal to a line segment. (b) shows the two outward pointing normal vectors that occur as a result of the intersection of two line segments at a nodal position. The resultant normal \mathbf{n} is computed by applying the parallelogram law of forces 94

- 5.1 Surface plots of the numerical results for actin concentration a_h and displacement solution \mathbf{u}_h . Parameter values used in the numerical simulations are selected such that the lowest non-zero wavenumber $k_{1,1}^2$ is excited. (a) is the predicted solution for $w_{1,1}$ from linear theory. (b) is the numerical result for actin concentration a_h while (c) is the numerical result for displacement solution \mathbf{u}_h . . . (a), (b) and (c) are all surface plots. In (b) and (c) a bar is used to specify the variation along the z-plane such that red signifies high values and blue signifies low values. 103
- 5.2 Surface plots of the numerical results for the actin concentration a_h and the displacement solution \mathbf{u}_h showing the replication of the eigenmode $-w_{0,2}$. (a) is a surface plot of the eigenmode $w_{0,2}$. (b) and (c) display the simulation results of actin concentration a_h and displacement solutions \mathbf{u}_h respectively at time $t = 3.61 \times 10^{-3}$. (d) displays the displacement solutions \mathbf{u}_h at time $t = 0.024$ having no oscillations at the points of discontinuity. The initial conditions used for actin concentrations are $a_c + \text{rnd} * \cos(x)$ 104
- 5.3 A surface plot of the numerical result for the displacement solution \mathbf{u}_h . Parameter values used in the numerical simulation are consistent with those displayed in Table 3.1 except that $\delta(l)$ is as defined in (5.1). Initial conditions as in Figure 5.2. 104
- 5.4 Surface plots of the numerical results of the actin concentration a_h and displacement solutions \mathbf{u}_h having mixed modes excited together with the reproduced solutions predicted from linear theory. (a) and (d) are the predicted solutions from linear theory for $w_{0,2} + 2w_{2,1}$ and $w_{3,1} - w_{0,2} - 3w_{2,1}$ respectively. The numerical results reproduce the following modes: (b)-(c) $w_{0,2} + 2w_{2,1}$, (e)-(f) $w_{3,1} - w_{0,2} - 3w_{2,1}$. ψ is chosen as given in Table 5.1 such that mixed modes are excited (refer to the list given in Table 3.5 for more detail on the eigenmodes isolated by a dispersion relation depending on the value of $\tilde{\psi}$ and ψ). 106
- 5.5 Surface plots of the numerical results of the actin concentration a_h and displacement solutions \mathbf{u}_h having higher modes excited together with the reproduced solutions predicted from linear theory. (a) and (d) are the predicted solutions from linear theory for $w_{4,1}$ and $w_{2,1}$ respectively. The numerical results reproduce the following modes: (b) - (c) $w_{4,1}$, and (e) - (f) $w_{2,1}$. ψ is chosen as given in Table 5.1 such that higher modes are excited (refer to the list given in Table 3.5 for more detail on the eigenmodes isolated by a dispersion relation depending on the value of $\tilde{\psi}$ and ψ). 107

- 5.6 (a) - (c) are graphical displays of the numerical results of the actin concentration a_h with $\Delta t = 1.0228 \times 10^{-2}$. Blue signifies the lowest values and red the highest values. Figure 5.6(d) is a plot of the area of the cell against the number of time-steps taken. It shows the area of the cell increasing with the number of time-steps taken. (e) shows a plot of the index of polarity against number of time steps. A black plus sign specifies the position of the cell centroid at time $t = 0$ 113
- 5.7 (a) - (c) are graphical displays of the numerical results of the actin concentration a_h . A finite element mesh with 2113 nodes was used, $\Delta t = 1.0228 \times 10^{-2}$. Blue signifies the lowest values and red the highest values. (d) is a plot of the area of the cell against the number of time-steps taken. It shows the area of the cell increasing with the number of time-step taken. (e) is a plot of the index of polarity against the number of time-steps taken. 114
- 5.8 (a) - (c) are graphical displays of the numerical results of the actin concentration a_h . A finite element mesh with 8321 nodes was used, $\Delta t = 1.0228 \times 10^{-3}$. Blue signifies the lowest values and red the highest values. (d) is a plot of the index of polarity against the number of time-steps taken. 115
- 5.9 (a) - (c) are graphical displays of the numerical results of the actin concentration a_h . A finite element mesh with 8321 nodes was used, $\Delta t = 1.0228 \times 10^{-3}$. Blue signifies the lowest values and red the highest values. (d) is a plot of the index of polarity against the number of time-steps taken. 116
- 5.10 (a) - (c) are graphical displays of the numerical results of the actin concentration a_h with $\Delta t = 1.0228 \times 10^{-3}$. Blue signifies the lowest values and red the highest values. (d) is a plot of the area of the cell against the number of time-steps taken. It shows the area of the cell increasing with the number of time-step taken. 117
- 5.11 A graphical display of the finite element mesh. At time $t = 0.1636$, the cell has deformed significantly but the finite element mesh is still suitable for numerical computations and describes the domain properly. (b) is the finite element mesh of the graphics given in (a) and has been enlarge for the sake of clarity. 118

- 5.12 Graphical display of the simulation results of the actin concentration. Blue denotes the lowest values and red the highest. These results were obtained at the following times: (a) $t = 1.2046 \times 10^{-3}$, (b) $t = 3.6137 \times 10^{-3}$, (c) $t = 0.0361$, and (d) $t = 0.5180$. The numerical value of the contractile tonicity $\tilde{\psi} = 70.366$ and that of the pressure coefficient $\tilde{p} = 0.433$. (e) is a plot of the area of the cell against the number of time-steps taken. 119
- 5.13 Graphical display of the simulation results of the actin concentration. Blue denotes the lowest values and red the highest. These results were obtained at the following times: (a) $t = 1.2046 \times 10^{-3}$, (b) $t = 3.6137 \times 10^{-3}$, (c) $t = 0.0361$, and (d) $t = 0.5180$. The numerical value of the contractile tonicity $\tilde{\psi} = 70.366$ and that of the pressure coefficient $\tilde{p} = -0.433$. (e) is a plot of the area of the cell against the number of time-steps taken. 120
- 5.14 Graphical display of the simulation results of the actin concentration. Blue denotes the lowest values and red the highest. These results were obtained at the following times: (a) $t = 1.2046 \times 10^{-3}$, (b) $t = 3.6137 \times 10^{-3}$, and (c) $t = 0.0722$. The numerical value of the contractile tonicity $\tilde{\psi} = 7.8 \times 10^3$ and that of the pressure coefficient $\tilde{p} = 0.026$. (d) is a plot of the area of the cell against the number of time-steps taken. 121
- 5.15 A plot of the index of polarity against the number of time-steps for simulation results with contractile tonicity $\tilde{\psi} = 7.8 \times 10^3$ and the pressure coefficient $\tilde{p} = 0.026$ 121
- 5.16 Graphical display of the simulation results of the actin concentration. Blue denotes the lowest values and red the highest. The numerical value of the contractile tonicity $\tilde{\psi} = 1.3 \times 10^3$ and the pressure coefficient $\tilde{p} = 0.026$ 122
- 5.17 A plot of the index of polarity against the number of time-steps for simulation results with contractile tonicity $\tilde{\psi} = 1.3 \times 10^3$ and the pressure coefficient $\tilde{p} = 0.03$ 122
- 5.18 (a) Epifluorescence image of a Swiss 3T3 fibroblast cell. F-actin is predominant at the cell periphery and is highest at the region where protrusions occur. (b) A simulated cell deformation for contractile tonicity $\tilde{\psi} = 1.3 \times 10^3$ and the pressure coefficient $\tilde{p} = 0.026$. The distribution of F-actin in the simulated cell is in qualitative agreement with experimental observations. 123

5.19	A qualitative comparison of the simulation result of cell deformations for mixed modes with those observed experimentally for an isolated fibroblast allowed to spread on a substrate <i>in vitro</i> . Observe that the cell shape changing from a roughly circular shape to an elongated one, consistent with the numerical experiment.	123
5.20	(a) is a plot of the simulation result for actin concentration at time $T = 0.10228$ with timestep size $\Delta t = 1.0228 \times 10^{-2}$. (b) is a plot of the simulation result for actin concentration at time $T = 0.10228$ with timestep size $\Delta t = 1.0228 \times 10^{-3}$	125

List of Tables

3.1	Dimensional parameters and their values as used in the mathematical model except where it is specified otherwise.	53
3.2	Non-dimensional parameters and their values as used in the nondimensionalized mathematical model except where it is specified otherwise. These parameter values were obtained from their dimensional counterpart by using (3.15). Here we have assume that $L = 1.0cm$ since we desire to carry out linear stabillity analysis on a unit disk and also numerical simulations of the model equations will be carried out on an initial domain that is equivalent to a unit disk.	55
3.3	Possibilities of stable and unstable modes to exist.	57
3.4	Zeros of the derivative of Bessel functions of the first kind: $j'_{m,n}$ $m = 0, \dots, 5$; $n = 1, \dots, 4$	64
3.5	A display of the values of $\tilde{\psi}$ (and their corresponding dimensional values of ψ) required by the dispersion relation in order to isolate at least two unstable wavenumbers.	67
4.1	L^2 errors of computed normal vectors to a circle.	94
5.1	Values of ψ and the initial conditions used for the excitation of mixed and higher modes presented in Figure 5.4.	105
5.2	Errors $L^\infty(L^2) := \sup_{(0,T)} \ a - a_h\ _{L^2(\Omega)}$ and experimental order of convergence (eoc) for the heat equation (5.2). The errors $L^\infty(L^2)$ decreases with decreasing mesh height h and the eoc approaches 2.0 with decreasing mesh height h	124

Nomenclature

$\delta(l)$	Kronecker delta
\mathbf{n}	Outward unit vector
$\mathbf{u} = (u, v)$	A vector of displacement of the elements of the actin network.
ν	Poisson's ratio
ϕ	Divergence of \mathbf{u}
β	Flow velocity of actin filaments
μ_1	Shear viscosity
μ_2	Bulk viscosity
ω_n	Domain velocity
σ_c	Contractile stress tensor
σ_e	Elastic stress tensor
σ_p	Pressure stress tensor
σ_v	Viscous stress tensor
ψ	A measure of the contractile tonicity
a	Actin filament concentration
a_c	Actin filament concentration at the chemical equilibrium
a_{sat}	Two times a_{sat} specifies the saturation concentration of actin filaments
D_a	A positive constant diffusion coefficient for actin filaments
E	Young's modulus

Chapter 1

Introduction

1.1 General overview

Cells are usually minute in size but complex in structure and dynamics. They are the smallest known basic unit of life and are capable of existing on their own in the form of a single cell organism such as amoeba. They can also exist as a group of cells (as found in multicellular organisms such as slime molds) working together to perform specific tasks towards the well being or detriment of the organism. They perform some cellular functions by responding to stimuli in their environment, usually by becoming polarised, moving, deforming (i.e a change in shape or size) and repositioning their intracellular organelles (Chen et al. 2000). Likewise in the absence of external stimuli, cells *in vitro* are found to deform spontaneously (Binamé et al. 2010; Maeda et al. 2008). It is now well established that the cortical actin filaments play an important part in both the spontaneous and migratory behaviour of cells, though the series of events that lead to each may be different (Stéphanou et al. 2004).

The migratory behaviour of cells plays a crucial role in many biological events (e.g. physiological and pathological process (Le Clainche and Carlier 2008)) such as immune response (Fleischer et al. 2007; Lauffenburger and Horwitz 1996; Ridley et al. 2003), wound healing, development of tissues (Xue et al. 2010), embryogenesis (Clark 1996; Stéphanou 2010), inflammation and the formation of tumour metastasis (Lauffenburger and Horwitz 1996; Stéphanou et al. 2008). A significant amount of work has been done in determining the migratory behaviour of cells. Most of this work has been done through theoretical studies, laboratory experiments and mathematical modelling of cell dynamics (Zaman et al. 2005). In the last few decades, a lot of studies were carried out in order to aid the understanding of biochemical processes of cell motility. These studies have improved our understanding of the order of events and the identification of some key molecular components that are actively involved in cell motility (Keren and Theriot 2008). Migration is the result of a cycle of multistep events (Rafelski and Theriot 2004; Xue et al.

2010) namely: protrusion of pseudopodia in front of the cell body (the protrusion must be large for migration to be sustained), the formation of new adhesion sites that connect the extracellular matrix to the actin cytoskeleton at the protrusion regions (Le Clainche and Carlier 2008), the development of traction, translocation of the cell body and the release of old adhesion sites at the rear of the cell (Ananthakrishnan and Ehrlicher 2007; Gupton et al. 2005; Lauffenburger and Horwitz 1996). These events depend on the mechanical properties of the cells which in turn are determined by the cytoskeleton and its associated proteins, cell structures as well as the surroundings with which the cells interact (Zhu et al. 2000). On the contrary, less work has been done towards the understanding of the spontaneous deformation of cells (Stéphanou et al. 2004). Spontaneous deformation is found to occur in both static and motile cells (Maeda et al. 2008). It has been hypothesised that spontaneous deformation of a cell is caused by an internal pressure generated in the cell cytoplasm as a result of the cortical actomyosin contraction. This pressure is assumed to be sufficient in pushing the cell membrane outward at positions where the membrane is not strongly linked to the cytoskeleton (Binamé et al. 2010; Paluch et al. 2005; 2006). It is clear that any work geared towards understanding the spontaneous dynamics of cells would shed more light on the mechanisms that govern cell dynamics and also improve understanding of the mechanisms and processes that prompt a static cell to begin to migrate.

Most of the recent studies on cell migration have focused on the mechanisms of cell-signalling that play a part towards the occurrence and sustenance of large-scale cell polarity while little attention has been given to the study of the mechanical and physical factors that engineer the large-scale coordination of cell dynamics (Keren and Theriot 2008). By coupling the interactions among the various mechanical and biochemical factors, a better understanding could be gained on the various cellular processes that regulate cell movement (Okeyo et al. 2009). Although there has been a considerable amount of work towards the study of the F-actin network dynamics, it is not fully understood how the mechanical forces produced by actomyosin contractility spatiotemporally control the F-actin flows and deformations (Okeyo et al. 2009). In Okeyo et al. (2009), it has been suggested that the mechanical forces originating from the actomyosin interactions are key to the occurrence of cell movement. Actin is a polymer that can exist either in filamentous form (F-actin) or in monomeric form (G-actin) (Chen et al. 2000) and F-actin is arranged in a paired helix of two protofilaments (Ananthakrishnan et al. 2006). The actin cortex is made up of short actin filaments that are arranged as a three-dimensional meshwork of approximately 50 nm (Ananthakrishnan et al. 2006) and underlies the cell membrane. The size of the meshwork increases towards the interior of the cell to approximately 300 nm (Ananthakrishnan et al. 2006). Actin filament usually undergoes rapid polymerisation (into F-actin) and depolymerisation (into G-actin) and this depends on physical or chemical conditions that influence the cell (Pullarkat et al. 2007). Its network is the most

prevalent and dynamic protein in the cell cytoskeleton and plays an important part in maintaining cell shape and locomotion (Pullarkat et al. 2007).

The aim of this work is to study cell deformations by considering both the mechanical and biochemical properties of the cortical network of actin filaments and its concentration. In this study, we adopt the hypothesis that the filaments will either push on the membrane when they polymerise in order to create more space for the extension of actin filaments or pull on the membrane when they contract. Contraction of the filaments occurs as a result of the interaction of actin with myosin which is a protein found in the cytoplasm. As a result of the interaction between actin filaments and myosin-II, stress fibres generate a contractile force that is used in cell locomotion and control of cell shape (Bischofs et al. 2008; Senju and Miyata 2009). We also assumed that the contraction of the network creates cytoplasmic flows throughout the cell which increase the pressure in the cytoplasm and push the membrane outward at locations where the membrane is not firmly linked to the actin network (Stéphanou et al. 2004).

Our model is a modification of a cytomechanical model by Stéphanou et al. (2004) which was an extension of an earlier model describing the actin cytogel by Lewis and Murray (1991; 1992). In our model we focus on the polymerisation kinetics of actin with regard to cell deformations as was done in Stéphanou et al. (2004) and Alt and Tranquillo (1995).

A two-dimensional (2D) approximation of the problem holds since the cell that we consider is an *in vitro* cell adhering on a 2D substrate. In an experimental condition the lamellipodial zone where the actin dynamics are taking place is very flat and can be considered 2D. In Stéphanou et al. (2004) the description of the actin dynamics was restricted to a one-dimensional circular active layer of radius r in order to avoid the problem involved in dealing with a free moving cell boundary. The radial movement of actin in the cell cortex was not considered but its tangential displacement was assumed to lead to a local increase or decrease in density on the circle which affect the intensity of the retraction force. Also the model equations were derived in the polar coordinate system. The limitation of the polar coordinate system is its difficulty in describing the evolution of a domain as it moves outside the origin of the polar coordinate. These limitations can be dealt with by using a different computational model for its numerical approximation based on, for example, a level set method (LSM) (Sethian 1996), a boundary element method (BEM) (Brebbia 1981; Crouch and Starfield 1983) or a finite element method (FEM) (Madzvamuse et al. 2003; Reddy 1993; Zienkiewicz et al. 2005). BEM is an efficient numerical tool that is very useful in the discretization of models where only the surface is of interest (Hofreither et al. 2010) and it is computationally expensive to obtain solutions in the interior of the domain. Also the application of the BEM to second-order inhomogeneous partial differential equations and nonlinear problems is much more difficult compared to the FEM (LaForce 2006). Mathematical models that describe cell dynamics are usually

non-linear in nature. FEM can be used easily to approximate non-linear problems (Reddy 1993; Sadd 2005). It can handle continuously deforming complex geometries (Madzvamuse 2006) and is thus perfect for modelling cell deformations. The LSM is an efficient numerical technique that can be used to track the motion of complex fronts as they evolve (Sethian 1996). The LSM method will not be implemented here but we intend to use it in future studies to track splitting and reconnecting cells.

There are various finite element computational strategies for moving boundary problems. An example is the moving grid finite element method which was introduced by Madzvamuse (2000) to study partial differential equations posed on complex evolving domains. It is a highly accurate, efficient and robust numerical method which has been used successfully to compute solutions of reaction-diffusion systems of biological models in growing and continuously deforming domains Madzvamuse (2006); Madzvamuse and Maini (2007); Madzvamuse et al. (2003; 2005). The novelty of the moving grid finite element method is its ability to allow the prescription of the nodal displacement of the computational grid points of the finite element mesh during the evolution of the domain (Madzvamuse 2006; Madzvamuse et al. 2005).

In view of these, we develop in this thesis a moving grid finite element computation of a cytomechanical model of cell deformation that is defined in a 2D cartesian coordinate system. We present our findings and show that this model is able to describe the intracellular actin dynamics and the resulting shapes and movements of protrusion and retraction of the membrane.

1.1.1 Outline of the thesis

In Chapter 2 we give a biological overview of the cell cytoskeleton, dynamics of actin filaments and the mechanism of cell movement. In Chapter 3 we introduce the cytomechanical model from first principles. Furthermore, in this Chapter we carry out linear stability theory in order to identify key bifurcation parameters as well as compute analytical solutions close to bifurcation points that will be used to validate numerical results. We introduce the moving finite element numerical scheme for the model in Chapter 4. In Chapter 5 we present our findings from the numerical simulations of the MGFEM. We show that this model is able to describe the intracellular actin dynamics and the resulting shapes and movements of protrusion and retraction of the membrane. Furthermore we highlight key parameters of the model that determine the cell membrane dynamics.

We introduce below some mathematical concepts and formulae.

1.2 Notation and mathematical preliminaries

1.2.1 Notation

Here we introduce some basic notation that will be used throughout the thesis.

We denote by \mathcal{R}^2 a two-dimensional euclidean space and

$$\mathcal{R}^2 = \{\mathbf{x} = (x, y) : x, y \in \mathcal{R}\}$$

with \mathcal{R} denoting a set of real numbers. An open and connected subset of \mathcal{R}^2 is known as a domain. We define our domain as $\Omega_t \subset \mathcal{R}^2$ which represents the continuously deforming and moving cell at time t and its corresponding boundary is represented by $\partial\Omega_t$, where $t \in I = [0, T_f]$. The area of $\partial\Omega_t$ for all $t \in I$ is denoted by $|\partial\Omega_t|$. In \mathcal{R}^2 we define $d\Omega_t = dxdy$ and ds is the element of arclength.

Here we let $g(\mathbf{x}(t), t)$ be scalar functions of class $C^0(\Omega_t \times R)$ and $\mathbf{w}(\mathbf{x}(t), t) = (w_1, w_2)$ a vector valued function of class $[C^0(\Omega_t \times R) \times C^0(\Omega_t \times R)]$, where $C^0(\Omega_t \times R)$ denotes a set of continuous functions in $\Omega_t \times R$. And we define the following operators.

The gradient operator

$$\nabla g = \left(\frac{\partial g}{\partial x}, \frac{\partial g}{\partial y} \right).$$

The divergence operator

$$\nabla \cdot \mathbf{w} = \frac{\partial w_1}{\partial x} + \frac{\partial w_2}{\partial y}.$$

The Laplace operator

$$\Delta g = \nabla \cdot \nabla g = \frac{\partial^2 g}{\partial x^2} + \frac{\partial^2 g}{\partial y^2}.$$

By ∇_λ we denote the gradient with respect to λ , where $\lambda(\mathbf{x}(t)) := (\lambda_1(\mathbf{x}(t)), \lambda_2(\mathbf{x}(t)), \lambda_3(\mathbf{x}(t)))$ denotes the barycentric coordinate system and

$$\nabla_\lambda g = \left(\frac{\partial g}{\partial \lambda_1}, \frac{\partial g}{\partial \lambda_2}, \frac{\partial g}{\partial \lambda_3} \right).$$

Ordinary derivatives are denoted using the Leibniz notation $dg/dx, d^2g/dx^2, \dots$, or the prime notation y', y'', \dots . Below we state some relevant mathematical concepts and formulae.

1.2.2 Some mathematical formulae

Here we let $g(\mathbf{x}(t), t)$ and $\mathbf{w}(\mathbf{x}(t), t)$ to be as defined above. We let also $r(\mathbf{x}(t), t)$ be a scalar function of class $C^0(\Omega_t \times R)$. And we recall the following theorems:

Gradient theorem

The gradient theorem is (Reddy 1993)

$$\int_{\Omega_t} \nabla r \, d\Omega_t = \int_{\partial\Omega_t} \mathbf{n} r \, ds, \quad (1.1)$$

where $\mathbf{n} = (n_1, n_2)$ is the outward unit normal to $\partial\Omega_t$ and n_1, n_2 are the rectangular components of \mathbf{n} (Larsson and Thomée 2003). Applying this to the product rg and afterwards utilizing the product rule gives

$$\int_{\Omega_t} (\nabla r)g \, d\Omega_t = - \int_{\Omega_t} (\nabla g)r \, d\Omega_t + \int_{\partial\Omega_t} \mathbf{n} r g \, ds.$$

By rewriting in component form, we obtain the following identities (Reddy 1993).

$$\int_{\Omega_t} \frac{\partial r}{\partial x} g \, d\Omega_t + \int_{\Omega_t} \frac{\partial g}{\partial x} r \, d\Omega_t = \int_{\partial\Omega_t} n_1 r g \, ds, \quad (1.2)$$

$$\int_{\Omega_t} \frac{\partial r}{\partial y} g \, d\Omega_t + \int_{\Omega_t} \frac{\partial g}{\partial y} r \, d\Omega_t = \int_{\partial\Omega_t} n_2 r g \, ds. \quad (1.3)$$

Divergence theorem

The divergence theorem is

$$\int_{\Omega_t} \nabla \cdot \mathbf{w} \, d\Omega_t = \int_{\partial\Omega_t} \mathbf{w} \cdot \mathbf{n} \, ds, \quad (1.4)$$

Green's formula

Applying the divergence theorem (1.4) to the product $g\nabla r$ we obtain the following identities known as the Green's formula (Larsson and Thomée 2003).

$$\int_{\Omega_t} \nabla r \cdot \nabla g \, d\Omega_t = \int_{\Omega_t} \Delta r \, g \, d\Omega_t + \int_{\partial\Omega_t} g \, \nabla r \cdot \mathbf{n} \, ds. \quad (1.5)$$

1.2.3 Spaces and norms

We define some important spaces and norms. Let $1 \leq p < \infty$, we define

$$L^p(\Omega_t) = \left\{ v(\mathbf{x}, t) \text{ a measurable function} : \int_{\Omega_t} |v(\mathbf{x}, t)|^p \, d\Omega_t < \infty \text{ for } \mathbf{x} \in \Omega_t, t \in I \right\}$$

and its corresponding norm

$$\|v(\mathbf{x}, t)\|_{L^p(\Omega_t)} = \left(\int_{\Omega_t} |v(\mathbf{x}, t)|^p \, d\Omega_t \right)^{\frac{1}{p}}.$$

The set $L^p(\Omega_t)$ is a Banach space. We define the following Hilbert space on Ω_t , $t \in I$:

$$H^1(\Omega_t) = \left\{ v(\mathbf{x}, t) \in L^2(\Omega_t), D^\alpha v \in L^2(\Omega_t), |\alpha| \leq 1 \right\},$$

for every $t \in I$, where $\alpha = (\alpha_1, \alpha_2)$, $|\alpha| = \alpha_1 + \alpha_2$ and D^α represents the distributional derivative at every time $t \in I$,

$$D^\alpha v = \frac{\partial^{|\alpha|} v}{\partial \alpha_1 x \partial \alpha_2 y}.$$

1.2.4 Reynolds transport theorem

Here we state the Reynolds transport theorem. This theorem shall be useful in the derivation of the moving grid finite element weak formulation.

Theorem 1.2.1. (Reynolds transport theorem) *Let $g(\mathbf{x}, t)$ be a scalar function defined on Ω_t and β be a flow velocity field then*

$$\frac{d}{dt} \int_{\Omega_t} g \, d\Omega_t = \int_{\Omega_t} \left(\frac{Dg}{Dt} + g \nabla \cdot \beta \right) d\Omega_t, \quad (1.6)$$

where D/Dt denotes a material derivative. A proof of this theorem can be found in [Acheson \(1990\)](#) and [Madzvamuse \(2000\)](#).

1.2.5 Method of Frobenius

The method of Frobenius ([Zill and Cullen 2000](#)) is usually used to solve an ordinary differential equation (ODE) by finding series solutions about a regular singular point.

Definition 1.2.1. (Regular singular points) *A singular point $x = x_0$ of a linear differential equation written in the form*

$$y'' + m(x)y' + z(x)y = 0$$

is said to be a regular singular point if $m^(x) = (x - x_0)m(x)$ and $z^*(x) = (x - x_0)^2 z(x)$ are both analytic at x_0 , i.e if they can be written in the form of a power series in $(x - x_0)$ with a positive radius of convergence.*

If an ODE has a regular singular point at $x = x_0$, then there exists at least one solution of the form ([Coleman 2005](#); [Zill and Cullen 2000](#))

$$y = (x - x_0)^\kappa \sum_{n=0}^{\infty} c_n (x - x_0)^n = \sum_{n=0}^{\infty} c_n (x - x_0)^{n+\kappa}, \quad (1.7)$$

where κ is a constant to be determined. The method of finding such a solution is called the method of Frobenius ([Zill and Cullen 2000](#)). We note that for $x_0 = 0$ the series (1.7)

reduces to

$$y = x^\kappa \sum_{n=0}^{\infty} c_n x^n. \quad (1.8)$$

1.2.6 Bessel's equation

The equation

$$x^2 y'' + xy' + (x^2 - \alpha^2)y = 0, \quad (1.9)$$

is known as the Bessel's equation. We present the analytical solution of this equation using the method of Frobenius (Coleman 2005; Zill and Cullen 2000). The analytical solution is well known (Coleman 2005; Zill and Cullen 2000) but we present it here for the sake of completeness. Here we focus only on non-negative integer values of α .

The Bessel's equation has a regular singular point at $x = 0$ thus there exist at least one solution of the form $y = x^\kappa \sum_{n=0}^{\infty} c_n x^n$. Substituting the last expression into (1.9) yields

$$\begin{aligned} x^2 y'' + xy' + (x^2 - \alpha^2)y &= \sum_{n=0}^{\infty} (n + \kappa)(n + \kappa - 1) c_n x^{n+\kappa} + \sum_{n=0}^{\infty} (n + \kappa) c_n x^{n+\kappa} \\ &+ \sum_{n=0}^{\infty} c_n x^{n+\kappa+2} - \alpha^2 \sum_{n=0}^{\infty} c_n x^{n+\kappa} = 0. \end{aligned}$$

By pulling out the first term of the first, second and fourth series we obtain

$$c_0(\kappa^2 - \alpha^2)x^\kappa + x^\kappa \sum_{n=1}^{\infty} [(n + \kappa)(n + \kappa - 1) + (n + \kappa) - \alpha^2] c_n x^n + x^\kappa \sum_{n=0}^{\infty} c_n x^{n+2} = 0,$$

or after combining the second and third series,

$$(\kappa^2 - \alpha^2)c_0 + [(\kappa + 1)^2 - \alpha^2]c_1 x + \sum_{n=2}^{\infty} \{[(n + \kappa)^2 - \alpha^2]c_n + c_{n-2}\}x^{n+\kappa} = 0. \quad (1.10)$$

A value of κ for which a solution is possible satisfies the indicial equation $\kappa^2 - \alpha^2 = 0$ (since the first term must be zero with $c_0 \neq 0$ otherwise we will have the 0 solution). The indicial roots are $\kappa = \pm\alpha$, where $\alpha \neq 0$. Substituting $\kappa = \alpha$, $\alpha > 0$, into (1.10) yields

$$[(\alpha + 1)^2 - \alpha^2]c_1 x + \sum_{n=2}^{\infty} \{[(n + \alpha)^2 - \alpha^2]c_n + c_{n-2}\}x^{n+\alpha} = 0. \quad (1.11)$$

Since (1.11) is identically zero, the identity property (Zill and Cullen 2000) implies that the coefficient of each power of x is equal to zero. Thus

$$[(\alpha + 1)^2 - \alpha^2]c_1 = (2\alpha + 1)c_1 = 0. \quad (1.12)$$

and

$$[(n + \alpha)^2 - \alpha^2]c_n + c_{n-2} = 0, \quad n = 2, 3, \dots \quad (1.13)$$

From (1.12) we have that $c_1 = 0$. And from (1.13) we have

$$n(n + 2\alpha)c_n = -c_{n-2}, \quad n = 2, 3, \dots \quad (1.14)$$

The relation (1.14) with $c_1 = 0$ implies that $c_3 = c_5 = c_7 = \dots = 0$, so for $n = 2, 4, 6, \dots$ we obtain, after choosing $n = 2k$, $k = 1, 2, 3, \dots$

$$c_{2k} = -\frac{c_{2k-2}}{2k(2k + 2\alpha)} = -\frac{c_{2k-2}}{2'k2'(k + \alpha)}.$$

This is a recurrence relation and is equivalent to (Coleman 2005; Zill and Cullen 2000)

$$c_{2k} = -\frac{(-1)^k}{2^{2k+\alpha}k!\Gamma(1 + \alpha + k)},$$

where $\Gamma(1 + \alpha + k)$ is the Gamma function. The Frobenius solution

$$\begin{aligned} y = J_\alpha(x) &= \sum_{k=0}^{\infty} c_{2k}x^{2k+\alpha} \\ &= \sum_{k=0}^{\infty} \frac{(-1)^k}{k!\Gamma(k + \alpha + 1)} \left(\frac{x}{2}\right)^{2k+\alpha}, \end{aligned}$$

where $J_\alpha(x)$ is known as the Bessel function of the first kind of order α . Also, for the indicial root $\kappa = -\alpha$, we proceed in the same way as above and obtain that

$$\begin{aligned} y = J_{-\alpha}(x) &= \sum_{k=0}^{\infty} c_{2k}x^{2k+\alpha} \\ &= \sum_{k=0}^{\infty} \frac{(-1)^k}{k!\Gamma(k - \alpha + 1)} \left(\frac{x}{2}\right)^{2k-\alpha}, \end{aligned}$$

where $J_{-\alpha}(x)$ is known as the Bessel function of the first kind of order $-\alpha$. For non-integers values of α , $J_{\alpha(x)}$ is bounded at $x = 0$, but $J_{-\alpha(x)}$ is not (Zill and Cullen 2000). This implies that they are linearly independent and the general solution of (1.9) for $x > 0$ is

$$y = C_1J_\alpha(x) + C_2J_{-\alpha}(x).$$

Let us define the function

$$Y_\alpha = \frac{(\cos \pi \alpha)J_\alpha(x) - J_{-\alpha}(x)}{\sin \pi \alpha}$$

for non-integer values of α . Y_α is known as the Bessel function of the second kind of order α and is also a solution of (1.9). Furthermore $J_{\alpha(x)}$ and Y_α are linearly independent.

Thus the general solution of (1.9) can be written as

$$y = C_1 J_\alpha(x) + C_2 Y_\alpha(x). \quad (1.15)$$

1.2.7 Modified Bessel's equation

The modified Bessel's equation of order α is

$$x^2 y'' + xy' - (x^2 + \alpha^2)y = 0. \quad (1.16)$$

This equation is solved using the method of Frobenius as was shown above for the Bessel's equation (1.9). The solution for non-negative integers, $x > 0$ is (Coleman 2005)

$$y = c_1 I_\alpha(x) + c_2 K_\alpha(x), \quad (1.17)$$

where

$$I_\alpha(x) = \sum_{k=0}^{\infty} \frac{1}{k! \Gamma(k + \alpha + 1)} \left(\frac{x}{2}\right)^{2k + \alpha}, \quad (1.18)$$

is a modified Bessel function of the first kind of order α and

$$K_\alpha(x) = \frac{\pi}{2} \frac{I_{-\alpha}(x) - I_\alpha(x)}{\sin \pi \alpha} \quad (1.19)$$

with

$$I_{-\alpha}(x) = \sum_{k=0}^{\infty} \frac{1}{k! \Gamma(k - \alpha + 1)} \left(\frac{x}{2}\right)^{2k - \alpha}. \quad (1.20)$$

$I_{-\alpha}(x)$ and $K_\alpha(x)$ are the modified Bessel function of the first kind of order $-\alpha$ and modified Bessel function of the second kind of order α respectively.

The Bessel and modified Bessel function will be used in Section 3.6.2 to obtain the analytical solution of the Neumann Laplacian on a disk.

Chapter 2

Biological overview of cell movement

2.1 Introduction

Cells are the basic unit of life capable of independent existence as observed in unicellular organisms (e.g. amoeba) or as a group as found in multicellular organisms (e.g. animals and plants). They are broadly divided into two types: namely eukaryotic and prokaryotic. Prokaryotic cells usually exist as unicellular organisms while eukaryotic cells can exist as unicellular organism (e.g. amoeba and yeast) or multicellular organisms like plants and animals ([Alberts et al. 2002](#); [Karp 1999](#)). Prokaryotes are organisms whose cells lack membrane bound organelles. Eukaryotes on the other hand, are organisms whose cells are organized into complex structures with organelles enclosed within membranes as found in multicellular organisms like plants and animals and single-cell organisms like yeast and amoeba. Though there are remarkable differences in the morphological features among single-cell and multicellular organisms, the molecular biology and biochemistry at the cellular level is basically the same ([Karp 1999](#)). In the human, there exist more than 200 different types of cells each physiologically and biochemically specialised for a specific function ([Stéphanou 2010](#)). Though cells are naturally built to carry out specific functions, in multicellular organisms, different cells come together to form tissues which work in harmony for the well being or detriment of the organism. For organisms with increasing level of complexity, tissues are organised into organs which are in turn organised into systems. The formation of tissues, organs and systems is usually achieved through cell replication and movement which makes cell movement a vital process for reproduction, maintenance and development in multicellular organisms ([Le Clainche and Carlier 2008](#)).

A general description of the structure, mechanism and dynamics of movement of a eukaryotic cell will be presented and particular emphasis would be on cytoskeleton which is the cell component that is largely responsible for deformation and movement. Relevant biological details required as a background for the development of the mathematical model will also be reviewed.

2.2 Description of an eukaryotic cell

Here we introduce the eukaryotic cell and discuss its essential components in order to set the stage for the description of cell movement.

2.2.1 Overview

A eukaryotic cell is composed of three main parts; the cell membrane, cytoplasm and nucleus. We present below their definitions.

Definition 2.2.1. (*Cell membrane*) This is a phospholipid bilayer with embedded proteins that separates the cell from its external environment. It serves as a substrate for enzymatic reactions and also controls the movement of substances in and out of cells by restricting diffusion ([Liu et al. 2008](#)).

Definition 2.2.2. (*Nucleus*) This is a membrane-bound organelle that contains most of the cell's genetic material (the DNA). It occupies about 10% of the total cell volume. The concentric lipid bilayer membrane are perforated at intervals which aids in transporting molecules between the nucleus and the cytosol. This membrane allows for various proteins that act on DNA to be concentrated at locations in the cell where they are needed ([Alberts et al. 2002](#)).

Definition 2.2.3. (*Cytoplasm*) This is the area between the cell membrane and the nucleus (see [Figure 2.1](#)) consisting of membrane-bound organelles and a network of filaments (called the cytoskeleton) suspended in the cytosol (a cytoplasmic matrix excluding the organelles). The cytoplasm contains an array of membrane-bound organelles such as mitochondria which are involved in the production of chemical energy necessary for cellular activities. It also contains organelles like the endoplasmic reticulum which are involved in the production of the cell's proteins and lipids. Also found in the cytoplasm are Golgi complexes which are involved in sorting, modification and transport of materials to specific cellular locations. ([Alberts et al. 2002](#); [Karp 1999](#)). The cytoskeletal network aid in cell movement and support ([Karp 1999](#)).

2.2.2 The cell cytoskeleton

The cytoskeleton is a complex network of filamentous protein polymers with associated proteins which provide internal organization and mechanical rigidity to cells ([Liu et al. 2008](#)). This is usually referred to as the internal cellular scaffold which controls cell shape, movement, division, transportation of organelles and numerous other vital functions ([Pullarkat et al. 2007](#)). Its main components are the microtubules, intermediate filaments, microfilaments ([Ananthakrishnan and Ehrlicher 2007](#); [Ananthakrishnan et al.](#)

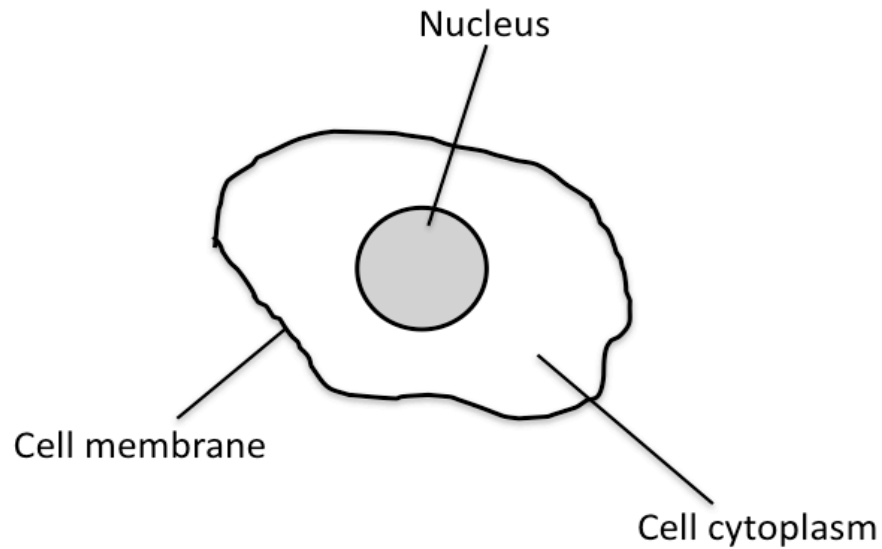


Figure 2.1: A schematic showing a cell with its three main components.

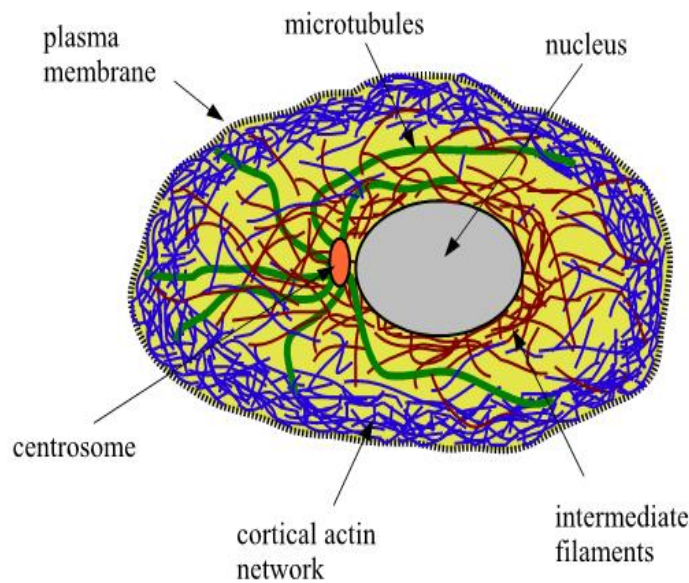


Figure 2.2: A schematic representation of the components of the cell showing the cytoskeletal filaments and some organelles (Pullarkat et al. 2007).

2006; Pullarkat et al. 2007; Zhu et al. 2000), motor proteins, crosslinking proteins, actomyosin complexes and regulation protein and ions (Pullarkat et al. 2007).

The microtubules, intermediate filaments and microfilaments (see Figure 2.2) are biopolymers that form an organized and coherent structure via entanglement, bundling, binding and crosslinking with other accessory proteins. Though all the filaments aid in cell movement, the microfilaments are the most essential (Ananthakrishnan and Ehrlicher 2007; Betz et al. 2006; Hofman et al. 1999). These can rapidly change and form organised

structures that are adapted for movement in response to the surrounding environment of the cell (Ananthakrishnan and Ehrlicher 2007).

These biopolymers are differentiated in terms of their rigidity which is measured as a function of the persistence length L_p (Ananthakrishnan and Ehrlicher 2007). The persistence length is the distance that the filament is bent by thermal forces, and is directly proportional to the rigidity and dependent on the filament length (Ananthakrishnan and Ehrlicher 2007; Morse 1998; Pampaloni et al. 2006).

Definition 2.2.4. (*Microtubule filaments*) These are polar, rod-like hollow polymers (Dogterom et al. 2005; Pullarkat et al. 2007). They are the stiffest of the biopolymer and approximately 25 nm in outer diameter (Pullarkat et al. 2007) with an L_p ranging from 100 to 5000 μm (Pampaloni et al. 2006). They are formed by the spontaneous assembly of tubulin protein subunits called tubulin monomers (Dogterom et al. 2005; Pullarkat et al. 2007) and are dynamic in nature (Dogterom et al. 2005). Usually one end is attached to a single microtubule-organising centre called a centrosome and it grows in length by polymerisation (Alberts et al. 2002; Dogterom et al. 2005). They exist in small numbers as isolated filaments and are not directly involved in important mechanical functions at the cellular level compared to microfilaments, except in cells like neurons where microtubules associated proteins bundle axons and dendrites into a tight core of aligned filaments that have a mechanical role. They serve as platform for the transport of intracellular materials, an example being the distribution of chromosomes between two newborn cells during mitosis (Pullarkat et al. 2007).

Definition 2.2.5. (*Intermediate filaments*) These are more flexible compared to microtubules and microfilaments (Zackroff and Goldman 1979). They have a L_p of approximately 0.3-1.0 μm and range in diameter from 8 to 12 nm (Pullarkat et al. 2007; Zackroff and Goldman 1979). Unlike microfilaments and microtubules they are not polarized and do not treadmill (Zackroff and Goldman 1979). Tread-milling is a phenomenon that occurs in actin filaments and microtubules when one end of the filament grows in length as a result of the addition of protein subunit while the other end shrinks as a result of the constant removal of the protein subunit from its end. Intermediate filaments are dynamic in nature (Helfand et al. 2004) but not as highly as the other filaments (Pullarkat et al. 2007). When exposed to physiological conditions that depolymerize microfilaments and microtubules, they mostly stay insoluble (Helfand et al. 2004; Pullarkat et al. 2007). They form a fibrous network that links the nucleus to the cell membrane (see Figure 2.2) serving as structural support to the cell and give resistance to shear stress (Ananthakrishnan and Ehrlicher 2007). In culture, cells can grow and move in the absence of intermediate filaments (Sarria et al. 1992) and they do not seem to show any direct active involvement in cellular activities (Lewis and Murray 1992; Pullarkat et al. 2007; Stéphanou 2010).

Definition 2.2.6. (*Microfilaments*) They are also known as actin filaments and are semi-

flexible polar polymers (Ananthakrishnan and Ehrlicher 2007; Kuusela and Alt 2009; Stéphanou 2010). They range in diameter from 6-10 nm (Ananthakrishnan and Ehrlicher 2007) and have a L_p length of approximately 10 μm - 17 μm (Gittes et al. 1993; Pullarkat et al. 2007). Actin is the most prevalent component of the cell cytoskeleton and plays a key role in maintaining cell shape, movement (Kim et al. 2009; Pullarkat et al. 2007; Stéphanou and Tracqui 2002) and the detection of external forces acting on the cell (Kim et al. 2009). It is assembled from its monomeric form called G-actin (Chen et al. 2000) and is usually arranged in a paired helix of two protofilaments (Ananthakrishnan et al. 2006). Actin is found predominantly in the area around the cell membrane called the cell cortex and its network at the cell cortex is sometimes referred to as the cortical actin network (see Figure 2.2). The cortex is made up of short actin filaments (F-actin) that are arranged as a three-dimensional mesh work of approximately 50 nm (Ananthakrishnan et al. 2006). The size of the mesh work increases from the membrane towards the interior of the cell to approximately 300 nm (Ananthakrishnan et al. 2006). They are highly dynamic in nature and rapidly polymerize into F-actin and depolymerise into G-actin and the forces generated by polymerisation is vital in the initiation of cell movement (see Figure 2.3).

Definition 2.2.7. (Motor proteins) These are molecular motors that generate mechanical forces when associated with F-actin or microtubules filaments (Pullarkat et al. 2007). They have the ability to carry out directed movement and they can transport organelles along the filaments or move the filaments themselves (Alberts et al. 2002; Pullarkat et al. 2007). They are grouped into two categories depending on the filaments along which they move, namely actin motors and microtubule motors. Actin motors are made up of the myosin family of proteins that carry out unidirectional movement along F-actin generating contractile forces as a consequence of this interaction. The contractile forces are necessary to perform mechanical functions such as cell shape maintenance, cell division and transportation of cellular organelles. Microtubule motors consist of kinesin and dyenin. Kinesin usually moves towards the plus-end of microtubules while dyenin moves towards the minus-end. They play a key role in cellular transport.

Definition 2.2.8. (Crosslinking proteins) They help in the connection of the cytoskeletal filaments. Examples of crosslinking proteins are Filamin, α -actinin (Ananthakrishnan and Ehrlicher 2007; Pullarkat et al. 2007) and fascin (Ananthakrishnan and Ehrlicher 2007). They are essential for controlling the assembly of filaments and help in establishing the elasticity of actin filament network (Pullarkat et al. 2007).

Definition 2.2.9. (Actomyosin complexes) These are complexes that result from the interaction of myosin motor proteins with actin filaments. Myosin II, a member of the myosin family of motor proteins, are capable of assembling into short bipolar chains which in turn

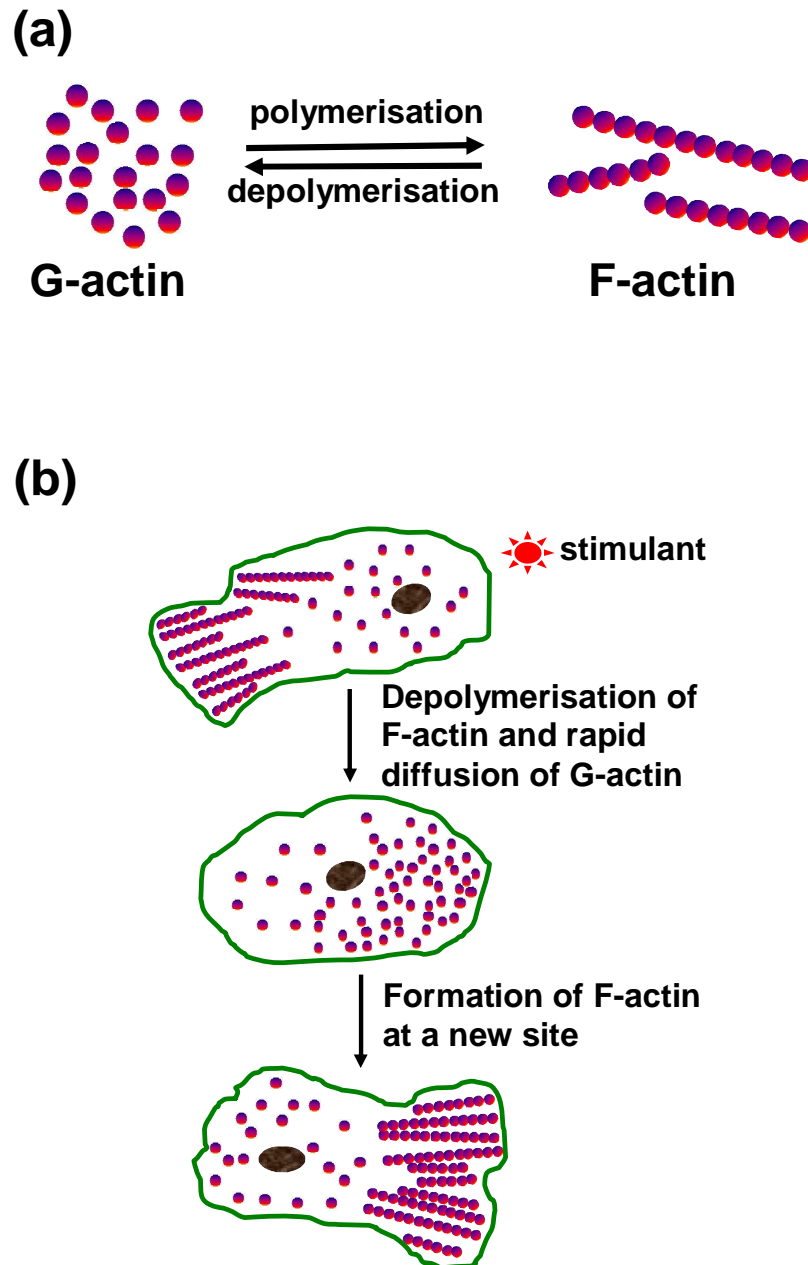


Figure 2.3: A schematic description of actin polymerisation and de-polymerisation kinetics. (a) is an illustration of actin polymerisation and de-polymerisation. (b) is an illustration of cell membrane protrusion in response to a stimulant. G-actin molecules rapidly diffuse towards the side closer to the stimulant and polymerises into F-actin. The force generated by the polymerisation causes the membrane to protrude towards the source of the stimulant.

interact with neighbouring actin filaments to generate active contractile stresses within the actin network. These stresses are necessary for regulating cell shape and also controlling cell movement. In eukaryotic cells, actomyosin complexes exist in a random network of highly cross-linked gel forming the actin cortex which is attached to the plasma membrane. A cell fragment containing only actomyosin complexes is capable of generating

and maintaining its movement ([Pullarkat et al. 2007](#)).

Definition 2.2.10. (*Regulatory proteins and ions*) Regulatory proteins also known as nucleation-promoting factors (NPFs) ([Pollard 2007](#)) are actively involved in the control of actin polymerisation/de-polymerisation kinetics and in the regulation of the activity of motor proteins ([Ananthakrishnan and Ehrlicher 2007](#)). Actin polymerisation promoting proteins such as nucleator proteins (e.g. Arp2/3 complex) initiate the assembly of new filaments. Other regulatory proteins like thymosin are able to bind and isolate a large amount of G-actin in the cell while others like profilin bind to G-actin monomer to form a complex which readily adds to the free plus end of an actin filament to affect polymerisation. On the other hand, cofilin also called actin depolymerising factor, is capable of binding to either the monomeric G-actin or the polymeric F-actin. The binding of cofilin along the length of actin filament causes it to twist more tightly creating a stress which weakens the interaction of subunits within the filament causing the filament to break. The activity of gelsolin an actin filament severing protein is activated by the presence of high concentration of cytosolic Ca^{2+} an important regulatory ion. Also, Ca^{2+} activates several protein-kinases which result in phosphorylation of myosin motors thus enhancing contractility of actomyosin complex ([Alberts et al. 2002](#); [Pullarkat et al. 2007](#)).

Among the cytoskeletal components, actin and its accessory proteins are the most vital for cell movement. In the next section we present a detailed description of actin, its dynamical nature and interactions with its accessory proteins ([Stéphanou and Tracqui 2002](#)).

2.3 Dynamics of actin filaments

Actin can exist as a monomeric G-actin or polymeric F-actin. The polymeric F-actin can undergo further polymerisation to form longer actin filament or depolymerise to form monomeric G-actin and this depends on its physical or biochemical surrounding conditions ([Pullarkat et al. 2007](#)). The changes from F-actin to G-actin and vice versa helps regulate the elastic property of the cell and are vital for cell movement ([Ananthakrishnan and Ehrlicher 2007](#)) and maintenance of cell shape ([Stéphanou and Tracqui 2002](#)). F-actin has two distinct ends: a fast growing end otherwise known as the plus end (oriented towards the membrane) with a critical actin monomer concentration C_p of $\sim 0.1 \mu\text{M}$ and a slow growing (minus) end with a critical actin monomer concentration of $C_m \sim 0.6 \mu\text{M}$ ([Alberts et al. 2002](#)). When the concentration of monomeric actin is higher than its critical concentration C_p , then F-actin polymerisation occurs at both ends but when the concentration is lower than the critical concentration C_m , F-actin depolymerises into G-actin ([Ananthakrishnan and Ehrlicher 2007](#)). When the actin monomer concentration lies between C_p and C_m , then only the plus end polymerises while the minus end

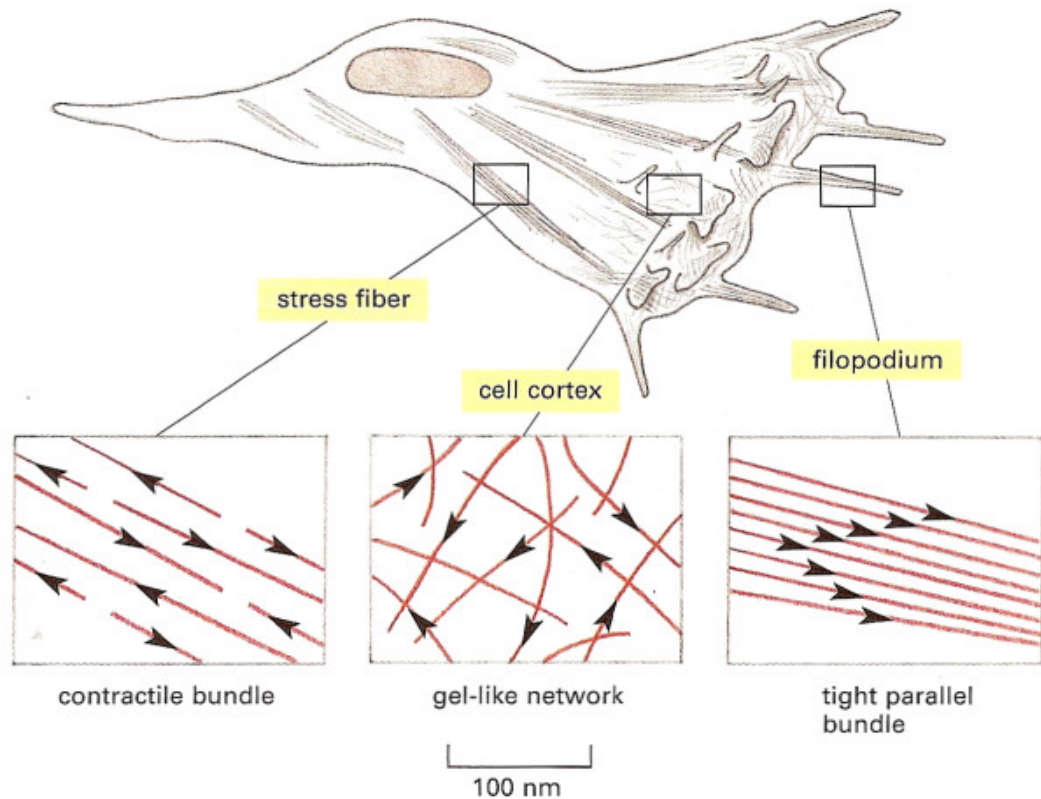


Figure 2.4: An illustration of a crawling cell with three areas enlarged to show the arrangement of actin filaments. Actin filaments are shown in red, the arrowheads are pointing towards the plus end (Alberts et al. 2002).

depolymerises (Ananthakrishnan and Ehrlicher 2007) a process known as tread-milling (Ananthakrishnan and Ehrlicher 2007). The tread-milling rate (0.1 subunits per sec. at the barbed end) is very slow hence it is unlikely to influence the overall actin filament growth in cells (Pollard 2007).

In physiological conditions, F-actin can assemble into different structures forming networks and bundles (Kaverina et al. 2002; Pollard et al. 2000) through its interaction with numerous accessory proteins (Pollard et al. 2000). The F-actin structures produce two major distinct types of cell protrusions, namely the lamellipodia (flat sheet-like protrusions) and filopodia (spiky protrusions) (Hoglund et al. 1980; Insall and Machesky 2009; Small 1981; Small et al. 1978; Svitkina et al. 1997). Lamellipodia contain actin networks while filopodia contain actin bundles (Hoglund et al. 1980; Small 1981; Small et al. 1978; Svitkina et al. 1997)(see Figure 2.4 for an illustration of actin network and bundles). Both lamellipodia and filopodia vary in length between $0.1 - 0.2\mu\text{m}$ and leads to migration (Urban et al. 2010).

2.3.1 Molecular mechanism of actin nucleation

Actin is the most predominant protein found in most eukaryotic cells and more than half of it is in its monomeric form. Actin monomers can spontaneously assemble into short oligomers which are unstable and readily dissociate because such assembly results from a monomer binding to a few other monomers. For a new stable long filament to form, the monomers must first assemble into a nucleus which is stabilised by multi monomer-monomer interactions which can then polymerise rapidly by adding more monomers. The process by which a stabilised nucleus is formed is called actin filament nucleation (Alberts et al. 2002). There exists a strong inhibition by profilin and thymosin- β 4 to nucleation of new filaments (Pollard and Borisy 2003) but once they are nucleated they can grow with or without the aid of accessory proteins (Insall and Machesky 2009). A dendritic nucleation hypothesis explains the assembly of actin filaments at the front of motile cells. An illustration of actin nucleation is shown in Figure 2.6 (Pollard 2007). Numerous proteins are associated with actin monomers to promote the process of actin nucleation but Arp2/3 complexes and formin play the major role in this process. Arp2/3 complex consists of seven subunits, but Arp2 and Arp3 are the only subunits that are involved in actin nucleation (Insall and Machesky 2009). It is biochemically inactive when isolated from its associated proteins (Insall and Machesky 2009; Machesky et al. 1999; Millard et al. 2004; Pollitt and Insall 2009) and is activated through interactions with VCA the C-terminal of WASP family protein and an actin filament (Insall and Machesky 2009). The WASP family regulates the activity of Arp2/3 complex by acting as intermediates to integrate signals from small GTPases (e.g. Rac and Cdc42), signal adapters (e.g. Grb2 and Nck) and membrane phospholipids (e.g. PIP2, and protein kinases) (Insall and Machesky 2009). Arp2/3 is activated if the signal is greater than the threshold for activation and converts the signal to actin polymerisation. Arp2/3 complex produces branched filaments by anchoring the pointed end of a new filament to an existing actin filament (Pollard 2007) (see Figure 2.5, (Insall and Machesky 2009)). This allows the free end of the new filament to continue to grow until stopped by a capping protein. These new filaments are usually nucleated at an angle of 70° from the sides of the existing filaments. They push out the leading edge of motile cells as they grow thus producing a lamellipodium (Pollard 2007). This has been observed under an electron microscope (Insall and Machesky 2009).

Formin is a member of a family of proteins with a formin homology-2 (FH2) domain (Pollard 2007) which binds actin. Some members of the formin family of protein have both formin homology-1 (FH1) (which binds profilin) and FH2 domain. They form a new filament nucleus from monomeric actin and stay bound to the growing end of the new actin filament and maintain the growth of the filament by encouraging the addition of more monomers (Romero et al. 2004). It also protects the actin filament against capping proteins that usually terminate the process of actin polymerisation. Formins produce un-

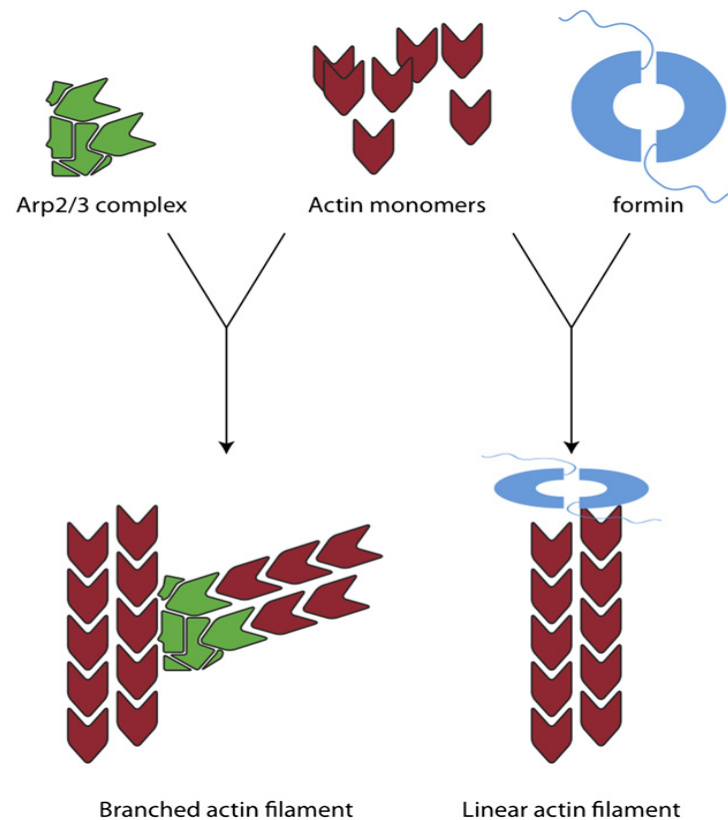


Figure 2.5: Schematic description of the activity of Arp2/3 complex and formins during actin nucleation in cells. Arp2/3 complex and formins initiate the production of new actin filaments via polymerisation of monomeric actin. Arp2/3 initiates the production of branched filaments while formins are dimers and are attached to the growing ends of actin filaments. Formin act by encouraging the growth of single filaments necessary for formation of actin bundles (Insall and Machesky 2009).

branched single filaments that are mostly oriented perpendicular to the membrane (Pollitt and Insall 2009). They act against capping proteins by staying attached to the barbed end (i.e. fast growing end) of the actin filament (see Figure 2.5 for an illustration (Insall and Machesky 2009)). These single filaments are necessary for the formation of actin bundles that produce filopodia. During the formation of filopodia, actin monomers that are ready for polymerisation are usually complexed to profilin (Insall and Machesky 2009). In living organisms multiple isoforms of profilin exist and some of them interact with formin to enhance actin polymerisation (Neidt et al. 2009). The profilin-actin complexes have a characteristic of rapid filament assembly and are produced through the help of a proline-rich sequence in the formin-homology 1 (FH1) region. Furthermore, the formin-homology 2 (FH2) domain (containing two antiparallel actin binding ends) encourages polymerisation by enhancing the addition of profilin-actin complexes to the barbed (growing) end of the filament (Xu et al. 2004).

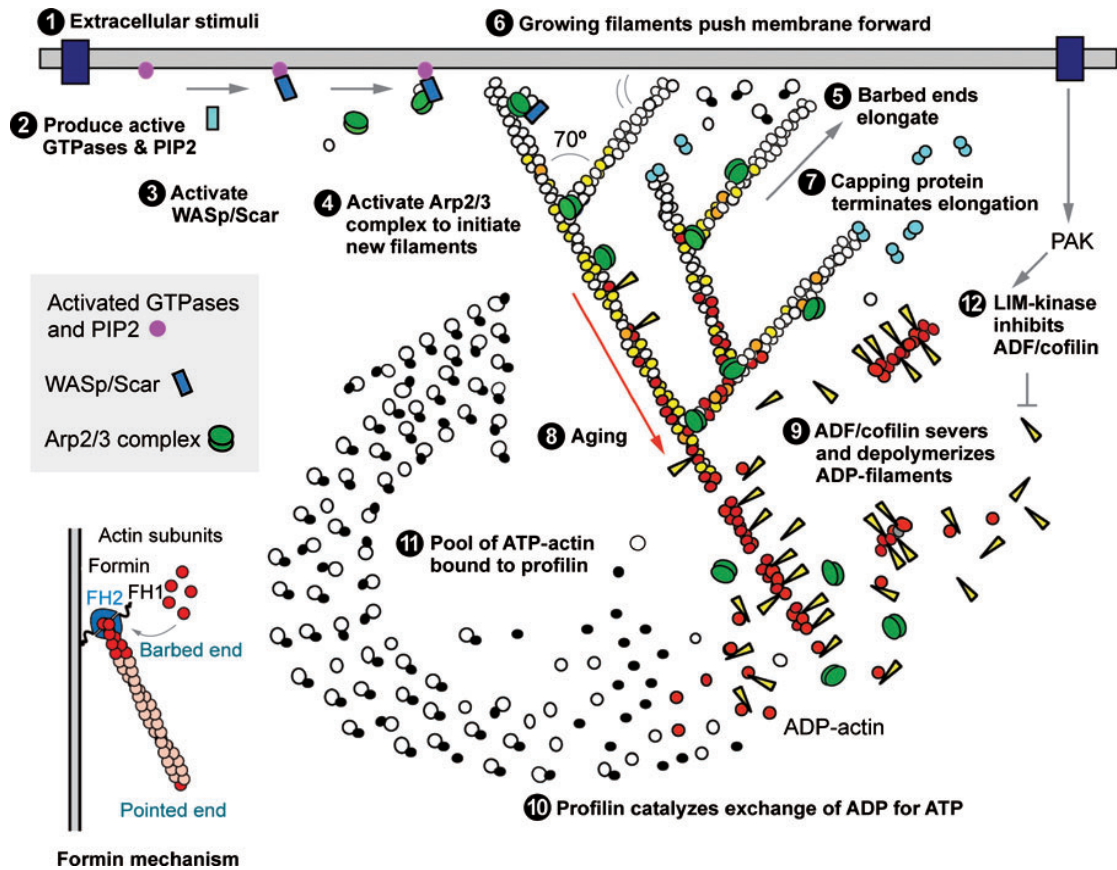


Figure 2.6: Schematic representation of the process of actin nucleation in cells. Nucleation promoting factors such as WASP and Scar/WAVE activates Arp2/3 complex to nucleate a branch. The growing ends of the filament branch grows until it is capped by capping proteins and pushes out the membrane as it grows thereby creating a lamellipodia (Kovar and Pollard 2004; Pollard 2007; Pollard and Borisov 2003; Pollard et al. 2000).

2.3.2 Actin depolymerisation enhancing proteins

In living cells the dynamics of actin filaments are essential because different physiological conditions require actin in different forms and this dynamism is achieved by actions of actin binding proteins. Some of the actin binding proteins enhance polymerization while others enhance de-polymerisation. All these proteins work in conjunction with numerous accessory proteins to coordinate the dynamics of actin network. The actin de-polymerising proteins include the cofilin and the gelsolin family of proteins (Ananthakrishnan and Ehrlicher 2007).

Cofilin is an actin de-polymerising protein that binds to both monomeric and filamentous form of actin. It binds along the length of actin filaments forcing it to twist more tightly. The mechanical stress produced through this binding weakens the interactions between actin subunits in the filaments thus enhancing severing. This also makes the ADP-actin subunits at the minus end of the filaments to dissociate, thus increasing

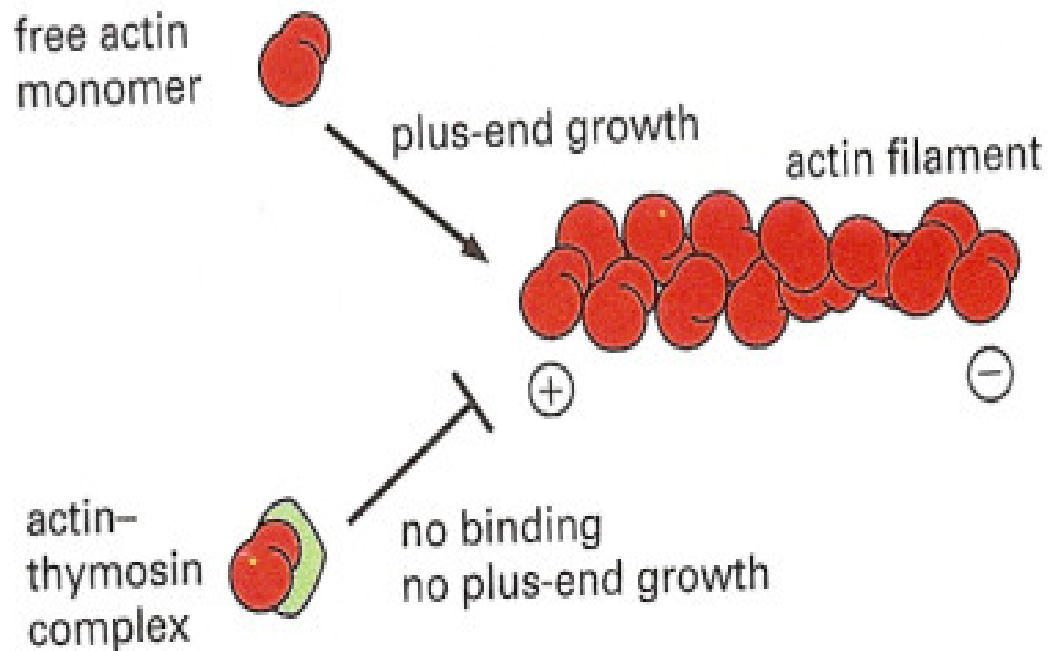


Figure 2.7: Actin-thymosin complex is sterically prevented from binding to the plus end of an actin filament (Alberts et al. 2002).

tread-milling (Alberts et al. 2002).

Gelsolin, another actin depolymerization protein, binds and severs actin filaments. It has two subunits that bind to two different sites on the actin subunit. One of the binding sites is exposed on the surface of the filament while the other is hidden in the longitudinal bond between the subunit. Once gelsolin severs an actin filament, it caps and remains bound to the plus end actin as an effective capping protein (Alberts et al. 2002; Ananthakrishnan and Ehrlicher 2007).

2.3.3 Actin binding and cross-linking proteins

Actin binding proteins such as profilin and thymosin aid in promoting the availability of actin monomers for polymerisation (Ananthakrishnan and Ehrlicher 2007). Thymosin is a small protein that binds to actin monomers sequestering them from getting involved in actin polymerisation (see 2.7 for an illustration). The thymosin-actin complex cannot associate with either the plus or minus end of the actin filaments and therefore cannot hydrolyse or exchange their bound nucleotide. When cellular conditions require for actin polymerisation, the sequestered thymosin-actin complex is made available for polymerisation by binding to another actin binding protein called profilin. Once profilin binds to thymosin-actin complex there occurs conformational changes that will result in the dis-

sociation of thymosin from actin but strengthening profilin-actin complex (Alberts et al. 2002; Ananthakrishnan and Ehrlicher 2007). The profilin actin complex can readily add onto the free plus end of an actin filament. The activity of profilin is regulated by intracellular mechanism like phosphorylation and inositol phospholipid binding. The ability of profilin to move thymosin sequestered actin to the cell membrane where actin polymerisation is required for the formation of actin-rich motile structures like filopodia and lamellipodia is crucial and this is why profilin is located in the cytosolic face of the cell membrane where it binds to acidic membrane phospholipids (Alberts et al. 2002; Pollard 2007).

Cross-linking and bundling proteins aid in the connection of actin network. Example of such proteins are filamin, α -actinin and fascin (Ananthakrishnan and Ehrlicher 2007). Single filaments are bundled together into a bundle by proteins such as fascin, fimbrin and scruin (Ananthakrishnan and Ehrlicher 2007).

2.4 Cell movement

Cell movement was first observed by van Leeuwenhoek in 1675 using a microscope slide (Ananthakrishnan and Ehrlicher 2007; Karp 1999). The microscopic observation of moving cells created a great deal of interest in understanding the reasons and mechanisms by which cells move. A lot of experimental work has been carried out to study the behaviour of cells both *in vivo* and *in vitro*. Alongside the experimental work, theoretical studies and mathematical modeling have been excellent tools in the acquisition of the available wealth of knowledge on cell movement. Despite all these studies, a total understanding of the regulation of molecular, biochemical and mechanical factors during cell movement is yet to be conceived.

Cells are very dynamic entities and they are capable of existing on their own (as found in unicellular organisms) or as a group of the same or different types of cells (as found in multicellular organisms). In multicellular organisms each type of cell is designed for a particular function and they are the basic functional unit. Large numbers of cells specialized for a particular function come together to make up tissue. They are also organized to form organs, and organ systems which work together to perform necessary tasks for the well being or detriment of the organism. Most of the essential tasks involves cell movement which is a vital and complex activity performed by all living organisms (Aizawa et al. 1996).

Cell movement plays important roles in many physiological and pathological process (Le Clainche and Carlier 2008) such as immune response (Fleischer et al. 2007; Lauffenburger and Horwitz 1996; Ridley et al. 2003), wound healing, development of tissues (Xue et al. 2010), embryogenesis (Clark 1996; Stéphanou 2010), inflammation and the formation of tumour metastasis (Lauffenburger and Horwitz 1996; Stéphanou et al. 2008). It is

thus imperative that cell movement be well understood because of its paramount role in key biological events necessary for development and function.

2.4.1 Mechanism of cell movement

Different types of cells exhibit various kinds of movements for example sperm cells move by swimming, prokaryotes such as bacteria move by the rotation of their flagellar motors (Alberts et al. 2002) but most animal cells migrate by crawling (Nobes and Hall 1999). The migratory modes of crawling cell can be grouped into mesenchymal and amoeboid depending on the structures that enhance the movement (Binamé et al. 2010). A detailed description of the migratory modes illustrated in Figure 2.8 is given below.

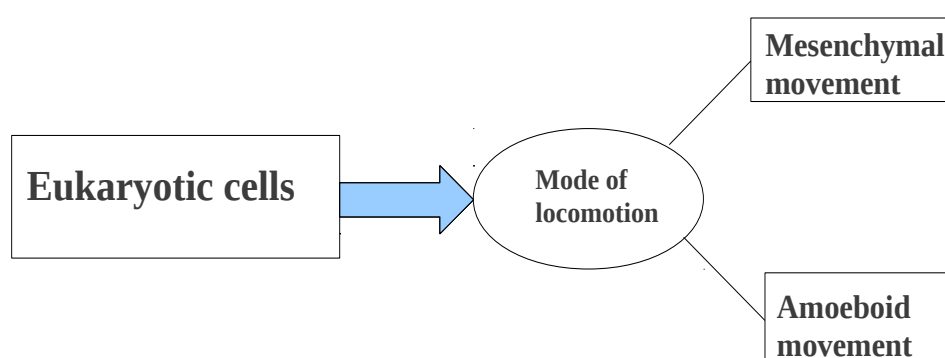


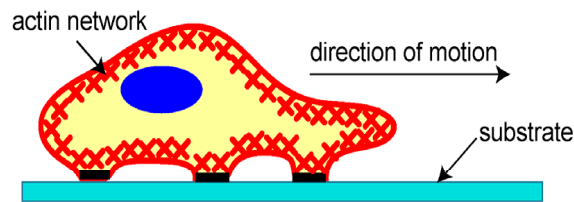
Figure 2.8: Schematic representation of the two modes of migration in eukaryotic cells.

Mesenchymal movement

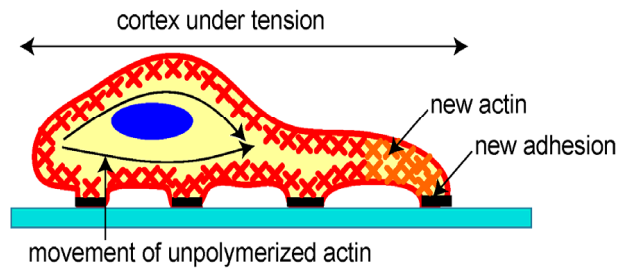
Mesenchymal movement is a mode of locomotion in which cells adopt an elongated and polarized morphology with lamellipodia (Binamé et al. 2010). Lamellipodia are flat sheet-like protrusions parallel to the substrate at the front of spreading and migrating cells (Small et al. 2002). These sheet-like protrusions first observed by Abercrombie et al. (1970) are otherwise known as the leading edge but they are called ‘ruffles’ when they coil upward (Abercrombie 1980; Abercrombie et al. 1970; 1971; Small et al. 2002).

Mesenchymal movement has been widely studied and the series of processes that lead to this mode of migration is known (Binamé et al. 2010). In mesenchymal movement, migration is the result of a cycle of multistep events (see Figure 2.9 for an illustration) beginning with protrusion of pseudopodia, the formation of new adhesion sites that connect the extracellular matrix to the actin cytoskeleton at the protrusion regions (Le Clainche and Carlier 2008), the development of traction, translocation of the cell body and the release of old adhesion sites at the rear of the cell (Ananthakrishnan and Ehrlicher 2007; Gupton et al. 2005; Lauffenburger and Horwitz 1996; Xue et al. 2010). These series of

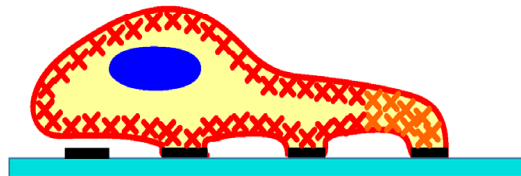
1) Protrusion of the Leading Edge



2) Adhesion at the Leading Edge



Deadhesion at the Trailing Edge



3) Movement of the Cell Body

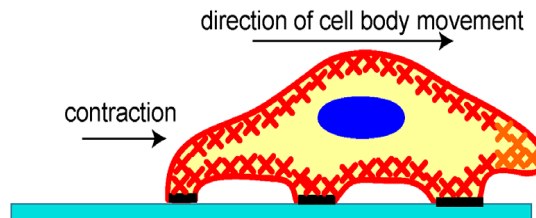


Figure 2.9: A schematic illustration of the three stages of mesenchymal mode of cell migration ([Ananthakrishnan and Ehrlicher 2007](#)).

events are counterbalanced by random membrane activities which subsequently encourage more protrusions and, if sustained, lead to a new direction of movement ([Binamé et al. 2010](#)). Meanwhile the protrusion of the pseudopodia in front of the cell body must be large for migration to be sustained. As a result, the cell migrates with directional migration on a short scale but after a long time it becomes random ([Binamé et al. 2010](#)) in the absence of external cues.

Mesenchymal migration is dependent on the proteolysis of extracellular matrix (ECM) and integrins of the migrating cells, and relies on the production of matrix metalloproteinases ([Parri et al. 2009](#); [Yamazaki et al. 2005](#)). Metalloproteinases disrupt regions of

adhesion of the cell to the ECM by targeting both integrins and matrix components (Binamé et al. 2010) thus creating a path for migration (Parri et al. 2009).

Amoeboid movement

Amoeboid movement is a primitive mode of cell migration (Parri et al. 2009). In this mode, migrating cells glide through the ECM, rather than degrading it, because cell-ECM adhesion is weak (Friedl et al. 1998) and there is no involvement of integrins (Binamé et al. 2010).

Amoeboid movement can occur in cells that do not possess actin for example nematode sperm (Robert and Stewart 1997) and in actin-rich cells such as fibroblasts (Stéphanou et al. 2008), *Dictyostelium discoideum* (Firtel and Meili 2000), leukocytes (Friedl and Weigelin 2008), hematopoietic stem cells (Giebel et al. 2004) both *in vivo* and in 3D cultures (Sahai and Marshall 2003). In actin-rich cells, amoeboid movement is believed to be induced by the interplay between an active contractile force and a passive hydrostatic pressure generated in the cell cytoskeleton.

Amoeboid movement is initiated by the production of blebs which are bubble-like protrusions on the surface of the cell occurring in both motile and non-motile cells. When they occur in non-motile cells they give rise to spontaneous deformation of the cell membrane. These spontaneous deformations occur without any external stimulant. An observation of unstimulated fibroblasts under an electron microscope reveal well organised spatial and temporal dynamics of the cell membrane protrusions and not random, as found in stimulated cells (Stéphanou et al. 2008). Internal pressure has been implicated as the key force that generate the membrane blebs that are observed at the front of protrusions in unstimulated cells and this is known to play a key role in cell deformation (Abraham et al. 1999; Bereiter-Hahn and Luers 1998; Charras et al. 2005).

It is assumed that blebs are initiated by either a local rupture of the actin cortex (Keller and Eggli 1998) or a local membrane dissociation from the actin cortex (Cunningham 1995). Localized contractile force generated by the actomyosin network can give rise to both conditions that initiate blebs. Myosin activation pathways like Rho-Kinase (ROCK) and myosin light chain kinase (MLCK) has been observed in non-motile and motile blebbing cells which is an evidence of its involvement in blebbing (Charras and Paluch 2008). The intracellular hydrostatic pressure generated by the actomyosin complex can locally weaken membrane-cortex adhesion or rupture actin cortex thus initiating a bleb (Charras and Paluch 2008). The detachment of membrane from actin cortex has been observed in motile cells like *Fundulus* deep cells (Fink), zebrafish PGCs (Blaser et al. 2006) and walker carcinosarcoma cells (Keller et al. 2002) while a local rupture of the actin cortex has also been observed in fixed walker carcinosarcoma cells (Charras and Paluch 2008; Keller et al. 2002).

Initially blebs are free of actin cytoskeleton but afterwards they begin to expand with

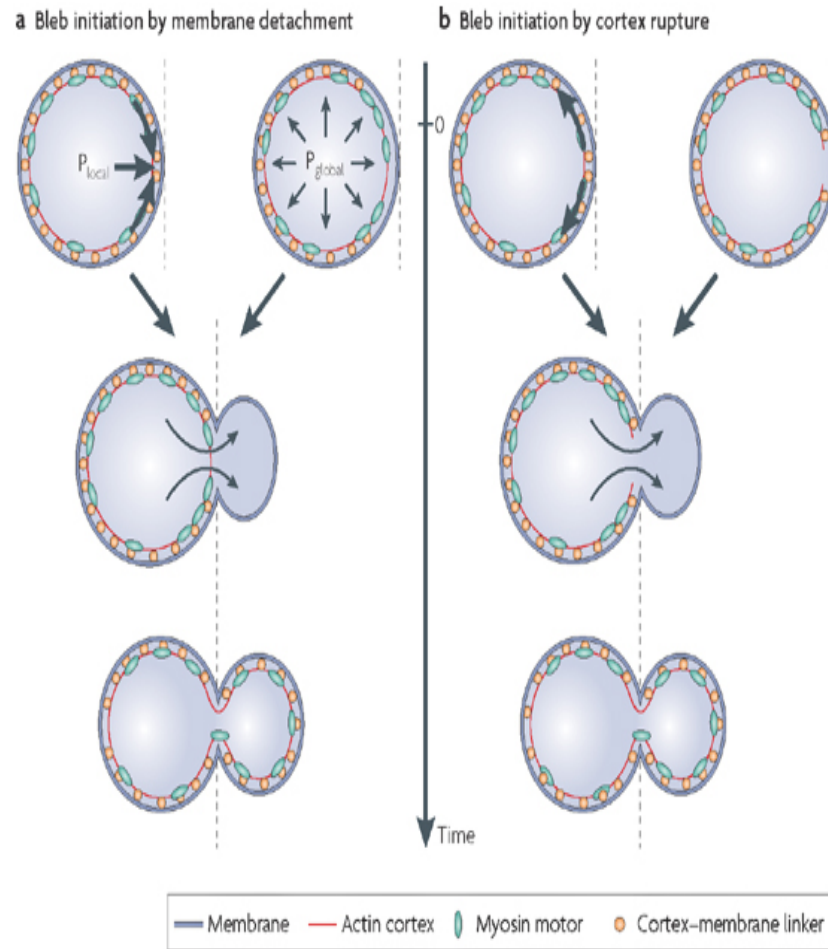


Figure 2.10: A schematic illustration of the initiation of blebs. They are formed either by the rupture of the cortex or by membrane detachment. In **a**, a local or global pressure resulting from a local or global contractile activity of actomyosin complex can detach the membrane from the cortex thereby initiating a bleb. In **b**, a local rupture of the cortex initiates a bleb. In both cases expansion of the bleb is caused by an intracellular hydrostatic pressure generated by the effect of the contractile stress on the cytosol (Charras and Paluch 2008).

influx of cytosol, actin, myosin and other accessory proteins. Thereafter actin and myosin interact together beneath the bleb and generate contractile stress which causes the bleb to retract as observed in non-migrating cells (Charras and Paluch 2008). On the other hand, in migrating cells retraction of the bleb does not always occur but instead the contractile stress originating from the rear of the cell translocates the cell body (Blaser et al. 2006; Charras and Paluch 2008). It has been observed experimentally that blebbing can initiate migration in motile cells like amoebae, embryonic cells, mammalian tumour cells (Blaser et al. 2006; Sahai and Marshall 2003; Trinkaus 1973; Yoshida and Soldati 2006). Blebbing is used by embryonic cells during embryogenesis (Blaser et al. 2006) and by tumour cells during metastasis (Fackler and Grosse 2008; Sahai and Marshall 2003; Yoshida and

[Soldati 2006](#)).

Blebbing is associated with extreme cell deformability, thus allowing them to easily pass through a mesh of extracellular matrix ([Wolf et al. 2003](#)). Also, since there is no involvement of integrins with only weak impact on the ECM, blebbing cells move through the mesh of ECM relatively quick. In contrast to mesenchymal migration, the inhibition of matrix proteases does not inhibit amoeboid movement which shows that the impact of blebbing cells on the ECM is weak. Cells moving on two dimensional (2D) surfaces usually form lamellipodia and filopodia which initiate mesenchymal movement while those moving on three dimensional (3D) surfaces have a preference for bleb driven migration. In cancerous cells, it has been observed that drugs which would usually prevent mesenchymal movement by inhibiting matrix proteases did not affect the spread of the tumour cells in 3D matrix ([Insall and Machesky 2009](#)). Recently, it has been observed that the mode of migration assumed by a cell is dependent on physiological conditions surrounding it for example, neutrophils and lymphocytes switch to bleb driven migration when substrate adhesion is reduced ([Insall and Machesky 2009](#); [Malawista et al. 2000](#); [Sroka et al. 2002](#)).

2.5 Project motivation

In the last few decades, a lot of studies have been carried out in order to aid the understanding of biochemical and biophysical processes that determine cell movement. Laboratory experiments, theoretical studies and mathematical modelling of cell dynamics have been utilised in most of the studies ([Zaman et al. 2005](#)). These have lead to the identification of some essential molecular components involved in cell movement and have also unravelled the sequence of events that determine cell movement ([Keren and Theriot 2008](#)). Mechanisms of cell-signalling which are involved in production and sustenance of large-scale cell polarity have been the focus of many of the recent studies on cell movement while studies on the mechanical and physical factors that engineer the large-scale coordination of cell dynamics have been of little interest ([Keren and Theriot 2008](#)). Cell movement is governed by a combination of chemical kinetics, transport and physical forces and movement of actin network interacting with their associated proteins hence it can be modelled mathematically by coupling together the models of continuum mechanics and biochemical kinetics ([Evans 1993](#); [Mogilner 2009](#); [Oster 1984](#)). A better understanding could be gained into the processes that regulate and control cell movement through the coupling of the interactions among the various biophysical and biochemical factors that control cell movement ([Okeyo et al. 2009](#)). Though extensive research on F-actin network dynamics have been carried out, a complete understanding of how the mechanical forces generated by actomyosin contractility control the spatio-temporal flow of F-actin and cell deformation is yet to be reached ([Okeyo et al. 2009](#)).

The primary aim of this work is to motivate a numerical method for the approximation of a mathematical model describing cell deformations. The model we will consider was initially developed to study cell deformations by considering both the biophysical and biochemical properties of the cortical network of actin filaments with its associated proteins. In this project, we adopt the hypothesis of a pressure-driven protrusion. We assume that the filaments will either push on the membrane when they polymerise in order to create more space for their growth or pull on the membrane when they contract. Contraction of the filaments occurs as a result of the interaction of actin with myosin-II in the cell cytoplasm. Due to their interaction, stress fibres generate a contractile force which is used in cell movement and cell shape control (Bischofs et al. 2008; Senju and Miyata 2009). We also assume that the contraction of the actin network creates cytoplasmic flows throughout the cell which increase the pressure in the cytoplasm and push the membrane outward at locations where the membrane is not firmly linked to the actin network (Alt and Tranquillo 1995; Stéphanou et al. 2004).

The model we consider is a modification of a cytomechanical model by Stéphanou et al. (2004) which was an extension of an earlier model describing the actin cytoskeleton by Lewis and Murray (1992). In the model by Lewis and Murray (1992), cell movement was assumed to be driven by cycles of solation (expansion) and gelation (contraction) of actin and believed to be controlled by the level of calcium (Stéphanou 2010). Solation of actin is believed to occur when a given threshold of calcium is reached which in turn activates the expansion of the actin gel thus pushing the membrane outwards. Re-gelation of actin occurs when the calcium level falls below its threshold which causes the network to contract again (Stéphanou et al. 2004). Later experimental studies showed the prevalence of actin filaments and polymerization promoting proteins at protruding regions of the cell and identified actin polymerization to be a key process in cell deformations and movements (Mogilner 2009). The model by Lewis and Murray (1992) was modified by Alt and Tranquillo (1995) to describe the polymerisation and de-polymerisation kinetics. In our model we focus on the polymerisation kinetics of actin with regard to cell deformations as was done in Stéphanou et al. (2004) and Alt and Tranquillo (1995).

We will implement a finite element numerical approximation of an extension of a cytomechanical model of cell deformations and then study the spatio-temporal dynamics of the cell by considering the interactions between the mechanical and biochemical properties of actin dynamics. We also seek to identify key parameters that determine cell movement.

Chapter 3

Mathematical description of cell movement

3.1 Introduction

The focus of this chapter is to introduce a mathematical model for cell deformation and then present a detailed mathematical analysis of the model. For many centuries, experimental biology was main stream in the quest to decipher the complexity of cell movement. In recent decades mathematical modelling and theoretical studies have contributed immensely in elucidating the understanding of the migratory behaviour of cells ([Zaman et al. 2005](#)) and is projected to take a leading role in future developments of cell movement ([Flaherty et al. 2007](#)). This is due to the ability of the increasingly sophisticated computer programs to perform complex simulations relating to biological systems even at the cellular level. With the help of these sophisticated computer programs the inherent problems like time consumption and high cost associated with laboratory experiments can be highly reduced ([Flaherty et al. 2007](#)).

Cell movement involves a vast number of different kinds of proteins all interacting in complex networks. The interaction of actin with its associated proteins is usually a major factor in the derivation of models for cell movement. For example, the process of cell membrane protrusion is usually modelled with respect to localized actin polymerisation ([Flaherty et al. 2007](#); [Gracheva and Othmer 2004](#); [Mogilner 2009](#)). Proposing an accurate model to account for the vast molecular interactions involved in cell movement is a non-trivial activity. This has greatly motivated the proposition of models based on single stages of cell movement such as protrusion, contraction and adhesion. The advantage of these type of models is that they allow for a higher level of resolution of each process which hitherto would not have been feasible in a unified model ([Pollard and Borisy 2003](#)).

Mathematical modelling of cell movement began as a result of the need to understand the process of actin tread-milling ([Mogilner 2009](#)). The initial models by [Hill and](#)

Kirschner (1982), Wegner (1976) and Oosawa and Asakura (1962) were geared at quantifying the actin treadmill and employed thermodynamics to study the nature and size of the force generated by actin polymerisation. These models provided basic ideas that are still used in new and complex models (Mogilner 2009). A model by Peskin et al. (1993) proposed a Brownian ratchet model to describe actin polymerisation as rigid ratchet mechanism which elongates by rectifying the Brownian motion of the membrane. According to this model, when the end of an actin filament comes into contact with a membrane, the membrane could diffuse away and thus create a gap. If this gap is large enough then the filaments will elongate by the addition of monomers to the growing end (Mogilner 2009; Pollard et al. 2000). An improvement of this model by Mogilner and Oster (1996) considers the filaments to be elastic springs whose behaviour is a function of the bending modulus of the filament and the angle it makes with a load (e.g. membrane) at its tip. The thermal fluctuations of actin filaments displaces the actin filaments from the membrane and creates a gap for the elongation of the filament (Mogilner 2009). The elastic restoring force of the filament acts to restore the elongated filament to its original position and gives rise to the protrusion of the membrane (Mogilner 2006; Mogilner and Oster 1996). This model was able to predict an optimal angle between the actin filament and the load for effective force transmission. Subsequent study showed that protrusion is not determined by the dynamics of individual filaments but by a dendritic actin network. This motivated the development of a model by Mogilner and Edelstein-Keshet (2002) to study protrusion based on the dendritic-nucleation hypothesis. By using a 1D model consisting of a system of partial differential equations describing the diffusion, reaction, filament elongation and de-polymerisation of actin alongside other processes observed during the nucleation of actin filaments they were able to show that the velocity of protrusion is directly proportional to the quantity of barbed ends around the front of the cell. The microscopic models described above were developed to study the local protrusion mechanism observed during cell movement (Mogilner 2009; Pollard et al. 2000). Continuum models have been developed to study the global behaviour of cell shape. Example of such models are: a two-phase fluid model for cytosol and the actin network (Alt and Dembo 1999), a one dimensional (1D) viscoelastic model of the cytoplasm and active stress generation (Gracheva and Othmer 2004), a 1D model for the actin distribution and its reaction (Mogilner et al. 2001) and a 2D elastic continuum model (Rubinstein et al. 2005). Another continuum model is the cytomechanical model that couples a force balance mechanical equation for actin network to a reaction-diffusion equation for the F-actin bio-chemical dynamics (Stéphanou et al. 2004). The model we consider is an extension of this model. In this chapter, we introduce the mathematical model from first principles and carry out a linear stability analysis to identify key model parameters that determine cell deformations.

3.2 General overview of the cytochemical model

The cytochemical model initially proposed by [Alt and Tranquillo \(1995\)](#) is based on the hypothesis of a pressure driven protrusion. The model assumes that cell deformation is as a result of the interaction between an internal hydrostatic pressure pushing on the membrane and the contractile force of the actin network pulling on the membrane through their link with the membrane. The intensity of this pulling force is assumed to vary within the cell and depends linearly on the local amount of F-actin available. Hence the higher the actin density the more the pulling force applied on the membrane. The model also considers the actin polymerisation kinetics to be regulated around a chemical equilibrium concentration ([Stéphanou et al. 2004](#)).

In [Alt and Tranquillo \(1995\)](#) and [Stéphanou et al. \(2004\)](#) the cytochemical model was represented in a polar coordinate system and the radial membrane extension of the cell was determined using a partial differential equation that describe forces like the hydrostatic pressure existing inside the cell, an active force which depends on local concentration of actin, additional curvature-dependent stress due to the surface tension of the cortical actin-membrane complex and a frictional force opposing the movement of the cell membrane. The partial differential equation for the membrane extension was coupled to a force balance mechanical equation describing the actin mechanical behaviour and a reaction-diffusion equation describing the actin polymerisation kinetics. This model was initially proposed to describe the membrane dynamics of round-shaped cells such as keratinocytes or leukocytes which have small protrusions around the cell body. It was developed and extended by [Stéphanou et al. \(2004\)](#) to take into account deformations with large amplitude such as those observed in resting fibroblasts.

Here the cytochemical model is represented in a cartesian coordinate and consist of two coupled systems of partial differential equations, namely (i) a force balance mechanical equation for actin network and (ii) a reaction-diffusion equation describing the concentration of F-actin, its random movement via diffusion, the convective and dilution effects due to cell movement and its kinetics of polymerisation and depolymerisation. The partial differential equation used in the previous models to determine the radial membrane extension is omitted here because we use a different coordinate system. Here the displacement of the membrane is specified by the displacement solutions of the force balance equation (details of this will be given later). Also, in previous cytochemical models actin polymerisation was considered to be a secondary event occurring spontaneously after the pressure force pushing on the membrane creates an adequate space for the intercalation of monomers but here we consider the polymerisation force to be a primary event that reinforces the osmotic pressure. This allows for the study of both the pressure-induced deformation dynamics observed in both non-motile and motile cell ([Bisnamé et al. 2010](#); [Charras and Paluch 2008](#)) and the actin polymerisation driven protrusion

dynamics observed largely in motile cells (Binamé et al. 2010).

The force balance mechanical equation is derived from continuum mechanics (Murray 1993) while the reaction-diffusion equation is derived from conservation equation exploiting conservation laws (Edelstein-Keshet 2005; Murray 1993). The model consist of two variables, the F-actin density and the actin displacement velocity in the cell. We motivate the derivation of the force balance mechanical equation and the reaction-diffusion equation from first principle and specify adequate boundary conditions necessary for the well-posedness of the coupled system.

3.3 Derivation of the model equations

Let $\Omega_t \subset \mathcal{R}^2$ be a simply connected bounded and continuously deforming domain representing the cell shape at time $t \in I = [0, T_f]$, $T_f > 0$ and $\partial\Omega_t$ be the boundary describing the cell. We begin by deriving the reaction-diffusion equation describing the actin biochemical dynamics (i.e the concentration of F-actin, its random movement via diffusion, convective and dilution effects due to shape movement and its kinetics of polymerisation and de-polymerisation) within the domain Ω_t . Next we will derive a force balance mechanical equation that describes the mechanical properties of actin filaments and couple it to the reaction-diffusion equation describing the actin biochemical dynamics on a continuously deforming domain Ω_t .

3.3.1 Reaction-diffusion equation for actin biochemical dynamics on a continuously deforming cell domain

Reaction-diffusion equations have been used in the modelling of a vast number of phenomena that arise in many areas of the natural sciences such as in geology, ecology, chemistry, physics and biology (Edelstein-Keshet 2005; Grindrod 2007; Murray 1993). Here we use it to model the actin biochemical dynamics on a continuously deforming cell domain.

At any given point, $\mathbf{x} = (x(t), y(t)) \in \Omega_t \subset \mathcal{R}^2$, let $a = a(\mathbf{x}(t), t)$ be the F-actin concentration and $\mathbf{u} = (u(\mathbf{x}(t), t), v(\mathbf{x}(t), t))^T$ be a vector of infinitesimal displacement of the elements of the actin network at position $\mathbf{x} \in \Omega_t$ at time $t \in I$. As a result of cell movement we define $\boldsymbol{\beta}$ to represent the flow velocity of the elements of the actin network. The position of any point in the domain is not constant but is dependent on time in order to account for the changes in cell shape as a result of cell deformation and movement. Actin filament concentration is defined to accommodate the time dependence of the spatial coordinates. That is at any given point, $\mathbf{x}(t) \in \Omega_t$, $a = a(\mathbf{x}(t), t)$ represents the actin filament concentration at $\mathbf{x}(t)$, $t \in I$. We denote by a constant parameter k_a the rate of polymerisation of actin filaments from the molecular G-actin component and the constant parameter a_c

the concentration of actin filaments at the chemical equilibrium which differentiates the states of polymerisation and de-polymerisation. The function $k_a(a_c - a)$ describes the net formation of actin filament from the molecular G-actin component. It models the degradation of F-actin a around the steady state a_c . Thus when the density of a decreases, it implies that it has depolymerized into G-actin.

We now derive a reaction-diffusion equation to model the biochemical dynamics of the actin filaments. The conservation equation states that the rate of change of the quantity of a material in Ω_t , $t \in I$ is equal to the net flux of the material through the boundary plus the net creation of the material within the domain. Applying the conservation equation to describe the biochemical dynamics of the actin filaments, we have that;

$$\frac{d}{dt} \int_{\Omega_t} a d\Omega_t = - \int_{\partial\Omega_t} \mathbf{J} \cdot \mathbf{n} dS + \int_{\Omega_t} k_a(a_c - a) d\Omega_t. \quad (3.1)$$

We assume that \mathbf{J} is a continuously differentiable function and we apply the divergence theorem (1.4) to (3.1) to obtain the following;

$$\frac{d}{dt} \int_{\Omega_t} a d\Omega_t = \int_{\Omega_t} \left(-\nabla \cdot \mathbf{J} + k_a(a_c - a) \right) d\Omega_t \quad (3.2)$$

The domain of integration is time dependent, hence we cannot swap the operation of differentiation with that of integration as is usually done on fixed domains. We proceed by applying the Reynolds transport theorem (1.6) to the term on the left of (3.2) to obtain

$$\int_{\Omega_t} \left(\frac{Da}{Dt} + a(\nabla \cdot \boldsymbol{\beta}) \right) d\Omega_t = \int_{\Omega_t} \left(-\nabla \cdot \mathbf{J} + k_a(a_c - a) \right) d\Omega_t, \quad (3.3)$$

where $\boldsymbol{\beta}$ denotes the flow velocity of actin filaments and $\frac{D}{Dt}$ is a material derivative:

$$\frac{Da}{Dt} = \frac{\partial a}{\partial t} + \boldsymbol{\beta} \nabla a$$

Upon replacing the definition of the material derivative $\frac{Da}{Dt}$ into (3.3), we get

$$\int_{\Omega_t} \left(\frac{\partial a}{\partial t} + \boldsymbol{\beta} \nabla a + a(\nabla \cdot \boldsymbol{\beta}) \right) d\Omega_t = \int_{\Omega_t} \left(-\nabla \cdot \mathbf{J} + k_a(a_c - a) \right) d\Omega_t. \quad (3.4)$$

We assume that actin filaments flow from regions of high concentration to regions of low concentration and its flux \mathbf{J} is proportional to the concentration gradient. Thus by Fick's law of mass diffusion we have that

$$\mathbf{J} = -D_a \nabla a, \quad (3.5)$$

and D_a is a positive constant diffusion coefficient for F-actin. Applying the product rule

(i.e $\nabla \cdot (a\boldsymbol{\beta}) = \boldsymbol{\beta} \nabla a + a(\nabla \cdot \boldsymbol{\beta})$) and Fick's law of mass diffusion to (3.4), we obtain the following

$$\int_{\Omega_t} \left(\frac{\partial a}{\partial t} + \nabla \cdot (a\boldsymbol{\beta}) - D_a \Delta a - k_a(a_c - a) \right) d\Omega_t = 0, \quad (3.6)$$

Since (3.6) holds for any arbitrary domain Ω_t at all time t and both integrands are continuous then the following equation is valid (Madzvamuse 2000),

$$\frac{\partial a}{\partial t} + \underbrace{\nabla \cdot (a\boldsymbol{\beta})}_{\text{convection}} - \underbrace{D_a \Delta a}_{\text{diffusion}} = \underbrace{k_a(a_c - a)}_{\text{polymerisation kinetic}}. \quad (3.7)$$

A relevant boundary condition is the zero-flux boundary condition ($\mathbf{n} \cdot \nabla a$) as it specifies that there is no flux of actin into the domain or out of it. Thus it enforces that actin filaments are confined to the domain and do not cross the boundary neither are they increased by external sources.

Remark 3.3.1. (Special case) When $\boldsymbol{\beta} = 0$, the reaction-diffusion equation (3.7) reduces to a reaction-diffusion equation on a fixed domain.

The reaction-diffusion equation (3.7) is coupled to a force balance mechanical equation which describes the mechanical properties of actin filaments. We present below the derivation of the force balance mechanical equation from continuum mechanics.

3.3.2 Force balance mechanical equation for actin dynamics

According to experimental observations, the active mechanical forces that determine cell deformation and movement are largely due to the mechanical properties of the actin network (Alt and Tranquillo 1995; Binamé et al. 2010; Charras and Paluch 2008; Stéphanou et al. 2004).

The network of actin filaments in the cell is modelled as a viscoelastic and contractile gel. As viscoelastic materials, they exhibit the characteristics of both viscous solutions and elastic solids when deforming. When an external force is applied to an elastic material it deforms but returns back to its original form after the force is removed. Thus elastic solids are said to have a perfect memory of their original shape. Viscous solutions do not have memory of their original shape and hence do not return to their original shape after an applied force is removed. Unlike purely elastic and viscous materials, viscoelastic materials have a partial memory of their original form. Like an elastic solid it shows an initial resistance to deformation when an external force is applied to it, this is then followed by a slow flow, similar to a viscous solution and once the force is removed it slowly returns towards its original form. A remarkable feature of viscoelastic property is that its deformation is dependent not only on the applied force but also on time (Bray 2001; Janmey 1991; Kundu and Cohen 2002).

The viscoelastic network of actin interacts with myosin II (a motor protein that is found in the cell cytoplasm) to generate contractile stress in the cell cytoplasm. As the network of actin filament contracts due to its interaction with myosin II, the filaments will become aligned into bundles and the contractile force developed will increase with time since on the bundles, myosin II molecules are favoured to work in the same direction and thus increasing the efficiency of the contraction (Bray 2001). We assume that during the contraction of the actin network, the actin filaments pull the cell membrane inwards as a result of their being attached to the membrane. We also assume that the contractions of the actin network also cause cytoplasmic flows which in turn induces an osmotic pressure in the cell cytoplasm. This pressure pushes the membrane outward at positions where the membrane is not firmly attached to the actin network (Stéphanou et al. 2004). Also an additional pressure due to the polymerisation of actin filaments from the monomeric G-actin acts around the membrane. As a result of pushing on the membrane when they polymerize in order to create adequate space for its extension. Although the dynamics of the network of actin filaments have been the focus of many studies, it is still not yet clear how these contractile forces spatiotemporally regulate the actin network dynamics. It was shown by Okeyo et al. (2009) that these contractile forces are the primary factor responsible for the realisation of the many mechanochemical processes that determine cell motility.

The viscoelastic and contractile properties are represented by stress tensors comprising viscous $\boldsymbol{\sigma}_v$, elastic $\boldsymbol{\sigma}_e$, contractile $\boldsymbol{\sigma}_c$ components, plus an additional pressure component $\boldsymbol{\sigma}_p$ representing the pressure in the cell. We assume that at the intracellular level, the cell complies to Newtonian dynamics such that inertial terms are negligible compared to viscous and elastic forces, hence motion ceases as soon as the forces are turned off (Lewis and Murray 1991; Purcell 1977). At any given point, $\mathbf{x} = (x(t), y(t)) \in \Omega_t \subset \mathcal{R}^2$, let $\mathbf{u} = (u(\mathbf{x}(t), t), v(\mathbf{x}(t), t))^T$ be a vector of infinitesimal displacement of the elements of the actin network at position $\mathbf{x} \in \Omega_t$ at time $t \in I$. Thus at any given time, the actin network is in mechanical equilibrium and satisfies the following equilibrium equation which is the force balance mechanical equation:

$$\nabla \cdot (\boldsymbol{\sigma}_v + \boldsymbol{\sigma}_e + \boldsymbol{\sigma}_c + \boldsymbol{\sigma}_p) = 0, \quad (3.8)$$

where $\boldsymbol{\sigma}_v$, $\boldsymbol{\sigma}_e$, $\boldsymbol{\sigma}_c$ and $\boldsymbol{\sigma}_p$ are the viscous, elastic, contractile and pressure component

stress tensors. These are defined as:

$$\boldsymbol{\sigma}_v = \mu_1 \frac{\partial \boldsymbol{\varepsilon}}{\partial t} + \mu_2 \frac{\partial \phi}{\partial t} \mathbf{I}, \quad (3.9)$$

$$\boldsymbol{\sigma}_e = \frac{E}{1+\nu} \left(\boldsymbol{\varepsilon} + \frac{\nu}{1-2\nu} \phi \mathbf{I} \right), \quad (3.10)$$

$$\boldsymbol{\sigma}_c = \sigma(a) \mathbf{I} = \psi a^2 e^{-a/a_{sat}} \mathbf{I}, \quad (3.11)$$

$$\boldsymbol{\sigma}_p = \frac{p(a)}{1+\phi} \mathbf{I} = \frac{p}{1+\phi} \left(1 + \frac{2}{\pi} \delta(l) \arctan a \right) \mathbf{I}, \quad (3.12)$$

where $\boldsymbol{\varepsilon} = \frac{1}{2}(\nabla \mathbf{u} + \nabla \mathbf{u}^T)$ is the strain tensor, \mathbf{I} is the identity tensor, $\phi = \nabla \cdot \mathbf{u}$ is the dilation, and μ_1 and μ_2 are the shear and bulk viscosities of the actin network respectively. Finally E and ν are the Young's modulus and Poisson ratio respectively. For the force balance mechanical equation we specify a stress free boundary. The function $\sigma(a)$ represents the contractile activity of the actomyosin network (see Figure 3.1). In the above formulation, a_{sat} is used to specify the saturation concentration of F-actin. Contraction of the network pulls the membrane inwards. The cell cytoplasm is made up of 80% water. Thus the contraction of actin network creates cytoplasmic flows which gives rise to an hydrostatic pressure in the cell cytoplasm. This pressure pushes the membrane outwards at regions where actin and the membrane is not firmly linked. In our model, we assume that the linking of the membrane to the actin network at any point on the membrane depends linearly on the amount of F-actin present at that point. Thus we model the contractile force using the stress tensor $\boldsymbol{\sigma}_c = \psi a^2 e^{a/a_{sat}} \mathbf{I}$ as a function of F-actin density. Hence the higher the actin density the more the pulling force applied on the membrane provided $a < 2a_{sat}$. When $a > 2a_{sat}$ then there are too much F-actin and the contractile force begins to decrease exponentially. This is due to compaction of the network which prevents further contraction (see Figure 3.1 for a plot of $\sigma(a)$ against the actin density a). In order to describe the pressure forces acting within the cell we make the following assumptions. We assume that the initial domain is a unit disk which we denote as Ω_0 and that there exists a family of bijective mappings that maps the points $\boldsymbol{\xi} = (\xi_x, \xi_y)$ of the initial domain to point \mathbf{x} on the current domain Ω_t . Let $l : \Omega_t \times I \rightarrow \mathcal{R}$ and it's corresponding function on the initial domain be $\hat{l} : \Omega_0 \times I \rightarrow [0, 1]$ where $\hat{l}(\boldsymbol{\xi}, t)$ is the distance between the centroid and the point $\boldsymbol{\xi}$ in the initial domain with $\hat{l}(\boldsymbol{\xi}, t) = l(\mathbf{x}(\boldsymbol{\xi}, t), t)$. The function $p(a)$ describes the pressure force in different regions governed by the heavy-side function:

$$\delta(l) = \begin{cases} 1 & \text{if the point } (\mathbf{x}, t) \text{ with } l(\mathbf{x}(\boldsymbol{\xi}, t), t) = \hat{l}(\boldsymbol{\xi}, t) \text{ is such that} \\ & \text{the distance } \sqrt{\xi_x^2 + \xi_y^2} > 0.8 \text{ in the initial domain,} \\ 0 & \text{elsewhere.} \end{cases} \quad (3.13)$$

This signifies that far from the membrane, only the osmotic component $p/(1 + \phi)$ of the pressure force exists within the network and depends on the dilation ϕ . In the vicinity of the membrane (i.e. where $\sqrt{\xi_x^2 + \xi_y^2} > 0.8 = l_0$), a polymerisation-induced pressure which depends on the local actin density reinforces the osmotic stress and pushes the membrane out at regions where the filaments are not firmly linked to the membrane (see Figure 3.2 for a graphical illustration). $\delta(l)$ is used here to specify the differences in pressure in the cell at the vicinity of the membrane and further away from it. We have assumed that the polymerisation of actin, which happens predominately at the vicinity of the membrane, induces a pressure that reinforces the osmotic pressure at the vicinity of the membrane.

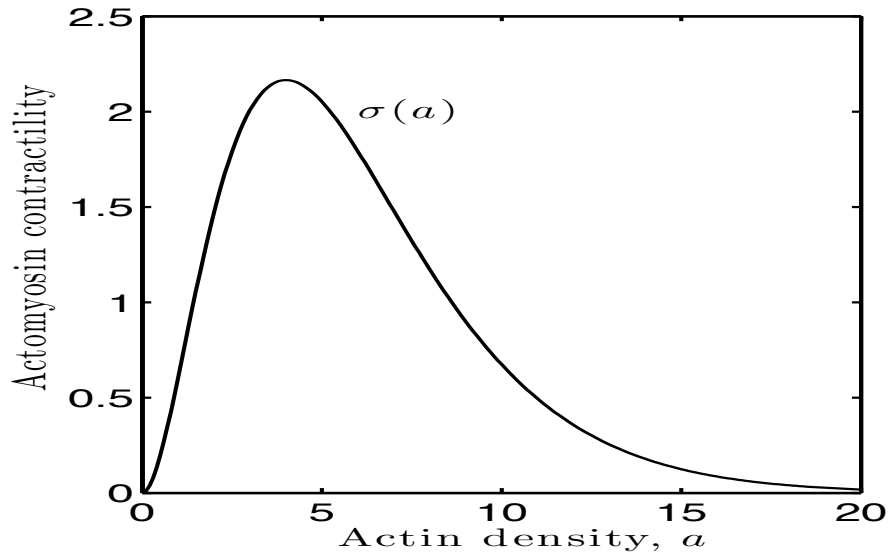
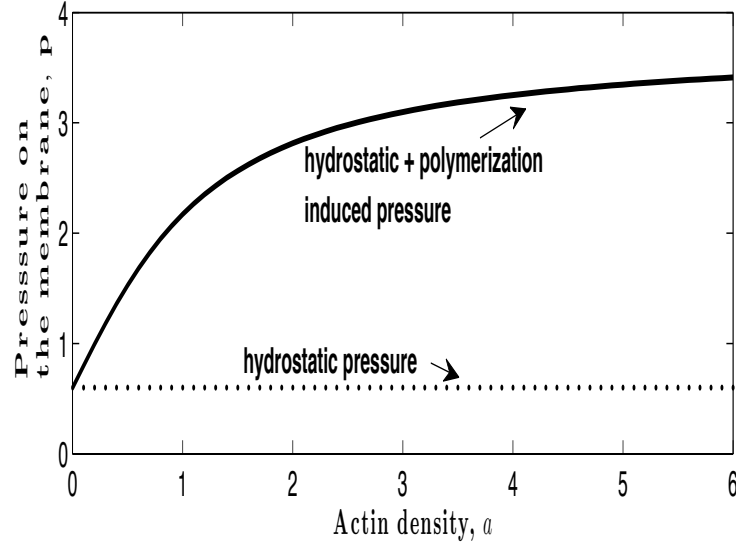


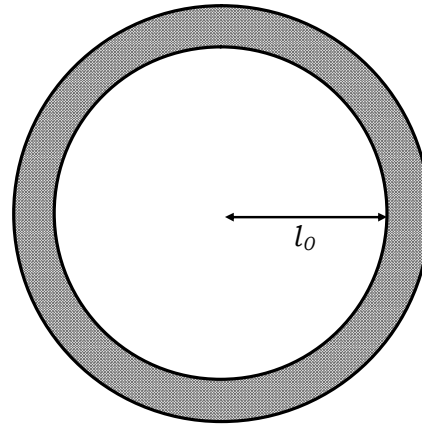
Figure 3.1: Function $\sigma(a)$ describing the actomyosin network contractility. The contractility first increases in a parabolic way with the actin density until a critical density of actin is reached, after which the contractility begins to decrease exponentially. This is due to compaction of the network which prevents further contraction. Here $a_{sat} = 1.1$ and $\psi = 1.0$.

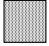

Remark 3.3.2. *The key differences between the present model and previous models by Stéphanou et al. (2004) and Alt and Tranquillo (1995) are highlighted below.*

1. *The present model unlike previous models by Stéphanou et al. (2004) and (Alt and Tranquillo 1995) considers the polymerisation force to be a primary event that reinforces the osmotic pressure.*
2. *In order to account for the polymerization-induced pressure acting at the vicinity of the membrane we have introduced the function δ to model the pressure force in (3.12).*



(a)



 Hydrostatic plus polymerization induced pressure
 Hydrostatic pressure

(b)

Figure 3.2: A graphical and pictorial description of the variation of the function $p(a)$ on a typical cell. In (a) the function $p(a)$ is shown describing the pressure force existing at the vicinity of the membrane. This force comprises of a passive hydrostatic component and an active polymerisation-induced force component corresponding to the force applied by the growing filaments pushing on the membrane to create the space required for their growth. In (b) a schematic illustration of the variation of the function $p(a)$ within a typical cell is shown, where $l_0 = 0.8$.

3. In *Stéphanou et al. (2004)* and *Alt and Tranquillo (1995)* periodic boundary conditions were incorporated in to the model but in the present model we specify a zero flux boundary condition. The zero flux boundary condition specifies that there is no flux of actin into the domain or out of it. This is relevant biologically because actin is always confined in the cell cytoplasm and is not increased by flux through the cell

membrane or flux out of the cell membrane.

4. Also unlike *Stéphanou et al. (2004)* and *(Alt and Tranquillo 1995)* the present model is represented in cartesian coordinate.
5. Unlike the work by *Gracheva and Othmer (2004)*, *Rubinstein et al. (2005)*, *Stéphanou et al. (2004)* and *Alt and Tranquillo (1995)* here a moving grid finite element method is proposed for the numerical approximation of a mathematical model of cell deformation.

3.3.3 The cytomechanical model

In summary, the cytomechanical model describing the actin dynamics is given by:

$$\nabla \cdot (\boldsymbol{\sigma}_v + \boldsymbol{\sigma}_e + \boldsymbol{\sigma}_c + \boldsymbol{\sigma}_p) = \mathbf{0} \quad \text{in } \boldsymbol{\Omega}_t, t \in I, \quad (3.14a)$$

$$\frac{\partial a}{\partial t} - D_a \Delta a + \nabla \cdot (a \boldsymbol{\beta}) - k_a(a_c - a) = 0 \quad \text{in } \boldsymbol{\Omega}_t, t \in I, \quad (3.14b)$$

$$\mathbf{u}(\mathbf{x}(t), t) = \mathbf{0} \quad \text{for } \mathbf{x} \in \boldsymbol{\Omega}_t, t = 0, \quad (3.14c)$$

$$a(\mathbf{x}(t), t) = a_0 \quad \text{for } \mathbf{x} \in \boldsymbol{\Omega}_t, t = 0, \quad (3.14d)$$

$$\boldsymbol{\beta} = \boldsymbol{\omega}_n \quad \text{for } \mathbf{x} \in \partial \boldsymbol{\Omega}_t, t \in I, \quad (3.14e)$$

$$\boldsymbol{\sigma}_v \cdot \mathbf{n} = \boldsymbol{\sigma}_e \cdot \mathbf{n} = \mathbf{n} \cdot \nabla a = 0 \quad \text{for } \mathbf{x} \in \partial \boldsymbol{\Omega}_t, t \in I, \quad (3.14f)$$

where all parameters and variables are as previously defined and as a result of cell movement we define $\boldsymbol{\omega}_n$ to represent the normal velocity of the cell boundary. Furthermore the outward unit vector normal to the boundary is denoted by $\mathbf{n} := (n_x, n_y)$. We define the initial domain $\boldsymbol{\Omega}_0, t = 0$, to be a unit disk. We prescribe the initial conditions for actin density a_0 to correspond to random small perturbations around the homogeneous steady state of the cell. This state biologically corresponds to the cell condition right after mitosis (i.e. cell division) with the cell having a perfectly circular shape. We assume that at the initial time, the cell is unstrained from its original position. On the boundary, we take the flow velocity of the actin network $\boldsymbol{\beta} = \boldsymbol{\omega}_n := \partial \mathbf{u} / \partial t$. Also in the interior of the domain we assume that $\boldsymbol{\beta} = \partial \mathbf{u} / \partial t$. Here \mathbf{u} is the infinitesimal displacement of the actin network at any given point in space and is modelled in the force balance mechanical equation (3.14a). The boundary conditions in (3.14e) specify a zero flux boundary for the reaction-diffusion equation (3.14b) and a stress free boundary for the force balance mechanical equation (3.14a). We note that the linking of actin filament to the membrane as described in Chapter 2 is modelled by assuming that the flow velocity of actin filament equals the cell domain velocity $\boldsymbol{\omega}_n$.

Remark 3.3.3. We note that in a previous work by *Stéphanou et al. (2004)*, the infinitesimal displacement $\mathbf{u}(\mathbf{x}(t), t)$ was taken to be the displacement of the elements of the actin

Table 3.1: Dimensional parameters and their values as used in the mathematical model except where it is specified otherwise.

Parameter	Meaning	Value	Ref.
E	Young's modulus of the actin network	1.5 dyn/cm^2	Estimated
ν	Poisson's ratio of the actin network	0.3	Estimated
D_a	Diffusion coefficient of actin	$0.012 \text{ cm}^2/\text{s}$	Stéphanou et al. (2004)
k_a	Polymerisation rate of the actin network	0.03 s^{-1}	Estimated
a_{sat}	Saturation concentration of F-actin	1.4 normalised density	Stéphanou et al. (2004)
μ_1	Shear viscosity of the actin network	$96.15 \text{ dyn} \cdot \text{s}/\text{cm}^2$	Bausch et al. (1998)
μ_2	Bulk viscosity of the actin network	$250 \text{ dyn} \cdot \text{s}/\text{cm}^2$	Bausch et al. (1998)
l_0	Specifies the vicinity of the membrane	80% of the cell radius	Estimated
a_c	F-actin concentration at the chemical equilibrium	1.0 normalised density	Derived from model

network from the original unstrained position. In this work, we compute the displacement $\mathbf{u}(\mathbf{x}(t), t)$ continuously given the previous positions of $\mathbf{x} \in \Omega_t$, at time $t \in I$.

This assumption implies that at each time t , the elastic forces in (3.14a) are negligible and the viscous forces dominate. An advantage of this modification is that the cell is no longer rigid but can translate, expand and contract.

3.4 Selection of parameter values

We assign value to the model parameters. We begin by assigning non-dimensional parameter values.

3.4.1 Determination of dimensional parameter values

We assign numerical values to all the dimensional model parameters except the pressure coefficient p and the contractile coefficient ψ . We note that we do not assign values to p and ψ yet because we desire to choose their values such that the dispersion relation will have a finite number of unstable modes. The dimensional parameter values are displayed in Table 3.1.

Some of the parameter values are close to those available in the literature. In Stéphanou et al. (2004), a diffusion coefficient D_a in the range $0.00962 - 0.134 \text{ cm}^2/\text{s}$ and an actin saturation concentration a_{sat} of 1.1 normalised density were used. Viscosity of Fibroblast cells is given in Bausch et al. (1998) to be 200 dyn/cm^2 . Here we choose the value of the shear viscosity to be $96.15 \text{ dyn} \cdot \text{s}/\text{cm}^2$ and the value of the bulk viscosity of the actin network $\mu_2 = 250 \text{ dyn} \cdot \text{s}/\text{cm}^2$ to be larger than that of the shear modulus. This is because F-actin is more resistant to compression than shear (Barnhart et al. 2011).

We note that the value of the F-actin diffusion and polymerization rates we used is not consistent with experimental observations. We highlight that for any arbitrary choice of diffusion coefficient used, linear analysis shows that ψ can be chosen to obtain any required mode of deformation. Also we do not seek to quantify our results with experimental observations thus assigning any arbitrary value to the diffusion coefficient is sufficient for our studies. In Chapter 5, we shall carried out test-cases with diffusion coefficient similar to those of filamentous actin obtainable from literatures to obtain cell deformation. And thus confirming the generality of our methodology. We would like to point out that the value of k_a does not influence the dynamics of the model greatly since after carrying out a nondimensionalization of the model equations (as will be shown later) we obtain equation (3.16) which is independent of k_a . Hence irrespective of the value of k_a the cell will deform in the same way. Again our methodology is much more general.

We desire to carry out linear stability analysis of the cytomechanical model. But first we non-dimensionalize the system of equations. This reduces the number of parameters making the mathematical analysis afterwards more amenable.

3.4.2 Nondimensionalisation and non-dimensional parameter values

Let the length scale L be a typical radius of a cell. Substituting the following dimensionless quantities into (3.14a) and (3.14b),

$$\left\{ \begin{array}{l} \tilde{t} = tk_a, \quad \tilde{a} = \frac{a}{a_c}, \quad \tilde{\mathbf{u}} = \frac{\mathbf{u}}{L}, \quad \tilde{\nabla} = L\nabla, \quad \tilde{\Delta} = L^2\Delta, \quad \tilde{a}_{sat} = \frac{a_{sat}}{a_c}, \\ \tilde{p} = p \frac{1+\nu}{E}, \quad \tilde{\phi} = \phi, \quad \tilde{\boldsymbol{\varepsilon}} = \boldsymbol{\varepsilon}, \quad \tilde{\mu}_i = \mu_i k_a \frac{1+\nu}{E}, \quad \tilde{\psi} = \psi a_c^2 \frac{1+\nu}{E}, \\ \tilde{\boldsymbol{\beta}} = \frac{\boldsymbol{\beta}}{k_a L}, \quad d = \tilde{D}_a = \frac{D_a}{k_a L^2}, \quad \tilde{l}_0 = \frac{l_0}{L} \end{array} \right. \quad (3.15)$$

results in

$$\left\{ \begin{array}{l} \tilde{\nabla} \cdot \left\{ (\tilde{\mu}_1 \tilde{\boldsymbol{\varepsilon}}_t + \tilde{\mu}_2 \tilde{\phi}_t \mathbf{I}) + (\tilde{\boldsymbol{\varepsilon}} + \nu' \tilde{\phi} \mathbf{I}) + \tilde{\psi} \tilde{a}^2 e^{-\tilde{a}/\tilde{a}_{sat}} \mathbf{I} \right\} + \\ \tilde{\nabla} \cdot \left\{ \frac{\tilde{p}}{1+\tilde{\phi}} \left[1 + \frac{2}{\pi} \delta(l) \arctan(\tilde{a}) \right] \mathbf{I} \right\} = 0, \\ \frac{\partial \tilde{a}}{\partial \tilde{t}} - d \tilde{\Delta} \tilde{a} + \tilde{\nabla} \cdot (\tilde{a} \tilde{\boldsymbol{\beta}}) = 1 - \tilde{a}, \end{array} \right. \quad (3.16)$$

where $\nu' = \frac{\nu}{1-2\nu}$, $\nu \neq 0.5$.

Using (3.15), we obtain the corresponding non-dimensional parameter values as displayed in Table 3.2. These non-dimensional parameter values will be helpful in the isolation and study of the dynamics of any isolated wavenumber $k^2 > 0$. Subsequently we will compare solutions predicted by linear stability theory with those obtained from numerical simulations.

Table 3.2: Non-dimensional parameters and their values as used in the nondimensionalized mathematical model except where it is specified otherwise. These parameter values were obtained from their dimensional counterpart by using (3.15). Here we have assume that $L = 1.0cm$ since we desire to carry out linear stability analysis on a unit disk and also numerical simulations of the model equations will be carried out on an initial domain that is equivalent to a unit disk.

Parameter	Meaning	Non-dimensional value
d	Diffusion coefficient of actin	0.4
\tilde{a}_{sat}	Saturation concentration of F-actin	1.4
$\tilde{\mu}_1$	Shear viscosity of the actin network	2.5
$\tilde{\mu}_2$	Bulk viscosity of the actin network	6.5
$\tilde{\psi}$	Contractility coefficient of the actin network	62.4
\tilde{p}	Pressure coefficient of the actin network	0.26
\tilde{l}_0	Specifies the vicinity of the membrane	0.8

3.5 Linear stability analysis on a fixed unit disc

We restrict linear stability analysis to be carried out on a static unit disk. The assumption is that for time $t = t_0 + n\Delta t$, $t > t_0$ with n small, the deformed cell domain is still very close to a unit disk. Hence linear analysis is valid on Ω_t provided $t \ll 1$ and $\Omega_t \approx \Omega_0$. Here Δt is a small time step.

The steady state solution of (3.16) is $a_s = 1$, $\mathbf{u}_s = \mathbf{0}$. We linearize the system of equations (3.16) by considering the stability of the steady state to small perturbations $\tilde{a} = a_s + \hat{a}$, and $\tilde{\mathbf{u}} = \mathbf{u}_s + \hat{\mathbf{u}}$, where \hat{a} and $\hat{\mathbf{u}}$ are small variations from the steady state. Substituting these into the nonlinear system (3.16) and neglecting all but the linear terms results in the following linear system of partial differential equations:

$$\begin{cases} \tilde{\nabla} \cdot [(\tilde{\mu}_1 \hat{\mathbf{e}}_t + \tilde{\mu}_2 \hat{\phi}_t \mathbf{I}) + (\hat{\mathbf{e}} + \nu' \hat{\phi} \mathbf{I}) + \sigma'(1) \hat{a} \mathbf{I} + \tilde{p}(1 - \hat{\phi}) \mathbf{I} + \tilde{p}^2_{\pi} \delta(l) \hat{a} \mathbf{I}] = \mathbf{0}, \\ \frac{\partial \hat{a}}{\partial t} - d \Delta \hat{a} + \tilde{\nabla} \cdot (\hat{\boldsymbol{\beta}}) + \hat{a} = 0, \end{cases} \quad (3.17)$$

where $\hat{\mathbf{e}}_t$, $\hat{\phi}_t$, $\hat{\phi}$ and $\hat{\boldsymbol{\beta}}$ are functions of $\hat{\mathbf{u}}$ and $\sigma'(1) = \frac{\partial \sigma(\tilde{a})}{\partial \tilde{a}} \Big|_{\tilde{a}=a_s}$. We now look for solutions to these linearized equations in the form of

$$\hat{a}(\mathbf{x}, t) = a^* \exp(\lambda t + i \mathbf{k} \cdot \mathbf{x}) \text{ and } \hat{\mathbf{u}}(\mathbf{x}, t) = \mathbf{u}^* \exp(\lambda t + i \mathbf{k} \cdot \mathbf{x}), \quad (3.18)$$

where λ and \mathbf{k} are respectively the growth rate (also known as an eigenvalue) and the wave vector and a^* and \mathbf{u}^* are small amplitudes. In the next section we will see the possible k 's that are allowed. If we substitute (3.18) into the linearized system (3.17) and require the

solution to be non-trivial, we obtain that (see for example (Lewis and Murray 1991)),

$$\begin{vmatrix} \lambda + dk^2 + 1 & \lambda ik \\ -ik\sigma'(1) - ik\tilde{p}\frac{2}{\pi}\delta(l) & \tilde{\mu}k^2\lambda + k^2(1 + v') - \tilde{p}k^2 \end{vmatrix} = 0, \quad (3.19)$$

where $\tilde{\mu} = \tilde{\mu}_1 + \tilde{\mu}_2$ and $k = |\mathbf{k}|$. The eigenvalues λ are solutions of the polynomial in λ given by the determinant of the matrix in (3.19) and is given by

$$k^2 [\mu\lambda^2 + b(k^2)\lambda + c(k^2)] = 0, \quad (3.20)$$

$$\begin{aligned} \text{where} \quad & b(k^2) = \tilde{\mu}dk^2 + [1 + v' + \tilde{\mu} - \sigma'(1) - \tilde{p} - \frac{2}{\pi}\tilde{p}\delta(l)], \\ \text{and} \quad & c(k^2) = d[1 + v' - \tilde{p}]k^2 + [1 + v' - \tilde{p}]. \end{aligned}$$

Solving (3.20) results in the dispersion relation

$$\lambda(k^2) = \frac{-b(k^2) \pm \sqrt{b^2(k^2) - 4\tilde{\mu}k^2c(k^2)}}{2\tilde{\mu}k^2}. \quad (3.21)$$

From the polynomial expression given in (3.20), it is obvious that the dispersion relation is indeterminate when $k^2 = 0$. Thus in the linear stability analysis we shall only consider $k^2 > 0$. Instability will occur for some wavenumber $k^2 > 0$ if the corresponding $\lambda(k^2)$ has $\text{Re}(\lambda) > 0$. Below we use Routh-Hurwitz stability criterion (Edelstein-Keshet 2005) to determine a sufficient condition on the coefficients of the polynomial (3.20) that would result in $\text{Re} \lambda(k^2) > 0$ for some $k^2 > 0$. A solution with $\text{Re} \lambda(k^2) > 0$ for some $k^2 > 0$ can exist if $b(k^2) < 0$ or $c(k^2) < 0$ or both (see Table 3.3).

Observe that $c(k^2)$ can either be positive or negative for all values of $k^2 > 0$ depending on the value of \tilde{p} . In particular, if $\tilde{p} > 1 + v'$ then $c(k^2)$ is negative for all values of $k^2 > 0$. $b(k^2)$ can take positive or negative values for some or all of $k^2 > 0$ and this depends on how small or large \tilde{p} and $\sigma'(1)$ are when compared with the other parameters in $b(k^2)$. Therefore instability can occur for some $k^2 > 0$ if one of the following conditions is satisfied:

1. $b(k^2) > 0$ and $c(k^2) < 0$ or
2. $b(k^2) < 0$ and $c(k^2) > 0$ or
3. $b(k^2) < 0$ and $c(k^2) < 0$ (see Table 3.3 for more detail).

Condition 1 and 3 above will have $c(k^2) < 0$ for all $k^2 > 0$. And the dispersion relation will have an infinite range of unstable modes. Condition 2 can have a dispersion relation with a finite range of unstable modes and shall be used in carrying out the linear stability analysis.

Remark 3.5.1. A reason for carrying out the linear stability theory is to validate the numerical scheme that we will implement in order to find an approximate solution to the model problem. This is usually carried out by showing that the numerical results obtained are consistent with predictions from the linear stability theory close to bifurcation points for some finite range of unstable modes. For the case where the dispersion relation has an infinite range of unstable modes, linear theory is unable to determine the mode that will be excited. Hence we restrict ourselves to the case where the dispersion relation isolates a finite range of unstable modes.

Table 3.3: Possibilities of stable and unstable modes to exist.

Possible conditions ($k^2 \neq 0$)	Types of mode	Sign of $\text{Re}(\lambda)$
$b(k^2) > 0$ and $c(k^2) > 0$	Stable modes for all $k^2 > 0$.	Negative
$b(k^2) > 0$ and $c(k^2) < 0$	Unstable modes will exist.	Positive
$b(k^2) < 0$ and $c(k^2) > 0$	Unstable modes will exist.	Positive
$b(k^2) < 0$ and $c(k^2) < 0$	Unstable modes will exist.	Positive

We now analyse $b(k^2) < 0$ in detail. We have that

$$b(k^2) = \tilde{\mu}dk^2 + [1 + \nu' + \tilde{\mu} - \sigma'(1) - \tilde{p} - \frac{2}{\pi}\tilde{p}\delta(l)] := \tilde{\mu}dk^2 + G < 0, \quad (3.22)$$

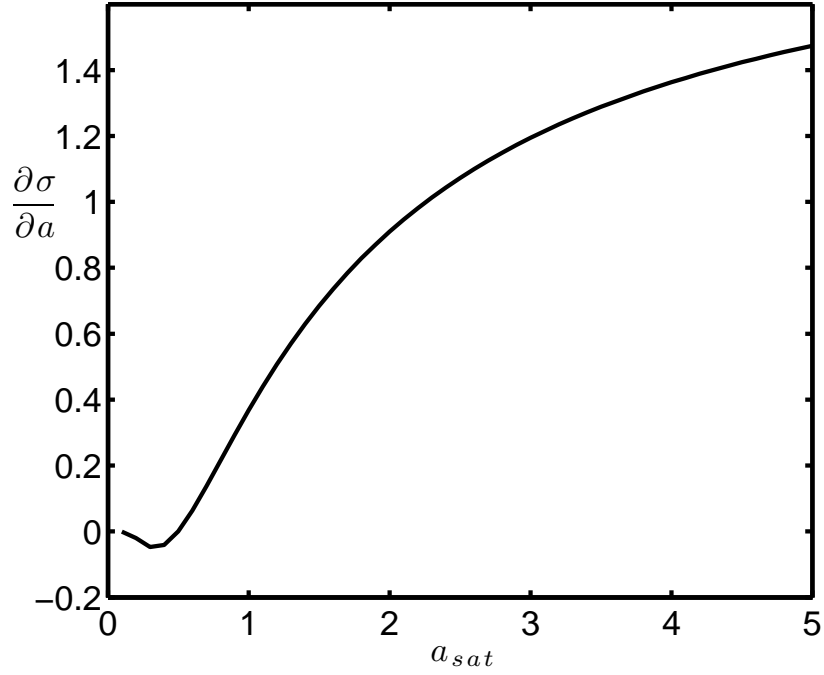
where $G := [1 + \nu' + \tilde{\mu} - \sigma'(1) - \tilde{p} - \frac{2}{\pi}\tilde{p}\delta(l)]$. Observe that $b(k^2)$ is less than zero for some k^2 if G takes negative values and $\tilde{\mu}dk^2 < |G|$. Sufficient conditions for $b(k^2)$ to take negative values for some $k^2 > 0$ are:

- (a) $G = 1 + \nu' + \tilde{\mu} - \sigma'(1) - \tilde{p} - \frac{2}{\pi}\tilde{p}\delta(l) < 0$,
- (b) $\tilde{\mu}dk^2 < |G| = \left|1 + \nu' + \tilde{\mu} - \sigma'(1) - \tilde{p} - \frac{2}{\pi}\tilde{p}\delta(l)\right|$,
- (c) $k_{crit}^2 \geq k_1^2$,

where $k_{crit}^2 = |G|/\tilde{\mu}d$ is the value of k^2 for which $b(k^2)$ is zero and k_1^2 is the first positive wavenumber. The last condition enforces that $b(k^2)$ is negative for at least the first wavenumber, k_1^2 . From condition (a) and (b) above, we require \tilde{p} or $\sigma'(1)$ to be sufficiently large in order for $b(k^2) < 0$ to exist for some $k^2 > 0$, where

$$\sigma'(1) := \frac{\partial \sigma(\tilde{a})}{\partial \tilde{a}} \Big|_{\tilde{a}=1} = \tilde{\psi} \left[-\frac{1}{\tilde{a}_{sat}} e^{-\frac{1}{\tilde{a}_{sat}}} + 2e^{-\frac{1}{\tilde{a}_{sat}}} \right]. \quad (3.23)$$

From (3.23), we see that $\sigma'(1)$ is dependent on \tilde{a}_{sat} and also proportional to $\tilde{\psi}$ (see Figure 3.3). In particular, if $\tilde{a}_{sat} = 0.5$ then $\sigma'(1) = 0$ and if $0 < \tilde{a}_{sat} < 0.5$ then $\sigma'(1) < 0$. When $\sigma'(1) < 0$ then $b(k^2) < 0$ will exist for some $k^2 > 0$ only if \tilde{p} is sufficiently


 Figure 3.3: A plot of $\sigma'(1)$ against \tilde{a}_{sat} with $\tilde{\psi} = 1.0$.

large such that the three sufficient conditions for $b(k^2) < 0$ are satisfied. Since zero-flux boundary conditions are specified on the boundary $\partial\Omega_t$, we assume that saturation concentration $2\tilde{a}_{sat} > a_s = 1.0$ where a_s is the steady state solution of actin concentration. We carry out a detailed analysis of the dispersion relation by considering the possibility of $b(k^2) < 0$ and $c(k^2) > 0$ for some $k^2 > 0$ to exist. The purpose of the linear stability theory are two-fold: (a) to validate the numerical scheme and (b) to identify key bifurcation parameters. We will show later that the numerical results are consistent with predictions from the linear stability theory close to bifurcation points.

In order to tell when an eigenvalue k^2 is isolated by a dispersion relation, we must first determine the value of k^2 . We note that the value assumed by k^2 depends on the domain of interest. Let $\mathbf{w}(\mathbf{x}) := (a(x), \mathbf{u}(x))^T$ denote the time independent eigenfunctions of the linear system of differential equation (3.17). By considering only the spatial variations in (3.17) we obtain the eigenvalue problem $\Delta \mathbf{w} = -k^2 \mathbf{w}$, where \mathbf{w} are time-independent eigenfunctions of the linear system of differential equation (3.17) and k^2 is its corresponding eigenvalue. The eigenvalue problem is defined on a unit disk corresponding to the initial domain. A solution of the eigenvalue problem gives the values of the eigenvalue k^2 and its corresponding eigenfunction w . In the next section, we present the solution of the eigenvalue problem.

3.6 Eigenfunctions on a unit disk

A wavenumber k^2 is the solution of the eigenvalue problem $\Delta \mathbf{w} = -k^2 \mathbf{w}$, $\mathbf{w} \neq 0$ with homogeneous Neumann boundary condition i.e $\mathbf{n} \cdot \nabla \mathbf{w} = 0$, where \mathbf{w} are time-independent eigenfunctions of the linear system of differential equation (3.17). In order to determine the value of k^2 , we use the separation of variables method to solve for an eigenfunction \mathbf{w} , $\mathbf{w} \neq 0$ and a wavenumber k^2 such that the eigenvalue problem is well defined. We note that the solutions of eigenvalue problems are known for simple domains such as a disk (Coleman 2005; Zill and Cullen 2000) but we present it here for the sake of completeness.

We convert the Laplacian operator to polar coordinates before applying the separation of variables method.

3.6.1 Laplace operator in polar coordinates

Consider a scalar function w such that

$$\Delta w = w_{xx} + w_{yy}, \quad (3.24)$$

then we can compute the Laplacian in Polar coordinate system by defining $x = r \cos \theta$ and $y = r \sin \theta$. Thus we have that

$$x_r = \cos \theta, \quad y_r = \sin \theta, \quad x_\theta = -r \sin \theta \quad \text{and} \quad y_\theta = r \cos \theta. \quad (3.25)$$

By applying chain rule we can obtain the following

$$\begin{cases} w_r &= w_x x_r + w_y y_r = w_x \cos \theta + w_y \sin \theta, \\ w_\theta &= w_x x_\theta + w_y y_\theta = -w_x r \sin \theta + w_y r \cos \theta. \end{cases} \quad (3.26)$$

Upon solving the simultaneous equation (3.26) for w_x and w_y , we obtain

$$\begin{cases} w_x &= w_r \cos \theta - \frac{1}{r} w_\theta \sin \theta, \\ w_y &= \frac{1}{r} w_\theta \cos \theta + w_r \sin \theta. \end{cases} \quad (3.27)$$

We note that

$$w_{xx} = \frac{\partial}{\partial x}(w_x) = \frac{\partial}{\partial x} \left(w_r \cos \theta - \frac{1}{r} w_\theta \sin \theta \right), \quad (3.28)$$

$$= w_{rr} \cos^2 \theta + \frac{1}{r^2} w_{\theta\theta} \sin^2 \theta - \frac{2}{r} w_{r\theta} \sin \theta \cos \theta + \frac{1}{r} w_r \sin^2 \theta + \frac{2}{r^2} w_\theta \sin \theta \cos \theta. \quad (3.29)$$

also

$$\begin{aligned} w_{yy} \frac{\partial}{\partial x}(w_x) &= \frac{\partial}{\partial x} \left(\frac{1}{r} w_\theta \cos \theta + w_r \sin \theta \right), \\ &= w_{rr} \sin^2 \theta + \frac{1}{r^2} w_{\theta\theta} \cos^2 \theta + \frac{2}{r} w_{r\theta} \sin \theta \cos \theta + \frac{1}{r} w_r \cos^2 \theta - \frac{2}{r^2} w_\theta \sin \theta \cos \theta. \end{aligned} \quad (3.30)$$

An expression of the Laplacian in Polar coordinate system is obtained by substituting (3.29) and (3.30) into (3.24). Thus yielding the following,

$$\Delta w = w_{rr} + \frac{1}{r} w_r + \frac{1}{r^2} w_{\theta\theta}. \quad (3.31)$$

3.6.2 Neumann Laplacian on a disk

Given a scalar function w such that $\mathbf{w} = (a(x), \mathbf{u}(x))^T := (w, w)$, the eigenvalue problem (3.32) is well defined for $w \neq 0$ satisfying,

$$\begin{aligned} \Delta w + \lambda w &= 0 \quad \text{in} \quad \Omega_0 = \{(x, y) : x^2 + y^2 \leq R^2\}, \\ \frac{\partial w}{\partial n} &= 0 \quad \text{on} \quad \partial\Omega_0. \end{aligned} \quad (3.32)$$

In order to solve the eigenvalue problem (3.32), we resort to the Polar coordinates system. We substitute (3.31) into (3.32) to obtain

$$\begin{aligned} w_{rr} + \frac{1}{r} w_r + \frac{1}{r^2} w_{\theta\theta} + \lambda w &= 0, \quad 0 < r < R, \quad -\infty < \theta < \infty, \\ w_r(R, \theta) &= 0 \quad -\infty < \theta < \infty, \end{aligned} \quad (3.33)$$

where $w_r := \partial w / \partial r$, $w_{rr} := \partial^2 w / \partial r^2$, $w_\theta := \partial w / \partial \theta$ and $w_{\theta\theta} := \partial^2 w / \partial \theta^2$. Since the point (r, θ) is the same as the point $(r, \theta + 2\pi)$, we require

$$w(r, \theta + 2\pi) = w(r, \theta)$$

for each θ , and each r in $0 < r < R$. In polar coordinates, it is possible to have equations with solutions which are unbounded at the origin (Coleman 2005). These solutions are not continuous, so we require

$$\lim_{r \rightarrow 0} w(r, \theta) < \infty, \quad -\infty < \theta < \infty, \quad (3.34)$$

which can be written as

$$w(0, \theta) < \infty.$$

In order to solve (3.33), we use the method of separation of variables. We search for solution of the form

$$w(r, \theta) = f(r)\Theta(\theta). \quad (3.35)$$

Upon substitution of (3.35) into the eigenvalue problem (3.33) with (3.34), and separating the ODEs we obtain the f equation

$$\begin{aligned} r^2 f'' + r f' + (\lambda r^2 - \mu) f &= 0, \\ f_r(R) &= 0, |f(0)| < \infty, \end{aligned}$$

and the Θ equation

$$\Theta'' + \mu \Theta = 0, \quad \Theta(\theta + 2\pi) = \Theta(\theta), \quad \Theta'(\theta + 2\pi) = \Theta'(\theta) \text{ for all } \theta.$$

The eigenvalues and eigenfunctions of the Θ -problem, are

$$\mu_m = m^2, \quad m = 0, 1, 2, \dots; \quad \Theta_0(\theta) = c_0, \quad \Theta_m(\theta) = c_m \cos m\theta + d_m \sin m\theta, \quad m = 1, 2, 3, \dots.$$

The f equation becomes

$$\begin{aligned} r^2 f'' + r f' + (\lambda r^2 - m^2) f &= 0, \\ f_r(R) &= 0, |f(0)| < \infty. \end{aligned}$$

In solving the f equation we consider each of the possible cases where $\lambda = 0$, $\lambda < 0$ and $\lambda > 0$.

Case 1: $\lambda = 0$

$\lambda = 0$ gives the Cauchy-Euler equation (Coleman 2005)

$$r^2 f'' + r f' - m^2 f = 0, \quad m = 0, 1, 2, \dots.$$

The general solution for $m = 0$ is

$$f(r) = c_1 + c_2 \ln r \quad \text{and}$$

for $m \neq 0$, is

$$f(r) = c_1 r^m + c_2 r^{-m}.$$

For both equations the boundary condition yields $c_1 = c_2 = 0$. Thus, $\lambda = 0$ is not an eigenvalue for any choice of m .

Case 2: $\lambda < 0$, $\lambda = -k^2$ ($k > 0$)

Here we have the following equation for f .

$$r^2 f'' + r f' - (k^2 r^2 + m^2) f = 0.$$

Upon using the change of variable $x = kr$ and $y = f(x)$ we obtain the following modified Bessel's equation of order m ,

$$x^2 y'' + x y' - (x^2 + m^2) y = 0.$$

The general solution of the modified Bessel's equation is presented in Section 1.2.7 (see equation (1.16)) and is equal to

$$f(r) = c_1 I_m(kr) + c_2 K_m(kr),$$

where I_m and K_m are the modified Bessel functions of order m . Considering that K_m is unbounded as $r \rightarrow 0$, we must have $c_2 = 0$ and, since $I'_m(kr) > 0$ for $k > 0$, we must also have $c_1 = 0$. Thus, there are no negative eigenvalues for all m .

Case 3: $\lambda > 0$, $\lambda = k^2$ ($k > 0$)

Here we have the following equation for f .

$$r^2 f'' + r f' + (k^2 r^2 - m^2) f = 0.$$

Upon using the change of variable $x = kr$ and $y = f(x)$ we obtain the following Bessel's equation of order m ,

$$x^2 y'' + x y' + (x^2 - m^2) y = 0.$$

The general solution of the Bessel's equation is presented in Section 1.2.6 (refer to (1.15)) and is equal to

$$f(r) = c_1 J_m(kr) + c_2 Y_m(kr),$$

where J_m and Y_m are Bessel functions of order m . Considering that Y_m is unbounded as $r \rightarrow 0$, then we must have that $c_2 = 0$. Upon applying the boundary condition at $r = R$ we have that

$$f_r(R) = c_1 J'_m(kR) = 0. \quad (3.36)$$

This implies that $c_1 = 0$ unless kR is a zero of the derivative of Bessel function J'_m . Again let $x = kr$ then $J'_m(x)$ is (Zill and Cullen 2000):

$$J'_m = \frac{m}{x} J_m - J_{m+1}.$$

A plot of function J'_m for $m = 0, 1, 2, 3$ is shown in Figure 3.4

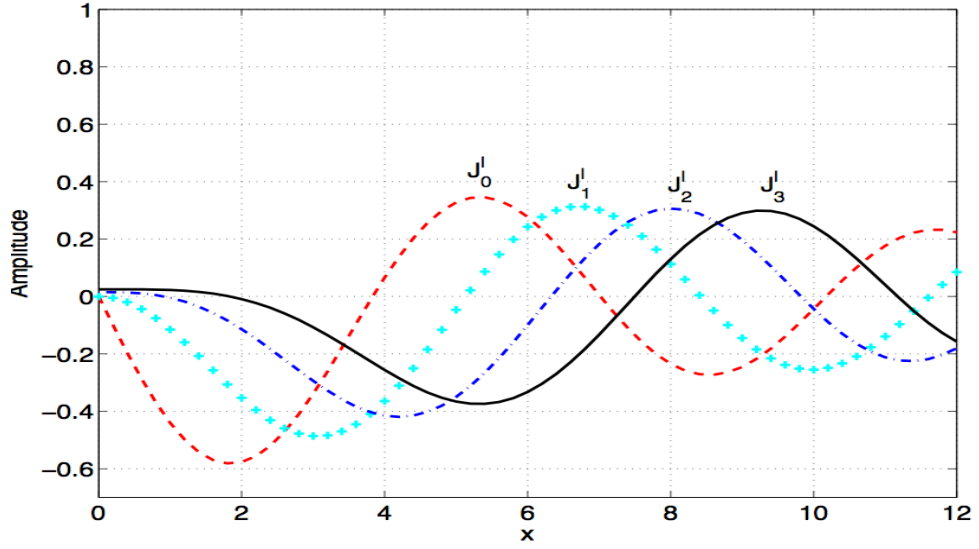


Figure 3.4: A plot showing the derivative of Bessel's function J'_m for $m = 0, 1, 2, 3$.

We note that each derivative of Bessel function J'_m has infinitely many positive zeros $j'_{m,n}$, $n = 1, 2, 3, \dots$, thus the eigenvalues are (as deduced from (3.36))

$$\lambda_{m,n} = (k_{m,n})^2 = (j'_{m,n}/R)^2, \quad m = 0, 1, 2, \dots; n = 1, 2, 3, \dots,$$

with corresponding eigenfunctions

$$f_{m,n}(r) = J_m(j'_{m,n}r/R), \quad m = 0, 1, 2, \dots; n = 1, 2, 3, \dots,$$

$\lambda = 0$ is an eigenvalue only for $m = 0$.

Thus the solution of problem (3.32) has discrete eigenvalues:

$$\lambda_{m,n} = (j'_{m,n}/R)^2, \quad m = 0, 1, 2, \dots, n = 1, 2, \dots,$$

where $j'_{m,n}$ is the n^{th} positive zero of J'_m (an exception is that $J'_{0,1} = 0$). The corresponding discrete eigenfunctions are given by:

$$w_{0,n}(r, \theta) = J_0(j'_{0,n}r/R) \quad \text{for } m = 0.$$

For $m \geq 1$,

$$w_{m,n}(r, \theta) = J_m(j'_{m,n}r/R)(c_m \cos m\theta + d_m \sin m\theta).$$

We note that

$$c_m \cos m\theta + d_m \sin m\theta = c \cos m(\theta - \theta_1),$$

Table 3.4: Zeros of the derivative of Bessel functions of the first kind: $j'_{m,n}$ $m = 0, \dots, 5$; $n = 1, \dots, 4$.

n	$j'_{0,n}$	$j'_{1,n}$	$j'_{2,n}$	$j'_{3,n}$	$j'_{4,n}$	$j'_{5,n}$
1	0.00000	1.84118	3.05424	4.20119	5.31755	6.41562
2	3.83170	5.33144	6.70613	8.01524	9.28240	10.51986
3	7.01558	8.53632	9.96947	11.34592	12.68191	13.98719
4	10.17346	11.70600	13.17037	14.58585	15.96411	17.31284

for constants c and θ_1 , hence the discrete eigenfunctions can be rewritten as follows

$$w_{m,n}(r, \theta) = J_m(j'_{m,n}r/R) \cos m\theta, \quad \text{for } m \geq 1$$

for constant c .

Values of $j'_{m,n}$ are obtained from the ‘Handbook of Mathematical Functions with Formulas, Graphs, and Mathematical Tables’ by Abramowitz and Stegun (Abramowitz and Stegun 1968). For the sake of completeness, in Table 3.4, we present some values of $j'_{m,n}$ for $m = 0, \dots, 5$ and $n = 1, \dots, 4$.

We summarise the results given above in Remark 3.6.1 below.

Remark 3.6.1. Consider a scalar function w such that $\Delta w = k^2 w$, $w \neq 0$, on a disk $\Omega_0 = \{(x, y) : x^2 + y^2 \leq R^2\}$ with homogeneous Neumann boundary condition. Then the discrete eigenvalues are given by,

$$k_{m,n}^2 = \left(j'_{m,n}/R\right)^2, \quad m = 0, 1, 2, \dots; \quad n = 1, 2, \dots, \quad (3.37)$$

with corresponding eigenfunctions, $w_{m,n}$ given by

$$w_{m,n}(r, \theta) = \begin{cases} J_0(j'_{0,n}r/R) & \text{if } m = 0, \\ J_m(j'_{m,n}r/R) c \cos m(\theta - \theta_1) & \text{if } m > 0. \end{cases} \quad n = 1, 2, \dots,$$

for constants c and θ_1 . Here J_m is the m^{th} Bessel function of the first kind and $j'_{m,n}$ is the n^{th} positive zero of J'_m (except for $j'_{0,1} = 0$), where J'_m denotes the derivative of the Bessel function J_m with respect to r .

We consider the lowest non-zero wavenumber $k_{1,1}^2 = (j'_{1,1}/R)^2$ and its corresponding vibration mode $w_{1,1}(r, \theta) = J_1(j'_{1,1}r/R) \cos \theta$. Using MATLAB, we compute a surface plot of the vibration mode $w_{1,1}$. The plot is shown in Figure 3.5. This plot will be useful in the comparison of the linear stability theory with the numerical results. A way of checking the validity of the numerical results is to show that the numerical scheme computes

spatially inhomogeneous steady state solutions which coincides with those predicted by linear stability theory close to bifurcation points (Madzvamuse 2000).

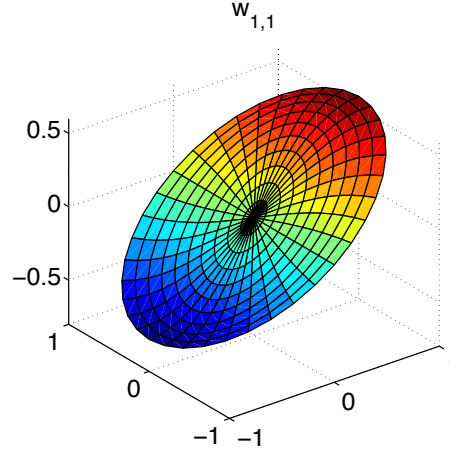


Figure 3.5: A surface plot of the vibration mode $w_{1,1}(r, \theta) = J_1(j'_{1,1}r) \cos \theta$ which corresponds to the lowest non-zero wavenumber $k^2_{1,1}$ on a unit disk.

3.7 Mode selection and the dispersion relation

We seek to identify parameter values for $c(k^2) > 0$ and $b(k^2) < 0$ to exist for a finite number of $k^2 > 0$. We continue to denote the non-dimensional model parameters by a tilde to avoid confusing it with their dimensional counterpart and we assign values to \tilde{p} and $\tilde{\psi}$ such that the dispersion relation isolates a finite number of wavenumbers. We begin by noting the following:

- If $c(k^2) > 0$ for some $k^2 > 0$ is required, then the value of the pressure coefficient \tilde{p} should be chosen such that the inequality $\tilde{p} < 1 + v'$ is satisfied. If this inequality is satisfied then $c(k^2) > 0$ for all wavenumbers k^2 (see (3.20) for the function $c(k^2)$). Thus we will have to rely on $b(k^2)$ for the isolation of a finite number of wavenumbers k^2 (this is a result of the Routh-Hurwitz stability criteria that gives a sufficient condition on the coefficients of the polynomial (3.20) that would result in $\text{Re } \lambda(k^2) > 0$ for some $k^2 > 0$).
- We require $b(k^2) < 0$ for some $k^2 > 0$. Recall that earlier in Section 3.5 we outlined the sufficient conditions for $b(k^2) < 0$ for some $k^2 > 0$. From these conditions we know that the value of $b(k^2)$ depends primarily on the value of the pressure coefficient \tilde{p} and the measure of the contractile tonicity $\tilde{\psi}$ for fixed values of \tilde{a}_{sat} .

Thus it is logical to use either \tilde{p} or $\tilde{\psi}$ as the bifurcation parameter but we prefer to use $\tilde{\psi}$ as the bifurcation parameter since there is no restriction on its value (note that \tilde{p} has a restriction on its value since it is required that $\tilde{p} < 1 + v'$ for $c(k^2)$ to be positive for any $k^2 > 0$).

3.7.1 Isolation of a finite range of unstable wavenumbers

Here we rely on $b(k^2)$ in order to produce a dispersion relation that isolates a finite range of unstable wavenumbers. $b(k^2)$ is a linear function of k^2 . We begin with the study of the dispersion relation that isolates the wavenumber $k_{1,1}^2$ as its only unstable non-zero wavenumber. The wavenumber $k_{1,1}^2$ is isolated by enforcing the following:

- $b(k^2) < 0$ for $k_{1,1}^2$ but greater than zero for all higher wavenumbers.
- $\tilde{p} < 1 + \nu'$ (recall that enforcing this restriction on \tilde{p} gives $c(k^2) > 0$ for all wavenumbers $k^2 > 0$). Given a Poisson's ratio $\nu := 0.3$ then $\nu' = 0.75$. Hence

$$\tilde{p} < 1 + \nu' = 1.75. \quad (3.38)$$

Thus to satisfy the inequality (3.38) we assign a value to $\tilde{p} = 0.26$. Next we assign a value to $\tilde{\psi}$ such that the three conditions for $b(k^2) < 0$ as given in Section 3.5 are satisfied for only $k_{1,1}^2$. Note that when the value of $\tilde{\psi}$ is gradually increased from $\tilde{\psi} = 0$ we obtain a Hopf bifurcation. If we continue to increase $\tilde{\psi}$ then we get a transition from a Hopf instability to a Turing's instability (See Figure 3.9(a)). A typical value of $\tilde{\psi}$ such that a Turing instability occurs with $k_{1,1}^2$ being the only non-zero wavenumber for which $b(k^2) < 0$ is $\tilde{\psi} = 62.4$ (corresponding dimensional value using the scaling (3.15) is $\psi = 72 \text{ dyn/cm}^2$) irrespective of the value of $\delta(l)$. A plot of $b(k^2)$ and the corresponding dispersion relation $\text{Re } \lambda(k^2)$ against k^2 is shown in Figure 3.6 for the case where $\delta(l) = 1$. The plot of $b(k^2)$ and the corresponding dispersion relation $\text{Re } \lambda(k^2)$ against k^2 for the case where $\delta(l) = 0$ is identical to that shown in Figure 3.6. We recall that it is not possible to isolate only one non-zero wavenumber except for the case where $k_{1,1}^2$ is isolated. For any wavenumber greater than $k_{1,1}^2$, we only have the choice of isolating the first 2 non-zero wavenumbers, the first 3 non-zero wavenumbers, the first 4 non-zero wavenumbers and so on. For illustrative purposes we present a plot in Figure 3.7 of $b(k^2)$ and the corresponding dispersion relation $\text{Re } \lambda(k^2)$ against k^2 where the first 2 non-zero wavenumbers have been isolated. In validating the numerical results we consider first the case where only $k_{1,1}^2$ is isolated. The advantage of this is that we can easily compare the linear stability theory with the numerical results without having to worry about the dynamics of mixed modes. Next we consider the dynamics of higher modes and mixed modes. To isolate the first 2 non-zero wavenumbers as shown in Figure 3.7, we carried on as we did for $k_{1,1}^2$ but in addition we enforced another condition which is that $k_2^2 < k_c^2 < k_3^2$ irrespective of if $\delta(l)$ in $b(k^2)$ is taken to be 1 or zero, where k_c^2 is the point when $b(k^2) = 0$, $k_2^2 := k_{2,1}^2$ and $k_3^2 := k_{0,1}^2$. See Table 3.5 for values of $\tilde{\psi}$ and the corresponding band of wavenumbers it isolates (all other model parameter values remain fixed and their values are given in Table 3.2). When a band of wavenumbers is linearly unstable, it is known that it becomes difficult to determine which eigenmode will be excited and

3.7. Mode selection and the dispersion relation

in such cases the initial conditions play a key role in determining which eigenmode is excited (Murray 1993). The principle of superposition (Zill and Cullen 2000) implies that any linear combination of eigenmodes is also a solution of the eigenvalue problem. Hence when a band of wavenumbers is isolated by a dispersion relation, it is possible that instead of a single mode being selected a linear combination of eigenmodes (i.e mixed modes) may evolve. In Section 5.1 we present numerical results that shows the important role played by the contractile coefficient and the choice of initial conditions on mode selection. For this purpose we present in Figure 3.8 surface plots of possible single and mixed modes that could evolve for bands of wavenumbers given in Table 3.5. Earlier,

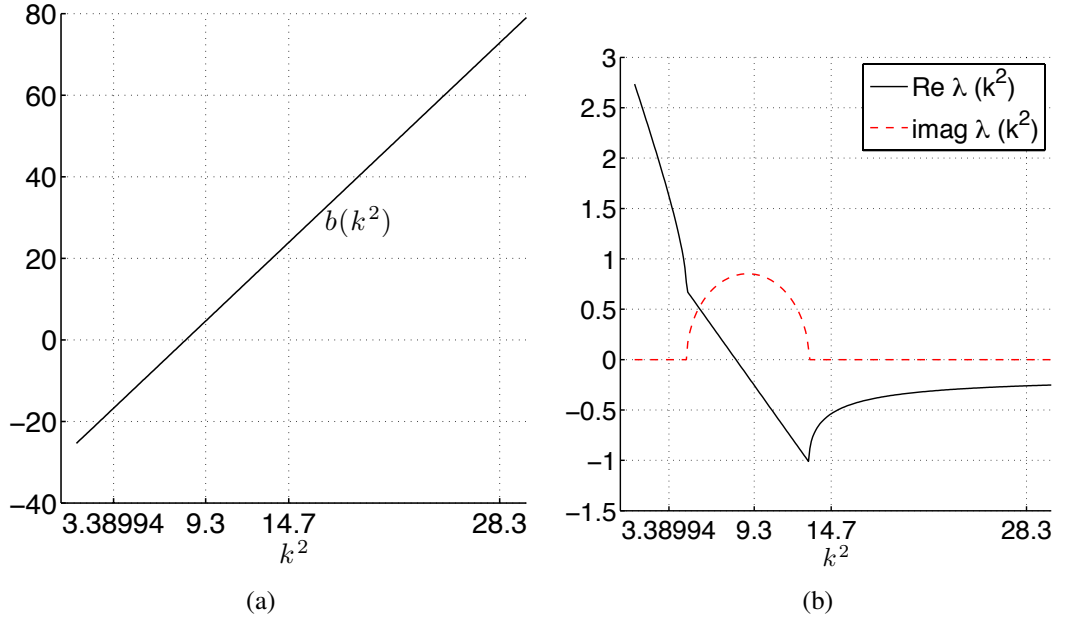


Figure 3.6: We present in (a) a plot of $b(k^2) < 0$ when $k_{1,1}^2 = 3.38994$ is the only excitable wavenumber. In (b) we show its corresponding dispersion relation $\text{Re } \lambda := \max(\text{Re } \lambda)$. In both cases $\delta(l) = 1$.

Table 3.5: A display of the values of $\tilde{\psi}$ (and their corresponding dimensional values of ψ) required by the dispersion relation in order to isolate at least two unstable wavenumbers.

Value of $\tilde{\psi}$	Value of ψ (dyn/cm ²)	wavenumbers isolated (i.e unstable)
62.439	72.045	$k_{0,1}^2, k_{1,1}^2$
95.327	109.993	$k_{0,1}^2, k_{1,1}^2, k_{2,1}^2$
131.869	152.157	$k_{0,1}^2, k_{1,1}^2, k_{2,1}^2, k_{0,2}^2$
174.767	201.654	$k_{0,1}^2, k_{1,1}^2, k_{2,1}^2, k_{0,2}^2, k_{3,1}^2, k_{4,1}^2$
270.094	311.647	$k_{0,1}^2, k_{1,1}^2, k_{2,1}^2, k_{0,2}^2, k_{3,1}^2, k_{4,1}^2, k_{1,2}^2, k_{5,1}^2$
317.758	366.643	$k_{0,1}^2, k_{1,1}^2, k_{2,1}^2, k_{0,2}^2, k_{3,1}^2, k_{4,1}^2, k_{1,2}^2, k_{5,1}^2, k_{2,2}^2$

we studied the dispersion relation with the value of the pressure coefficient \tilde{p} fixed but the

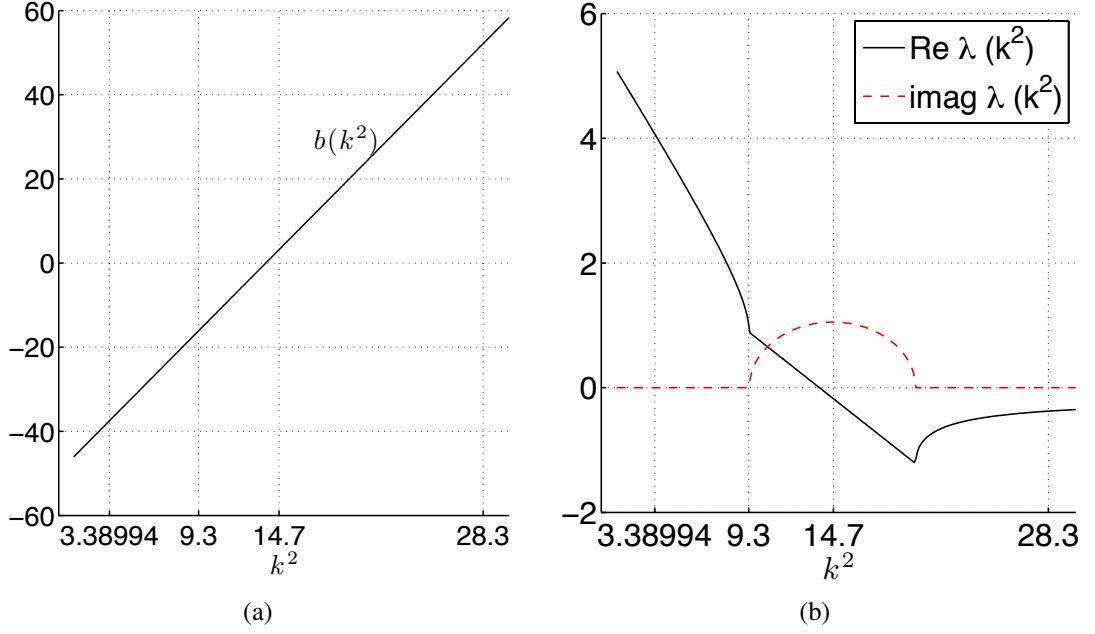


Figure 3.7: We present in (a) a plot of $b(k^2) < 0$ when the first 2 non-zero wavenumbers $k_{1,1}^2 = 3.38994$ and $k_{2,1}^2 = 9.32838$ are the only excitable wavenumbers. In (b) we show the corresponding dispersion relation $\text{Re } \lambda := \max(\text{Re } \lambda)$. In both cases $\delta(l) = 1$.

contractility tonicit $\tilde{\psi}$ varied. Various other combinations of $\tilde{\psi}$ and \tilde{p} are possible, hence we study below the parameter space $(\tilde{\psi}, \tilde{p})$.

3.7.2 Parameter space

The spatiotemporal patterns occur in dynamical systems when driven away from equilibrium. The occurrence of these patterns are due to the emergence of symmetry-breaking bifurcations (Cross and Hohenberg 1993; Moreo et al. 2010). According to Moreo et al. (2010) and Yang et al. (2002) we can classify these into three types of instabilities on the basis of a linear stability analysis of a homogeneous steady state, (1) a Turing bifurcation resulting in patterns that are stationary in time and oscillatory in space; (2) a Hopf bifurcation resulting in oscillations that are uniform in space and periodic in time ; and (3) a wave bifurcation resulting in patterns that are oscillatory in both time and space.

Here we keep all parameters given in Table 3.2 fixed except the pressure coefficient \tilde{p} and the contractile tonicit $\tilde{\psi}$. We make a plot of the parameter space $(\tilde{\psi}, \tilde{p})$ showing spaces that lie in a region of Hopf instability ($\text{Re}(\lambda) < 0$ and $\text{Imag}(\lambda) > 0$), oscillatory instability ($\text{Re}(\lambda) > 0$ and $\text{Imag}(\lambda) > 0$) or Turing instability ($\text{Re}(\lambda) > 0$ and $\text{Imag}(\lambda) = 0$). This plot is presented in Figure 3.9(a) for the case where $b(k^2)$ has $\delta(l) = 1$. Note that for $\delta(l) = 0$ the parameter space plot is identical to that shown in Figure 3.9(a). In Figure 3.9(a) we observe that there exists Hopf, oscillatory and Turing instability regions where all have a dispersion relation that isolates $k_{1,1}^2$ as the only non-zero wavenumber.

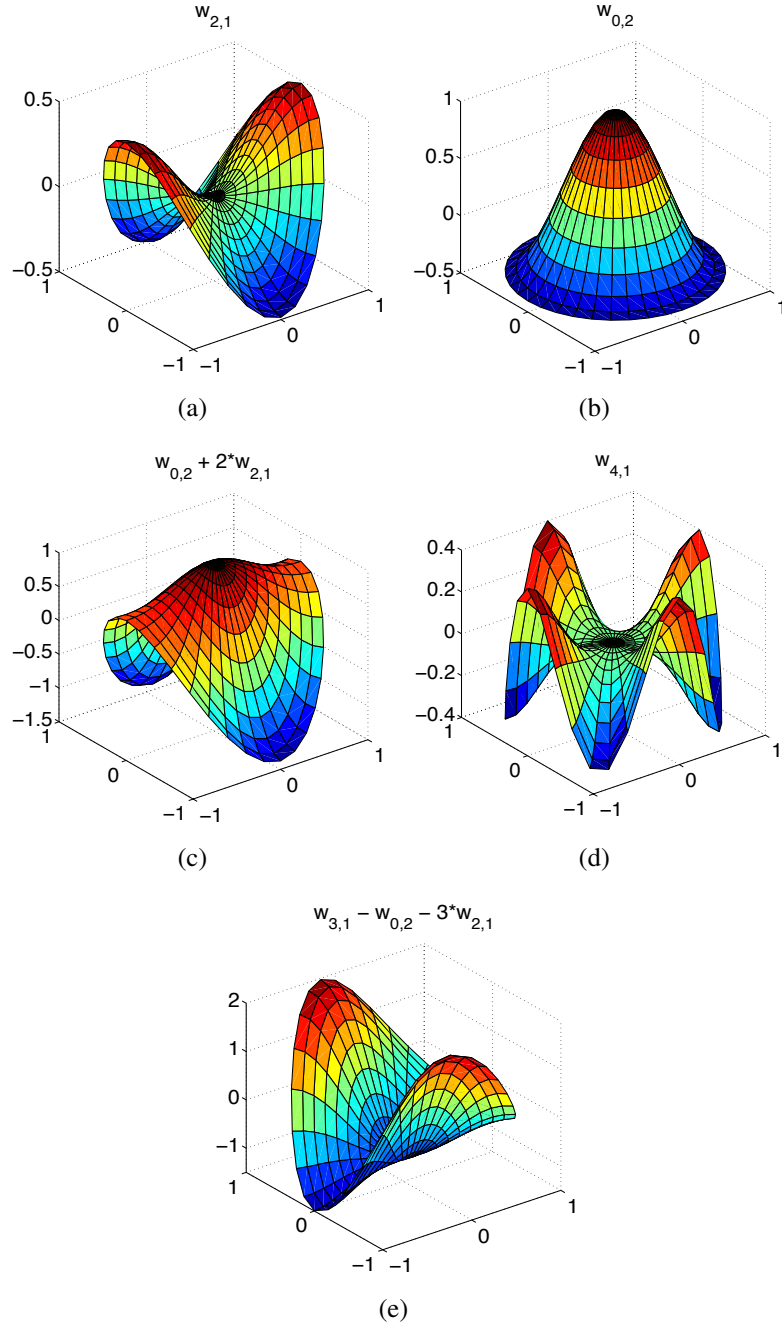


Figure 3.8: Surface plots of selected eigenmodes for some bands of wavenumbers displayed in Table 3.5.

The ash area (H) signifies the region of Hopf instability with a dispersion relation that isolates $k_{1,1}^2$ as the only unstable non-zero wavenumber. The region (dark blue) preceding that of Hopf instability represents the region where the uniform steady state is always stable for all wavenumbers k^2 . Immediately after the Hopf instability region we have a purple region (OS1) where an oscillatory instability exists for $k_{1,1}^2$. The green region is a Turing instability region and has a dispersion relation that isolates $k_{1,1}^2$ as the only unstable non-zero wavenumber. In the purple region (OS2) an oscillatory instability exists for $k_{2,1}^2$. The light blue region is also a Turing instability region and has a dispersion relation that

3.7. Mode selection and the dispersion relation

isolates the first two non-zero wavenumbers $k_{1,1}^2$ and $k_{2,1}^2$. If we keep $\tilde{\psi}$ constant say $\tilde{\psi} = 38.24$, and then varying \tilde{p} from 0 to 1.74, we observe (from the parameter space plot shown in Figure 3.9(a) for $\delta(l) = 1$) that there exists a transition from an oscillatory to a Turing instability. We make another plot to illustrate better the transition from an oscillatory to a Turing instability for $\tilde{\psi} = 38.24$ by plotting the values of the real and imaginary parts of λ as \tilde{p} varies from 0 to 1.74. This plot is shown in Figure 3.9(b) and 3.9(c) for $\delta(l) = 1$ and $\delta(l) = 0$ respectively. Alternatively, if we keep \tilde{p} constant say $\tilde{p} = 0.8$ and then vary $\tilde{\psi}$ from 30 to 60 then we obtain a transition from a stable region to Hopf instability region to an oscillatory instability region and then finally to a Turing instability region for both the case where $\delta(l) = 1$ (i.e. where $\sqrt{\xi_x^2 + \xi_y^2} > 0.8 = l_0$) and $\delta(l) = 0$ (i.e. where $\sqrt{\xi_x^2 + \xi_y^2} < 0.8 = l_0$), $k^2 > 0$ (see Figure 3.9(a)). It is natural to wonder how the solution would behave say in the case where $\tilde{\psi} = 38.24$ and \tilde{p} is varied from 0 to 1.74 such that a transition from an oscillatory instability to a Turing instability occurs. We studied this numerically by finding the numerical approximation of the model problem (3.14) using the finite element method along with the equivalent numerical value of \tilde{p} which we obtained from the scaling given in (3.15).

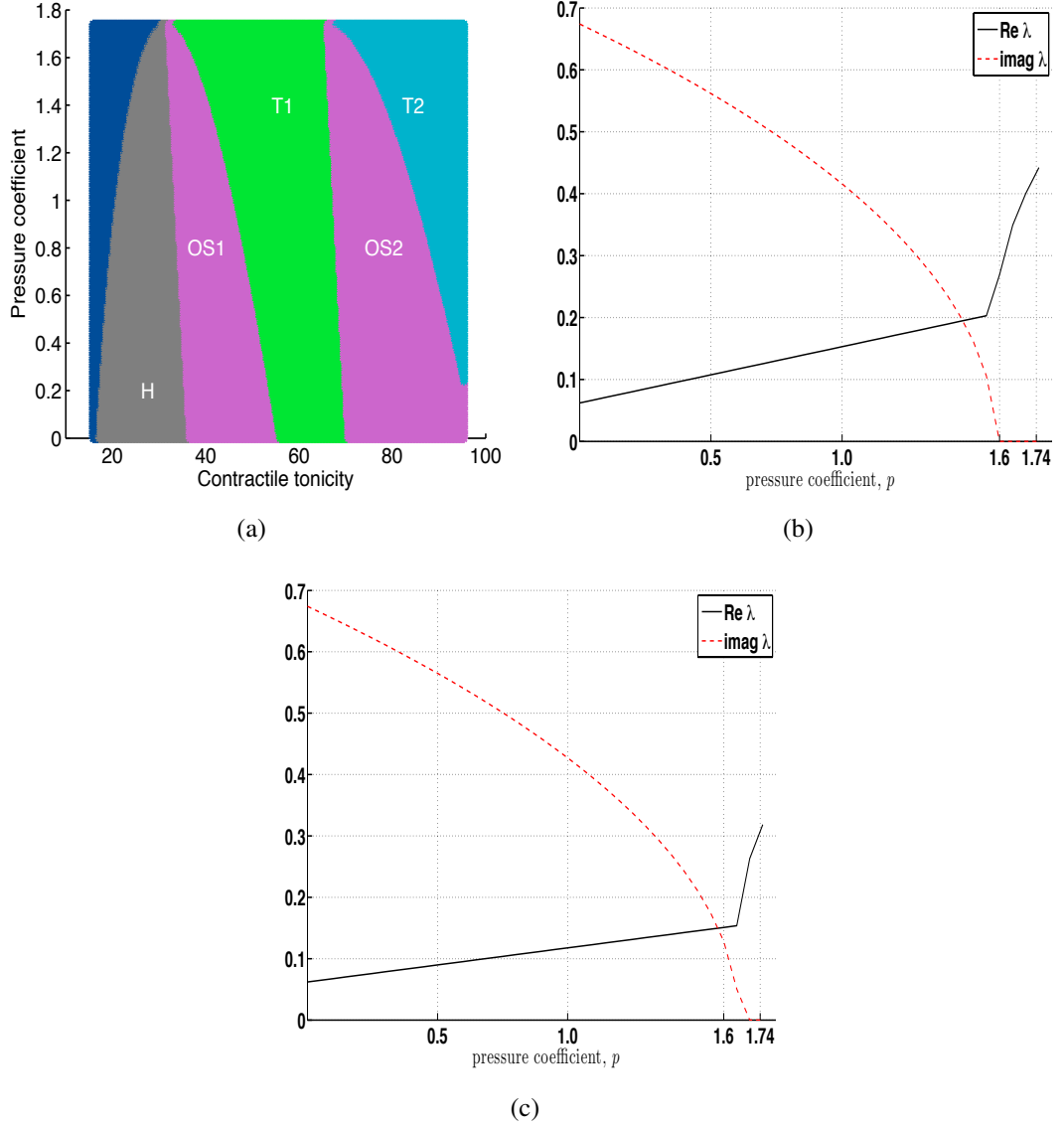


Figure 3.9: We present in (a) parameter space plot of the pressure coefficient \tilde{p} against the contractile tonicity $\tilde{\psi}$ showing the regions where instability exist for $\delta(l) = 1$. The ash area (H) signifies the region of Hopf instability with a dispersion relation that isolates $k_{1,1}^2$ as the only unstable non-zero wavenumber. The region (dark blue) preceding that of Hopf instability represents the region where the uniform steady state is always stable for all wavenumbers k^2 . Immediately after the Hopf instability region we have a purple region (OS1) where an oscillatory instability exists for $k_{1,1}^2$. The green region is a Turing instability region and has a dispersion relation that isolates $k_{1,1}^2$ as the only unstable non-zero wavenumber. In the purple region (OS2) an oscillatory instability exists for $k_{2,1}^2$. The light blue region is also a Turing instability region and has a dispersion relation that isolates the first two non-zero wavenumbers. And in (b) and (c) we show how the variation of \tilde{p} results in a transition from an oscillatory instability to a Turing instability for $\tilde{\psi} = 38.24$. In (b) $\delta(l) = 1$ and (c) $\delta(l) = 0$.

3.8 Summary

In this Chapter, we introduced a cytomechanical model for cell deformation from first principles. The model consists of two coupled system of equations, namely a force balance equation (derived from continuum mechanics) and a reaction-diffusion equation (derived from conservation equation exploiting conservation laws). The model assumes that cell deformation is as a result of the interaction between an internal hydrostatic pressure pushing on the membrane, an active polymerization-induced pressure pushing on the membrane and the contractile force of the actin network pulling on the membrane through their link with the membrane. The model consist of two variables namely, the F-actin density and the actin displacement velocity in the cell. A detailed mathematical analysis of the cytomechanical model was carried out using linear stability theory. The reason for carrying out the linear stability theory is to validate the numerical scheme that will be introduced in the next chapter. This is usually carried out by showing that the numerical results obtained are consistent with predictions from the linear stability theory close to bifurcation points for some finite range of unstable modes. In the linear stability analysis, a study of the dispersion relation showed that the parameter $\tilde{\psi}$ which describes the measure of the contractile tonicity is an appropriate bifurcation parameter. Thus by varying the value of $\tilde{\psi}$ we showed that the dispersion relation could isolate a finite range of wavenumbers. Also surface plots of predicted solutions for a couple of eigenfunctions corresponding to the wavenumbers isolated by the dispersion relation were also presented. These predictions from linear stability theory will be helpful in the validation of the numerical scheme introduced in the next chapter.

Chapter 4

A moving grid finite element method for cell movement

4.1 Introduction

The aim of this chapter is to solve the cytomechanical model (3.14) describing the dynamics of movements and shape changes of the cell. The model is a highly complex and non-linear system of equations with complex geometry as such an exact solution is difficult to compute and analytical solution is not feasible. In situations where exact solutions to mathematical problems are difficult to obtain an approximate solution is usually sought using numerical simulation methods (Reddy 1993). A lot of numerical simulation methods have been developed and are widely available in the literature. A determining factor in choosing a numerical method is usually the ease in which a method can be applied to a problem at hand and the ability of the method to produce highly accurate solutions in comparison with other available methods. The key factors being accuracy, efficiency and robustness of the numerical method (Madzvamuse 2006; Reddy 1993). On fixed domains with simple geometry, numerical simulations are usually done using the finite difference scheme due to the ease in which the method is applied (Crampin et al. 1999; Liszka and Orkisz 1980; Morton and Mayers 1994). The application of the finite difference scheme to continuously changing domains is usually non-trivial and encounters difficulty in dealing with a continuously deforming moving boundary (Madzvamuse et al. 2005).

Numerical simulations of the cytomechanical model has been done by Alt and Tranquillo (1995) and Stéphanou et al. (2004) based on the finite difference scheme. Existing difficulties in solving the cytomechanical model due to using the finite difference scheme can be overcome by using a different simulation method for example, a boundary element method (BEM) (Brebbia 1981; Crouch and Starfield 1983), a level set method (LSM) (Sethian 1996) or a finite element method (FEM) (Madzvamuse et al. 2003; Reddy 1993; Zienkiewicz et al. 2005). Since the cytomechanical model is a second order inhomoge-

neous and non-linear system of partial differential equations, the application of the BEM to its numerical approximation is much more difficult compared to FEM (LaForce 2006). The LSM will not be implemented here but could be implemented in the future to model splitting and reconnecting cells.

In order to avoid the problem involved in dealing with a free moving cell boundary, in Stéphanou et al. (2004) the description of the actin dynamics was restricted to a one-dimensional circular active layer of radius, r . As a result, the radial movements of actin in the cell cortex were not considered and only tangential displacements were assumed to lead to a local increase or decrease in density on the circle which affect the intensity of the retraction force.

The model was represented in the polar coordinate system. We reiterate here as stated in the introduction that the polar coordinate system has difficulty in describing the evolution of a cell as it moves outside the origin of the polar coordinate system.

In view of these, we develop in this chapter a moving grid finite element model (MGFEM) of the cytomechanical model that is defined in a 2D cartesian coordinate system. The MGFEM is a novel extension of the finite element method to moving boundary problems introduced by Madzvamuse (2000) to study partial differential equations posed on complex evolving domains. It is a highly accurate, efficient and robust numerical method which has been used successfully in Madzvamuse (2006); Madzvamuse et al. (2003; 2005) and Madzvamuse and Maini (2007) for the numerical simulation of reaction-diffusion systems on growing and continuously deforming domains with complex geometries. The novelty of the moving grid finite element method is its ability to allow the prescription of the nodal displacement of the computational grid points of the finite element mesh during the evolution of the domain. It is able to accommodate a priori descriptions of the grid displacement (Madzvamuse 2000), a computed grid displacement (which are solutions of a partial differential equation of an unknown variable) or a grid displacement generated by minimizing the residual of the differential equation (Baines 1994; Miller and Miller 1981) (as developed by Miller and Miller (1981) in the moving finite element). The difference between the moving finite element and MGFEM is the derivation of the grid displacement (Madzvamuse et al. 2005).

Here the displacement of the computational grid are prescribed as the displacement solutions of the force balance equation. The moving grid finite element method of the reaction-diffusion equations (3.14b) has already been established (Madzvamuse et al. 2005) but this is not the case for the force balance equation (3.14a). Here the main aim is to develop a MGFEM of the cytomechanical model by deriving a MGFEM of the force balance equation and then couple it to that of the reaction-diffusion equation.

In Section 4.3 we derive the weak formulation for the cytomechanical model. And we present a finite element discretisation of the model in Section 4.4. In Section 4.5 we describe the method of computation of the the domain evolution. Finally in Section 4.6

we describe the techniques of implementation of the MGFEM.

4.2 Basic concept of the moving grid finite element method

Finite element methods are based on the idea of dividing a domain of interest into sub-domains using simplexes such that the whole domain is approximated as a collection of these simplexes (Reddy 1993). These simplexes are otherwise known as elements and their vertices are called nodes. The model equations are described on each element and the solution is approximated over the element by polynomials in terms of nodal values and then assembled at the nodes to form an approximate system of equations for the whole domain. For time dependent problems, this gives rise to a system of ordinary differential equations and a temporal approximation is required, often using finite difference formula for the time derivative. The resulting system of equations are solved to obtain the desired unknown quantities at the nodes.

The moving grid finite element method is based on the same idea; the key difference being the introduction of a domain velocity and movement. The technique in which the domain movement is accounted for distinguishes it from other moving finite element methods (Madzvamuse 2006). The derivation of the moving grid finite element method for the cytochemical model involves four main steps: (1) Derivation of the weak formulation of the differential equation. (2) Approximation of the actin concentration solution (and displacement solution) over the finite elements (that involves a spatial and temporal approximation) to obtain a system of algebraic equations in terms of nodal values of actin concentration solution (and displacement solution). (3) Assembly of the element equations. (4) Incorporation of the domain velocity and movement.

The derivation of the finite element weak formulation of the cytochemical model is presented below.

4.3 Derivation of the weak formulation

For completeness, we restate here the cytochemical model for cell movement and deformations on a continuously deforming cell:

$$\nabla \cdot (\boldsymbol{\sigma}_v + \boldsymbol{\sigma}_e + \boldsymbol{\sigma}_c + \boldsymbol{\sigma}_p) = \mathbf{0} \quad \text{in } \boldsymbol{\Omega}_t, t \in I, \quad (4.1a)$$

$$\frac{\partial a}{\partial t} - D_a \Delta a + \nabla \cdot (a \boldsymbol{\beta}) - k_a(a_c - a) = 0 \quad \text{in } \boldsymbol{\Omega}_t, t \in I, \quad (4.1b)$$

$$\mathbf{u}(\mathbf{x}(t), t) = \mathbf{0} \quad \text{for } \mathbf{x} \in \boldsymbol{\Omega}_t, t = 0, \quad (4.1c)$$

$$a(\mathbf{x}(t), t) = a_0 \quad \text{for } \mathbf{x} \in \boldsymbol{\Omega}_t, t = 0, \quad (4.1d)$$

$$\boldsymbol{\beta} = \boldsymbol{\omega}_n \quad \text{for } \mathbf{x} \in \partial \boldsymbol{\Omega}_t, t \in I, \quad (4.1e)$$

$$\boldsymbol{\sigma}_v \cdot \mathbf{n} = \boldsymbol{\sigma}_e \cdot \mathbf{n} = \mathbf{n} \cdot \nabla a = 0 \quad \text{for } \mathbf{x} \in \partial \boldsymbol{\Omega}_t, t \in I, \quad (4.1f)$$

where in (4.1a), $\boldsymbol{\sigma}_v$, $\boldsymbol{\sigma}_e$, $\boldsymbol{\sigma}_c$ and $\boldsymbol{\sigma}_p$ are the viscous, elastic, contractile and pressure component stress tensors. These are defined as:

$$\boldsymbol{\sigma}_v = \mu_1 \frac{\partial \boldsymbol{\varepsilon}}{\partial t} + \mu_2 \frac{\partial \phi}{\partial t} \mathbf{I}, \quad (4.2)$$

$$\boldsymbol{\sigma}_e = \frac{E}{1+\nu} \left(\boldsymbol{\varepsilon} + \frac{\nu}{1-2\nu} \phi \mathbf{I} \right), \quad (4.3)$$

$$\boldsymbol{\sigma}_c = \sigma(a) \mathbf{I} = \psi a^2 e^{-a/a_{sat}} \mathbf{I}, \quad (4.4)$$

$$\boldsymbol{\sigma}_p = \frac{p(a)}{1+\phi} \mathbf{I} = \frac{p}{1+\phi} \left(1 + \frac{2}{\pi} \delta(l) \arctan a \right) \mathbf{I}, \quad (4.5)$$

respectively. $a = a(\mathbf{x}(t), t)$ is the F-actin concentration and $\mathbf{u} = (u(\mathbf{x}(t), t), v(\mathbf{x}(t), t))^T$ is a vector of displacement of the elements of the actin network at position $\mathbf{x} \in \boldsymbol{\Omega}_t$ at time $t \in I$. $\boldsymbol{\beta}$ represents the flow velocity of the elements of the actin network and $\boldsymbol{\omega}_n$ the normal velocity of the boundary. $\mathbf{n} = (n_x, n_y)$ is the outward unit vector normal to the boundary. $\boldsymbol{\varepsilon} = \frac{1}{2}(\nabla \mathbf{u} + \nabla \mathbf{u}^T)$ is the strain tensor, \mathbf{I} is the identity tensor, $\phi = \nabla \cdot \mathbf{u}$ is the dilation, ψ is a measure of the contractile tonicity, p is the pressure coefficient and μ_1 and μ_2 are the shear and bulk viscosities of the actin network respectively. Finally E and ν are the Young's modulus and Poisson ratio respectively.

In 3.14b, a_c is a constant parameter representing the F-actin concentration at the chemical equilibrium. It differentiates the states of polymerisation and depolymerization. The polymerisation rate is given by k_a and D_a is a positive diffusion coefficient for F-actin. On the boundary, we take the flow velocity of the actin network $\boldsymbol{\beta} = \boldsymbol{\omega}_n := \partial \mathbf{u} / \partial t$. Here \mathbf{u} is the displacement of the actin network at any given point in space and is computed as the displacement solution obtained from the force balance equation 3.14a. In the interior of the domain, we assume that $\boldsymbol{\beta} = \partial \mathbf{x} / \partial t := \partial \mathbf{u} / \partial t$ where $\partial \mathbf{x} / \partial t$ is the mesh velocity. Thus we have a Lagrangian description of the domain evolution.

The force balance equation will be decoupled first into a system of two partial differential equations for ease of implementation of the weak formulation and the derivation of the weak formulation of the force balance equation will be presented. Next we derive the weak formulation of the reaction-diffusion equation.

4.3.1 Weak formulation of the force balance equation

The force balance equation on a continuously deforming cell domain $\boldsymbol{\Omega}_t$ $t \in [0, T_f]$ is

$$\nabla \cdot (\boldsymbol{\sigma}_v + \boldsymbol{\sigma}_e + \boldsymbol{\sigma}_c + \boldsymbol{\sigma}_p) = \mathbf{0} \quad \text{in } \boldsymbol{\Omega}_t, t \in I, \quad (4.6a)$$

$$\mathbf{u}(\mathbf{x}(t), t) = \mathbf{0} \quad \text{for } \mathbf{x} \in \boldsymbol{\Omega}_t, t = 0, \quad (4.6b)$$

$$\boldsymbol{\sigma}_v \cdot \mathbf{n} = \boldsymbol{\sigma}_e \cdot \mathbf{n} = \mathbf{0} \quad \text{for } \mathbf{x} \in \partial \boldsymbol{\Omega}_t, t \in I, \quad (4.6c)$$

4.3. Derivation of the weak formulation

where in (4.6a), $\boldsymbol{\sigma}_v$, $\boldsymbol{\sigma}_e$, $\boldsymbol{\sigma}_c$ and $\boldsymbol{\sigma}_p$ are the viscous, elastic, contractile and pressure component stress tensors as defined in (4.2)-(4.5). Before we begin, we simplify the force balance equation by decoupling it into a system of two differential equations; we do so by substituting the values of $\boldsymbol{\sigma}_v$, $\boldsymbol{\sigma}_e$, $\boldsymbol{\sigma}_c$ and $\boldsymbol{\sigma}_p$ into the force balance equation (4.6a) and then decoupling the resulting equation. This necessitates the expression of the stress tensors in tensor-matrix forms. In order to write the stress tensors in tensor-matrix form we note that the dilation ϕ by definition is $\phi := \nabla \cdot \mathbf{u} = \frac{\partial u}{\partial x} + \frac{\partial v}{\partial y}$ and the stain tensor $\boldsymbol{\varepsilon}$ is:

$$\boldsymbol{\varepsilon}(\mathbf{u}) = \frac{1}{2}(\nabla \mathbf{u} + (\nabla \mathbf{u})^T) = \begin{pmatrix} \frac{\partial u}{\partial x} & \frac{1}{2}(\frac{\partial v}{\partial x} + \frac{\partial u}{\partial y}) \\ \frac{1}{2}(\frac{\partial v}{\partial x} + \frac{\partial u}{\partial y}) & \frac{\partial v}{\partial y} \end{pmatrix} \in \mathcal{R}^{2 \times 2}.$$

By using the above representation of the strain tensor $\boldsymbol{\varepsilon}$ and the dilation ϕ , we represent the stress tensors $\boldsymbol{\sigma}_c$, $\boldsymbol{\sigma}_p$, $\boldsymbol{\sigma}_e$ and $\boldsymbol{\sigma}_v$ (defined in (4.2)-(4.5)) in two-dimensional tensor-matrix forms as follows:

$$\boldsymbol{\sigma}_c = \begin{pmatrix} \psi a^2 e^{-a/a_{sat}} & 0 \\ 0 & \psi a^2 e^{-a/a_{sat}} \end{pmatrix} \in \mathcal{R}^{2 \times 2},$$

$$\boldsymbol{\sigma}_v = \begin{pmatrix} (\mu_1 + \mu_2) \frac{\partial \dot{u}}{\partial x} + \mu_2 \frac{\partial \dot{v}}{\partial y} & \frac{\mu_1}{2} (\frac{\partial \dot{v}}{\partial x} + \frac{\partial \dot{u}}{\partial y}) \\ \frac{\mu_1}{2} (\frac{\partial \dot{v}}{\partial x} + \frac{\partial \dot{u}}{\partial y}) & \mu_2 \frac{\partial \dot{u}}{\partial x} + (\mu_1 + \mu_2) \frac{\partial \dot{v}}{\partial y} \end{pmatrix} \in \mathcal{R}^{2 \times 2},$$

$$\boldsymbol{\sigma}_e = \frac{E'}{2} \begin{pmatrix} (v' + 2) \frac{\partial u}{\partial x} + v' \frac{\partial v}{\partial y} & \frac{\partial v}{\partial x} + \frac{\partial u}{\partial y} \\ \frac{\partial v}{\partial x} + \frac{\partial u}{\partial y} & v' \frac{\partial u}{\partial x} + (v' + 2) \frac{\partial v}{\partial y} \end{pmatrix} \in \mathcal{R}^{2 \times 2},$$

and

$$\boldsymbol{\sigma}_p = \begin{pmatrix} \frac{p}{1+\phi} (1 + \frac{2}{\pi} \delta(l) \arctan a) & 0 \\ 0 & \frac{p}{1+\phi} (1 + \frac{2}{\pi} \delta(l) \arctan a) \end{pmatrix} \in \mathcal{R}^{2 \times 2},$$

where $E' = E/(1 + \nu)$, $\nu' = \nu/(1 - 2\nu)$ and E and ν are the Young's modulus and Poisson ratio respectively. We substitute the matrix tensor representation of the stress tensors into (4.6a) to obtain the force balance equation in matrix tensor form which is then decoupled into a system of two equations. The decoupled system of differential equations

of the force balance equation is thus:

$$\begin{aligned} \frac{\partial}{\partial x} \left(\mathbf{D}_{11} \frac{\partial \dot{u}}{\partial x} + \mathbf{D}_{12} \frac{\partial \dot{v}}{\partial y} \right) + \frac{\partial}{\partial y} \left[\mathbf{D}_{33} \left(\frac{\partial \dot{u}}{\partial y} + \frac{\partial \dot{v}}{\partial x} \right) \right] + \frac{\partial}{\partial x} \left(\mathbf{C}_{11} \frac{\partial u}{\partial x} + \mathbf{C}_{12} \frac{\partial v}{\partial y} \right) \\ + \frac{\partial}{\partial y} \left[\mathbf{C}_{33} \left(\frac{\partial u}{\partial y} + \frac{\partial v}{\partial x} \right) \right] = -\frac{\partial f_1}{\partial x}, \end{aligned} \quad (4.7a)$$

and

$$\begin{aligned} \frac{\partial}{\partial x} \left[\mathbf{D}_{33} \left(\frac{\partial \dot{u}}{\partial y} + \frac{\partial \dot{v}}{\partial x} \right) \right] + \frac{\partial}{\partial y} \left(\mathbf{D}_{12} \frac{\partial \dot{u}}{\partial x} + \mathbf{D}_{22} \frac{\partial \dot{v}}{\partial y} \right) + \frac{\partial}{\partial y} \left(\mathbf{C}_{12} \frac{\partial u}{\partial x} + \mathbf{C}_{22} \frac{\partial v}{\partial y} \right) \\ + \frac{\partial}{\partial x} \left[\mathbf{C}_{33} \left(\frac{\partial u}{\partial y} + \frac{\partial v}{\partial x} \right) \right] = -\frac{\partial f_2}{\partial y}, \end{aligned} \quad (4.7b)$$

where

$$\begin{aligned} f_1 \equiv f_2 &= \left[\frac{P}{1+\phi} \left(1 + \frac{2}{\pi} \delta(l) \arctan a \right) + \psi a^2 e^{-a/a_{sat}} \right], \\ \mathbf{D}_{11} &= \mathbf{D}_{22} = \mu_1 + \mu_2, \quad \mathbf{D}_{12} \equiv \mathbf{D}_{21} = \mu_2, \quad \mathbf{D}_{33} = \mu_1/2, \\ \mathbf{C}_{11} \equiv \mathbf{C}_{22} &= \frac{E(1-\nu)}{(1+\nu)(1-2\nu)}, \quad \mathbf{C}_{12} \equiv \mathbf{C}_{21} = \frac{E\nu}{(1+\nu)(1-2\nu)} \text{ and } \mathbf{C}_{33} = \frac{E}{2(1+\nu)}. \end{aligned}$$

$\phi = \nabla \cdot \mathbf{u}$ is the dilation, ψ is a measure of the contractile tonicity and μ_1 and μ_2 are the shear and bulk viscosities of the actin network respectively. E and ν are the Young's modulus and Poisson ratio respectively.

In order to derive the weak formulation of the force balance equation, we multiply the system of partial differential equations (4.7) by a test function $w_1(\mathbf{x}, t) \in H^1(\Omega_t)$, $t \in I$, and using Green's formula (1.5) we integrate the partial differential equations over the domain Ω_t and apply the boundary conditions (4.6c). We note that the boundary condition (4.6c) implies that the boundary term vanishes after carrying out the integration over the domain. The weak formulation is thus: Find $u(\mathbf{x}, t), v(\mathbf{x}, t) \in H^1(\Omega_t)$, $t \in I$ such that

$$\begin{aligned} \int_{\Omega_t} \frac{\partial w_1}{\partial x} \left(\mathbf{D}_{11} \frac{\partial \dot{u}}{\partial x} + \mathbf{D}_{12} \frac{\partial \dot{v}}{\partial y} + \mathbf{C}_{11} \frac{\partial u}{\partial x} + \mathbf{C}_{12} \frac{\partial v}{\partial y} \right) + \frac{\partial w_1}{\partial y} \left[\mathbf{D}_{33} \left(\frac{\partial \dot{u}}{\partial y} + \frac{\partial \dot{v}}{\partial x} \right) \right] \\ + \frac{\partial w_1}{\partial y} \left[\mathbf{C}_{33} \left(\frac{\partial u}{\partial y} + \frac{\partial v}{\partial x} \right) \right] d\Omega_t = \int_{\Omega_t} w_1 \frac{\partial f_1}{\partial x} d\Omega_t, \end{aligned} \quad (4.8a)$$

and

$$\begin{aligned} \int_{\Omega_t} \frac{\partial w_1}{\partial y} \left(\mathbf{D}_{12} \frac{\partial \dot{u}}{\partial x} + \mathbf{D}_{22} \frac{\partial \dot{v}}{\partial y} + \mathbf{C}_{12} \frac{\partial u}{\partial x} + \mathbf{C}_{22} \frac{\partial v}{\partial y} \right) + \frac{\partial w_1}{\partial x} \left[\mathbf{D}_{33} \left(\frac{\partial \dot{u}}{\partial y} + \frac{\partial \dot{v}}{\partial x} \right) \right] \\ + \frac{\partial w_1}{\partial x} \left[\mathbf{C}_{33} \left(\frac{\partial u}{\partial y} + \frac{\partial v}{\partial x} \right) \right] d\Omega_t = \int_{\Omega_t} w_1 \frac{\partial f_2}{\partial y} d\Omega_t, \end{aligned} \quad (4.8b)$$

for all $w_1(\mathbf{x}, t) \in H^1(\Omega_t)$, $t \in I$. The integrals on the right hand side of the weak formula-

tion (4.8) are difficult to evaluate. To show this we write them out explicitly as:

$$\begin{cases} \int_{\Omega_t} w_1 \frac{\partial f_1}{\partial x} d\Omega_t &= \int_{\Omega_t} w_1 \frac{\partial}{\partial x} \left[\frac{p}{1+\phi} \left(1 + \frac{2}{\pi} \delta(l) \arctan a \right) + \psi a^2 e^{-a/a_{sat}} \right] d\Omega_t, \\ \int_{\Omega_t} w_1 \frac{\partial f_2}{\partial y} d\Omega_t &= \int_{\Omega_t} w_1 \frac{\partial}{\partial y} \left[\frac{p}{1+\phi} \left(1 + \frac{2}{\pi} \delta(l) \arctan a \right) + \psi a^2 e^{-a/a_{sat}} \right] d\Omega_t, \end{cases} \quad (4.9)$$

since $f_1 \equiv f_2 = \frac{p}{1+\phi} \left(1 + \frac{2}{\pi} \delta(l) \arctan a \right) + \psi a^2 e^{-a/a_{sat}}$. In view of this, we state the following identities which can be derived using the gradient and divergence theorems and are useful in the sequel in rewriting the weak form in a computationally efficient form. Let $r(\mathbf{x}, t)$ and $g(\mathbf{x}, t)$ be scalar functions of class $C^0(\Omega_t)$ defined in $\Omega_t \subset \mathbb{R}^2$ and also let $\mathbf{n} = (n_1, n_2)$ denote the outward unit vector normal to $\partial\Omega_t$ for time $t \in I$. Then the following identities (derived from the gradient theorem (1.1), see (1.2) and (1.3)) hold:

$$\begin{cases} \int_{\Omega_t} r \frac{\partial g}{\partial x} d\Omega_t &= - \int_{\Omega_t} g \frac{\partial r}{\partial x} d\Omega_t + \int_{\partial\Omega_t} n_1 r g ds, \\ \int_{\Omega_t} r \frac{\partial g}{\partial y} d\Omega_t &= - \int_{\Omega_t} g \frac{\partial r}{\partial y} d\Omega_t + \int_{\partial\Omega_t} n_2 r g ds, \end{cases} \quad (4.10)$$

where ds is the element of arclength. Using the identities (4.10) we can rewrite the weak form as follows: Find $u(\mathbf{x}, t), v(\mathbf{x}, t) \in H^1(\Omega_t)$, $t \in I$ such that

$$\begin{aligned} \int_{\Omega_t} \frac{\partial w_1}{\partial x} \left(\mathbf{D}_{11} \frac{\partial \dot{u}}{\partial x} + \mathbf{D}_{12} \frac{\partial \dot{v}}{\partial y} + \mathbf{C}_{11} \frac{\partial u}{\partial x} + \mathbf{C}_{12} \frac{\partial v}{\partial y} \right) + \frac{\partial w_1}{\partial y} \left[\mathbf{D}_{33} \left(\frac{\partial \dot{u}}{\partial y} + \frac{\partial \dot{v}}{\partial x} \right) \right] \\ + \frac{\partial w_1}{\partial y} \left[\mathbf{C}_{33} \left(\frac{\partial u}{\partial y} + \frac{\partial v}{\partial x} \right) \right] d\Omega_t = - \int_{\Omega_t} f_1 \frac{\partial w_1}{\partial x} d\Omega_t \\ + \int_{\partial\Omega_t} n_1 f_1 w_1 ds, \end{aligned} \quad (4.11a)$$

and

$$\begin{aligned} \int_{\Omega_t} \frac{\partial w_1}{\partial y} \left(\mathbf{D}_{12} \frac{\partial \dot{u}}{\partial x} + \mathbf{D}_{22} \frac{\partial \dot{v}}{\partial y} + \mathbf{C}_{12} \frac{\partial u}{\partial x} + \mathbf{C}_{22} \frac{\partial v}{\partial y} \right) + \frac{\partial w_1}{\partial x} \left[\mathbf{D}_{33} \left(\frac{\partial \dot{u}}{\partial y} + \frac{\partial \dot{v}}{\partial x} \right) \right] \\ + \frac{\partial w_1}{\partial x} \left[\mathbf{C}_{33} \left(\frac{\partial u}{\partial y} + \frac{\partial v}{\partial x} \right) \right] d\Omega_t = - \int_{\Omega_t} f_2 \frac{\partial w_1}{\partial y} d\Omega_t \\ + \int_{\partial\Omega_t} n_2 f_2 w_1 ds, \end{aligned} \quad (4.11b)$$

for all $w_1(\mathbf{x}, t) \in H^1(\Omega_t)$, $t \in I$. Here n_1 and n_2 are the direction cosines of the outward unit vector, \mathbf{n} normal to $\partial\Omega_t$ for time $t \in I$ (i.e. n_1 is the cosine of the angle between the positive x direction and the vector \mathbf{n} and n_2 is the cosine of the angle between the positive y direction and the vector \mathbf{n}). Since the test functions we use are piecewise linear

basis functions and their spatial derivatives are easy and straight forward to compute, the weak formulation as expressed in (4.11) is a lot easier to compute compared to (4.8). We say that $u(\mathbf{x}, t)$, $v(\mathbf{x}, t)$ are weak solutions of the force balance equation (4.6a) if $u(\mathbf{x}, t)$, $v(\mathbf{x}, t) \in H^1(\Omega_t)$ and (4.11) holds. Here we have assumed that $a(\mathbf{x}, t)$ is known and is the solution of the reaction-diffusion equation (4.1b).

Remark 4.3.1. *We would like to note that we do not actually compute the derivatives of the delta function but we transfer these derivatives to the test function by using identities (4.10).*

4.3.2 Weak formulation of the reaction-diffusion equation

Here we recall the reaction-diffusion equation for the actin bio-chemical dynamics for completeness and derive a finite element model for this equation. The reaction-diffusion equation for the actin bio-chemical dynamics is:

$$\frac{\partial a}{\partial t} - D_a \Delta a + \nabla \cdot (a \boldsymbol{\beta}) - k_a (a_c - a) = 0, \quad (4.12)$$

where $a = a(\mathbf{x}(t), t)$ is the F-actin concentration and $\boldsymbol{\beta}$ represents the flow velocity of the elements of the actin network. a_c is a constant parameter representing the F-actin concentration at the chemical equilibrium. It differentiates the states of polymerisation and depolymerization. The polymerisation rate is given by k_a and D_a is a positive diffusion coefficient for F-actin.

By applying the product rule to the transport term in the reaction-diffusion equation (4.12), we can rewrite the reaction-diffusion equation as follows:

$$\frac{\partial a}{\partial t} - D_a \Delta a + (\nabla a) \cdot \boldsymbol{\beta} + a (\nabla \cdot \boldsymbol{\beta}) - k_a (a_c - a) = 0. \quad (4.13)$$

We would like to represent the partial time derivative in the reaction-diffusion equation (4.13) in terms of the material derivative. In view of this, we introduce the material derivative of the actin concentration a . Let Da/Dt be a material derivative, then the material derivative of the actin concentration a is defined as (Reddy 1993);

$$\frac{Da}{Dt} = \frac{\partial a}{\partial t} + (\nabla a) \cdot \boldsymbol{\beta}. \quad (4.14)$$

Upon substituting the material derivative (4.14) into (4.13), we obtain the following differential equation,

$$\frac{Da}{Dt} - D_a \Delta a + a (\nabla \cdot \boldsymbol{\beta}) - k_a (a_c - a) = 0. \quad (4.15)$$

In order to obtain the weak formulation we multiply (4.15) by a test function $w_2(\mathbf{x}, t) \in H^1(\Omega_t)$, $t \in \mathbf{I}$ then we integrate by parts and apply the boundary condition $\mathbf{n} \cdot \nabla a = 0$

(see (4.1f)) :

$$\int_{\Omega_t} \left[w_2 \frac{Da}{\partial t} + a w_2 (\nabla \cdot \boldsymbol{\beta}) + D_a \nabla a \cdot \nabla w_2 + k_a a w_2 \right] d\Omega_t = \int_{\Omega_t} k_a a_c w_2 d\Omega_t. \quad (4.16)$$

Using the product rule, the differential equation (4.16) can be rewritten as:

$$\begin{aligned} \int_{\Omega_t} \left[\frac{D(aw_2)}{\partial t} - a \frac{Dw_2}{\partial t} + aw_2 (\nabla \cdot \boldsymbol{\beta}) + D_a \nabla a \cdot \nabla w_2 \right] d\Omega_t + \int_{\Omega_t} k_a aw_2 d\Omega_t \\ = \int_{\Omega_t} k_a a_c w_2 d\Omega_t. \end{aligned} \quad (4.17)$$

Using the Reynolds transport theorem (see Section 1.2.4), we rewrite (4.17) such that the weak formulation reads: Find $a(\mathbf{x}, t) \in H^1(\Omega_t)$, $t \in \mathbf{I}$ such that

$$\begin{aligned} \frac{d}{dt} \int_{\Omega_t} aw_2 d\Omega_t + \int_{\Omega_t} (D_a \nabla a \cdot \nabla w_2 + k_a aw_2) d\Omega_t = \int_{\Omega_t} \left(k_a a_c w_2 + a \frac{Dw_2}{Dt} \right) d\Omega_t, \\ \forall w_2 \in H^1(\Omega_t). \end{aligned} \quad (4.18)$$

A stability analysis of the reaction-diffusion equation is given in Appendix A. We show the existence of a weak solution of (4.15) in Appendix B. These results are known but are only presented for the sake of completeness.

4.3.3 Weak formulation of the coupled problem

The weak formulation of the coupled problem (4.1) is thus: Find $a(\mathbf{x}, t)$, $u(\mathbf{x}, t)$, $v(\mathbf{x}, t) \in H^1(\Omega_t)$, $t \in I$ such that

$$\begin{aligned} \int_{\Omega_t} \frac{\partial w_1}{\partial x} \left(\mathbf{D}_{11} \frac{\partial \dot{u}}{\partial x} + \mathbf{D}_{12} \frac{\partial \dot{v}}{\partial y} + \mathbf{C}_{11} \frac{\partial u}{\partial x} + \mathbf{C}_{12} \frac{\partial v}{\partial y} \right) + \frac{\partial w_1}{\partial y} \left[\mathbf{D}_{33} \left(\frac{\partial \dot{u}}{\partial y} + \frac{\partial \dot{v}}{\partial x} \right) \right] \\ + \frac{\partial w_1}{\partial y} \left[\mathbf{C}_{33} \left(\frac{\partial u}{\partial y} + \frac{\partial v}{\partial x} \right) \right] d\Omega_t = - \int_{\Omega_t} f_1 \frac{\partial w_1}{\partial x} d\Omega_t \\ + \int_{\partial\Omega_t} n_1 f_1 w ds, \end{aligned} \quad (4.19a)$$

$$\begin{aligned} \int_{\Omega_t} \frac{\partial w_1}{\partial y} \left(\mathbf{D}_{12} \frac{\partial \dot{u}}{\partial x} + \mathbf{D}_{22} \frac{\partial \dot{v}}{\partial y} + \mathbf{C}_{12} \frac{\partial u}{\partial x} + \mathbf{C}_{22} \frac{\partial v}{\partial y} \right) + \frac{\partial w_1}{\partial x} \left[\mathbf{D}_{33} \left(\frac{\partial \dot{u}}{\partial y} + \frac{\partial \dot{v}}{\partial x} \right) \right] \\ + \frac{\partial w_1}{\partial x} \left[\mathbf{C}_{33} \left(\frac{\partial u}{\partial y} + \frac{\partial v}{\partial x} \right) \right] d\Omega_t = - \int_{\Omega_t} f_2 \frac{\partial w_1}{\partial y} d\Omega_t \\ + \int_{\partial\Omega_t} n_2 f_2 w_1 ds, \end{aligned} \quad (4.19b)$$

and

$$\begin{aligned} \frac{d}{dt} \int_{\Omega_t} a w_2 d\Omega_t + \int_{\Omega_t} (D_a \nabla a \cdot \nabla w_2 + k_a a w_2) d\Omega_t = \int_{\Omega_t} k_a a_c w_2 d\Omega_t \\ + \int_{\Omega_t} a \frac{D w_2}{Dt} d\Omega_t, \end{aligned} \quad (4.19c)$$

for all $w_1(\mathbf{x}, t)$, $w_2(\mathbf{x}, t) \in H^1(\Omega_t)$, $t \in I$.

4.3.4 Finite-dimensional subspaces

Let $\Omega_{h,t}$, $t \in I$ be a bounded domain triangulated by $\mathcal{T}_{h,t}$. Each triangular partition is known as an element S . We use barycentric coordinates as the local coordinate system on the elements of the triangulation. Let $\bar{\mathbb{P}}$ be a finite dimensional function space defined on \bar{S} , where \bar{S} is a reference element:

$$\bar{S} := \left\{ (\lambda_1, \dots, \lambda_3) \in \mathcal{R}^3; 0 \leq \lambda_k \leq 1, \sum_{k=1}^3 \lambda_k = 1 \right\}$$

then there exists a one-to-one mapping from \bar{S} to S . Also let $\{\mathbf{x}_1, \mathbf{x}_2, \mathbf{x}_3\}$ denote the vertices of the element S . Then the following parameterisation using barycentric coordinates over the element S can be defined (Dziuk and Elliott 2007),

$$\mathbf{x}(\lambda_1, \lambda_2, \lambda_3, t) = \sum_{k=1}^3 \lambda_k \mathbf{x}_k(t). \quad (4.20)$$

Let $w(\mathbf{x}(t)) : \Omega_t \rightarrow \mathcal{R}$, $t \in I$, be a finite element function on an element S defined by a finite dimensional function space $\bar{\mathbb{P}}$ on a reference element \bar{S} and the mapping λ^S from

the reference element \bar{S} to S such that $w(\mathbf{x}(t)) = \bar{w}(\lambda^S(\mathbf{x}(t)))$, where \bar{w} is defined on \bar{S} . We define the space $\mathcal{X}^h(t) \subset H^1(\Omega_t)$:

$$\mathcal{X}^h(t) = \{w \in C^0(\Omega_t); \bar{w} \in \bar{\mathbb{P}} \text{ for all } S \in \mathcal{T}_{h,t}, t \in I\}.$$

4.4 Finite element discretization of the model

We discretize the problem (4.19) using the classical Galerkin method. At each time $t, t \in I$, we discretize Ω_t into a finite unstructured triangular partition $\Omega_{h,t}$ of non-overlapping triangles, where h is the maximum size of the largest triangle. Each triangular partition is known as an element S and the set of these finite triangular elements is called a mesh and we denote this mesh by $\mathcal{T}_{h,t}$. For the finite element mesh we require that no vertex of any element lie on the interior of a side of another element and $S_i \cap S_j = \emptyset$ if $i \neq j$. Thus

$$\bar{\Omega}_{h,t} = \bigcup_{S(t) \in \mathcal{T}_{h,t}} S(t).$$

Definition 4.4.1. (*Shape regularity; Johnson (1987)*)

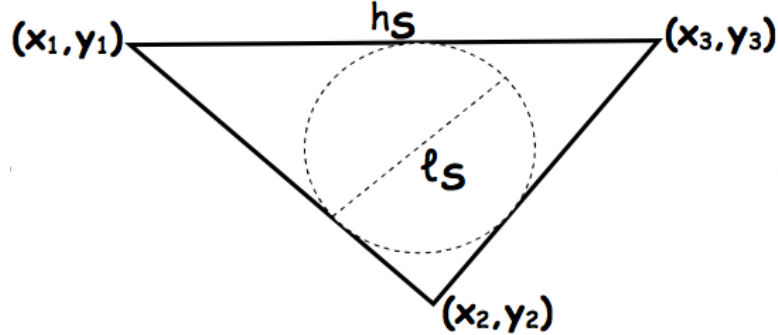


Figure 4.1: A description of a typical element S of the triangulation $\mathcal{T}_{h,t}$.

Let h_S be the longest side of S (otherwise known as the diameter of S), ρ_S the diameter of the circle inscribed in S (see Figure 4.1) and

$$h = \max_{S \in \mathcal{T}_{h,t}} h_S.$$

A triangulation $\mathcal{T}_{h,t}$ is shape regular if there exists a positive constant ζ independent of h such that

$$\frac{\rho_S}{h_S} \geq \zeta \quad \forall S \in \mathcal{T}_{h,t}, t \in I. \quad (4.21)$$

The constant ζ is a measure of the minimum angle in any $S \in \mathcal{T}_{h,t}, t \in I$. The regularity condition (4.21) specifies that the elements S are not allowed to be arbitrary thin.

The triangulation $\mathcal{T}_{h,t}$ for all $t \in I$ is shape regular.

4.4. Finite element discretization of the model

The discretised problem of the coupled system(P_S) of (4.19) reads: Find $a_h(\mathbf{x}, t)$, $u_h(\mathbf{x}, t)$, $v_h(\mathbf{x}, t) \in \mathcal{X}^h(t)$, $t \in I$ such that

$$\begin{aligned} \int_{\Omega_{h,t}} \frac{\partial w_h^1}{\partial x} \left(\mathbf{D}_{11} \frac{\partial \dot{u}_h}{\partial x} + \mathbf{D}_{12} \frac{\partial \dot{v}_h}{\partial y} + \mathbf{C}_{11} \frac{\partial u_h}{\partial x} + \mathbf{C}_{12} \frac{\partial v_h}{\partial y} \right) + \frac{\partial w_h^1}{\partial y} \left[\mathbf{D}_{33} \left(\frac{\partial \dot{u}_h}{\partial y} + \frac{\partial \dot{v}_h}{\partial x} \right) \right] \\ + \frac{\partial w_h^2}{\partial y} \left[\mathbf{C}_{33} \left(\frac{\partial u_h}{\partial y} + \frac{\partial v_h}{\partial x} \right) \right] d\Omega_{h,t} = - \int_{\Omega_{h,t}} f_1 \frac{\partial w_h^1}{\partial x} d\Omega_{h,t} \\ + \int_{\partial\Omega_{h,t}} n_1 f_1 w_h^1 ds, \quad (4.22a) \end{aligned}$$

$$\begin{aligned} \int_{\Omega_{h,t}} \frac{\partial w_h^1}{\partial y} \left(\mathbf{D}_{12} \frac{\partial \dot{u}_h}{\partial x} + \mathbf{D}_{22} \frac{\partial \dot{v}_h}{\partial y} + \mathbf{C}_{12} \frac{\partial u_h}{\partial x} + \mathbf{C}_{22} \frac{\partial v_h}{\partial y} \right) + \frac{\partial w_h^1}{\partial x} \left[\mathbf{D}_{33} \left(\frac{\partial \dot{u}_h}{\partial y} + \frac{\partial \dot{v}_h}{\partial x} \right) \right] \\ + \frac{\partial w_h^1}{\partial x} \left[\mathbf{C}_{33} \left(\frac{\partial u_h}{\partial y} + \frac{\partial v_h}{\partial x} \right) \right] d\Omega_{h,t} = - \int_{\Omega_{h,t}} f_2 \frac{\partial w_h^1}{\partial y} d\Omega_{h,t} \\ + \int_{\partial\Omega_{h,t}} n_2 f_2 w_h^1 ds, \quad (4.22b) \end{aligned}$$

and

$$\begin{aligned} \frac{d}{dt} \int_{\Omega_{h,t}} a_h w_h^2 d\Omega_{h,t} + \int_{\Omega_{h,t}} (D_a \nabla a_h \cdot \nabla w_h^2 + k_a a_h w_h^2) d\Omega_{h,t} = \int_{\Omega_{h,t}} k_a a_c w_h^2 d\Omega_{h,t} \\ + \int_{\Omega_{h,t}} a \frac{D w_h^2}{Dt} d\Omega_{h,t}, \quad (4.22c) \end{aligned}$$

for all $w_h^1(\mathbf{x}, t)$, $w_h^2(\mathbf{x}, t) \in \mathcal{X}^h(t)$. Let nde represent the total number of degrees of freedom of the nodes for the finite element discretization. Also let the set

$$\left\{ \varphi_i, \varphi_i \in \mathcal{X}^h(t) \subset H^1(\Omega_t), \quad i = 1, \dots, nde \right\} \quad (4.23)$$

represent piecewise linear finite element nodal basis functions satisfying

$$\varphi_i(\mathbf{x}_j, t) = \begin{cases} 1 & \text{if } i = j, \\ 0 & \text{if } i \neq j. \end{cases}$$

We seek to find the finite element numerical approximation $a_h(\mathbf{x}, t)$, $u_h(\mathbf{x}, t)$, $v_h(\mathbf{x}, t) \in \mathcal{X}^h(t) \subset \mathcal{X}(\Omega_t)$ expressed as linear combinations of the linear nodal basis functions φ_i of the form

$$\begin{aligned} a_h(\mathbf{x}, t) = \sum_{i=1}^{nde} \mathbf{a}_i(t) \varphi_i(\mathbf{x}, t), \quad u_h(\mathbf{x}, t) = \sum_{i=1}^{nde} \mathbf{U}_i(t) \varphi_i(\mathbf{x}, t), \quad \text{and} \\ v_h(\mathbf{x}, t) = \sum_{i=1}^{nde} \mathbf{V}_i(t) \varphi_i(\mathbf{x}, t). \quad (4.24) \end{aligned}$$

We assume that the number of nde in Ω_t is large enough such that a_h , u_h and v_h is a good approximation of a , u and v respectively.

Linear interpolation on a triangular element

We seek to determine a linear approximation over each element S such that $a_h(x, y, t) = c_1(t) + c_2(t)x(t) + c_3(t)y(t)$. We let c_k ($k = 1, \dots, 3$) and the spatial coordinates to be time dependent because of domain deformation and evolution. At each node of the element (x_k, y_k, t) , ($k = 1, \dots, 3$) we require that $a_h(x_k, y_k, t) = \alpha_i$ and therefore the following holds:

$$\alpha_1(t) = c_1(t) + c_2(t)x_1(t) + c_3(t)y_1(t), \quad (4.25)$$

$$\alpha_2(t) = c_1(t) + c_2(t)x_2(t) + c_3(t)y_2(t), \quad (4.26)$$

$$\alpha_3(t) = c_1(t) + c_2(t)x_3(t) + c_3(t)y_3(t). \quad (4.27)$$

A solution of this system of algebraic equation specifies the values of the time dependent constants c_1, c_2, c_3 as follows:

$$c_1(t) = \frac{1}{2A_{123}(t)} (\alpha_1 \alpha_1(t) + \alpha_2 \alpha_2(t) + \alpha_3 \alpha_3(t)), \quad (4.28)$$

$$c_2(t) = \frac{1}{2A_{123}(t)} (\beta_1 \alpha_1(t) + \beta_2 \alpha_2(t) + \beta_3 \alpha_3(t)), \quad (4.29)$$

$$c_3(t) = \frac{1}{2A_{123}(t)} (\tau_1 \alpha_1(t) + \tau_2 \alpha_2(t) + \tau_3 \alpha_3(t)), \quad (4.30)$$

where $A_{123}(t)$ is the area of the triangle and $\alpha_i = x_j(t)y_k(t) - x_k(t)y_j(t)$, $\beta_i = y_j(t) - y_k(t)$, and $\tau_i = -(x_j(t) - x_k(t))$, with $i \neq j \neq k$ and i, j, k permute in natural order. Substituting (4.28) - (4.30) into $a_h(x, y, t) = c_1(t) + c_2(t)x(t) + c_3(t)y(t)$ results in $a_h(x, y, t) = \sum_{j=1}^3 \alpha_j(t) \varphi_j(x(t), y(t))$ where $\varphi_j(x(t), y(t))$, ($i = 1 \dots 3$) is equal to

$$\varphi_1 = \frac{1}{2A_{123}(t)} (\alpha_1 + \beta_1 x(t) + \tau_1 y(t)), \quad (4.31)$$

$$\varphi_2 = \frac{1}{2A_{123}(t)} (\alpha_2 + \beta_2 x(t) + \tau_2 y(t)), \quad (4.32)$$

$$\varphi_3 = \frac{1}{2A_{123}(t)} (\alpha_3 + \beta_3 x(t) + \tau_3 y(t)). \quad (4.33)$$

These are called linear Lagrange basis functions. We assume that u_h and v_h are represented by the same linear Lagrange basis functions (4.31) - (4.33), hence a conformal finite element method.

Transformation of local basis functions to a reference simplex

We denote the local basis functions on a reference element \bar{S} by $\bar{\varphi}_i$ with $i = 1, 2, 3$. The local basis function φ_i , $i = 1, 2, 3$ on an element $S \in \mathcal{T}_{h,t}$ can be obtained by

$$\varphi_i(\mathbf{x}(t)) = \bar{\varphi}_i(\lambda^S(\mathbf{x}(t))),$$

where λ^S is the barycentric coordinate for a point (x, y, t) in an element S .

Lemma 4.4.1. (Transport property of basis functions (Dziuk and Elliott 2007)) *The finite element space on the discretised domain is a space of continuous piecewise linear functions whose nodal basis functions have the following property;*

$$\left. \frac{D\varphi_i}{Dt} \right|_S = 0. \quad (4.34)$$

Proof. The basis functions $\varphi_i(\mathbf{x}, t)$ $j = 1, 2, 3$ on S satisfies $\varphi_i(\mathbf{x}(t)) = \bar{\varphi}_i(\lambda^S(\mathbf{x}(t)))$, where λ^S is the barycentric coordinates for a point (x, y, t) in S . And the material derivative of $\varphi_i(\mathbf{x}(t))$ on an element S yields

$$\frac{D}{Dt} \varphi_i(\mathbf{x}(t)) = \frac{D}{Dt} \bar{\varphi}_i(\lambda^S(\mathbf{x}(t))) = 0$$

because $\lambda^S = (\lambda_1, \lambda_2, \lambda_3)$ satisfies $0 \leq \lambda_k \leq 1$, $k = 1, 2, 3$ for a point (x, y, t) on S . \square

4.4.1 Semi-discrete model of the force balance equation

In order to write the semi-discrete finite element approximation of the force balance equation in block matrices form, we substitute w_h^1 and w_h^2 by the basis function φ_j , ($j = 1, \dots, nde$), u_h and v_h by their corresponding values as given in (4.24) into (4.22a) and (4.22b), then the resulting semi-discrete system of algebraic equations can be written in compact-matrix-vector form as:

$$\begin{bmatrix} [\mathbf{A}^{11}(t)] & [\mathbf{A}^{12}(t)] \\ [\mathbf{A}^{12}(t)]^T & [\mathbf{A}^{22}(t)] \end{bmatrix} \begin{Bmatrix} \left\{ \frac{d\mathbf{U}}{dt}(t) \right\} \\ \left\{ \frac{d\mathbf{V}}{dt}(t) \right\} \end{Bmatrix} + \begin{bmatrix} [\mathbf{B}^{11}(t)] & [\mathbf{B}^{12}(t)] \\ [\mathbf{B}^{12}(t)]^T & [\mathbf{B}^{22}(t)] \end{bmatrix} \begin{Bmatrix} \{\mathbf{U}(t)\} \\ \{\mathbf{V}(t)\} \end{Bmatrix} = \begin{Bmatrix} \{\mathbf{F}^1(t)\} \\ \{\mathbf{F}^2(t)\} \end{Bmatrix} \quad (4.35)$$

where $\begin{Bmatrix} \{\mathbf{U}(t)\} \\ \{\mathbf{V}(t)\} \end{Bmatrix}$ are solutions of the finite element semi-discrete scheme (4.35). In (4.35) we denote by $\{\mathbf{U}(t)\} = (\mathbf{U}_1(t), \dots, \mathbf{U}_{nde}(t))$, $\{\mathbf{V}(t)\} = (\mathbf{V}_1(t), \dots, \mathbf{V}_{nde}(t))$, $\left\{ \frac{d\mathbf{U}}{dt}(t) \right\} = \left(\frac{d\mathbf{U}_1}{dt}(t), \dots, \frac{d\mathbf{U}_{nde}}{dt}(t) \right)$ and $\left\{ \frac{d\mathbf{V}}{dt}(t) \right\} = \left(\frac{d\mathbf{V}_1}{dt}(t), \dots, \frac{d\mathbf{V}_{nde}}{dt}(t) \right)$ vectors of the solutions and their derivatives. $[\mathbf{A}^{kl}(t)]$, $[\mathbf{B}^{kl}(t)]$, ($k, l = 1, 2$) and $\mathbf{F}(t) := (\{\mathbf{F}^1(t)\}, \{\mathbf{F}^2(t)\})^T$ are the time dependent stiffness matrices and the generalised force vector respectively. The entries of the time dependent stiffness matrices and the generalised force vector for $(i, j$

$= 1, \dots, nde)$ are defined by:

$$\mathbf{A}_{ij}^{11}(t) := \int_{\Omega_{h,t}} \left(\mathbf{D}_{11} \frac{\partial \varphi_i(\mathbf{x}(t))}{\partial x} \frac{\partial \varphi_j(\mathbf{x}(t))}{\partial x} + \mathbf{D}_{33} \frac{\partial \varphi_i(\mathbf{x}(t))}{\partial y} \frac{\partial \varphi_j(\mathbf{x}(t))}{\partial y} \right) d\Omega_{h,t},$$

$$\mathbf{A}_{ij}^{22}(t) := \int_{\Omega_{h,t}} \left(\mathbf{D}_{33} \frac{\partial \varphi_i(\mathbf{x}(t))}{\partial x} \frac{\partial \varphi_j(\mathbf{x}(t))}{\partial x} + \mathbf{D}_{22} \frac{\partial \varphi_i(\mathbf{x}(t))}{\partial y} \frac{\partial \varphi_j(\mathbf{x}(t))}{\partial y} \right) d\Omega_{h,t},$$

$$\mathbf{A}_{ij}^{12}(t) := \mathbf{A}_{ji}^{21}(t) = \int_{\Omega_{h,t}} \left(\mathbf{D}_{12} \frac{\partial \varphi_i(\mathbf{x}(t))}{\partial x} \frac{\partial \varphi_j(\mathbf{x}(t))}{\partial y} + \mathbf{D}_{33} \frac{\partial \varphi_i(\mathbf{x}(t))}{\partial y} \frac{\partial \varphi_j(\mathbf{x}(t))}{\partial x} \right) d\Omega_{h,t},$$

with:

$$\mathbf{B}_{ij}^{11}(t) := \int_{\Omega_{h,t}} \left(\mathbf{C}_{11} \frac{\partial \varphi_i(\mathbf{x}(t))}{\partial x} \frac{\partial \varphi_j(\mathbf{x}(t))}{\partial x} + \mathbf{C}_{66} \frac{\partial \varphi_i(\mathbf{x}(t))}{\partial y} \frac{\partial \varphi_j(\mathbf{x}(t))}{\partial y} \right) d\Omega_{h,t},$$

$$\mathbf{B}_{ij}^{22}(t) := \int_{\Omega_{h,t}} \left(\mathbf{C}_{33} \frac{\partial \varphi_i(\mathbf{x}(t))}{\partial x} \frac{\partial \varphi_j(\mathbf{x}(t))}{\partial x} + \mathbf{C}_{22} \frac{\partial \varphi_i(\mathbf{x}(t))}{\partial y} \frac{\partial \varphi_j(\mathbf{x}(t))}{\partial y} \right) d\Omega_{h,t},$$

$$\mathbf{B}_{ij}^{12}(t) := \mathbf{B}_{ji}^{21}(t) = \int_{\Omega_{h,t}} \left(\mathbf{C}_{12} \frac{\partial \varphi_i(\mathbf{x}(t))}{\partial x} \frac{\partial \varphi_j(\mathbf{x}(t))}{\partial y} + \mathbf{C}_{33} \frac{\partial \varphi_i(\mathbf{x}(t))}{\partial y} \frac{\partial \varphi_j(\mathbf{x}(t))}{\partial x} \right) d\Omega_{h,t},$$

and

$$\begin{aligned} \mathbf{F}_j^1(t) &:= - \int_{\Omega_{h,t}} f_1(\mathbf{x}(t)) \frac{\partial \varphi_j(\mathbf{x}(t))}{\partial x} d\Omega_{h,t} + \int_{\partial\Omega_{h,t}} n_1 f_1(\mathbf{x}(t)) \varphi_j(\mathbf{x}(t)) ds, \\ \mathbf{F}_j^2(t) &= - \int_{\Omega_{h,t}} f_2(\mathbf{x}(t)) \frac{\partial \varphi_j(\mathbf{x}(t))}{\partial y} d\Omega_{h,t} + \int_{\partial\Omega_{h,t}} n_2 f_2(\mathbf{x}(t)) \varphi_j(\mathbf{x}(t)) ds. \end{aligned}$$

For convenience's sake, we denote

$$[\mathbf{A}(t)] := \begin{bmatrix} [\mathbf{A}^{11}(t)] & [\mathbf{A}^{12}(t)] \\ [\mathbf{A}^{12}(t)]^T & [\mathbf{A}^{22}(t)] \end{bmatrix}, \quad [\mathbf{B}(t)] := \begin{bmatrix} [\mathbf{B}^{11}(t)] & [\mathbf{B}^{12}(t)] \\ [\mathbf{B}^{12}(t)]^T & [\mathbf{B}^{22}(t)] \end{bmatrix},$$

$$\{\mathbf{U}(t)\} := \left\{ \begin{matrix} \{\mathbf{U}(t)\} \\ \{\mathbf{V}(t)\} \end{matrix} \right\}, \quad \left\{ \frac{d\mathbf{U}}{dt}(t) \right\} := \left\{ \begin{matrix} \left\{ \frac{d\mathbf{U}}{dt}(t) \right\} \\ \left\{ \frac{d\mathbf{V}}{dt}(t) \right\} \end{matrix} \right\} \quad \text{and} \quad \{\mathbf{F}(t)\} := \left\{ \begin{matrix} \{\mathbf{F}^1(t)\} \\ \{\mathbf{F}^2(t)\} \end{matrix} \right\}.$$

More compactly, we rewrite the semi-discrete finite element model for the force balance equation (4.35) in the form

$$[\mathbf{A}(t)] \left\{ \frac{d\mathbf{U}}{dt}(t) \right\} + [\mathbf{B}(t)] \{\mathbf{U}(t)\} = \mathbf{F}(t). \quad (4.36)$$

Remark 4.4.1. We note that some entries of the block matrices $[\mathbf{A}]$ and $[\mathbf{B}]$ are non-symmetric matrices. These entries are $[\mathbf{A}^{12}]$, $[\mathbf{A}^{12}]^T$, $[\mathbf{B}^{12}]$ and $[\mathbf{B}^{12}]^T$. A square matrix,

say X , is a non-symmetric matrix if the entries x_{ij} of X , are such that

$$x_{ij} \neq x_{ji}.$$

Since some entries of the block matrices $[\mathbf{A}]$ and $[\mathbf{B}]$ are non-symmetric matrices then $[\mathbf{A}]$ and $[\mathbf{B}]$ are non-symmetric block matrices.

4.4.2 Semi-discrete model of the reaction-diffusion equation

In order to write the semi-discrete finite element approximation of the reaction-diffusion equation in matrix-vector form, we substitute w_h by the basis function φ_j , ($j = 1, \dots, nde$) and a_h by its corresponding value as given in (4.24) into (4.22c). Then we apply the transport property of basis functions as given in Lemma 4.4.1 (the transport property states that $D\varphi_j/Dt = 0$). Upon applying the transport property of basis functions we obtain the following semi-discrete system of algebraic equations which we have written in compact-matrix-vector form:

$$\frac{d}{dt} \left(\mathbf{M}(t) \{ \mathbf{a}(t) \} \right) + \left(D_a \mathbf{K}(t) + k_a \mathbf{M}(t) \right) \{ \mathbf{a}(t) \} = k_a a_c \mathbf{H}(t), \quad (4.37)$$

where $\{ \mathbf{a} \} = (\mathbf{a}_1, \dots, \mathbf{a}_{nde})$ are actin concentration solutions of the semi-discrete scheme (4.37). \mathbf{M} , \mathbf{K} , \mathbf{H} are the time dependent mass and stiffness matrices, and force vector respectively. The entries of the time dependent matrices and the force vector are defined respectively as:

$$\begin{aligned} \mathbf{M}_{ij}(t) &:= \int_{\Omega_{h,t}} \varphi_i(\mathbf{x}(t)) \varphi_j(\mathbf{x}(t)) d\Omega_{h,t}, \quad \mathbf{K}_{ij}(t) := \int_{\Omega_{h,t}} \nabla \varphi_i(\mathbf{x}(t)) \cdot \nabla \varphi_j(\mathbf{x}(t)) d\Omega_{h,t}, \\ \text{and} \quad \mathbf{H}_j(t) &:= \int_{\Omega_{h,t}} \varphi_j(\mathbf{x}(t)) d\Omega_{h,t}. \end{aligned}$$

4.4.3 Fully discrete scheme of the coupled problem

We discretise the time interval $(0, T_f]$ into a finite number n of uniform subintervals such that

$$0 = t^0 < t^1 \dots < t^n = T_f.$$

The size of each time interval $\Delta t := t^{n+1} - t^n$.

In order to obtain a fully discrete finite element model of the coupled problem, we consider a modified implicit finite differentiation formula for the time integration of the semi-discrete finite element model of the force balance equation and the reaction-diffusion equation as given in (4.36) and (4.37) respectively. Thus the fully discrete finite element

model of the coupled problem is given by

$$([\mathbf{A}(t^n)] + \Delta t [\mathbf{B}(t^n)]) \{\mathbf{U}\}^{n+1} = [\mathbf{A}(t^n)] \{\mathbf{U}\}^n + \Delta t \mathbf{F}(\mathbf{t}^n), \quad (4.38a)$$

and

$$[(1 + \Delta t k_a) \mathbf{M}(t^{n+1}) + \Delta t (D_a \mathbf{K}(t^{n+1}))] \{\mathbf{a}\}^{n+1} = \mathbf{M}(t^n) \{\mathbf{a}\}^n + \Delta t k_a a_c \mathbf{H}(t^n), \quad (4.38b)$$

where $\{\mathbf{U}\}^n$, $\{\mathbf{U}\}^{n+1}$ are the displacement solutions computed at time t^n and t^{n+1} respectively, and $\{\mathbf{a}\}^n$, $\{\mathbf{a}\}^{n+1}$ are the actin concentrations at time t^n and t^{n+1} respectively. For the numerical implementation, the initial data $\{\mathbf{U}\}^0$ and $\{\mathbf{a}\}^0$ are interpolated on the initial mesh $\Omega_{h,0}$. All integral are evaluated using Gauss numerical quadrature (Reddy 1993). At each time t , $t \in I$, we assemble the finite elements to obtain the system of linear algebraic equations (4.38). This system (4.38a) is solved using a generalised minimal residual method (GMRES) (Sadd and Schultz 1986) while that of (4.38b) is solved using a conjugate gradient method (CG) with diagonal pre-conditioner (Hestenes and Stiefel 1952; Saad 2003).

The implementation of the numerical scheme was carried out by extending the functions in ALBERTA-2.0 ¹. ALBERTA is a flexible and efficient finite element toolbox written in C language. The choice of ALBERTA is due to its advantages over most widely available finite element software as far as the discretised problem (4.38) is concerned. A few advantages are; the availability of data structures for easy and efficient assembly of the discretised problem, the implementation of hierarchical meshes, mesh modification algorithms for global refinement, availability of highly efficient and fast solvers and also the availability of quadrature formulae for numerical integration (Schmidt et al. 2006).

The implementation of the solver GMRES and CG with diagonal pre-conditioner for solving the system of linear algebraic equations (4.38) is available in ALBERTA library.

4.5 Computation of the evolution of the domain

In order to track the evolution of the domain accurately, we specify a Lagrangian kinematic description of the domain. We assume that the displacement of the boundary of the domain occurs only in the direction that is normal to its boundary. The displacement of the domain boundary at any time t corresponds to the solutions of the force balance equation $\mathbf{U}(\mathbf{x}, t)$ at the boundary which in turn are dependent on the local concentration of the actin filament $\mathbf{a}(\mathbf{x}, t)$ at any particular space and time. The displacement of the interior nodes of the mesh is chosen to be equal to the flow velocity $\boldsymbol{\beta}$ (i.e. $\boldsymbol{\beta} = \dot{\mathbf{x}}$). On the boundary we assume that $\boldsymbol{\beta} = \boldsymbol{\omega}_n := \partial \mathbf{U} / \partial t$, where \mathbf{U} is the displacement solution of

¹[http:// www.alberta-fem.de](http://www.alberta-fem.de)

4.6. Numerical implementation of the moving grid finite element method

the force balance equation.

Let Ω_{t^n} and $\Omega_{t^{n+1}}$ be the domain at time t^n and t^{n+1} respectively. If we consider a time interval $[t^n, t^{n+1}]$ and assume that the spatial coordinates of Ω_{t^n} and $\Omega_{t^{n+1}}$ are known. Then we can define a first order linear approximation of the flow velocity as follows:

$$\beta(\mathbf{x}(t^n), t^n) = \frac{\mathbf{x}(t^{n+1}) - \mathbf{x}(t^n)}{\Delta t}, \quad (4.39)$$

where $\Delta t = t^{n+1} - t^n$ defines the time-step. We define a linear approximation of the domain $\Omega_{t^{n+1}}$ such that

$$\mathbf{x}(t^{n+1}) = \mathbf{x}(t^n) + \Delta t \boldsymbol{\omega}_n(\mathbf{x}(t^n), t^n). \quad (4.40)$$

By substituting the above expression for $\beta(\mathbf{x}(t^n), t^n) := \boldsymbol{\omega}_n(\mathbf{x}(t^n), t^n)$ into (4.40) and given \mathbf{U}^{n+1} results in mesh movement. where \mathbf{U}^{n+1} is the displacement solution of the force balance equation at time t^n (and specifies the displacement of the domain at time t^n). A Lagrangian kinematic description of the interior nodes of the mesh is used thus 4.40 equally specifies the position of the interior nodes.

A limitation of the Lagrangian kinematic description is that the minimum angle condition for the mesh elements can be violated for non-constant mesh velocity and large mesh velocity. A remedy is to introduce a monitor function to check the quality of the mesh (say after a couple of mesh movements) and re-mesh when the elements are no longer favourable. Though this was not done here, we note that this aspect is left for a future work.

Here the displacement solutions of the force balance equation are small in value hence mesh velocity is small. For the time interval we considered, no mesh refinement was required.

Remark 4.5.1. *We remark again that the computation of the displacement of the domain (as defined above) is substantially different from that of the [Stéphanou et al. \(2004\)](#) model.*

4.5.1 Numerical computations

The fully discrete coupled problem is solved iteratively. We present in Algorithm 4.5.1 the numerical algorithm for the method.

4.6 Numerical implementation of the moving grid finite element method

We outlined in Section 4.5.1, Algorithm 4.5.1, the steps for the implementation of the moving grid finite method. We present here a detailed description of the method. We begin by describing the technique of generating the finite element mesh and we describe

4.6. Numerical implementation of the moving grid finite element method

Algorithm 1 [Fully discrete scheme]

Initialise \mathbf{U}^0 and \mathbf{a}^0 . Set the time-step size to Δt .

FOR $n = 1, \dots, T_F$ with time-step size Δt **DO**

Assemble $\mathbf{M}(t^n)$, $\mathbf{H}(t^n)$, $[\mathbf{A}(t^n)]$, $[\mathbf{B}(t^n)]$ and $\mathbf{F}(t^n)$.

Solve for $\{\mathbf{U}\}^{n+1}$ in (4.38a).

Compute the new domain from the value of $\{\mathbf{U}\}^{n+1}$

Assemble $\mathbf{M}(t^{n+1})$ and $\mathbf{K}(t^{n+1})$ on the new domain.

Solve for $\{\mathbf{a}\}^{n+1}$ in (4.38b).

END FOR

the technique of computation of the unit normals of the force vector \mathbf{F} in (4.35). Next we show the technique of evaluation of the time dependent matrices $[\mathbf{A}(t)]$, $[\mathbf{B}(t)]$, $\mathbf{M}(t)$, $\mathbf{K}(t)$ and the time dependent force vectors $\mathbf{F}(t)$ and $\mathbf{H}(t)$. First we detail mesh generation.

4.6.1 Mesh generation

The mesh $\Omega_{h,t}$ is a simply connected bounded domain consisting of triangular elements S , which satisfies that $S_i \cap S_j = \emptyset$ if $i \neq j$ and no vertex of any element lies on the interior of another element. Thus

$$\bar{\Omega}_{h,t} = \bigcup_{S(t) \in \mathcal{T}_{h,t}} S(t).$$

At the initial time $t = 0$, the mesh $\Omega_{h,0}$ is a triangulation of a unit disc. $\Omega_{h,0}$ is generated from a global refinement of a macro triangulation with projection of boundary nodes. The incorporation of node projection to the refinement process is necessary to produce a better approximation of the unit disc and is described below. During the mesh refinement ALBERTA creates new nodes at the midpoint of the refinement edges of the elements. We project the new nodes on the boundary of the mesh on the the surface $g(x,y) = x^2 + y^2 - 1 = 0$ (see Figure 4.2). Let us denote by (x_r, y_r) a new node created at a refinement edge located on the boundary of the mesh then its new coordinates after nodal projection will become $(x_r / \sqrt{x_r^2 + y_r^2}, y_r / \sqrt{x_r^2 + y_r^2})$. After a nodal projection, a global refinement is done (see Figure 4.2). We present in Figure 4.3(a) - (c) the mesh after 1, 2, 3 and 4 global refinements respectively. By incorporating the nodal projection to the mesh refinement process we observe that a better approximation of the unit disk is obtained with successive global refinements.

For time $t > 0$ the number of mesh points remains constant and the position of the nodes of the mesh $\Omega_{h,t}$, $t \in I$ are specified by the displacement solution of the force balance equation using (??).

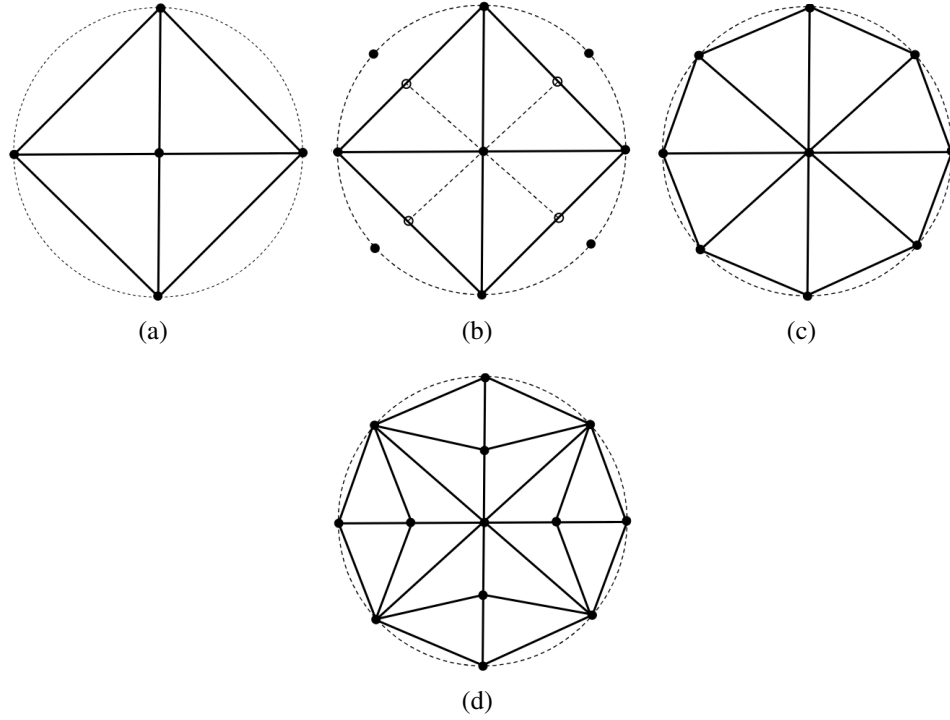


Figure 4.2: An illustration of the technique of global refinement with node projection. Refinement edge midpoints denoted by \circ are projected to the surface $g(x, y) = x^2 + y^2 - 1 = 0$ and are added to the nodes of the mesh denoted by \bullet . (a) shows the macro triangulation and the surface $g(x, y) = 0$ in dash line. (b), (c) and (d) show the refinement edge midpoints \circ , the projection of the refinement edge midpoints to the line $g(x, y) = 0$ and the mesh after one global refinement of the macro triangulation respectively. This technique eventually produces an affine mesh for linear finite element discretisation of Ω_t after a few global refinements.

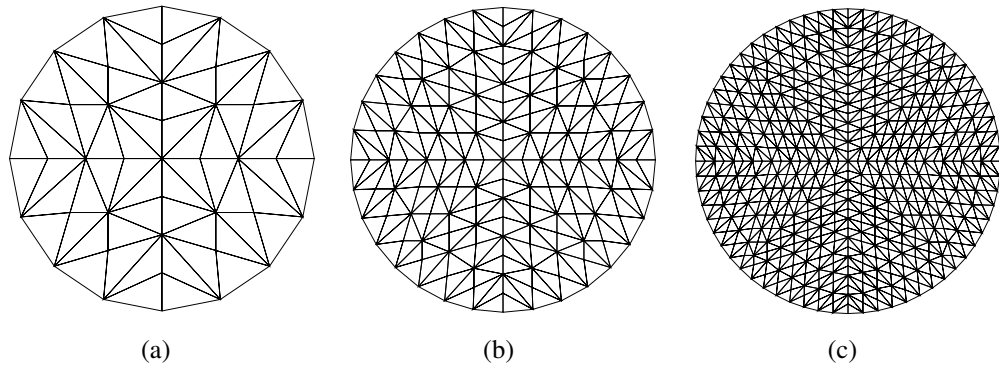


Figure 4.3: Affine mesh for linear finite element discretisation of Ω_0 : (a), (b) and (c) show the grid after two, three and four global refinements of the macro triangulation respectively. Successive refinement with nodal projection produces a better approximation of the boundary $g(x, y) = x^2 + y^2 - 1 = 0$.

4.6.2 Computation of the unit normal

The force vector \mathbf{F} in (4.35) consists of two terms: one with an integration over the domain and another with integration over the boundary. The term requiring an integration

4.6. Numerical implementation of the moving grid finite element method

over the boundary consist of the unit vector $\mathbf{n} = (n_1, n_2)$ normal to the boundary $\partial\Omega$. We discuss below the technique for the computation of \mathbf{n} on the polygonal unit circle corresponding to the boundary of $\Omega_{h,0}$. The exact normals of a unit circle can be calculated analytically and are known (Zill and Cullen 2000). We show that as the number of boundary nodes increases (via global refinement of the mesh) the mesh height h decreases and the numerically computed unit normals converges to the exact normal of a unit circle.

Given a line \mathbf{L} with end points $P_1 = (x_1, y_1)$ and $P_2 = (x_2, y_2)$. Then a vector $\mathbf{N} = (N_1, N_2)$ normal to the line \mathbf{N} is (Burkardt 2009)

$$N_1 = y_1 - y_2$$

$$N_2 = x_2 - x_1.$$

The unit normal vector $\mathbf{n} = (n_1, n_2)$ to \mathbf{L} is then obtained by dividing the normal vector \mathbf{N} by its magnitude such that

$$\begin{aligned} n_1 &= \frac{y_1 - y_2}{\sqrt{(y_1 - y_2)^2 + (x_2 - x_1)^2}} \\ n_2 &= \frac{x_2 - x_1}{\sqrt{(y_1 - y_2)^2 + (x_2 - x_1)^2}}. \end{aligned} \quad (4.41)$$

Given a boundary of a closed surface with nodal points P_i ($i = 1, \dots, nde$) having coordinates (x_i, y_i) , where nde denotes the total number of nodes, then the outward pointing unit vector normal to any line segment $[i, i+1]$ (see for example Figure 4.4(a)) is

$$\begin{aligned} n_1 &= \frac{y_i - y_{i+1}}{\sqrt{(y_i - y_{i+1})^2 + (x_{i+1} - x_i)^2}}, \\ n_2 &= \frac{x_{i+1} - x_i}{\sqrt{(y_i - y_{i+1})^2 + (x_{i+1} - x_i)^2}}. \end{aligned} \quad (4.42)$$

For the sake of simplicity, we describe below the procedure for the computation of the vectors normal to the boundary of the initial mesh $\partial\Omega_{h,0}$ which corresponds to a unit circle. Let us assume that we traverse $\partial\Omega_{h,0}$ in an anticlockwise direction then the direction of the thumb in the right hand thumb rule specifies the outward pointing direction of the unit normal. And the unit vector normal to a line segment is defined by (4.42) (see for example Figure 4.4(a)). We check the accuracy of the computed normals by comparing the computed normal vectors \mathbf{n}_{comp} at nodal positions to the exact value of the normal vectors \mathbf{n}_{exct} to a circle. The exact normal vectors to points (x, y) on a unit circle defined by a function $g(x, y) = x^2 + y^2 - 1 = 0$ is $\mathbf{n}(x, y) = \nabla g(x, y)$ (Zill and Cullen 2000). We note that at the nodal points of $\partial\Omega_{h,0}$, two outward pointing normal vectors occur as a result

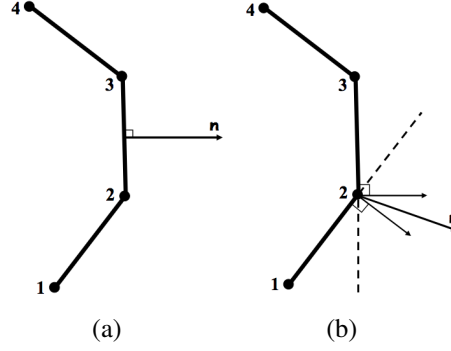


Figure 4.4: (a) is a cross-section of a polygonal circle showing the outward pointing unit vector normal to a line segment. (b) shows the two outward pointing normal vectors that occur as a result of the intersection of two line segments at a nodal position. The resultant normal \mathbf{n} is computed by applying the parallelogram law of forces

Mesh	No. of global refinement	Mesh size	$\ \mathbf{n}_{exct} - \mathbf{n}_{comp}\ _{L^2(\partial\Omega_{h,0})}$
1	0	1.414	0.8284
2	1	0.707	0.3045
3	2	0.353	0.1087
4	3	0.177	0.0385

Table 4.1: L^2 errors of computed normal vectors to a circle.

of the intersection of two line segments at these points (see 4.4(b)). Hence the resultant normal vector \mathbf{n}_{comp} at nodal points is computed by applying the parallelogram law of forces.

In Table 5.2 we show that the computed normals converge to the exact normal in the L^2 norm as the number of mesh points increases. In Table 5.2 the mesh with no global refinement corresponds to a macro triangulation. Now that we have computed the normals, we show in the next section how to assemble/compute global matrices required for the moving grid finite element method.

4.6.3 Evaluation of the global matrices and force vectors

Here we describe the technique of evaluating the global mass matrix $\mathbf{M}(t)$, the global stiffness matrices $\mathbf{K}(t)$, the block matrices $[\mathbf{A}(t)]$ and $[\mathbf{B}(t)]$ and the load vectors $\mathbf{F}(t)$ and $\mathbf{H}(t)$.

Assembly of the global mass and stiffness matrices corresponding to $\mathbf{M}(t)$ and $\mathbf{K}(t)$ respectively

In practice, the entries of these matrices are usually computed by summing the local contributions from the different triangular elements of the mesh. The local basis functions

4.6. Numerical implementation of the moving grid finite element method

on an element S are given implicitly by the basis functions on the reference simplex \bar{S} by the mapping λ^S (as described in Section 4.4). In view of these we write the entries of the global mass matrices $\mathbf{M}_{ij}(t)$ and the global stiffness matrix $\mathbf{K}_{ij}(t)$ as follows. Let $\Xi_{i,j} = \text{supp}(\varphi_i) \cap \text{supp}(\varphi_j)$ then

$$\begin{aligned}\mathbf{M}_{ij}(t) &= \sum_{S \in \mathbf{\Omega}_{h,t}} \int_S \varphi_i(\mathbf{x}(t)) \varphi_j(\mathbf{x}(t)) d\mathbf{\Omega}_{h,t} \\ &= \sum_{\substack{S \in \mathbf{\Omega}_{h,t} \\ S \in \Xi_{i,j}}} \int_S \bar{\varphi}^{i_S}(\lambda(\mathbf{x}(t))) \bar{\varphi}^{j_S}(\lambda(\mathbf{x}(t))) d\mathbf{\Omega}_{h,t},\end{aligned}$$

and

$$\begin{aligned}\mathbf{K}_{ij}(t) &= \sum_{S \in \mathbf{\Omega}_{h,t}} \int_S \nabla \varphi_i(\mathbf{x}(t)) \cdot \nabla \varphi_j(\mathbf{x}(t)) d\mathbf{\Omega}_{h,t} \\ &= \sum_{\substack{S \in \mathbf{\Omega}_{h,t} \\ S \in \Xi_{i,j}}} \int_S \nabla_{\lambda} \bar{\varphi}^{i_S}(\lambda(\mathbf{x}(t))) \cdot \left(\Lambda(t) \Lambda^T(t) \right) \nabla_{\lambda} \bar{\varphi}^{j_S}(\lambda(\mathbf{x}(t))) d\mathbf{\Omega}_{h,t},\end{aligned}$$

for all $t \in I$, where $\text{supp}(\varphi_i)$ denotes the support of the basis function φ_i and i_S and j_S denote the local indices on the element S corresponding to the global indices i and j . Also $\Lambda(\mathbf{x})$:

$$\Lambda = \begin{pmatrix} \frac{\partial \lambda_1}{\partial x} & \frac{\partial \lambda_1}{\partial y} \\ \frac{\partial \lambda_2}{\partial x} & \frac{\partial \lambda_2}{\partial y} \\ \frac{\partial \lambda_3}{\partial x} & \frac{\partial \lambda_3}{\partial y} \end{pmatrix} \in \mathcal{R}^{3 \times 2}$$

is the Jacobian of the barycentric coordinates on S .

Assembly of the block matrices $[\mathbf{A}(t)]$ and $[\mathbf{B}(t)]$

In order to assembly/compute the block matrices $[\mathbf{A}(t)]$ and $[\mathbf{B}(t)]$ occurring in (4.38a) we define

$$\mathbf{D}_{1133} = \begin{pmatrix} \mathbf{D}_{11} & 0 \\ 0 & \mathbf{D}_{33} \end{pmatrix}, \quad \mathbf{D}_{3322} = \begin{pmatrix} \mathbf{D}_{33} & 0 \\ 0 & \mathbf{D}_{22} \end{pmatrix} \quad \text{and} \quad \mathbf{D}_{1233} = \begin{pmatrix} 0 & \mathbf{D}_{12} \\ \mathbf{D}_{33} & 0 \end{pmatrix}.$$

For the block matrix $[\mathbf{A}(t)]$ we define the entries by $\mathbf{A}_{ij}^{11}(t)$, $\mathbf{A}_{ij}^{22}(t)$, $\mathbf{A}_{ij}^{12}(t)$, $\mathbf{A}_{ij}^{21}(t)$ (as in (4.35)). Next we compute the entries of these block matrices by summing the local contributions from the different triangular elements of the mesh and then we let the local basis functions on an element S be given implicitly by the basis functions on the reference

4.6. Numerical implementation of the moving grid finite element method

simplex \bar{S} by the mapping λ^S (as described in Section 4.4) and we obtain the following:

$$\begin{aligned} \mathbf{A}_{ij}^{11}(t) &= \sum_{S \in \mathbf{\Omega}_{h,t}} \int_S \left(\mathbf{D}_{11} \frac{\partial \varphi_i(\mathbf{x}(t))}{\partial x} \frac{\partial \varphi_j(\mathbf{x}(t))}{\partial x} + \mathbf{D}_{33} \frac{\partial \varphi_i(\mathbf{x}(t))}{\partial y} \frac{\partial \varphi_j(\mathbf{x}(t))}{\partial y} \right) d\mathbf{\Omega}_{h,t} \\ &= \sum_{\substack{S \in \mathbf{\Omega}_{h,t} \\ S \in \mathbf{\Xi}_{i,j}}} \int_S \nabla_{\lambda} \bar{\varphi}^{is}(\lambda(\mathbf{x}(t))) \cdot \left(\Lambda(t) \mathbf{D}_{1133} \Lambda(t) \right) \nabla_{\lambda} \bar{\varphi}^{js}(\lambda(\mathbf{x}(t))) d\mathbf{\Omega}_{h,t}, \end{aligned}$$

$$\begin{aligned} \mathbf{A}_{ij}^{22}(t) &= \sum_{S \in \mathbf{\Omega}_{h,t}} \int_S \left(\mathbf{D}_{33} \frac{\partial \varphi_i(\mathbf{x}(t))}{\partial x} \frac{\partial \varphi_j(\mathbf{x}(t))}{\partial x} + \mathbf{D}_{22} \frac{\partial \varphi_i(\mathbf{x}(t))}{\partial y} \frac{\partial \varphi_j(\mathbf{x}(t))}{\partial y} \right) d\mathbf{\Omega}_{h,t} \\ &= \sum_{\substack{S \in \mathbf{\Omega}_{h,t} \\ S \in \mathbf{\Xi}_{i,j}}} \int_S \nabla_{\lambda} \bar{\varphi}^{is}(\lambda(\mathbf{x}(t))) \cdot \left(\Lambda(t) \mathbf{D}_{3322} \Lambda(t) \right) \nabla_{\lambda} \bar{\varphi}^{js}(\lambda(\mathbf{x}(t))) d\mathbf{\Omega}_{h,t}, \end{aligned}$$

and

$$\begin{aligned} \mathbf{A}_{ij}^{12}(t) &= \mathbf{A}_{ij}^{21}(t) \\ &= \sum_{S \in \mathbf{\Omega}_{h,t}} \int_S \left(\mathbf{D}_{12} \frac{\partial \varphi_i(\mathbf{x}(t))}{\partial x} \frac{\partial \varphi_j(\mathbf{x}(t))}{\partial y} + \mathbf{D}_{33} \frac{\partial \varphi_i(\mathbf{x}(t))}{\partial y} \frac{\partial \varphi_j(\mathbf{x}(t))}{\partial x} \right) d\mathbf{\Omega}_{h,t} \\ &= \sum_{\substack{S \in \mathbf{\Omega}_{h,t} \\ S \in \mathbf{\Xi}_{i,j}}} \int_S \nabla_{\lambda} \bar{\varphi}^{is}(\lambda(\mathbf{x}(t))) \cdot \left(\Lambda(t) \mathbf{D}_{1233} \Lambda(t) \right) \nabla_{\lambda} \bar{\varphi}^{js}(\lambda(\mathbf{x}(t))) d\mathbf{\Omega}_{h,t}, \end{aligned}$$

for all $t \in I$. We also define

$$\mathbf{C}_{1133} = \begin{pmatrix} \mathbf{C}_{11} & 0 \\ 0 & \mathbf{C}_{33} \end{pmatrix}, \quad \mathbf{C}_{3322} = \begin{pmatrix} \mathbf{C}_{33} & 0 \\ 0 & \mathbf{C}_{22} \end{pmatrix} \quad \text{and} \quad \mathbf{C}_{1233} = \begin{pmatrix} 0 & \mathbf{C}_{12} \\ \mathbf{C}_{33} & 0 \end{pmatrix}.$$

For the block matrix $[\mathbf{B}(t)]$ we define the entries by $\mathbf{B}_{ij}^{11}(t)$, $\mathbf{B}_{ij}^{22}(t)$, $\mathbf{B}_{ij}^{12}(t)$, $\mathbf{B}_{ij}^{21}(t)$ (as in (4.35)). Next we compute the entries of these block matrices by summing the local contributions from the different triangular elements of the mesh and then we let the local basis functions on an element S be given implicitly by the basis functions on the reference simplex \bar{S} by the mapping λ^S (as described in Section 4.4) and we obtain the following:

$$\begin{aligned} \mathbf{B}_{ij}^{11}(t) &= \sum_{S \in \mathbf{\Omega}_{h,t}} \int_S \left(\mathbf{C}_{11} \frac{\partial \varphi_i(\mathbf{x}(t))}{\partial x} \frac{\partial \varphi_j(\mathbf{x}(t))}{\partial x} + \mathbf{C}_{33} \frac{\partial \varphi_i(\mathbf{x}(t))}{\partial y} \frac{\partial \varphi_j(\mathbf{x}(t))}{\partial y} \right) d\mathbf{\Omega}_{h,t} \\ &= \sum_{\substack{S \in \mathbf{\Omega}_{h,t} \\ S \in \mathbf{\Xi}_{i,j}}} \int_S \nabla_{\lambda} \bar{\varphi}^{is}(\lambda(\mathbf{x}(t))) \cdot \left(\Lambda(t) \mathbf{C}_{1133} \Lambda(t) \right) \nabla_{\lambda} \bar{\varphi}^{js}(\lambda(\mathbf{x}(t))) d\mathbf{\Omega}_{h,t}, \end{aligned}$$

4.6. Numerical implementation of the moving grid finite element method

$$\begin{aligned}
\mathbf{B}_{ij}^{22}(t) &= \sum_{S \in \mathbf{\Omega}_{h,t}} \int_S \left(\mathbf{C}_{33} \frac{\partial \varphi_i(\mathbf{x}(t))}{\partial x} \frac{\partial \varphi_j(\mathbf{x}(t))}{\partial x} + \mathbf{C}_{22} \frac{\partial \varphi_i(\mathbf{x}(t))}{\partial y} \frac{\partial \varphi_j(\mathbf{x}(t))}{\partial y} \right) d\mathbf{\Omega}_{h,t} \\
&= \sum_{\substack{S \in \mathbf{\Omega}_{h,t} \\ S \in \Xi_{i,j}}} \int_S \nabla_\lambda \bar{\varphi}^{is}(\lambda(\mathbf{x}(t))) \cdot \left(\Lambda(t) \mathbf{C}_{3322} \Lambda(t) \right) \nabla_\lambda \bar{\varphi}^{js}(\lambda(\mathbf{x}(t))) d\mathbf{\Omega}_{h,t},
\end{aligned}$$

and

$$\begin{aligned}
\mathbf{B}_{ij}^{12}(t) &= \mathbf{B}_{ij}^{21}(t) \\
&= \sum_{S \in \mathbf{\Omega}_{h,t}} \int_S \left(\mathbf{C}_{12} \frac{\partial \varphi_i(\mathbf{x}(t))}{\partial x} \frac{\partial \varphi_j(\mathbf{x}(t))}{\partial y} + \mathbf{C}_{33} \frac{\partial \varphi_i(\mathbf{x}(t))}{\partial y} \frac{\partial \varphi_j(\mathbf{x}(t))}{\partial x} \right) d\mathbf{\Omega}_{h,t} \\
&= \sum_{\substack{S \in \mathbf{\Omega}_{h,t} \\ S \in \Xi_{i,j}}} \int_S \nabla_\lambda \bar{\varphi}^{is}(\lambda(\mathbf{x}(t))) \cdot \left(\Lambda(t) \mathbf{C}_{1233} \Lambda(t) \right) \nabla_\lambda \bar{\varphi}^{js}(\lambda(\mathbf{x}(t))) d\mathbf{\Omega}_{h,t},
\end{aligned}$$

for all $t \in I$. The integrals in the above mass matrix $\mathbf{M}(t)$, stiffness matrix $\mathbf{K}(t)$ and block matrices $[\mathbf{A}(t)]$ and $[\mathbf{K}(t)]$ are evaluated numerical using the Gauss numerical quadrature. The Gauss numerical quadrature will be described later in this section. We describe below the assembly of the force vectors $\mathbf{F}^1(t)$, $\mathbf{F}^2(t)$ and $\mathbf{H}(t)$.

Assembly of the force vectors $\mathbf{F}^1(t)$, $\mathbf{F}^2(t)$ and $\mathbf{H}(t)$

The entries of the force vectors $\mathbf{F}_j^1(t)$, $\mathbf{F}_j^2(t)$ and $\mathbf{H}_j(t)$ are also computed by summing over the local contributions from the different triangular elements of the mesh. Thus for $\mathbf{F}_j^1(t)$, $\mathbf{F}_j^2(t)$ and $\mathbf{H}_j(t)$ we obtain

$$\begin{aligned}
\mathbf{F}_j^1(t) &= - \sum_{S \in \mathbf{\Omega}_{h,t}} \int_S f_1(\mathbf{x}(t)) \frac{\partial \varphi_j(\mathbf{x}(t))}{\partial x} d\mathbf{\Omega}_{h,t} + \sum_{L=S \cap \partial \mathbf{\Omega}_{h,t}} \int_L n_1 f_1(\mathbf{x}(t)) \varphi_j(\mathbf{x}(t)) ds \\
&= - \sum_{\substack{S \in \mathbf{\Omega}_{h,t} \\ S \subset \text{supp}(\varphi_j)}} \int_S f_1(\mathbf{x}(t)) \left(\sum_{k=1}^3 \frac{\partial \bar{\varphi}^{js}(\lambda(\mathbf{x}(t)))}{\partial \lambda_k} \frac{\partial \lambda_k(\mathbf{x}(t))}{\partial x} \right) d\mathbf{\Omega}_{h,t} \\
&\quad + \sum_{\substack{L=S \cap \partial \mathbf{\Omega}_{h,t} \\ S \subset \text{supp}(\varphi_j)}} \int_L n_1 f_1(\mathbf{x}(t)) \bar{\varphi}^{js}(\lambda(\mathbf{x}(t))) ds,
\end{aligned}$$

4.6. Numerical implementation of the moving grid finite element method

$$\begin{aligned}
\mathbf{F}_j^2(t) &= - \sum_{S \in \mathbf{\Omega}_{h,t}} \int_S f_2(\mathbf{x}(t)) \frac{\partial \varphi_j(\mathbf{x}(t))}{\partial x} d\mathbf{\Omega}_{h,t} + \sum_{L=S \cap \partial \mathbf{\Omega}_{h,t}} \int_L n_2 f_2(\mathbf{x}(t)) \varphi_j(\mathbf{x}(t)) ds \\
&= - \sum_{\substack{S \in \mathbf{\Omega}_{h,t} \\ S \subset \text{supp}(\varphi_j)}} \int_S f_2(\mathbf{x}(t)) \left(\sum_{k=1}^3 \frac{\partial \bar{\varphi}^{js}(\lambda(\mathbf{x}(t)))}{\partial \lambda_k} \frac{\partial \lambda_k(\mathbf{x}(t))}{\partial x} \right) d\mathbf{\Omega}_{h,t} \\
&\quad + \sum_{\substack{L=S \cap \partial \mathbf{\Omega}_{h,t} \\ S \subset \text{supp}(\varphi_j)}} \int_L n_2 f_2(\mathbf{x}(t)) \bar{\varphi}^{js}(\lambda(\mathbf{x}(t))) ds,
\end{aligned}$$

and

$$\mathbf{H}_j(t) = \sum_{S \in \mathbf{\Omega}_{h,t}} \int_S \varphi_j(\mathbf{x}(t)) d\mathbf{\Omega}_{h,t} = \sum_{\substack{S \in \mathbf{\Omega}_{h,t} \\ S \subset \text{supp}(\varphi_j)}} \int_S \bar{\varphi}^{js}(\lambda(\mathbf{x}(t))) d\mathbf{\Omega}_{h,t}$$

for all $t \in I$. The integrals in the force vectors \mathbf{F}^1 , \mathbf{F}^2 and \mathbf{H} are evaluated using Gauss numerical quadrature and requires the use of Gauss quadrature points and weights. The Gauss points and weights are usually defined on a standard element \hat{S} :

$$\hat{S} := \text{conv hull}\{\hat{\mathbf{x}}_1 = \mathbf{0}, \hat{\mathbf{x}}_2 = \mathbf{e}_1, \hat{\mathbf{x}}_3 = \mathbf{e}_2\},$$

where \mathbf{e}_i , ($i = 1, 2, 3$) are the unit vectors in \mathcal{R}^2 and *conv hull* denotes the convex hull. The convex hull of the set $\boldsymbol{\eta} := \{\hat{\mathbf{x}}_1 = \mathbf{0}, \hat{\mathbf{x}}_2 = \mathbf{e}_1, \hat{\mathbf{x}}_3 = \mathbf{e}_2\}$ is the smallest 2D polygon that contains $\boldsymbol{\eta}$. This necessitates that we first transform all integrals to the standard element before the application of the Gauss numerical quadrature.

Transformation of integrals from a typical element S to the standard element \hat{S}

The numerical integration of the matrices and vectors are carried out over the standard element. We transform the integrals to the standard element and afterwards numerical integration is carried out using a quadrature formula.

Given an element with vertex coordinates $\mathbf{x}_1, \mathbf{x}_2, \mathbf{x}_3$, we assume that there exist a mapping $\mathbf{F}_S : \hat{S} \rightarrow S$ which is invertible and differentiable. Then the vertices $\mathbf{x}_1, \mathbf{x}_2$ and \mathbf{x}_3 of the element S are the points $\mathbf{F}_S(\mathbf{x}_1)$, $\mathbf{F}_S(\mathbf{x}_2)$ and $\mathbf{F}_S(\mathbf{x}_3)$ respectively defined by

$$\mathbf{F}_S(\hat{\mathbf{x}}) := \mathbf{Q}_S \hat{\mathbf{x}} + \mathbf{x}_1,$$

with the matrix $\mathbf{Q}_S := [\mathbf{x}_2 - \mathbf{x}_1 \quad \mathbf{x}_3 - \mathbf{x}_1]$. Once the integrals are transformed from a typical element S to the standard element \hat{S} numerical quadrature is applied for numerical integration. For illustrative purpose, we consider a given function $\bar{\varphi}^{js}$, $j_S = 1, 2, 3$. The

integral transformation from S to \hat{S} yields,

$$\begin{aligned} \int_S \bar{\varphi}^{js}(\lambda(\mathbf{x}(t))) d\Omega_{h,t} &= \int_{\hat{S}} \bar{\varphi}^{js}(\lambda(\hat{\mathbf{x}}(t))) |DF_S(\hat{\mathbf{x}})| d\hat{\mathbf{x}} \\ &= 2|S| \int_{\hat{S}} \bar{\varphi}^{js}(\lambda(\hat{\mathbf{x}}(t))) d\hat{\mathbf{x}}, \end{aligned} \quad (4.43)$$

where DF_S is the Jacobian of \mathbf{F}_S . After the integral have been transformed from a typical element S to the standard element \hat{S} we implement the Gauss numerical quadrature for the numerical integration.

Gauss numerical quadrature

A Gauss numerical quadrature on \hat{S} is a set $\{(w_k, \lambda_k) \in \mathcal{R} \times \mathcal{R}^3; k = 1, \dots, nq\}$, where w_k are the Gaussian weights and λ_k are the Gauss quadrature points. Each λ_k is given in barycentric coordinates such that

$$\int_{\hat{S}} g(\hat{\mathbf{x}}) d\hat{\mathbf{x}} = \sum_{k=1}^{nq} w_k g(\hat{\mathbf{x}}(\lambda_k)).$$

In the implementation, we take $nq = 6$ on a triangular element and $nq = 3$ on a line element. The number of Gauss points nq required to integrate a polynomial of degree d_{eg} (exactly) over a line L is (Reddy 1993):

$$nq = \begin{cases} \frac{1}{2} [(d_{eg} + 1)], & \text{if } (d_{eg} + 1) \text{ is even,} \\ \frac{1}{2} [(d_{eg} + 2)], & \text{if } (d_{eg} + 1) \text{ is odd.} \end{cases}$$

4.7 Summary

In this Chapter, we developed a moving grid finite element method of the cytomechanical model. In Section 4.3.1 and Section 4.3.2 we derived the weak formulation of the force balance equation and the weak formulation of the reaction-diffusion equation respectively. Finite element discretization of the model was carried out in Section 4.4 using the classical Galerkin method. The resulting semi-discrete finite element model of the force balance equation and the reaction-diffusion equation was then discretised in time to obtain a fully discrete scheme. The time discretisation of the semi-discrete finite element model of the force balance equation and the reaction-diffusion equation was carried out by using a modified implicit finite differentiation formula. The moving grid finite element method requires a specification of the grid movement. Thus in Section 4.5 we described the method for the computation of the grid movement. Numerical implementation of the

moving grid finite element method was given in Section 4.6.

In the next chapter we will present numerical results obtained from the moving grid finite element model. We will begin by validating the moving grid finite element numerical scheme using predicted solutions from linear stability theory. We will also study the dynamics of actin and its effect on cell deformation.

Chapter 5

Numerical simulation of cell movement

5.1 Introduction

The first aim of this chapter is to verify the moving grid finite element numerical scheme described in Chapter 4 for consistency with predictions from linear theory close to bifurcation points. The second is to use the scheme to investigate actin dynamics, cell deformations and movements.

The initial domain we consider is a unit disk Ω_0 . We assume that at time t_s $0 < t_s \ll 1$ the domain evolution is negligible and based on this assumption we are able to compare the finite element solutions to predictions from linear stability theory. Thus by assuming slow domain evolution, we validate the numerical results by comparing the moving grid finite element solutions to those predicted by linear stability theory. We show in Section 5.2 that the numerical scheme computes spatially inhomogeneous steady state solutions which are consistent with those predicted by linear stability theory close to bifurcation points.

We show in Section 5.3 that far from bifurcation points the numerical scheme is also able to replicate predicted results from linear theory and depends on the perturbation used in the initial conditions.

Also far away from instability, we show that this model is able to describe the intracellular actin dynamics and the resulting shapes and movements of the membrane. In particular, by varying the pressure coefficient and the measure of the contractile tonicity parameter, the model behaviour gives uniform expansions, contractions and irregular deformations of the cell membrane with the cell centre staying mostly unchanged in the majority of the cases considered. The model also allow us to compare the actin distribution at the vicinity where large deformations occur and the results we obtain are found to be consistent with those observed experimentally. The perturbations used in the initial conditions determines the dynamics of actin and cell shape. The simulation results for cell deformation and movement are given in Section 5.4.

Throughout this chapter we let $t = n\Delta t$, where Δt and n denote the time-step size and number of time-steps respectively. In all our simulations rnd denotes a randomly generated number between 10^{-3} and 10^{-5} selected from a uniform distribution.

5.2 Validating numerical results close to bifurcation points

In this section we validate the numerical results by comparing the numerical results to those obtained by using linear stability theory close to bifurcation points.

5.2.1 Excitation of the eigenmode $w_{1,1}$

We present the numerical results for actin concentration a_h and the displacement solutions \mathbf{u}_h in Figure 5.1(b) and 5.1(c) respectively. These results are consistent with those predicted by linear stability theory as given in Figure 3.5. The initial conditions used were $1.0009 + rnd * \sin(x)$, a finite element mesh with 2113 nodes was used and $\Delta t = 1.0228 \times 10^{-2}$. Numerical results in Figure 5.1(b) and 5.1(c) were obtained after 2 and 4 time-steps respectively.

Unlike the analytical solution given in Figure 5.1 which was plotted using Matlab the numerical simulation results are visualized and plotted in Paraview. An attempt at inserting an axes for the coordinates in Paraview was made but the coordinates of the resulting axes was not legible. Hence the axes were omitted. This is a limitation of Paraview. I would like to note that during the validation of a numerical scheme using predictions from linear stability theory, the replication of the predicted pattern as show in Figure 5.1 is usually required. Also the amplitude of the predicted pattern is often different from those obtained from numerical simulation (Madzvamuse 2000). Thus no comparison of the coordinates of the predicted pattern with the numerical result is required.

We note that if the initial conditions are choosed to be equal to $1.0 + rnd$, with all parameters unchanged then the mode $-w_{0,2}$ is excited.

5.2.2 Excitation of the eigenmode: $-w_{0,2}$

Let us fix $\tilde{p} = 1.646$ and $\tilde{\psi} = 38.24$ respectively. For these parameter choices, the dispersion relation again isolates the lowest non-zero wavenumber $k_{1,1}^2$. The initial conditions of the actin concentration are chosen to be equal to $a_c + rnd * \cos(x)$. We found that by choosing the perturbations in the initial conditions to be $rnd * \cos(x)$, we encouraged the excitation of the eigenmode $-w_{0,2}$, where $w_{0,2}$ is the lowest eigenmode. The numerical simulation results are shown in Figure 5.2 for the actin concentrations a_h and the displacement solutions \mathbf{u}_h . For the sake of the comparison of the eigenmode $w_{0,2}$ to the numerical solutions we present in Figure 5.2(a) a plot of the eigenmode $w_{0,2}$.

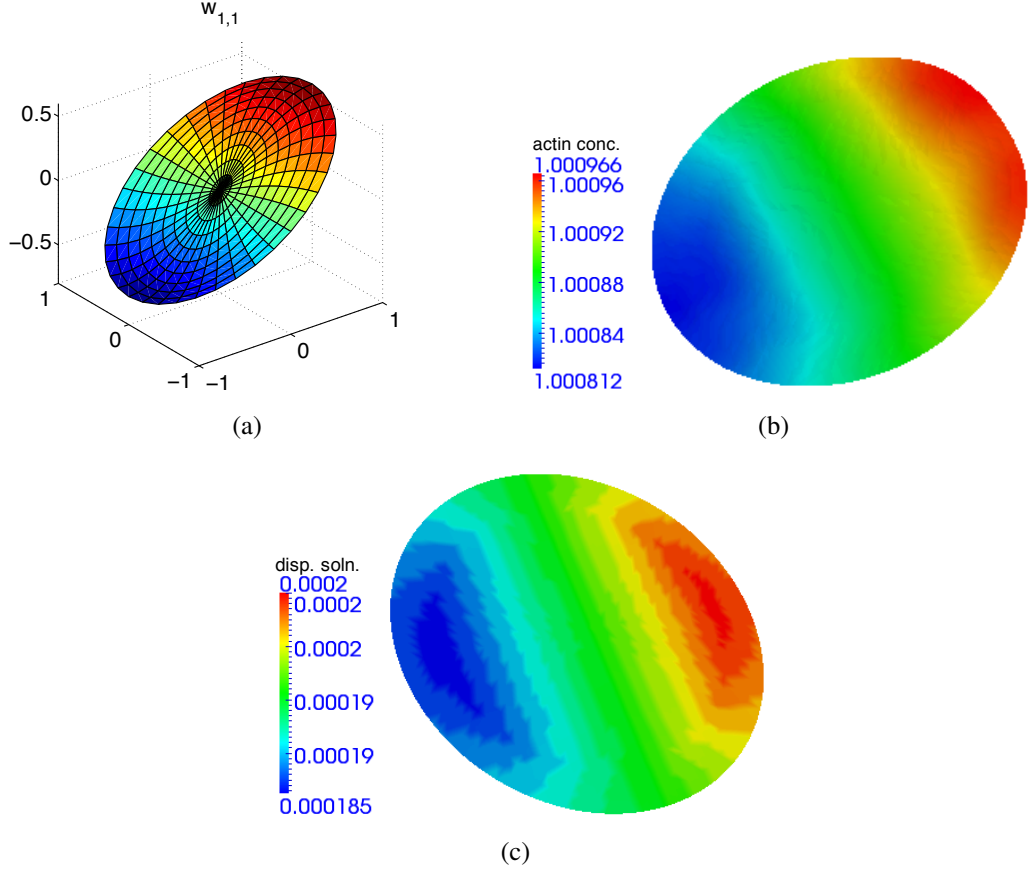


Figure 5.1: Surface plots of the numerical results for actin concentration a_h and displacement solution \mathbf{u}_h . Parameter values used in the numerical simulations are selected such that the lowest non-zero wavenumber $k_{1,1}^2$ is excited. (a) is the predicted solution for $w_{1,1}$ from linear theory. (b) is the numerical result for actin concentration a_h while (c) is the numerical result for displacement solution \mathbf{u}_h . (a), (b) and (c) are all surface plots. In (b) and (c) a bar is used to specify the variation along the z-plane such that red signifies high values and blue signifies low values.

In Figure 5.2(c), we observe that the displacement solutions \mathbf{u}_h has its highest value around the points where $x^2 + y^2 = 0.8$. These points correspond to the points where $\delta(l)$ is discontinuous. From the linear analysis in Section 3.7.1, we know that the dispersion relation is discontinuous at the points where $\delta(l)$ is discontinuous. To further illustrate the effect of the discontinuity of $\delta(l)$ on the numerical results, we redefine $\delta(l)$ such that $\delta(l) = 1$ on the boundary of the domain and zero elsewhere, i.e.

$$\delta(l) = \begin{cases} 1 & \text{on the cell membrane (i.e the domain boundary),} \\ 0 & \text{elsewhere.} \end{cases} \quad (5.1)$$

The numerical simulation with $\delta(l)$ defined as in (5.1) gives numerical results where the displacement solution \mathbf{u}_h has its highest value around the boundary (see Figure 5.3 for a surface plot of the displacement solutions).

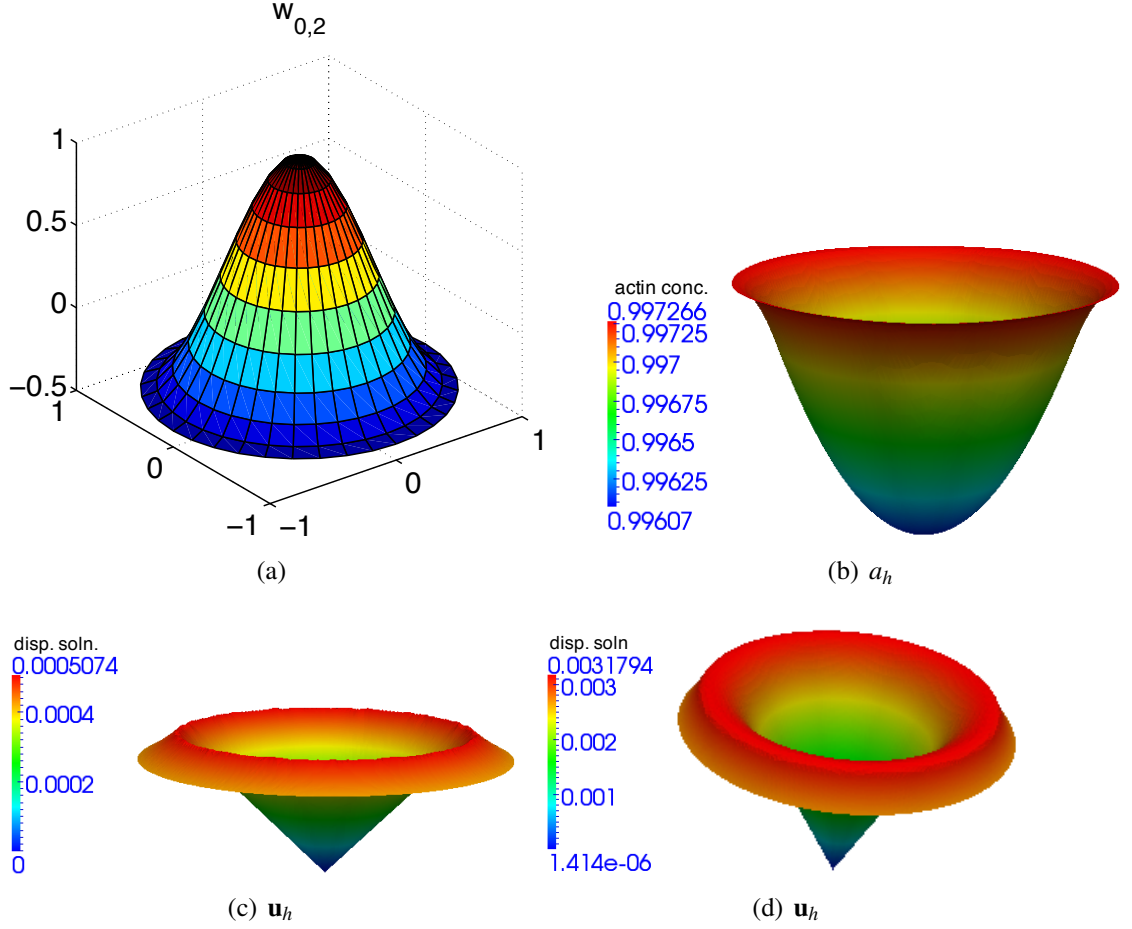


Figure 5.2: Surface plots of the numerical results for the actin concentration a_h and the displacement solution \mathbf{u}_h showing the replication of the eigenmode $-w_{0,2}$. (a) is a surface plot of the eigenmode $w_{0,2}$. (b) and (c) display the simulation results of actin concentration a_h and displacement solutions \mathbf{u}_h respectively at time $t = 3.61 \times 10^{-3}$. (d) displays the displacement solutions \mathbf{u}_h at time $t = 0.024$ having no oscillations at the points of discontinuity. The initial conditions used for actin concentrations are $a_c + \text{rnd} * \cos(x)$.

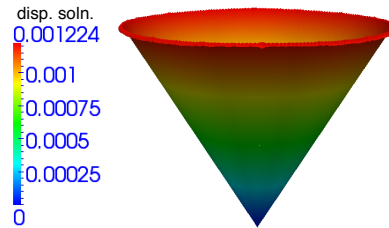


Figure 5.3: A surface plot of the numerical result for the displacement solution \mathbf{u}_h . Parameter values used in the numerical simulation are consistent with those displayed in Table 3.1 except that $\delta(l)$ is as defined in (5.1). Initial conditions as in Figure 5.2.

5.3 Validating numerical results far from bifurcation points

Far from the bifurcation points of $k_{1,1}^2$, we have the possibility of exciting mixed or higher modes. Below we present the numerical results for actin concentration a_h and displacement solutions \mathbf{u}_h showing the excitation of mixed and higher modes.

5.3. Validating numerical results far from bifurcation points

Table 5.1: Values of ψ and the initial conditions used for the excitation of mixed and higher modes presented in Figure 5.4.

Figure	Value of ψ (dyn/cm ²)	Initial conditions for the actin concentration	No. of nodes	Time-step size Δt
Figure 5.4(b) and 5.4(c)	3.1×10^2	$1.0 + 0.1 \cos x $	8321	1.0228×10^{-3}
Figure 5.4(e) and 5.4(f)	2.0×10^2	$1.0 + 0.1 \sin^2 y $	8321	1.0228×10^{-3}
Figure 5.5(b) and 5.5(c)	3.67×10^2	$1.0 + 0.1 \sin x \sin y $	8321	1.0228×10^{-3}
Figure 5.5(e) and 5.5(f)	1.1×10^2	$1.0 + \left \sum_{i=1}^{20} 0.1 \sin x \sin y \right $	2113	1.0228×10^{-2}

5.3.1 Excitation of mixed modes

The excitation of mixed modes is possible if the value of $\tilde{\psi}$ is allowed to vary while all other parameters value are fixed (see Table 3.5 for possible values of $\tilde{\psi}$ and the corresponding number of modes the dispersion relation isolates). We present in Figure 5.4 the simulation results for actin concentration a_h and the displacement solutions showing the excitation of mixed modes. All graphics were saved after no more than 15 time-steps. We present in Table 5.1 the value of ψ used in the numerical simulations. A comparison of the predicted solutions from linear theory (Figure 5.4(a) and (d)) with the numerical results (Figure 5.4(b)-(c) and Figure 5.4(e)-(f)) show that the numerical scheme reproduces results in close agreement to those predicted by linear stability theory for the mixed modes for the actin concentration. The displacement solutions are naturally small with small amplitudes since they generate the velocity for the domain deformation. Hence we do not expect solution profiles corresponding to the displacement to have high amplitudes compared the actin concentration profiles.

5.3.2 Excitation of higher modes

The excitation of higher modes is also possible if the value of $\tilde{\psi}$ is allowed to vary while all other parameters value are fixed (see Table 3.5 for possible values of $\tilde{\psi}$ and the corresponding number of modes the dispersion relation isolates). We present in Figure 5.5 the simulation results for actin concentration a_h and the displacement solutions showing the excitation of higher modes. All graphics were saved after no more than 15 time-steps. We present in Table 5.1 the value of ψ used in the numerical simulations. A comparison of the predicted solutions from linear theory (Figure 5.5(a) and (d)) with the numerical results (Figure 5.5(b)-(c) and Figure 5.5(e)-(f)) show that the numerical scheme reproduces results in close agreement to those predicted by linear stability theory for the mixed and higher modes for the actin concentration. The displacement solutions are naturally small with small amplitudes since they generate the velocity for the domain deformation. Hence we do not expect solution profiles corresponding to the displacement to have high

5.4. Numerical simulations of cell dynamics far away from bifurcation points

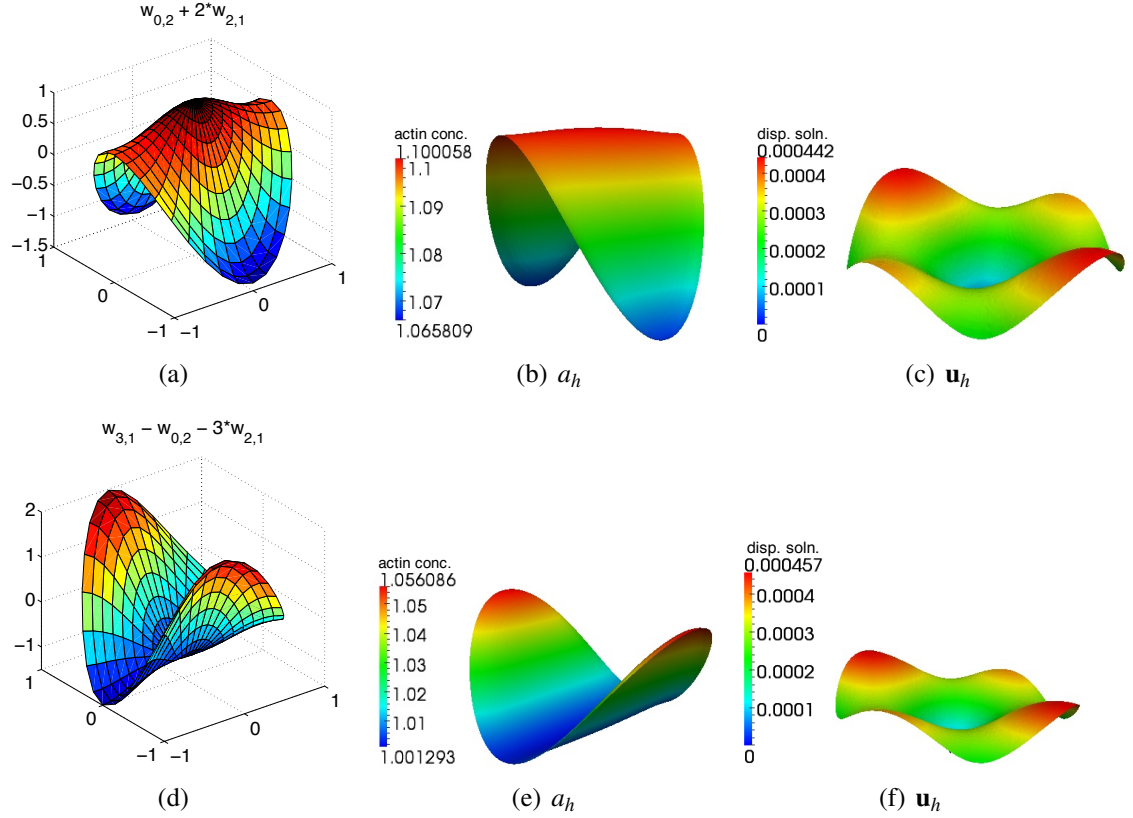


Figure 5.4: Surface plots of the numerical results of the actin concentration a_h and displacement solutions \mathbf{u}_h having mixed modes excited together with the reproduced solutions predicted from linear theory. (a) and (d) are the predicted solutions from linear theory for $w_{0,2} + 2w_{2,1}$ and $w_{3,1} - w_{0,2} - 3w_{2,1}$ respectively. The numerical results reproduce the following modes: (b)-(c) $w_{0,2} + 2w_{2,1}$, (e)-(f) $w_{3,1} - w_{0,2} - 3w_{2,1}$. ψ is chosen as given in Table 5.1 such that mixed modes are excited (refer to the list given in Table 3.5 for more detail on the eigenmodes isolated by a dispersion relation depending on the value of $\tilde{\psi}$ and ψ).

amplitudes compared with the actin concentration profiles.

5.4 Numerical simulations of cell dynamics far away from bifurcation points

From now onwards, we will present the numerical experiments carried out in Section 5.2 by considering the long time behaviour far away from the unit disk where linear stability theory no longer holds.

The numerical results show that regions where there is a high actin concentration result in large cell deformations and movement. If the actin concentration is uniformly distributed, then cell deformation and movement is also uniform and isotropic. In all our results, from now onwards, we only present 2D plots corresponding to the actin concentration. The 2D plots corresponding to the displacement are either in (or out of) phase

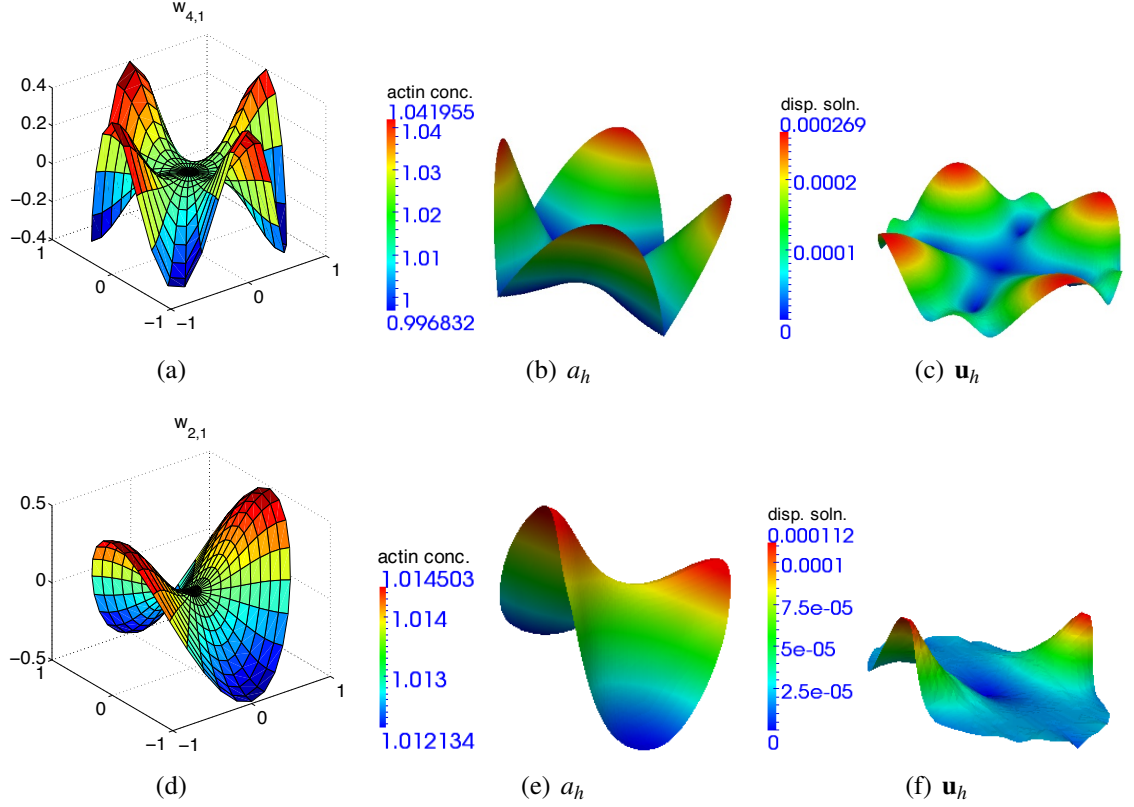


Figure 5.5: Surface plots of the numerical results of the actin concentration a_h and displacement solutions \mathbf{u}_h having higher modes excited together with the reproduced solutions predicted from linear theory. (a) and (d) are the predicted solutions from linear theory for $w_{4,1}$ and $w_{2,1}$ respectively. The numerical results reproduce the following modes: (b) - (c) $w_{4,1}$, and (e) - (f) $w_{2,1}$. ψ is chosen as given in Table 5.1 such that higher modes are excited (refer to the list given in Table 3.5 for more detail on the eigenmodes isolated by a dispersion relation depending on the value of $\tilde{\psi}$ and ψ).

with those of the actin concentration.

5.4.1 Cell deformation for the case where the eigenmode $w_{1,1}$ is excited

In Figure 5.6 we present numerical results computed with parameter values selected such that $w_{1,1}$ is excited initially (see Figure 5.1). It can be observed that at the early stages ($t = 0.5114$), Figure 5.6(a) the cell expands uniformly, with actin uniformly distributed around the periphery (boundary) of the cell. Further growth ($t = 1.7183$, Figure 5.6(b)), the cell moves in the positive x - direction and continues to expand. It is clear that where there is a high actin concentration, the cell moves preferentially in that direction. At time ($t = 3.365$, Figure 5.6(c)), the cell has translated and expanded significantly and continues to do so. We present in 5.6(d) a plot of the area of the cell against the number of time-steps demonstrating clearly cell expansion during translation and in 5.6(e) we plot the index of polarity against the number of time steps. The index of polarity is the ratio between the

5.4. Numerical simulations of cell dynamics far away from bifurcation points

short axis and long axis of the smallest ellipse in which the simulated cell is defined.

5.4.2 Cell deformation for higher and mixed modes

Here we consider the cell deformation and cell movement for the cases when mixed or higher modes are excited initially.

Cell deformation for the case when the mixed mode $w_{2,1}$ is excited initially

In Figure 5.7 we present numerical results with parameter values selected such that $w_{2,1}$ is excited initially. In this plot we observe that as time increases the domain size is increasing and protruding in 2 fronts but not translating. Actin density is highest at the periphery where protrusion occurs. We present in Figure 5.7(d) a plot of the area of the cell against the number of time-steps. It is clear that the cell is expanding but its centre of origin remains fixed. A plot of the index of polarity against the number of time-steps taken is given in Figure 5.7(e).

Cell deformation for the case when $w_{3,1} - w_{0,2} - 3 * w_{2,1}$ is excited initially

The cell deformation for the case when the mixed mode $w_{3,1} - w_{0,2} - 3 * w_{2,1}$ is excited initially is shown in Figure 5.8. We observe in this plot that the cell size is increasing along the y-axis and protruding on two fronts. It is not translating and the x-range is decreasing (i.e. in some parts of the domain the cell is contracting inwards). After $n = 130$ time-steps ($t = 0.1329$) actin concentration is still high at the regions where protrusion occurs. In general the area of the cell is decreasing. A plot of the index of polarity against the number of time-steps taken is shown in Figure 5.8(d).

Cell deformation for the case when the mixed mode $w_{0,2} - 2 * w_{2,1}$ is excited

The cell deformation for the case when the mixed mode $w_{0,2} - 2 * w_{2,1}$ is excited is presented in Figure 5.9. In this figure, we observe that the size of the cell is increasing along the y-axis and protruding on two fronts. It is not translating and the x-range is decreasing (i.e. some parts of the cell domain are contracting). Initially actin is high in the middle region of the cell domain. After $n = 50$ time-steps ($t = 0.0511$) actin concentration is high around the centroid and this is also observed to be the case after $n = 146$ ($t = 1.493$) though the region of highest actin concentration decreases. A plot of the index of polarity against the number of time-steps taken is shown in Figure 5.9(d).

Cell deformation for the case when the mode $w_{4,1}$ is excited

The cell deformation for the case when the mixed mode $w_{4,1}$ is excited is presented in Figure 5.10. From Figure 5.10 we observe that the cell is increasing in size and actin con-

centration is highest at regions where protrusion is highest. We present in Figure 5.10(d) a plot of the area of the cell against the number of time-steps illustrating the increase in cell area.

5.5 Numerical investigation of the dynamics of parameter space $(\tilde{\psi}, \tilde{p})$

On carrying out numerical simulations with parameter values selected from the parameter space $(\tilde{\psi}, \tilde{p})$ close to bifurcation points (see Figure 3.9(a)), we observed that for some choices of $(\tilde{\psi}, \tilde{p})$ in the Hopf region close to the oscillatory region the simulation result gives stationary solutions for actin chemical concentrations that are consistent with those predicted for the eigenmode $c_1 w_{0,1}$ when the initial conditions used for actin concentrations are $a_c + \text{rnd} * \cos(x)$. Fixing $\tilde{\psi} = 38.24$ and decreasing \tilde{p} vertically from 1.75 to 0 we observe that the solutions of the actin concentration reproduce the stationary solutions that are predicted for the eigenmode $c_1 w_{0,1}$ for all values of \tilde{p} considered.

We note that the parameter \tilde{p} can be chosen such that at regions close to the boundary of the domain an oscillatory instability exists and further away from the boundary a Hopf instability occurs. This is possible because of $\delta(l)$ in $b(k^2)$. In such a case where an oscillatory instability exists close to the boundary and further away from the boundary a Hopf instability occurs, numerical simulations give results that are consistent with those predicted for the Turing space from linear theory for the eigenmode $c_1 w_{0,1}$ (results not shown).

We present below the simulation results of parameter spaces with initial conditions for the actin concentrations equal to $a_c + \text{rnd} * \cos(x)$ fixed. The observed dynamics of the cell where uniform expansion, uniform contraction and non-uniform deformations of the cell. A finite element mesh with 8321 nodes was used with $\Delta t = 6.0228 \times 10^{-4}$.

Uniform cell expansion

If we choose the value of the pressure coefficient \tilde{p} to be equal to 3.0 (with all other parameter values staying unchanged as given in Table 3.2), we observe that the cell deformations correspond to those obtained when $c_1 w_{0,1}$ is excited.

From numerical simulations, we observed that the deformation of the cell is consistent with those obtained when $c_1 w_{0,1}$ is excited, provided $b(k^2)$ isolates only the first non-zero unstable mode $k_{1,1}^2$ and the initial conditions are chosen to be equal to $a_c + \text{rnd} * \cos(x)$.

We also observe that for fixed values of \tilde{p} such that $0 < \tilde{p} < 1.75$ the dynamics of the cell (corresponding to uniform expansions of the cell) is dependent on the value of the contractile tonicity $\tilde{\psi}$ (refer to Figure 3.9(a) for a parameter space plot $(\tilde{\psi}, \tilde{p})$). An example is the following: Taking $(\tilde{\psi}, \tilde{p}) = (70.366, 0.026)$ or $(\tilde{\psi}, \tilde{p}) = (70.366, 0.433)$

gives uniform cell expansions while $(\tilde{\psi}, \tilde{p}) = (3.033 \times 10^4, 0.026)$, gives non-uniform cell deformations (results not shown). The simulation results showing the actin concentration solutions with uniform expansions are shown in Figure 5.12 for $(\tilde{\psi}, \tilde{p}) = (70.366, 0.433)$. In Figure 5.12(e) we present a plot of the area of the cell against the number of time-steps taken to show the rate at which the area is increasing. $(\tilde{\psi}, \tilde{p}) = (70.366, 0.433)$

Uniform cell contraction

For the sake of numerical experiment, we allow p to take a negative value. By choosing $\tilde{p} = -0.433$ and $\tilde{\psi} = 70.366$ we observe the cell contracting uniformly at positions that are equidistant from the centroid of the cell domain. And the concentration of actin increases from the boundary to the centroid. We show in Figure 5.13 the actin concentration solutions at a time (a) $t = 1.2046 \times 10^{-3}$, (b) $t = 3.6137 \times 10^{-3}$, (c) $t = 0.0361$ and (d) $t = 0.5180$. The initial conditions of actin concentration are still equal to $a_c + \text{rnd} * \cos(x)$.

Non-uniform cell deformation

Non-uniform cell deformations occur if all parameter values in Table 3.2 stay unchanged but $\tilde{\psi}$ is increased or by choosing parameter values $\tilde{\psi}$ and \tilde{p} far away from bifurcation points (refer to Figure 3.9(a) for a parameter space plot of $(\tilde{\psi}, \tilde{p})$). Below we give the parameter values and the simulation results for both cases where non-uniform cell deformations occur. Here the initial conditions of actin concentration are given by $a_c + \text{rnd} * \cos(x)$.

- If all model parameter values are kept fixed as given in Table 3.2, taking increasing values of $\tilde{\psi}$ results in non-uniform cell deformations. For example taking $\tilde{\psi} = 1.04 \times 10^5$, we observed from the numerical results that the cell deforms non-uniformly and rapidly making it impossible to capture the solutions and the numerical algorithm fails.
- If we choose $\tilde{\psi}$ and \tilde{p} arbitrarily such that the parameter space $(\tilde{\psi}, \tilde{p})$ is very far from bifurcation points (for example, $\tilde{\psi} = 7.8 \times 10^3$ and $\tilde{p} = 0.026$), we observe non-uniform cell contraction with actin localised around the centroid of the cell (see Figure 5.14). In Figure 5.14(d) we present a plot of the cell area. A plot of the index of polarity against the number of time-steps taken is given in Figure 5.15.
- We recall that the simulation results presented in Figure 5.15 was obtained for $\tilde{p} = 0.026$ and $\tilde{\psi} = 7.8 \times 10^3$. Now if we decrease only $\tilde{\psi}$ such that $\tilde{\psi} = 1.3 \times 10^3$, we observe cell deformations which agree qualitatively to those observed experimentally (Senju and Miyata 2009). It can be observed that actin concentration is

high at the periphery of the cell boundary and is highest at regions where protrusions occur. In Figure 5.16, we present the graphical display of the simulation results of the actin concentration. A plot of the index of polarity against the number of time-steps taken is given in Figure 5.17. We can infer from these results that the dynamics of the cell domain, the distribution of actin filaments are related to the pressure coefficient p and the contractile tonicity ψ .

5.6 Numerical simulation on a realistic cell

Here we choose parameters such that they are consistent with those available in the literature such that Young's modulus E of the actin filament is 4000 dyn/cm^2 (Dayel et al. 2009), diffusion coefficient D_a of the actin filament is $1.6 \times 10^{-10} \text{ cm}^2/\text{s}$ (Lanni and Ware 1984); (Simon et al. 1988), the polymerization rate k_a is $66/\text{s}$ (Watanabe 2010), the values of the poisson ratio ν , shear and bulk viscosities μ_1 and μ_2 respectively are as given in Table 3.1. A cell of radius $10 \text{ }\mu\text{m}$ (0.001 cm) is assumed. We also assume that the pressure coefficient is 800 dyn/cm^2 and the contractile tonicity is $6.9 \times 10^4 \text{ dyn/cm}^2$. We note that for these choice of dimensional parameter values the equivalent non-dimensional parameter values would have a dispersion relation that isolates more than 7 wavenumbers inclusive of $k_{4,1}^2$. We used an initial perturbation for actin equal to $|r \sin x \sin y|$ in order to bias the excitation of the mode $w_{4,1}$. The numerical simulation result gives protrusion on four fronts and is similar to the result given in Fig. 5.10.

5.7 Qualitative comparison with experimental observations I

Here we compare Figure 5.16(f) with experimental observations. The distribution of F-actin in cells has been well studied and epifluorescence images are available in the literature. Figure 5.18(a) shows an epifluorescence image of a Swiss 3T3 fibroblast cell obtained from (Senju and Miyata 2009). The fibroblast was stained by the authors for F-actin after being allowed to spread for 1 hour. The epifluorescence image shows that F-actin is predominant at the cell periphery and is highest at the regions where protrusions occur. The simulation results presented in Figure 5.18(b) are thus consistent with the experimental observations.

5.8 Qualitative comparison with experimental observations II

Here we compare Figure 5.8 showing the deformation of a cell with experimental observations of isolated fibroblast spreading *in vitro* on a substrate as given in Stéphanou et al. (2008). We present this in Figure 5.19. In this figure, we observe that the simulated fibroblast cell deforms similar to that observed experimentally. The rates of deformations are different in both cases. We note that though some experimentally measured parameter values were used in the numerical experiments some model parameter values were estimated or normalized hence we do not expect the simulated cell to have the same rate of deformation with the experimentally observed cell. Thus we neglect the time scale of deformation and make a qualitative comparison of the cell shape as it changes from being roughly circular to being elongated as it spreads out (refer to Figure 5.19).

Remark 5.8.1 (Key model parameters). *Based on the linear stability analysis and the numerical simulation results we are able to identify key parameters that control cell deformations with respect to the model problem. The contractile tonicity ψ is the bifurcation parameter and determines the transition from stable to unstable state. The actin saturation concentration a_{sat} and the pressure coefficient were also found to play a key role in cell deformations.*

5.9 Limitation of the model

Through our the numerical simulations, we observe that the volume of the cell changes continuously with time. This means that the cell will either expands to infinity or collapses to zero. Clearly the model lacks volume conservation. A remedy would be to introduce a mechanism for volume conservation of the cell and stop the infinite expansions and contractions of the cell.

Our model succeeds in presenting a general methodology that describes the hypothesis of the existence of a pressure-driven protrusion in the cell but a lot more parameters and variables would have to be incorporated in to the model in order to accurately model the complete process of cell movement.

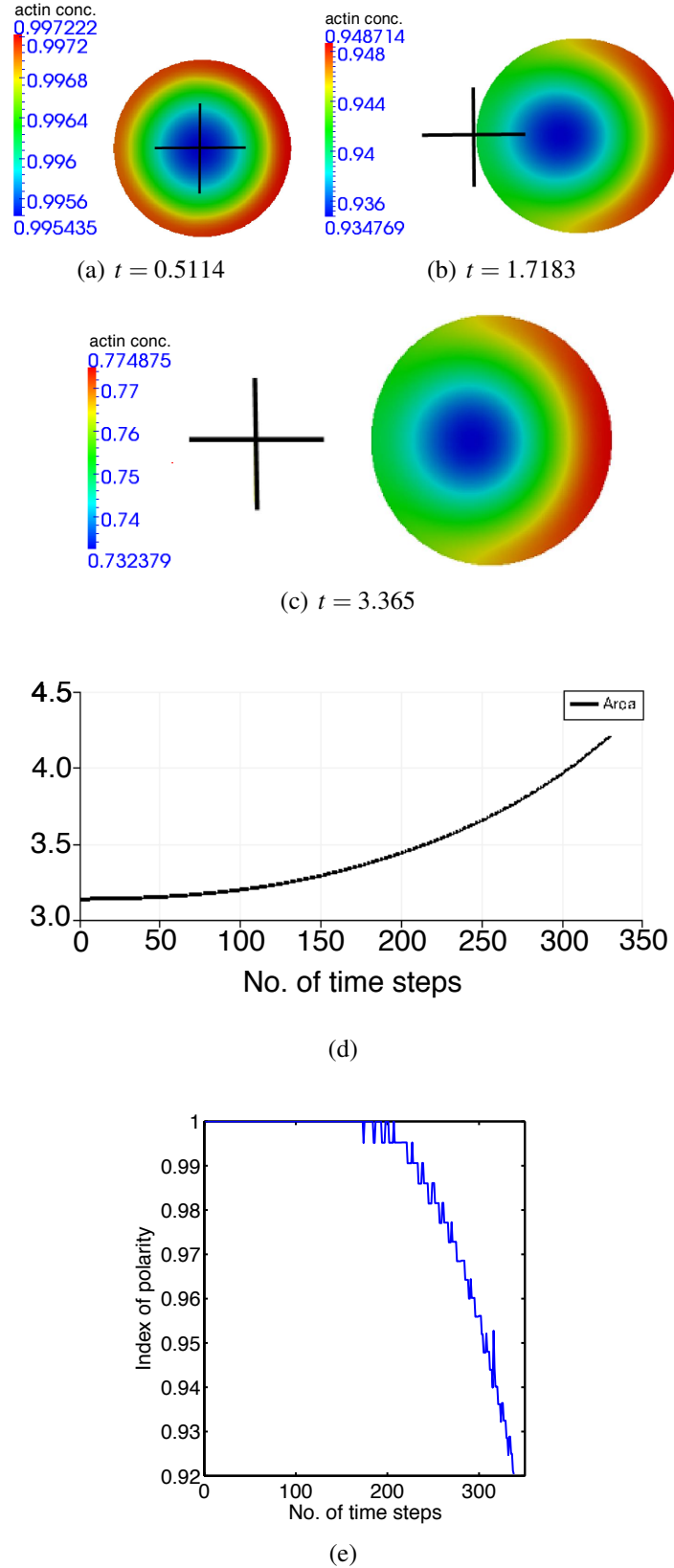


Figure 5.6: (a) - (c) are graphical displays of the numerical results of the actin concentration a_h with $\Delta t = 1.0228 \times 10^{-2}$. Blue signifies the lowest values and red the highest values. Figure 5.6(d) is a plot of the area of the cell against the number of time-steps taken. It shows the area of the cell increasing with the number of time-steps taken. (e) shows a plot of the index of polarity against number of time steps. A black plus sign specifies the position of the cell centroid at time $t = 0$.

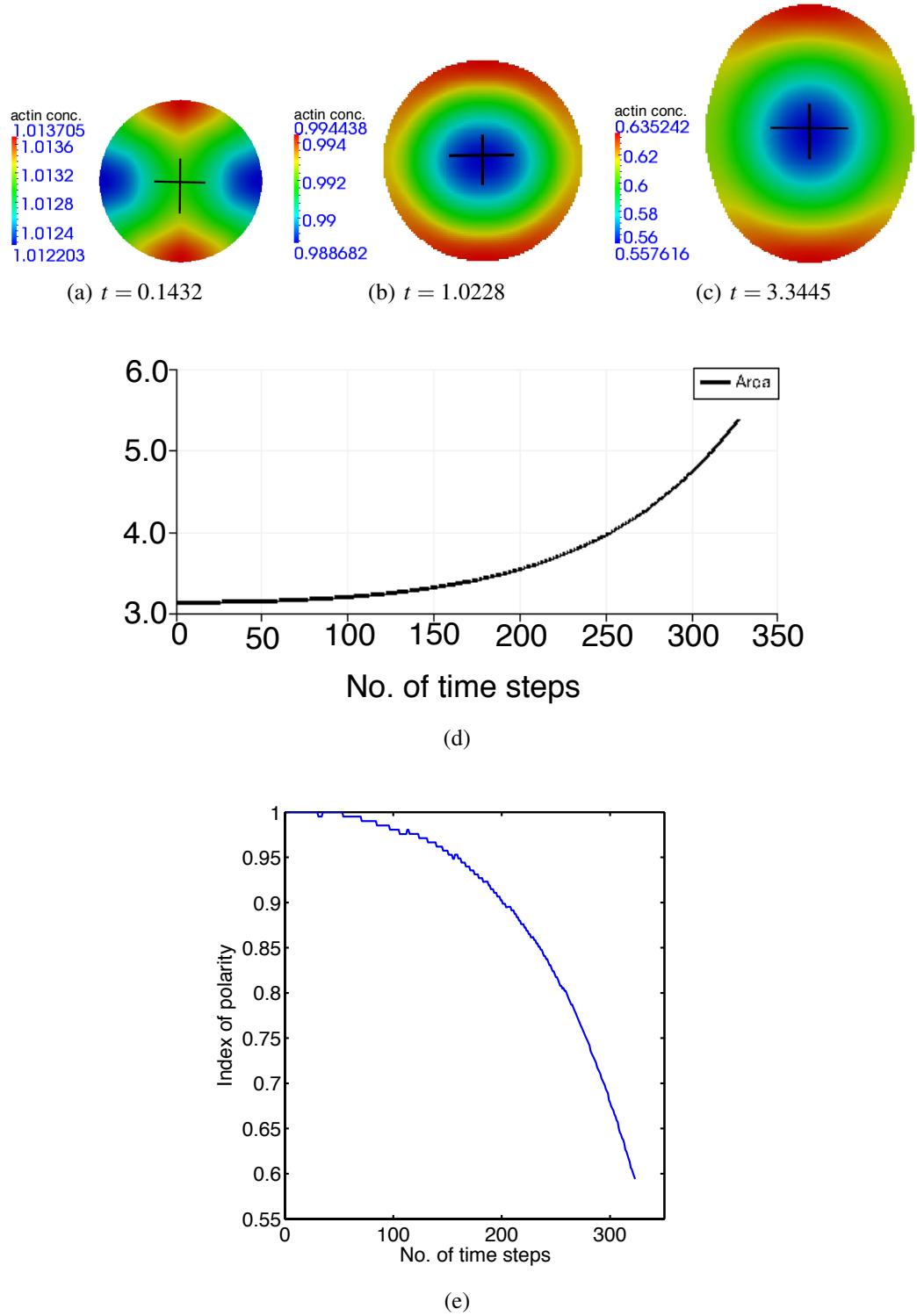


Figure 5.7: (a) - (c) are graphical displays of the numerical results of the actin concentration a_h . A finite element mesh with 2113 nodes was used, $\Delta t = 1.0228 \times 10^{-2}$. Blue signifies the lowest values and red the highest values. (d) is a plot of the area of the cell against the number of time-steps taken. It shows the area of the cell increasing with the number of time-step taken. (e) is a plot of the index of polarity against the number of time-steps taken.

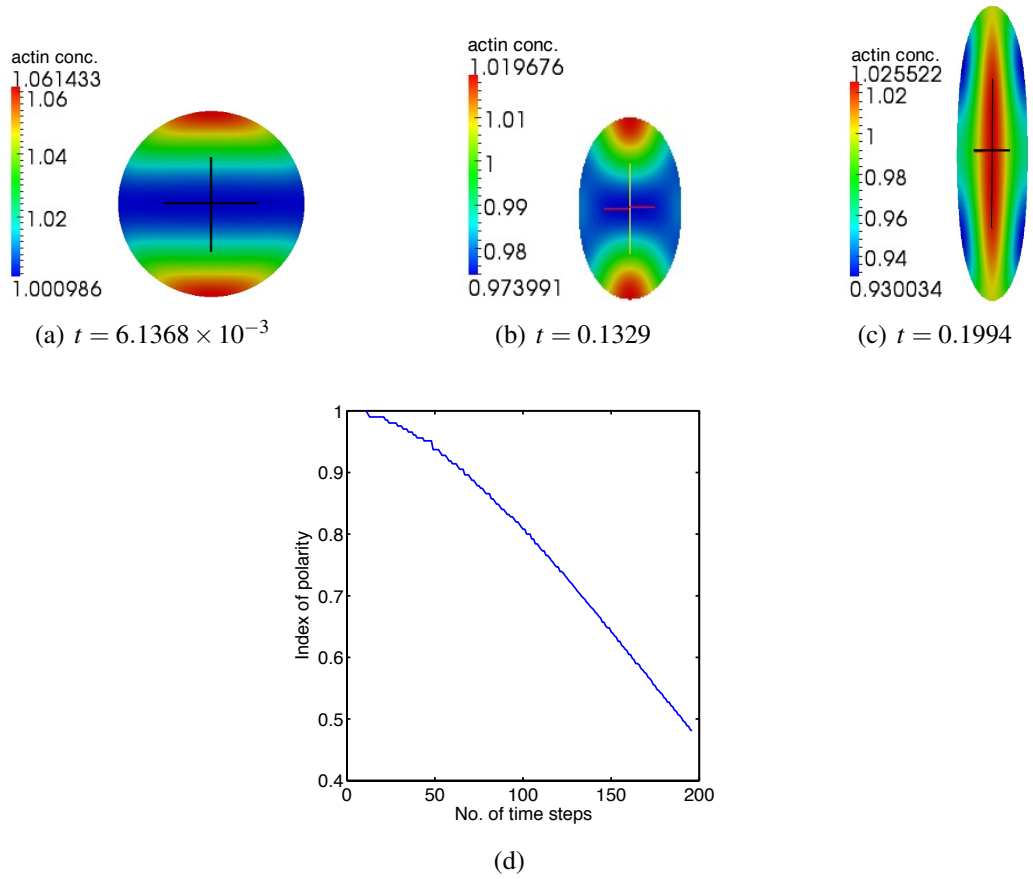


Figure 5.8: (a) - (c) are graphical displays of the numerical results of the actin concentration a_h . A finite element mesh with 8321 nodes was used, $\Delta t = 1.0228 \times 10^{-3}$. Blue signifies the lowest values and red the highest values. (d) is a plot of the index of polarity against the number of time-steps taken.

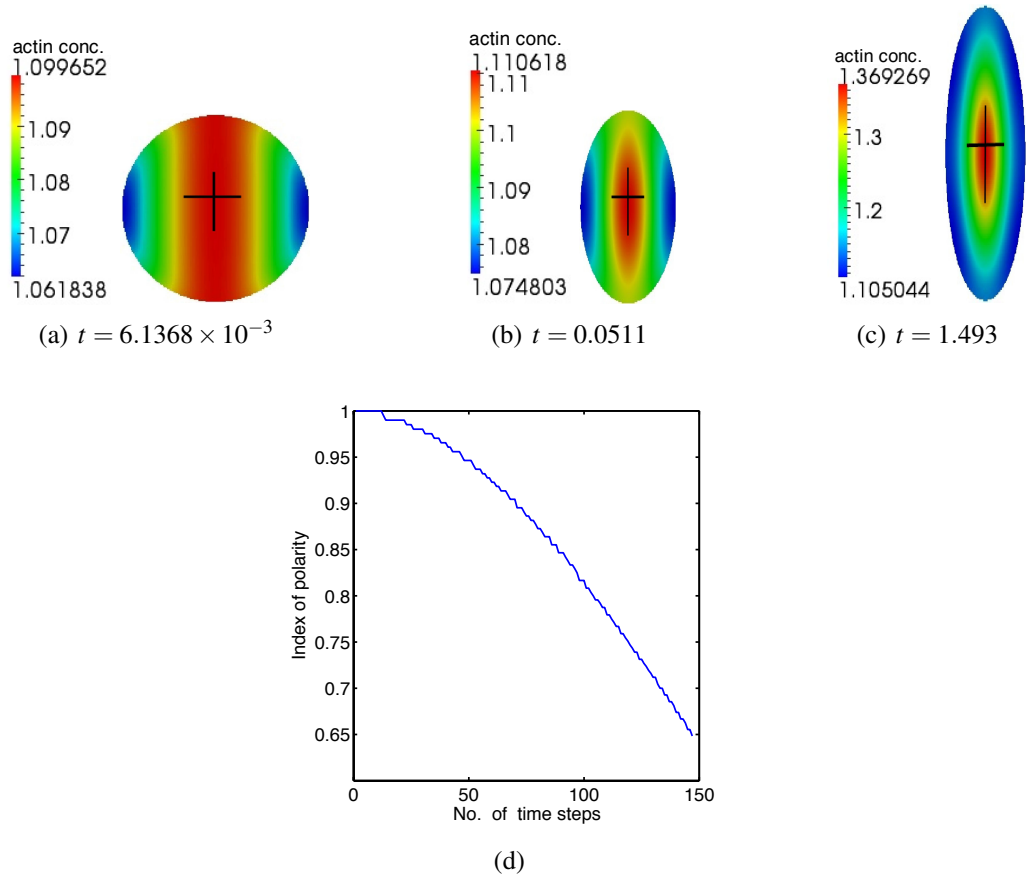


Figure 5.9: (a) - (c) are graphical displays of the numerical results of the actin concentration a_h . A finite element mesh with 8321 nodes was used, $\Delta t = 1.0228 \times 10^{-3}$. Blue signifies the lowest values and red the highest values. (d) is a plot of the index of polarity against the number of time-steps taken.

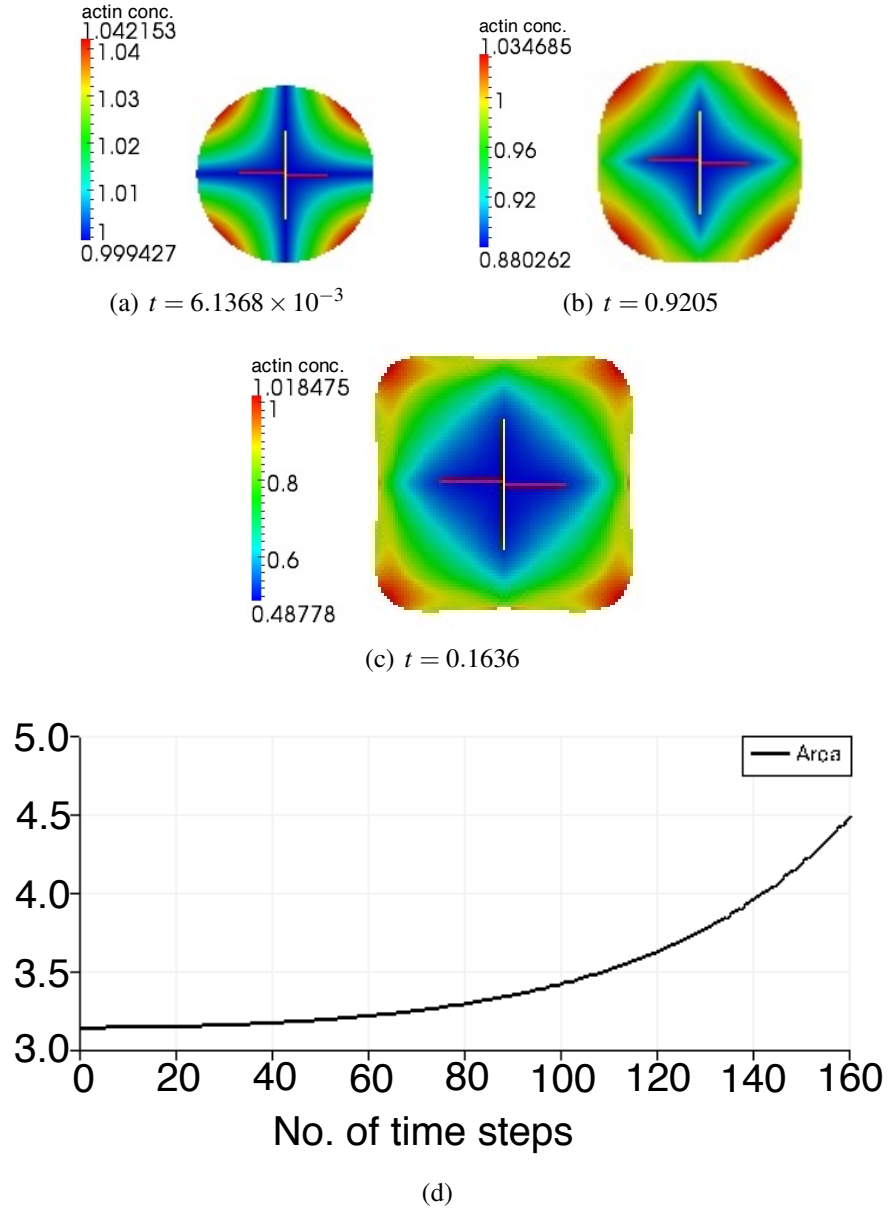
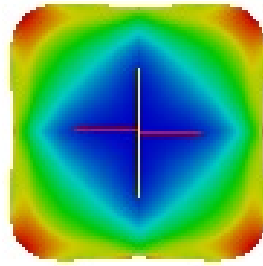
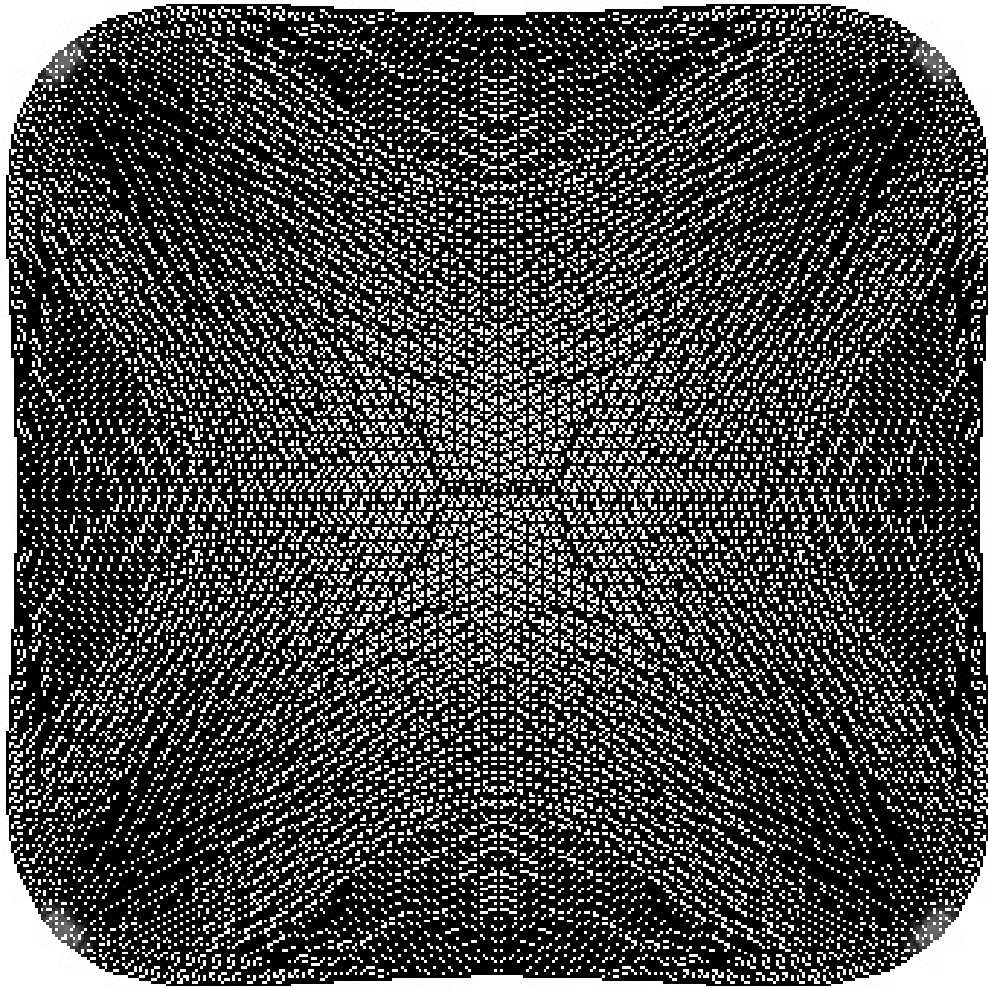


Figure 5.10: (a) - (c) are graphical displays of the numerical results of the actin concentration a_h with $\Delta t = 1.0228 \times 10^{-3}$. Blue signifies the lowest values and red the highest values. (d) is a plot of the area of the cell against the number of time-steps taken. It shows the area of the cell increasing with the number of time-step taken.



(a)



(b)

Figure 5.11: A graphical display of the finite element mesh. At time $t = 0.1636$, the cell has deformed significantly but the finite element mesh is still suitable for numerical computations and describes the domain properly. (b) is the finite element mesh of the graphics given in (a) and has been enlarge for the sake of clarity.

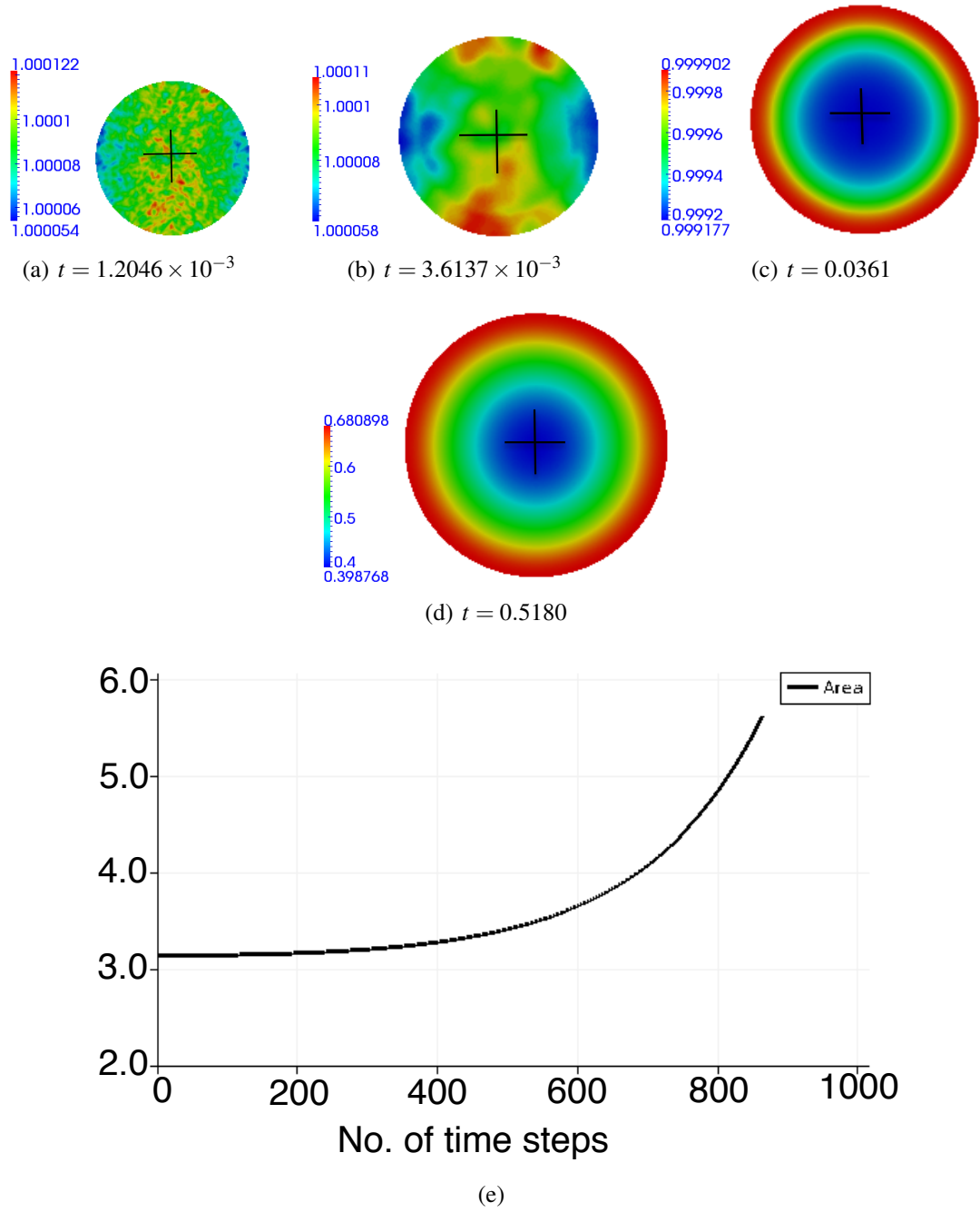


Figure 5.12: Graphical display of the simulation results of the actin concentration. Blue denotes the lowest values and red the highest. These results were obtained at the following times: (a) $t = 1.2046 \times 10^{-3}$, (b) $t = 3.6137 \times 10^{-3}$, (c) $t = 0.0361$, and (d) $t = 0.5180$. The numerical value of the contractile tonicity $\tilde{\psi} = 70.366$ and that of the pressure coefficient $\tilde{p} = 0.433$. (e) is a plot of the area of the cell against the number of time-steps taken.

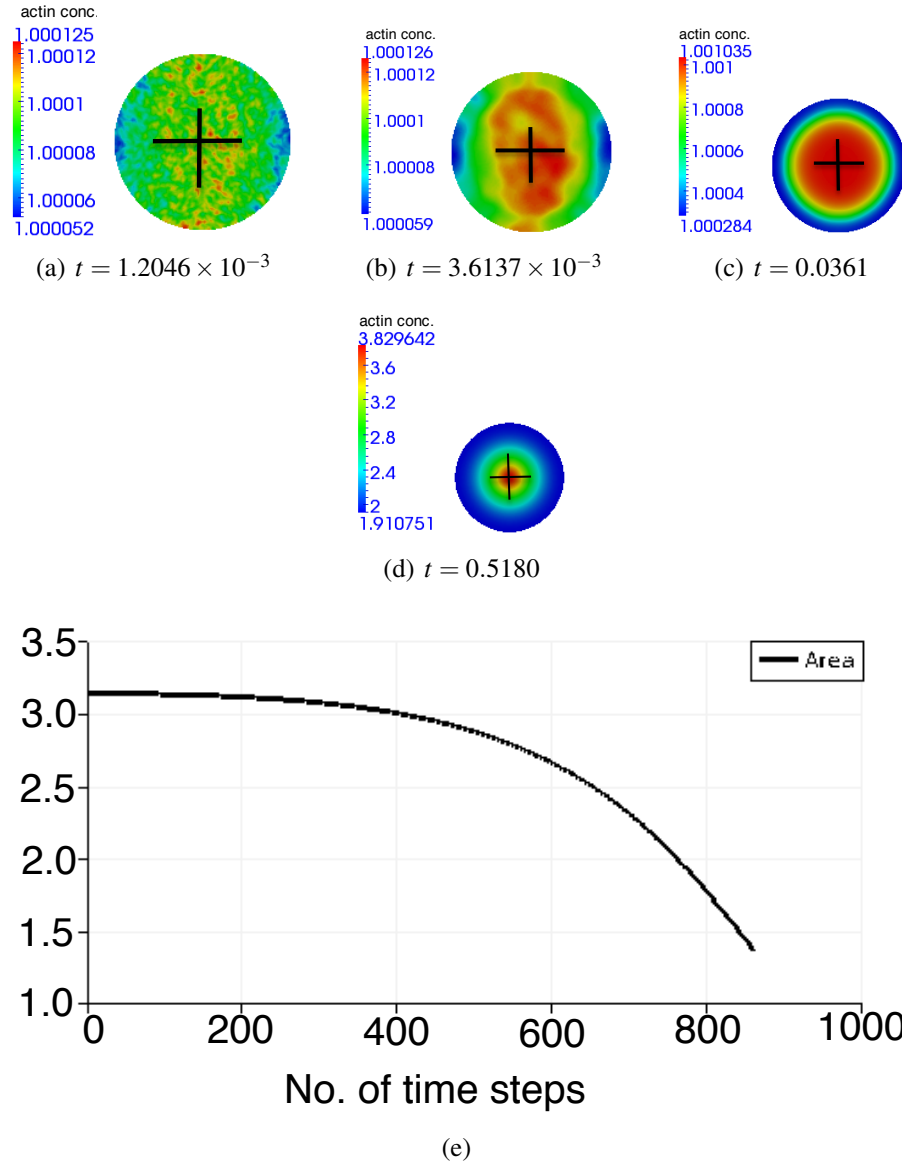


Figure 5.13: Graphical display of the simulation results of the actin concentration. Blue denotes the lowest values and red the highest. These results were obtained at the following times: (a) $t = 1.2046 \times 10^{-3}$, (b) $t = 3.6137 \times 10^{-3}$, (c) $t = 0.0361$, and (d) $t = 0.5180$. The numerical value of the contractile tonicity $\tilde{\psi} = 70.366$ and that of the pressure coefficient $\tilde{p} = -0.433$. (e) is a plot of the area of the cell against the number of time-steps taken.

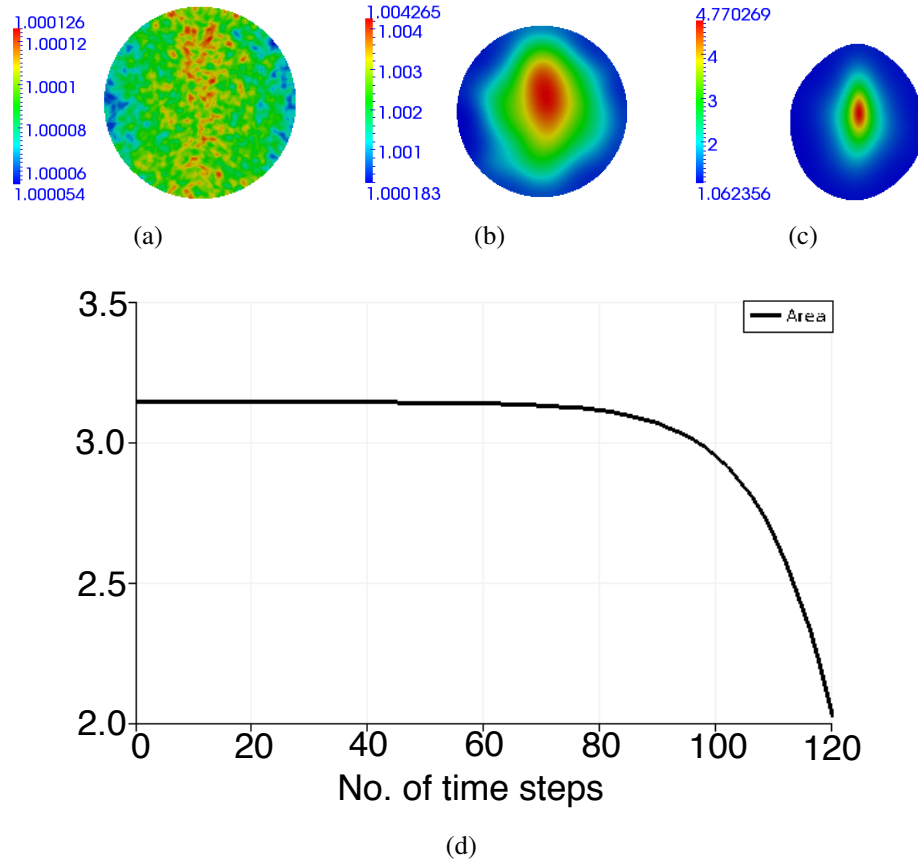


Figure 5.14: Graphical display of the simulation results of the actin concentration. Blue denotes the lowest values and red the highest. These results were obtained at the following times: (a) $t = 1.2046 \times 10^{-3}$, (b) $t = 3.6137 \times 10^{-3}$, and (c) $t = 0.0722$. The numerical value of the contractile tonicity $\tilde{\psi} = 7.8 \times 10^3$ and that of the pressure coefficient $\tilde{p} = 0.026$. (d) is a plot of the area of the cell against the number of time-steps taken.

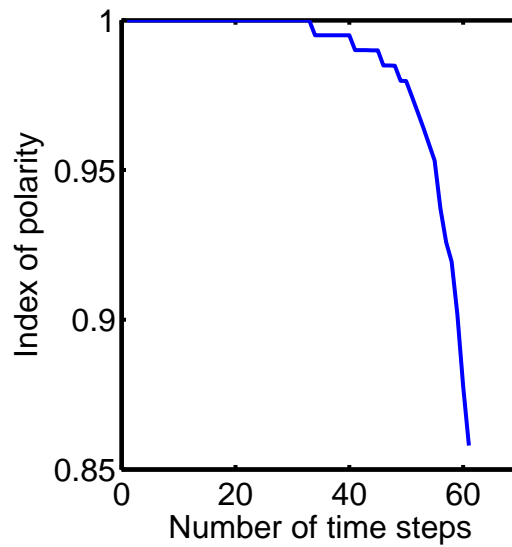


Figure 5.15: A plot of the index of polarity against the number of time-steps for simulation results with contractile tonicity $\tilde{\psi} = 7.8 \times 10^3$ and the pressure coefficient $\tilde{p} = 0.026$.

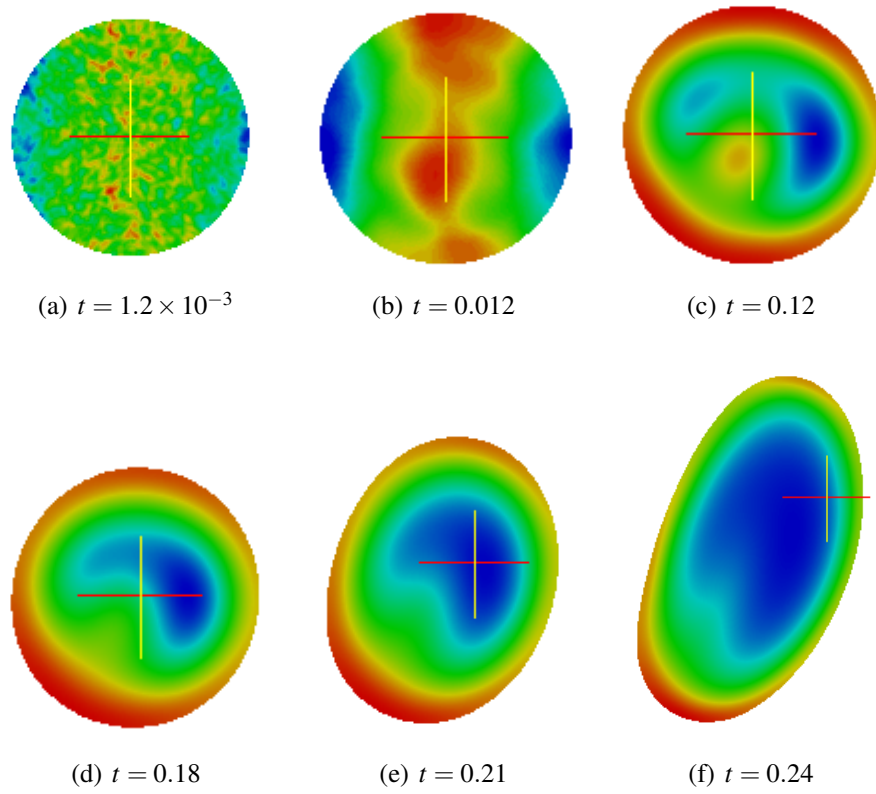


Figure 5.16: Graphical display of the simulation results of the actin concentration. Blue denotes the lowest values and red the highest. The numerical value of the contractile tonicity $\tilde{\psi} = 1.3 \times 10^3$ and the pressure coefficient $\tilde{p} = 0.026$.

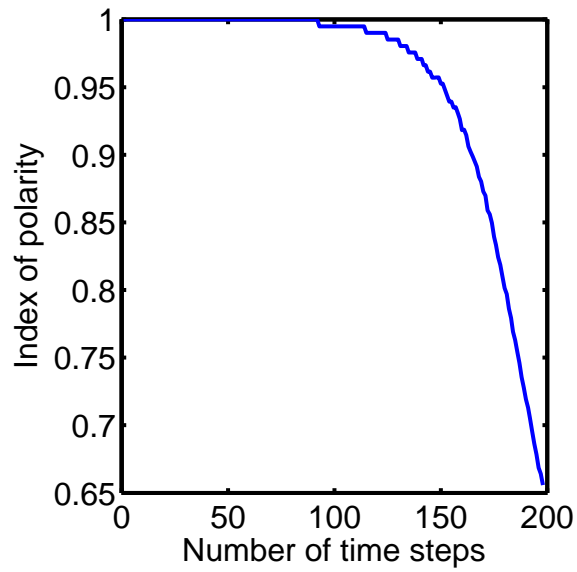


Figure 5.17: A plot of the index of polarity against the number of time-steps for simulation results with contractile tonicity $\tilde{\psi} = 1.3 \times 10^3$ and the pressure coefficient $\tilde{p} = 0.03$.

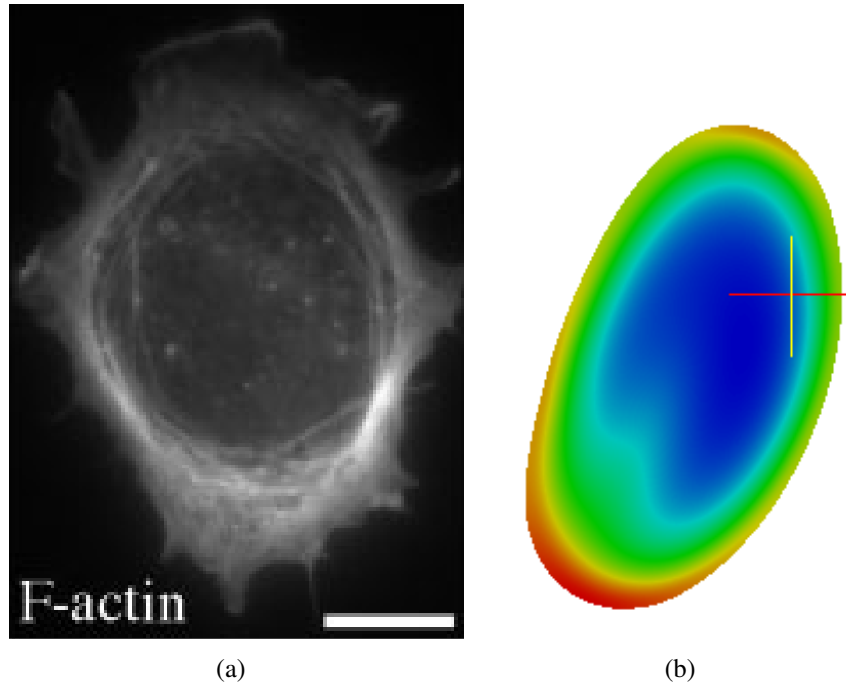


Figure 5.18: (a) Epifluorescence image of a Swiss 3T3 fibroblast cell (Senju and Miyata 2009). F-actin is predominant at the cell periphery and is highest at the region where protrusions occur. (b) A simulated cell deformation for contractile tonicity $\tilde{\psi} = 1.3 \times 10^3$ and the pressure coefficient $\tilde{p} = 0.026$. The distribution of F-actin in the simulated cell is in qualitative agreement with experimental observations (Senju and Miyata 2009).

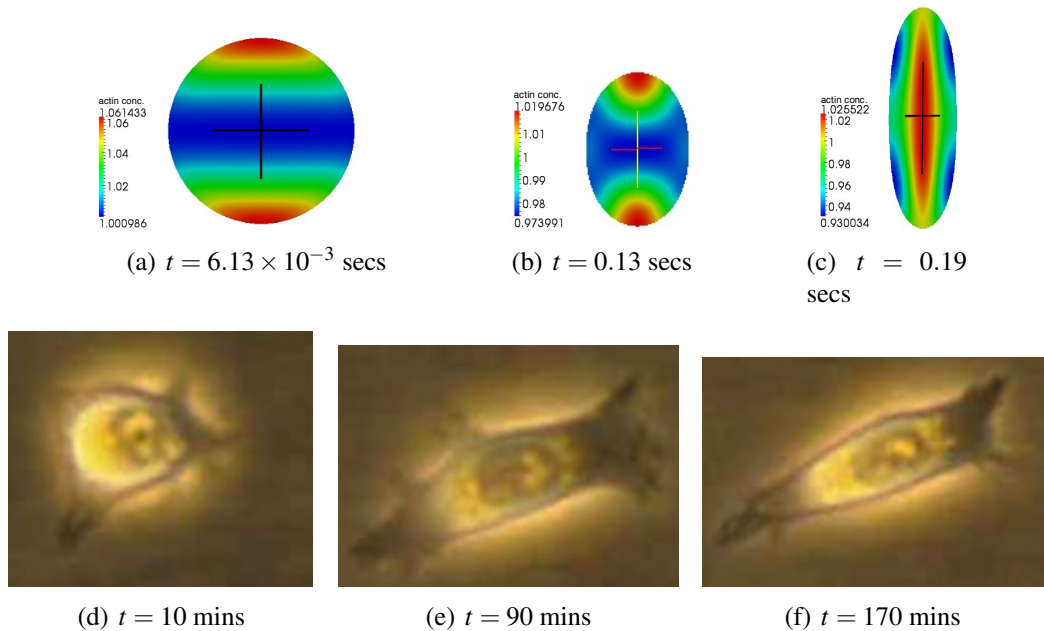


Figure 5.19: A qualitative comparison of the simulation result of cell deformations for mixed modes with those observed experimentally for an isolated fibroblast allowed to spread on a substrate *in vitro* (Stéphanou et al. 2008). Observe that the cell shape changing from a roughly circular shape to an elongated one, consistent with the numerical experiment.

h	$\Delta t = 0.1h^2$	$L^\infty(L^2)$	eoc
3.1415930	0.986961	0.56233220	-
1.5707970	0.246740	0.3173985	0.825
7.8539850×10^{-1}	0.061685	0.8405291×10^{-1}	1.917
3.9269925×10^{-1}	0.015421	0.2121861×10^{-1}	1.986
$1.96349625 \times 10^{-1}$	3.85532×10^{-3}	0.5315953×10^{-2}	1.997
$9.81748120 \times 10^{-2}$	9.63830×10^{-4}	0.1329648×10^{-2}	1.998

Table 5.2: Errors $L^\infty(L^2) := \sup_{(0,T)} \|a - a_h\|_{L^2(\Omega)}$ and experimental order of convergence (eoc) for the heat equation (5.2). The errors $L^\infty(L^2)$ decreases with decreasing mesh height h and the eoc approaches 2.0 with decreasing mesh height h .

5.10 Numerical experiments

1). Here we neglect the domain velocity β by assuming that $\beta = 0$ and verify the finite element numerical simulation result for the actin concentrations on a fixed unit disk. In the absence of domain velocity the reaction-diffusion equation takes the form of a heat equation with exact solution $a = a_c$, a constant function. Numerical simulation with $a_c = 1.0$ on a fixed unit disk gives the solution $a = 1.0$. Thus the numerical result is consistent with the exact result.

We now seek to show that the finite element method satisfies the aprior estimate $\|a - a_h\|_{L^2(\Omega)} \approx h^\alpha$, where α is the order of convergence (Reddy 1993). We consider the function $e^{-t} \cos(x)$ an exact solution of

$$\frac{\partial a}{\partial t} - D_a \Delta a = (D_a - 1)e^{-t} \cos(x) \quad \text{in } \Omega \subset \mathcal{R}^2 \times (0, T), \quad (5.2a)$$

$$\mathbf{n} \cdot \nabla a = 0 \quad \text{for } \mathbf{x} \in \partial\Omega \times (0, T), \quad (5.2b)$$

where Ω corresponds to $[0, \pi] \times [0, \pi]$ with the boundary denoted $\partial\Omega$. Initial data is $a_0(x) = \cos(x)$. In order to show the order of convergence for L^2 errors we choose the coupling $\Delta t = ch^2$, where h denotes the mesh height and c is a constant. Here we assume that $c = 0.1$. Any positive value can be assigned to D_a . Here we assume that $D_a := 0.3$. In Table 5.2 we show the experimental order of convergence for the norm

$$L^\infty(L^2) := \sup_{(0,T)} \|a - a_h\|_{L^2(\Omega)}.$$

for the time interval $[0, T]$, $T = 6$. Let $Er(h_1)$ and $Er(h_2)$ denote the errors for the mesh height h_1 and h_2 respectively then the experimental order of convergence is $eoc(h_1, h_2) = \log \frac{Er(h_1)}{Er(h_2)} \left(\log \frac{h_1}{h_2} \right)^{-1}$ (Dziuk and Elliott 2007). The value of eoc corresponds to α and converges to 2.0 as shown in Table 5.2. We note that on a continuously deforming cell, the exact solutions are unknown and as such we are unable to show any order of conver-

gence.

2). We consider a time interval $[0, T]$, $T > 0$. We present in Figure 5.20 the numerical simulation results of the moving grid finite element method of the cytomechanical model. We note that in Figure 5.20 the time interval used is small and initially the defor-

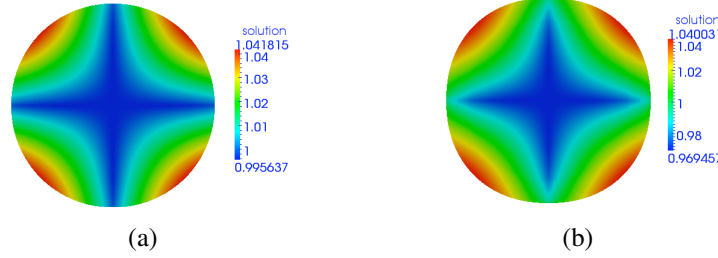


Figure 5.20: (a) is a plot of the simulation result for actin concentration at time $T = 0.10228$ with timestep size $\Delta t = 1.0228 \times 10^{-2}$. (b) is a plot of the simulation result for actin concentration at time $T = 0.10228$ with timestep size $\Delta t = 1.0228 \times 10^{-3}$.

mations are small and this makes the two graphs appear to be in agreement but for larger time intervals this is not the case. This is due to the fact that the equations are nonautonomous and there are no uniform steady states during domain evolution. We would also like to state that a plot of the errors $\|a^{n+1} - a^n\|_{L^2(\Omega_{h,t})}$ against time shows that the errors grows exponentially with time.

5.11 Summary

In this Chapter, we validated the moving grid finite element scheme for consistency with predictions from linear stability theory. We showed that the moving grid finite element method produced results that are consistent with predictions from linear stability theory. Upon validating the numerical scheme we proceeded to study the dynamics of actin and its influence on cell deformation. Numerical simulations of cell deformation gave uniform expansion, uniform contraction and irregular deformation of the cell. The distribution of actin filaments is related to the pressure coefficient, p and the contractile tonicity ψ . Depending on the values of p and ψ the simulation results gave rise to uniform expansion, uniform contraction or non-uniform cell deformations. For the cases where contractions occur, actin density was highest around the centroid of the cell while for the cases where expansions occur actin density was highest around the cell periphery. For the case of non-uniform cell deformations actin density was predominant at the periphery of the cell and was highest at regions with the highest curvature. We also observed cell membrane protrusions on two and four fronts. We note that experimental observations realised on L929 fibroblasts show that cells exhibit a maximum of four simultaneous protrusions (additional ones are transitory) (Stéphanou et al. 2004).

A limitation of the model is the lack of cell volume conservation. It was observed that the cell volume increased or decreased infinitely which is not consistent with experimental studies. A future work would be to incorporate a mechanism for volume conservation in the model to aid in conserving the cell volume.

Chapter 6

Conclusions and future work

6.1 Conclusion

In this work, we proposed and implemented an efficient numerical method to study cell dynamics. Cells are the smallest basic unit of life but highly complex in structure and dynamics. More than 200 different types of cells make up the human body and each of them is physiologically and biochemically specialised for a specific function (Stéphanou 2010). Though the different cells are specific in their roles, in higher and structurally complex organisms, different cells come together to form tissues which work in harmony for the well being or detriment of the organism. As the structural complexity of an organism increases, tissues are organised into organs which are in turn organised into systems. The importance of studying cell movements cannot be overemphasised because vital processes like reproduction, maintenance and development in multicellular organisms involve cell replication and movement (Le Clainche and Carlier 2008). Also cell movement plays a crucial role in many physiological and pathological processes (Le Clainche and Carlier 2008) such as immune response (Fleischer et al. 2007; Lauffenburger and Horwitz 1996; Ridley et al. 2003), wound healing, development of tissues (Xue et al. 2010), embryogenesis (Clark 1996; Stéphanou 2010), inflammation and the formation of tumour metastasis (Lauffenburger and Horwitz 1996; Stéphanou et al. 2008). In this work, we studied cell deformation and movement as a consequence of the dynamics of actin filaments and their interaction with associated proteins. Three key phases were covered: Mathematical modelling, linear stability analytical study and numerical simulations using the moving grid finite element.

Mathematical modelling and theoretical studies have played a significant role in unravelling the processes involved in cell migration (Zaman et al. 2005) and is projected to take a leading role in future developments of cell movement (Flaherty et al. 2007). The increasing relevance of mathematical modelling is due to high performance of sophisticated computer programs in solving complex equations describing biological systems even at the cellular level. The high cost and time consumption associated with laboratory

experiments can be highly reduced with the help of the sophisticated computer programs (Flaherty et al. 2007).

The mathematical model that we considered is a cytomechanical model consisting of two coupled system of equations. The equations takes into account both the biochemical and biomechanical properties of the actin filaments and their interaction with associated proteins: the first equation is a force balance mechanical equation describing the displacement of the cell generated by the actin network. In deriving this equation we assume that at the intracellular level, the cell complies to Newtonian dynamics such that inertial terms are negligible compared to viscous and elastic forces hence motion ceases as soon as the forces are turned off (Lewis and Murray 1991; Purcell 1977). Thus at any given time, the actin network is in mechanical equilibrium under the action of the viscoelastic, contractile and pressure forces generated by the actin network. And the second equation is a reaction-diffusion equation describing the polymerization kinetics of actin filaments and its movement via diffusion and convective effects as a result of changes in cell shape (Stéphanou et al. 2004).

In order to understand the behaviour of the system close to bifurcation points, a detailed linear stability analytical theory was carried out. This enabled us to reduce the number of parameter values within the system but more importantly, we were able to identify two critical parameters underpinning the bifurcation process: the contractile tonicity and the pressure. The contractile tonicity was identified as the bifurcation parameter that determines the transition from a stable homogeneous steady state to non-uniform inhomogeneous solutions. Far away from the bifurcation points, linear theory does not hold, thereby necessitating the use of novel numerical methods.

Unlike previous studies (Alt and Tranquillo 1995; Stéphanou et al. 2004), we proposed a moving grid finite element method introduced in 2000 by (Madzvamuse 2000) to study partial differential equations posed on complex evolving domains. This numerical method is a natural candidate capable, not only of solving the model system, but also of dealing with complex cell shape deformation and movement. By using linear stability theory close to bifurcation points we validated our numerical results which gave confidence in the applicability of the choice of the numerical method. Far away from the bifurcation points, numerical solutions of the model system produced a variety of scenarios of the cell deformation and cell movement such as uniform cell expansion and contraction, and non-uniform cell deformations (for example, cell protrusions). The numerical results clearly demonstrate that regions with high actin concentrations result in large cell deformation and cell movement in complete agreement with experimental observations (Senju and Miyata 2009). Equivalently, regions of the cell with large displacements result in high actin concentrations. If the actin concentration is uniformly distributed, then the cell either expands or contracts uniformly and isotropically.

We summarise our observations as follows:

- The distribution of actin filaments is related to the pressure coefficient, p and the contractile tonicity ψ . Depending on the values of p and ψ the simulation results gave rise to uniform expansion, uniform contraction or non-uniform cell deformations.
- For the cases where contractions occur, actin density was highest around the centroid of the cell while for the cases where expansions occur actin density was highest around the cell periphery.
- For the case of non-uniform cell deformations actin density was predominant at the periphery of the cell and was highest at regions with the highest curvature (see Fig. 5.16). For $\tilde{\psi} = 7.8 \times 10^3$ actin density was localized at the centroid of the cell and the boundary was contracting non-uniformly (see Fig. 5.14).
- Actin filaments play a key part in cell deformations and such deformations are a function of the contractile tonicity and an adequate counter pressure is required in the cell to prevent it from shrinking as a result of the contractile forces.
- We assumed that the pressure in the cell was due to the contraction of the network creating cytoplasmic flows throughout the cell thus increasing the pressure and was reinforced by a polymerization induced pressure at the vicinity of the cell boundary. We modelled this by introducing the heavy-side function which allowed us to study the pressure-induced protrusions and actin filaments polymerization-induced protrusions.

6.2 Future work

Possible future works are

- I). Introduce a mechanism for volume conservation of the cell to stop the infinite expansions and contractions of the cell.
- II). Coupling the force balance equation with a coupled system of reaction-diffusion equations modelling the interactions of actin filaments with myosin II and integrin proteins responsible for cell adhesions.
- III). Introducing an additional model for chemotaxis.

IV). Introducing obstacles (rigid bodies) such that cells can move around these as they move towards some sources.

V). Modelling interactions between multiple moving cells.

References

- M. Abercrombie. The crawling movement of metazoan cells. *Proc. R. Soc. London B Biol. Sci.*, 207:129–147, 1980. [36](#)
- M. Abercrombie, J. E. Heaysman, and S. M. Pegrum. The locomotion of fibroblasts in culture i. movements of the leading edge. *Experimental Cell Research*, 59:393–398, 1970. [36](#)
- M. Abercrombie, J. E. Heaysman, and S. M. Pegrum. The locomotion of fibroblasts in culture iv electron microscopy of the leading lamella. *Experimental Cell Research*, 67: 359–367, 1971. [36](#)
- V. C. Abraham, D. Krishnamurthi, T. Lansing, and F. Lanni. The actin based nanomachine at the leading edge of migrating cells. *Biophys. J.*, 77:1721–1732, 1999. [38](#)
- Milton Abramowitz and Irene A. Stegun. *Handbook of Mathematical functions with formulas, graphs, and Mathematical tables*. US Dept of Commerce, 1968. [64](#)
- D. J. Acheson. *Elementary fluid dynamics*. Oxford Applied Mathematics and Computing Science. Clarendon Press, Oxford, 1990. [19](#)
- H. Aizawa, K. Sutoh, and I. Yahara. Overexpression of cofilin stimulates bundling of actin filaments, membrane ruffling, and cell movement in dictyostelium. *The Journal of Cell Biology*, 132(3):335–344, 1996. [35](#)
- B. Alberts, A. Johnson, J. Lewis, M. Raff, K. Roberts, and P. Walter. *Molecular Biology of the Cell*. Garland Science, 4th edition, 2002. [4](#), [23](#), [24](#), [26](#), [27](#), [29](#), [30](#), [31](#), [34](#), [35](#), [36](#)
- W. Alt and M. Dembo. Cytoplasm dynamics and cell motion: two phase flow models. *Math. Biosci.*, 156:207–228, 1999. [43](#)
- W. Alt and R. T. Tranquillo. Basic morphogenetic system modeling shape changes of migrating cells: How to explain fluctuating lamellipodial dynamics. *J. Biol. Syst.*, 3: 905–916, 1995. [15](#), [41](#), [44](#), [47](#), [50](#), [51](#), [52](#), [73](#), [128](#)

- R. Ananthakrishnan and A. Ehrlicher. The forces behind cell movement. *Int. J. Biol. Sci.*, 3:303–317, 2007. 14, 24, 25, 26, 27, 29, 30, 33, 34, 35, 36, 37
- R. Ananthakrishnan, J. Gusk, and J. Käs. Cell mechanics: Recent advances with a theoretical perspective. *Recent Res. Devel. Biophys.*, 5:39–69, 2006. 14, 24, 27
- M. J. Baines. *Moving finite elements, monographs on numerical analysis*. Clarendon Press, Oxford, 1994. 74
- E. L. Barnhart, Kun-Chun Lee, K. Keren, A. Mogilner, and J. Theriot. An adhesion-dependent switch between mechanisms that determine motile cell shape. *PLoS Biology*, 9, May 2011. 53
- A. R. Bausch, F. Ziemann, A. A. Boulbitch, K. Jacobson, and E. Sackmann. Local measurements of viscoelastic parameters of adherent cell surfaces by magnetic bead microrheometry. *Biophys. J.*, 75:2038–2049, 1998. 53
- J. Bereiter-Hahn and H. Luers. Subcellular tension fields and mechanical resistance of the lamella front related to the direction of locomotion. *Cell Biochem. and Biophys.*, 29:243–262, 1998. 38
- T. Betz, D. Lim, and J. A. Kas. Neuronal growth: a bistable stochastic process. *Phys. Rev. Lett.*, 96:098103, 2006. 25
- F. Binamé, G. Pawiak, P. Roux, and U. Hibner. What makes cells move: requirements and obstacles for spontaneous cell motility. *Mol. Biosyst.*, 6:648–61, Apr. 2010. 13, 14, 36, 37, 38, 44, 45, 47
- I. Bischofs, F. Klein, D. Lehnert, M. Bastmeyer, and U. Schwarz. Filamentous network mechanics and active contractility determine cell and tissue shape. *Biophys. J.*, 95: 3488–3496, 2008. 15, 41
- H. Blaser, M. Reichman-Fried, I. Castanon, K. Dumstrei, F. L. Marlow, K. Kawakami, L. Solnica-Krezel, C-P. Heisenberg, and E. Raz. Migration of zebrafish primordial germ cells: a role for myosin contraction and cytoplasmic flow. *Dev. Cell*, 11:613–627, 2006. 38, 39
- D. Bray. *Cell Movement: from molecules to motility*. Garland, 2001. 47, 48
- C. A. Brebbia. *Boundary element methods*. Berlin-Heiddberg-New York: Springer, 1981. 15, 73
- J. Burkardt. Computational geometry lab: barycentric coordinates in triangles. http://people.sc.fsu.edu/~jburkardt/presentations/cg_lab_barycentric_triangles, 2009. Accessed: October. 93

- G. Charras and E. Paluch. Blebs lead the way: how to migrate without lamellipodia. *Nat. Rev. Mol. Cell Biol.*, 9:730–736, 2008. [38](#), [39](#), [44](#), [47](#)
- G. T. Charras, J. C. Yarrow, M. A. Horton, L. Mahadevan, and T. J. Mitchison. Non-equilibration of hydrostatic pressure in blebbing cells. *Nature*, 435:365–369, 2005. [38](#)
- H. Chen, B. W. Bernstein, and J. R. Bamburg. Regulating actin-filament dynamics in vivo. *Trends Biochem Sci.*, 25:19–23, 2000. [13](#), [14](#), [27](#)
- R. A. F. Clark. *The molecular and cellular biology of wound repair*. Plenum Press New York, 1996. [13](#), [35](#), [127](#)
- M. P. Coleman. *An introduction to partial differential equation with MATLAB*. CRC Press LLC, 2005. [19](#), [20](#), [21](#), [22](#), [59](#), [60](#), [61](#)
- E. J. Crampin, E. A. Gaffney, and P. K. Maini. Reaction and diffusion on growing domains: Scenarios for robust pattern formation. *Bull. Math. Biol.*, 61:1093–1120, 1999. [73](#)
- M. C. Cross and P. C. Hohenberg. Pattern formation outside of equilibrium. *Reviews of Modern Physics*, 65:851–1112, 1993. [68](#)
- S. L. Crouch and A. H. Starfield. *Boundary element methods in solid mechanics*. London: George Allen & Unwin, 1983. [15](#), [73](#)
- C. C. Cunningham. Actin polymerization and intracellular solvent flow in cell surface blebbing. *J. Cell Biol.*, 129:1589–1599, 1995. [38](#)
- M. J. Dayel, O. Akin, M. Landeryou, V. Risca, and et al Mogilner, A. In silico reconstitution of actin-based symmetry breaking and motility. *PLoS Biol.*, 7:e1000201, 2009. doi: 10.1371/journal.pbio.1000201. [111](#)
- M. Dogterom, J. W. Kerssemakers, G. Romet-Lemonne, and E. M. Janson. Force generation by dynamic microtubules. *Curr. Opin. Cell. Biol.*, 17:67–74, 2005. [26](#)
- G. Dziuk and C. M. Elliott. Finite elements on evolving surfaces. *IMA J. Numer. Anal.*, 27:262–292, 2007. [82](#), [86](#), [124](#), [147](#), [150](#), [152](#)
- L. Edelstein-Keshet. *Mathematical models in Biology*. Society for Industrial and Applied Mathematics, 2005. [45](#), [56](#)
- E. Evans. New physical concepts for cell amoeboid motion. *Biophys. J.*, 64:1306–1322, 1993. [40](#)

- O. T. Fackler and R. Grosse. Cell motility through plasma membrane blebbing. *J. Cell Biol.*, 181:879–884, 2008. 39
- R. D. Fink. In vivo cytoskeletal dynamics of living fish embryos movie #2:deep cell circus movements: Actin dynamics. mount holyoke college. <http://www.mtholyoke.edu/courses/rfink/Researchvideopages/rvideo3.htm>. Accessed July, 2011. 38
- R. A. Firtel and R. Meili. Dictyostelium: a model for regulated cell movement during morphogenesis. *Curr. Opin. Genet. Dev.*, 10:421–7, 2000. 38
- B. Flaherty, J. P. McGarry, and P. E. McHugh. Mathematical models of cell motility. *Cell Biochem. Biophys.*, 49:14–28, 2007. 42, 127, 128
- F. Fleischer, R. Ananthakrishnan, S. Eckel, H. Schmidt, J. Käs, V. Svitkina, and B. Michael. Actin network architecture and elasticity in lamellipodia of melanoma cells. *New Journal of Physics*, 9:420, 2007. 13, 35, 127
- L. Formaggia and F. Nobile. A stability analysis for the arbitrary lagrangian eulerian formulation with finite elements. *East-West J. Numer. Math.*, 7(2):105–131, 1999. 143
- P. Friedl and B. Weigelin. Interstitial leukocyte migration and immune function. *Nat. Immunol.*, 9:960–9, 2008. 38
- P. Friedl, K. S. Zanker, and E. B. Brocker. Cell migration strategies in 3-d extracellular matrix: differences in morphology, cell matrix interactions, and integrin function. *Microsc. Res. Tech.*, 43:369–78, 1998. 38
- B. Giebel, D. Corbeil, J. Beckmann, J. Hohn, D. Freund, K. Giesen, J. Fischer, G. Kogler, and P. Wernet. Segregation of lipid raft markers including cd133 in polarized human hematopoietic stem and progenitor cells. *Blood*, 104:2332–8, 2004. 38
- F. Gittes, B. Mickey, J. Nettleton, and J. Howard. Flexural rigidity of microtubules and actin filaments measured from thermal fluctuations in shape. *J. Cell Biol.*, 120:923–34, 1993. 27
- M. Gracheva and H. G. Othmer. A continuum model of motility in ameboid cells. *Bulletin of Mathematical Biology*, 66:167–193, 2004. 42, 43, 52
- P. Grindrod. *Patterns and waves*. Peter Grindrod, 2007. 45
- L. S. Gupton, K. L. Anderson, T. P. Kole, R. S. Fischer, A. Ponti, S. E. Hitchcock-DeGregori, G. Danuser, V. M. Fowler, D. Wirtz, D. Hanein, and C. M. Waterman-Storer. Cell migration without a lamellipodium: translation of actin dynamics into cell movement mediated by tropomyosin. *The Journal of Cell Biology*, 168:619–631, 2005. 14, 36

- B. T. Helfand, L. Chang, and R. D. Goldman. Intermediate filaments are dynamic and motile elements of cellular architecture. *J Cell Sci.*, 117:133–41, 2004. [26](#)
- M. R. Hestenes and E. Stiefel. Methods of conjugate gradients for solving linear systems. *Journal of Research of the National Bureau of Standards*, 49, 1952. [89](#)
- T. L. Hill and M. W. Kirschner. Bioenergetics and kinetics of microtubule and actin filament assembly-disassembly. *Int. Rev. Cytol.*, 78:1–125, 1982. [42](#)
- P. Hofman, L. d’Andrea, E. Guzman, E. Selva, G. Le Negrata, D. F. Far, E. Lemichez, P. Boquet, and B. Rossi. Neutrophil f-actin and myosin but not microtubules functionally regulate transepithelial migration induced by interleukin 8 across a cultured intestinal epithelial monolayer. *Eur Cytokine Netw.*, 10:227–36, 1999. [25](#)
- C. Hofreither, U. Langer, and S. Tomar. Large-scale scientific computing, 7th international conference, Issc 2009. In I. Lirkov, S. Margenov, and J. Waśniewski, editors, *Boundary element simulation of linear water waves in a model basin*. Springer-Verlag Berlin Heidelberg, 2010. [15](#)
- A. S. Hoglund, R. Karlsson, E. Arro, B. A. Fredriksson, and U. Lindberg. Visualization of the peripheral weave of microfilaments in glia cells. *J. Muscle Res. Cell Motil.*, 1: 127–146, 1980. [30](#)
- R. H. Insall and L. M. Machesky. Actin dynamics at the leading edge: From simple machinery to complex networks. *Developmental Cell*, 17, September 2009. [30](#), [31](#), [32](#), [40](#)
- P. A. Janmey. Mechanical properties of cytoskeletal polymers. *Current Opinion in Cell Biology*, 2:4–11, 1991. [47](#)
- Claes Johnson. *Numerical solution of partial differential equations by the finite element method*. University of Cambridge, 1987. [83](#)
- G. Karp. *Cell and molecular biology: concepts and experiments*. John Wiley & Sons, Inc., 1999. [23](#), [24](#), [35](#)
- I. Kaverina, O. Krylyshkina, , and J. V. Small. Regulation of substrate adhesion dynamics during cell motility. *Int J Biochem Cell Biol.*, 34:746–61, 2002. [30](#)
- H. Keller and P. Eggli. Protrusive activity, cytoplasmic compartmentalization, and restriction rings in locomoting blebbing walker carcinosarcoma cells are related to detachment of cortical actin from the plasma membrane. *Cell. Motil. Cytoskeleton*, 41: 181–193, 1998. [38](#)

- H. Keller, P. Rentsch, and J. Hagmann. Differences in cortical actin structure and dynamics document that different types of blebs are formed by distinct mechanisms. *Exp. Cell Res.*, 277:161–172, 2002. [38](#)
- K. Keren and J. A. Theriot. Biophysical aspects of actin-based cell motility in fish epithelial keratocytes. In P. Lenz, editor, *Cell Motility: Biological and Medical Physics, Biomedical Engineering*. Springer Science and Business Media, LLC, 2008. [13](#), [14](#), [40](#)
- T. Kim, W. Hwang, H. Lee, and R. D. Kamm. Computational analysis of viscoelastic properties of crosslinked actin networks. *PLoS Comput. Biol.*, 5:e1000439, 2009. [27](#)
- D. R. Kovar and T. D. Pollard. Insertional assembly of actin filament barbed ends in association with formins produces piconewton forces. *Proc. Natl. Acad. Sci.*, 101:14725–30, 2004. [33](#)
- P. K. Kundu and I. M. Cohen. *Fluid mechanics*. Academic Press, 2002. [47](#)
- E. Kuusela and W. Alt. Continuum model of cell adhesion and migration. *J. Math. Biol.*, 58:135–161, 2009. [27](#)
- T. LaForce. Pe281 boundary element method course notes, June 2006. [15](#), [74](#)
- F. Lanni and B. R. Ware. Detection and characterization of actin monomers, oligomers, and filaments in solution by measurement of fluorescence photobleaching recovery. *Biophys. J.*, 46:97–110, 1984. [111](#)
- S. Larsson and V. Thomée. *Partial differential equations with numerical methods*. Springer-Verlag Berlin Heidelberg New York, 2003. [18](#)
- D. A. Lauffenburger and A. F. Horwitz. Cell migration: A physically integrated molecular process. *Cell*, 84:359–369, 1996. [13](#), [14](#), [35](#), [36](#), [127](#)
- C. Le Clainche and M-F. Carlier. Regulation of actin assembly associated with protrusion and adhesion in cell migration. *Physiol. Rev.*, 88:489–513, 2008. [13](#), [14](#), [23](#), [35](#), [36](#), [127](#)
- M. A. Lewis and J. D. Murray. Analysis of stable two-dimensional patterns in contractile cytogel. *J. Nonlinear Sci.*, 1:289–311, 1991. [15](#), [48](#), [56](#), [128](#), [152](#)
- M. A. Lewis and J. D. Murray. Analysis of dynamic and stationary pattern formation in the cell cortex. *J. Biol. Syst.*, 31:25–71, 1992. [15](#), [26](#), [41](#), [152](#)
- T. Liszka and J. Orkisz. The finite difference method at arbitrary irregular grids and its application in applied mechanics. *Comput. Struct.*, 11:83–95, 1980. [73](#)

- A. P. Liu, D. L. Richmond, L. Maibaum, S. Pronk, P. L. Geissler, and D. A. Fletcher. Membrane-induced bundling of actin filaments. *nature physics*, Vol. 4, October 2008. [24](#)
- L. M. Machesky, R. D. Mullins, H. N. Higgs, D. A. Kaiser, L. Blanchoin, R. C. May, M. E. Hall, and T. D. Pollard. Scar, a wasp-related protein, activates nucleation of actin filaments by the arp2/3 complex. *Proc. Natl. Acad. Sci. USA*, 96:3739–3744, 1999. [31](#)
- A. Madzvamuse. Time-stepping schemes for moving grid finite elements applied to reaction-diffusion systems on fixed and growing domains. *Journal of Computational Physics*, 214:239–263, 2006. [16](#), [73](#), [74](#), [75](#)
- A. Madzvamuse and P. K. Maini. Velocity-induced numerical solutions of reaction-diffusion systems on fixed and growing domains. *J. of Comp. Phys.*, 224:100–119, 2007. [16](#), [74](#)
- A. Madzvamuse, A. J. Wathern, and P. K. Maini. A moving grid finite element method applied to a model biological pattern generator. *Journal of Computational Physics*, 190:478–500, 2003. [15](#), [16](#), [73](#), [74](#)
- A. Madzvamuse, P. K. Maini, and A. J. Wathen. A moving grid finite element method for the simulation of pattern generation by turing models on growing domains. *Journal of Scientific Computing*, 24(2):247–262, 2005. [16](#), [73](#), [74](#)
- Anotida Madzvamuse. A numerical approach to the study of spatial pattern formation. *DPhil thesis, Exeter college, Trinity term, University of Oxford*, Trinity term 2000. [16](#), [19](#), [47](#), [65](#), [74](#), [102](#), [128](#)
- Y. T. Maeda, J. Inose, M. Y. Matsuo, S. Iwaya, and M. Sano. Ordered patterns of cell shape and orientational correlation during spontaneous cell migration. *PLoS ONE*, 3: e3734, 2008. [13](#), [14](#)
- S. E. Malawista, A. de Boisleury Chevance, and L. A. Boxer. Random locomotion and chemotaxis of human blood polymorphonuclear leukocytes from a patient with leukocyte adhesion deficiency-1: normal displacement in close quarters via chimneying. *Cell. Motil. Cytoskeleton*, 46:183–189, 2000. [40](#)
- T. H. Millard, S. J. Sharp, and L. M. Machesky. Signalling to actin assembly via the wasp (wiskott-aldrich syndrome protein): family proteins and the arp2/3 complex. *Biochem. J.*, 380:1–17, 2004. [31](#)
- K. Miller and R. N. Miller. Moving finite elements. *SIAM J. Num. Anal.*, 18:1019–1032, 1981. [74](#)

- A. Mogilner. On the edge: modelling protrusion. *Current Opinion in Cell Biology*, 18: 32–39, 2006. [43](#)
- A. Mogilner. Mathematics of cell motility: have we got its number? *J. Math. Biol.*, 58: 105–134, 2009. [40](#), [41](#), [42](#), [43](#)
- A. Mogilner and L. Edelstein-Keshet. Regulation of actin dynamics in rapidly moving cells: a quantitative analysis. *Biophys. J.*, 83:1237–1258, September 2002. [43](#)
- A. Mogilner and G. Oster. Cell motility driven by actin polymerisation. *Biophys. J.*, 71: 3030–3045, 1996. [43](#)
- A. Mogilner, E. Marland, and D. Bottino. A minimal model of locomotion applied to the steady gliding movement of fish keratocyte cells. In H. Othmer and P. Maini, editors, *Pattern formation and morphogenesis: basis processes*. New York, Springer, 2001. [43](#)
- P. Moreo, E. A. Gaffney, J. M. Garca-Aznar, and M. Doblaré. On the modelling of biological patterns with mechanochemical models: Insights from analysis and computation. *Bulletin of Mathematical Biology*, 72:400–431, 2010. [68](#)
- D. Morse. Viscoelasticity of concentrated isotropic solutions of semi-flexible polymers. 1. model and stress tensor. *Macromolecules*, 31:7030–7044, 1998. [26](#)
- K. W. Morton and D. F. Mayers. *Numerical solution of partial differential equations*. Cambridge University Press, 1994. [73](#)
- J. D. Murray. *Mathematical Biology*. Springer-Verlag, 1993. [45](#), [67](#), [152](#)
- E. M. Neidt, B. J. Scott, and D. R. Kovar. Formin differentially utilizes profilin isoforms to rapidly assemble actin filaments. *J. Biol. Chem.*, 284:673–684, 2009. [32](#)
- C. D. Nobes and A. Hall. Rho gtpases control polarity, protrusion, and adhesion during cell movement. *J Cell Biol.*, 144:1235–1244, 1999. [36](#)
- K. O. Okeyo, T. Adachi, J. Sunaga, and M. Hojo. Actomyosin contractility spatiotemporally regulates actin network dynamics in migrating cells. *Journal of Biomechanics*, 42(15):2540–2548, 2009. [14](#), [40](#), [48](#)
- F. Oosawa and S. Asakura. A theory of linear and helical aggregations of macromolecules. *J. Mol. Biol.*, 4:10–21, 1962. [43](#)
- G. F. Oster. On the crawling of cells. *J. Embryol. Exp. Morphol.*, 83:329–364, 1984. [40](#)
- E. Paluch, M. Piel, J. Prost, M. Bornens, and C. Sykes. Cortical actomyosin breakage triggers shape oscillations in cells and cell fragments. *Biophys. J.*, 89:724–733, 2005. [14](#)

- E. Paluch, C. Sykes, J. Prost, and M. Bornens. Dynamic modes of the cortical actomyosin gel during cell locomotion and division. *Trends Cell Biol.*, 16:5–10, 2006. [14](#)
- F. Pampaloni, G. Lattanzi, A. Jonas, T. Surrey, E. Frey, and E. L. Florin. Thermal fluctuations of grafted microtubules provide evidence of a length-dependent persistence length. *Proc. Natl. Acad. Sci. USA*, 103:10248–53, 2006. [26](#)
- M. Parri, M. L. Taddei, F. Bianchini, L. Calorini, and P. Chiarugi. EphA2 reexpression prompts invasion of melanoma cells shifting from mesenchymal to amoeboid-like motility style. *Cancer Res.*, 69:2072–2081, 2009. [37](#), [38](#)
- C. S. Peskin, G. M. Odell, and G. F. Oster. Cellular motions and thermal fluctuations: the brownian ratchet. *Biophys. J.*, 65:316–324, July 1993. [43](#)
- T. D. Pollard. Regulation of actin filament assembly by arp2/3 complex and formins. *Annu. Rev. Biophys. Biomol. Struct.*, 36:451–77, 2007. [29](#), [30](#), [31](#), [33](#), [35](#)
- T. D. Pollard and G. Borisy. Cellular motility driven by assembly and disassembly of actin filaments. *Cell*, 112:453–465, 2003. [31](#), [33](#), [42](#)
- T. D. Pollard, L. Blanchoin, and R. D. Mullins. Molecular mechanisms controlling actin filament dynamics in nonmuscle cells. *Annu. Rev. Biophys. Biomol. Struct.*, 29:545–76, 2000. [30](#), [33](#), [43](#)
- A. Y. Pollitt and R. H. Insall. Wasp and scar/wave proteins: the drivers of actin assembly. *JOURNAL OF CELL SCIENCE*, 122:2575–2578, 2009. [31](#), [32](#)
- P. A. Pullarkat, A. Fernández, and A. Ott. Rheological properties of the eukaryotic cell cytoskeleton. *Physics Reports*, 449:29–53, 2007. [14](#), [15](#), [24](#), [25](#), [26](#), [27](#), [29](#)
- E. Purcell. Life at low reynolds number. *Amer. J. Phys.*, 45:1–11, 1977. [48](#), [128](#)
- S. M. Rafelski and J. A. Theriot. Crawling toward a unified model of cell motility: spatial and temporal of regulation of actin dynamics. *Annu. Rev. Biochem.*, 73:209–239, 2004. [13](#)
- J. N. Reddy. *An introduction to the finite element method*. McGraw-Hill, 1993. [15](#), [16](#), [18](#), [73](#), [75](#), [80](#), [89](#), [99](#), [124](#), [144](#)
- A. J. Ridley, M. A. Schwartz, K. Burridge, R. A. Firtel, M. H. Ginberg, G. Borisy, J. T. Parsons, and A. R. Horwitz. Cell migration: Integrating signal from front to back. *Science*, 302:1704–1709, 2003. [13](#), [35](#), [127](#)
- T. M. Robert and M. Stewart. Nematode sperm: amoeboid movement without actin. *Trends in Cell Biology*, 7:368–373, 1997. [38](#)

- S. Romero, C. Le Clainche, D. Didry, C. Egile, D. Pantaloni, and M. F. Carlier. Formin is a processive motor that requires profilin to accelerate actin assembly and associated atp hydrolysis. *Cell*, 119:419–429, 2004. [31](#)
- B. Rubinstein, K. Jacobson, and A. Mogilner. Multiscale two-dimensional modeling of a motile simple-shaped cell. *Multiscale Model. Simul.*, 3:413–439, 2005. [43](#), [52](#)
- Y. Saad. *Iterative methods for sparse linear systems*. Society for Industrial and Applied Mathematics, 2003. [89](#)
- M. H. Sadd. *Elasticity: theory, applications and numerics*, volume 2. Elsevier, North Holland, 2005. [16](#)
- Y. Sadd and M. H. Schultz. Gmres: A generalized minimal residual algorithm for solving non-symmetric linear systems. *SIAM J. Sci. Stat. Comput.*, 7:856–869, 1986. [89](#)
- E. Sahai and C. J. Marshall. Differing modes of tumour cell invasion have distinct requirements for rho/rock signalling and extracellular proteolysis. *Nature Cell Biol.*, 5: 711–719, 2003. [38](#), [39](#)
- A. J. Sarria, R. P. Sankhavaram, and R. M. Evans. A functional role for vimentin intermediate filaments in metabolism of lipoprotein derived cholesterol in human sw13 cells. *J. Biol. Chem.*, 267:19455–63, 1992. [26](#)
- A. Schmidt, K. G. Siebert, D. Köster, and C. Heine. *Design of adaptive finite element software: The finite element toolbox ALBERTA*, 11 December 2006. Version: ALBERTA-2.0. [89](#)
- Y. Senju and H. Miyata. The role of actomyosin contractility in the formation and dynamics of actin bundles during fibroblast spreading. *J. Biochem*, 145(2):137–150, 2009. [15](#), [41](#), [110](#), [111](#), [123](#), [128](#)
- J. A. Sethian. *Level Set Methods: Evolving Interfaces in Geometry, Fluid Mechanics, Computer Vision and Materials Sciences*. Cambridge University Press, 1996. [15](#), [16](#), [73](#)
- J. R. Simon, A. Gough, E. Urbank, F. Wang, and F. Lanni. Analysis of rhodamine and fluorescein-labeled f-actin diffusion in vitro by fluorescence photobleaching recovery. *Biophys. J.*, 54:801–815, 1988. [111](#)
- J. V. Small. Organization of actin in the leading edge of cultured cells: influence of osmium tetroxide and dehydration on the ultrastructure of actin meshworks. *J. Cell Biol.*, 91:695–705, 1981. [30](#)

- J. V. Small, G. Isenberg, and J. E. Celis. Polarity of actin at the leading edge of cultured cells. of the peripheral weave of microfilaments in glia cells. *Nature*, 272:638–639, 1978. [30](#)
- J. V. Small, T. Stradal, E. Vignal, and K. Rottner. The lamellipodium: where motility begins. *TRENDS in Cell Biology*, Vol. 12(No. 3), March 2002. [36](#)
- J. Sroka, M. von Gunten, G. A. Dunn, and H. U. Keller. Phenotype modulation in non-adherent and adherent sublines of walker carcinosarcoma cells: the role of cell-substratum contacts and microtubules in controlling cell shape, locomotion and cytoskeletal structure. *Int. J. Biochem. Cell Biol.*, 34:882–899, 2002. [40](#)
- A. Stéphanou. *Spatio-temporal dynamics of the cell: characterization from images and computer simulations*. Lambert Academic Publishing, 2010. ISBN 9783838337920. [13](#), [23](#), [26](#), [27](#), [35](#), [41](#), [127](#)
- A. Stéphanou and P. Tracqui. Cytomechanics of cell deformations and migration: from model to experiment. *C. R Biologies*, 325:1–14, 2002. [27](#), [29](#)
- A. Stéphanou, M.A.J. Chaplain, and P. Tracqui. A mathematical model for the dynamics of large membrane deformations of isolated fibroblasts. *Bulle. Math. Biol.*, 66:1119–1154, 2004. [13](#), [14](#), [15](#), [41](#), [43](#), [44](#), [47](#), [48](#), [50](#), [51](#), [52](#), [53](#), [73](#), [74](#), [90](#), [125](#), [128](#)
- A. Stéphanou, Eleni Mylona, M. Chaplain, and P. Tracqui. A computational model of cell migration coupling the growth of focal adhesions with oscillatory cell protrusions. *Journal of Theoretical Biology*, 253:701–716, 2008. [13](#), [35](#), [38](#), [112](#), [123](#), [127](#)
- T. M. Svitkina, A. B. Verkhovsky, K. M. McQuade, and G. G. Borisy. Analysis of the actin-myosin ii system in fish epidermal keratocytes: mechanism of cell body translocation. *J. Cell Biol.*, 139:397–415, 1997. [30](#)
- J. P. Trinkaus. Surface activity and locomotion of fundulus deep cells during blastula and gastrula stages. *Dev. Biol. Cell Biology*, 30:69–103, 1973. [39](#)
- E. Urban, S. Jacob, M. Nemethova, G. P. Resch, and J. V. Small. Electron tomography reveals unbranched networks of actin filaments in lamellipodia. *Nature Cell Biology*, 12:429–435, 2010. [30](#)
- N. Watanabe. Inside view of cell locomotion through single-molecule: fast f-/g-actin cycle and g-actin regulation of polymer restoration. *Proc. Jpn. Acad.*, 86, 2010. [111](#)
- A. Wegner. Head to tail polymerization of actin. *J. Mol. Biol.*, 108:139–150, 1976. [43](#)

- K. Wolf, R. Muller, S. Borgmann, E. B. Brocker, and P. Friedl. Amoeboid shape change and contact guidance: T-lymphocyte crawling through fibrillar collagen is independent of matrix remodeling by mmps and other proteases. *Blood*, 102:3262–9, 2003. [40](#)
- Y. Xu, J. B. Moseley, I. Sagot, F. Poy, D. Pellman, B. L. Goode, and M. J. Eck. Crystal structures of a formin homology-2 domain reveal a tethered dimer architecture. *Cell*, 116:711–723, 2004. [32](#)
- F Xue, D. M. Janzen, and D. A. Knecht. Contribution of filopodia to cell migration: A mechanical link between protrusion and contraction. *Int. J. Cell Biol.*, 2010. 507821. [13](#), [35](#), [36](#), [127](#)
- D. Yamazaki, S. Kurisu, and T. Takenawa. Regulation of cancer cell motility through actin reorganization. *Cancer Sci.*, 96:379–86, 2005. [37](#)
- L. Yang, M. Dolnik, A. M. Zhabotinsky, and I. R. Epstein. Pattern formation arising from interactions between turing and wave instabilities. *J. Chem. Phys.*, 117:7259–7265, 2002. [68](#)
- K. Yoshida and T. Soldati. Dissection of amoeboid movement into two mechanically distinct modes. *J. Cell Sci.*, 119:3833–3844, 2006. [39](#)
- R. V. Zackroff and R. D. Goldman. In vitro assembly of intermediate filaments from baby hamster kidney (bhk-21) cells. *Proc. Natl. Acad. Sci. USA*, 76:6226–6230, 1979. [26](#)
- M. H. Zaman, R. D. Kamm, P. Matsudaira, and D. A. Lauffenburger. Computational model for cell migration in three-dimensional matrices. *Biophysical Journal*, 89:1389–1397, 2005. [13](#), [40](#), [42](#), [127](#)
- C. Zhu, G. Bao, and N. Wang. Cell mechanics: Mechanical response, cell adhesion and molecular deformation. *Annu Rev. Biomed. Eng.*, 2:189–226, 2000. [14](#), [25](#)
- O. C. Zienkiewicz, R. L. Taylor, and J. Z. Zhu. *The finite element method: Its basis and fundamentals*. Elsevier Butterworth-Heinemann, 2005. [15](#), [73](#)
- D. G. Zill and M. R. Cullen. *Advanced Engineering Mathematics*. Jones and Bartlett Publishers International, Inc., 2000. [19](#), [20](#), [21](#), [59](#), [62](#), [67](#), [93](#)

Appendix A

Stability analysis

The reaction-diffusion equation is a linear equation hence its error analysis is easy to show but for force balance equation this is more involved and complicated because of the presence of non-linearity. Hence we only show some stability estimates for the reaction-diffusion equation.

A.1 Stability analysis of the reaction-diffusion equation

A stability analysis of a linear advection diffusion problem in an arbitrary Lagrangian Eulerian frame is given in [Formaggia and Nobile \(1999\)](#). We show some stability estimates for the reaction-diffusion equation by applying some of the techniques used in [Formaggia and Nobile \(1999\)](#). We recall the following identities. Let $g(\mathbf{x}, t) \in H^1(\Omega_t)$ be a function defined on Ω_t , $t \in I$ then from Reynolds transport theorem the following identities hold for any arbitrary subdomain $\mathcal{V}_t \subseteq \Omega_t$:

$$\frac{d}{dt} \int_{\mathcal{V}_t} g \, d\Omega_t = \int_{\mathcal{V}_t} \left(\frac{Dg}{Dt} + g \nabla \cdot \boldsymbol{\beta} \right) d\Omega_t, \quad (\text{A.1})$$

where $\boldsymbol{\beta}$ is the flow velocity. Similarly

$$\begin{aligned} \frac{d}{dt} \int_{\mathcal{V}_t} g^2 \, d\Omega_t &= \int_{\mathcal{V}_t} \left(\frac{D}{Dt}(g^2) + g^2 \nabla \cdot \boldsymbol{\beta} \right) d\Omega_t \\ \implies \int_{\mathcal{V}_t} \frac{D}{Dt}(g^2) \, d\Omega_t &= \frac{d}{dt} \int_{\mathcal{V}_t} g^2 \, d\Omega_t - \int_{\mathcal{V}_t} g^2 \nabla \cdot \dot{\mathbf{x}} \, d\Omega_t \\ &= \frac{d}{dt} \|g\|_{L^2(\mathcal{V}_t)}^2 - \int_{\mathcal{V}_t} g^2 \nabla \cdot \dot{\mathbf{x}} \, d\Omega_t. \end{aligned} \quad (\text{A.2})$$

A.1. Stability analysis of the reaction-diffusion equation

We recall the reaction-diffusion equation for the actin biochemical dynamics below for the sake of completeness.

$$\frac{\partial a}{\partial t} - D_a \Delta a + \nabla \cdot (a \boldsymbol{\beta}) - k_a(a_c - a) = 0 \quad \text{in } \boldsymbol{\Omega}_t, t \in I, \quad (\text{A.3})$$

Let Da/Dt be a material derivative, then the material derivative of the actin concentration a is defined as (Reddy 1993);

$$\frac{Da}{Dt} = \frac{\partial a}{\partial t} + (\nabla a) \cdot \boldsymbol{\beta}$$

We write the reaction-diffusion equation in terms of the material derivative as given below

$$\frac{Da}{Dt} - D_a \Delta a + a(\nabla \cdot \boldsymbol{\beta}) - k_a(a_c - a) = 0 \quad (\text{A.4})$$

We multiply by a and integrate over $\boldsymbol{\Omega}_t$ to obtain

$$\int_{\boldsymbol{\Omega}_t} a \left(\frac{Da}{Dt} + a(\nabla \cdot \boldsymbol{\beta}) \right) d\boldsymbol{\Omega}_t + \int_{\boldsymbol{\Omega}_t} (D \nabla a \cdot \nabla a + k_a a^2) d\boldsymbol{\Omega}_t = \int_{\boldsymbol{\Omega}_t} k_a a_c a d\boldsymbol{\Omega}_t. \quad (\text{A.5})$$

From product rule, we have that

$$a \frac{Da}{Dt} = \frac{1}{2} \frac{D}{Dt} (a^2).$$

Thus (A.5) becomes;

$$\begin{aligned} \int_{\boldsymbol{\Omega}_t} \left(\frac{1}{2} \frac{D}{Dt} (a^2) + a^2 \nabla \cdot \boldsymbol{\beta} \right) d\boldsymbol{\Omega}_t + D_a \|\nabla a\|_{L^2(\boldsymbol{\Omega}_t)}^2 + k_a \|a\|_{L^2(\boldsymbol{\Omega}_t)}^2 \\ = k_a a_c \|a\|_{L^1(\boldsymbol{\Omega}_t)}. \end{aligned} \quad (\text{A.6})$$

By applying the identity (A.2) to (A.6) we obtain the following estimate;

$$\begin{aligned} \frac{1}{2} \frac{d}{dt} \|a\|_{L^2(\boldsymbol{\Omega}_t)}^2 + D_a \|\nabla a\|_{L^2(\boldsymbol{\Omega}_t)}^2 + k_a \|a\|_{L^2(\boldsymbol{\Omega}_t)}^2 = k_a a_c \|a\|_{L^1(\boldsymbol{\Omega}_t)} \\ - \frac{1}{2} \int_{\boldsymbol{\Omega}_t} a^2 \nabla \cdot \boldsymbol{\beta} d\boldsymbol{\Omega}_t. \end{aligned} \quad (\text{A.7})$$

Time integration

We integrate (A.7) in time from t_0 to T_f . And we obtain that

$$\begin{aligned} \int_{t_0}^{T_f} \frac{d}{ds} \|a\|_{L^2(\Omega_s)}^2 ds + 2D_a \int_{t_0}^{T_f} \|\nabla a\|_{L^2(\Omega_s)}^2 ds + 2k_a \int_{t_0}^{T_f} \|a\|_{L^2(\Omega_s)}^2 ds = \\ 2k_a a_c \int_{t_0}^{T_f} \|a\|_{L^1(\Omega_s)} ds - \int_{t_0}^{T_f} \int_{\Omega_s} a^2 \nabla \cdot \boldsymbol{\beta} d\Omega_s ds. \end{aligned} \quad (\text{A.8})$$

Which yields

$$\begin{aligned} \|a(t)\|_{L^2(\Omega_t)}^2 + 2D_a \int_{t_0}^{T_f} \|\nabla a\|_{L^2(\Omega_s)}^2 ds + 2k_a \int_{t_0}^{T_f} \|a\|_{L^2(\Omega_s)}^2 ds = \|a(t_0)\|_{L^2(\Omega_{t_0})}^2 \\ + 2k_a a_c \int_{t_0}^{T_f} \|a\|_{L^1(\Omega_s)} ds - \int_{t_0}^{T_f} \int_{\Omega_s} a^2 \nabla \cdot \boldsymbol{\beta} d\Omega_s ds. \end{aligned} \quad (\text{A.9})$$

We assume that the following bounds exist;

$$\begin{aligned} \int_{\Omega_t} a^2 \nabla \cdot \boldsymbol{\beta} d\Omega_t &\leq \int_{\Omega_t} |a|^2 |\nabla \cdot \boldsymbol{\beta}| d\Omega_t \\ &\leq \|\nabla \cdot \boldsymbol{\beta}\|_{L^2(\Omega_t)} \int_{\Omega_t} |a|^2 d\Omega_t = \|\nabla \cdot \boldsymbol{\beta}\|_{L^2(\Omega_t)} \|a\|_{L^2(\Omega_t)}^2. \end{aligned}$$

Therefore (A.9) becomes

$$\begin{aligned} \|a(t)\|_{L^2(\Omega_t)}^2 + 2D_a \int_{t_0}^{T_f} \|\nabla a\|_{L^2(\Omega_s)}^2 ds + 2k_a \int_{t_0}^{T_f} \|a\|_{L^2(\Omega_s)}^2 ds \leq \|a(t_0)\|_{L^2(\Omega_{t_0})}^2 \\ + 2k_a a_c \int_{t_0}^{T_f} \|a\|_{L^1(\Omega_s)} ds + \int_{t_0}^{T_f} \|\nabla \cdot \boldsymbol{\beta}\|_{L^2(\Omega_t)} \|a\|_{L^2(\Omega_s)}^2 ds. \end{aligned} \quad (\text{A.10})$$

Using a Gronwall argument we arrive at the estimate

$$\begin{aligned} \|a(t)\|_{L^2(\Omega_t)}^2 + 2D_a \int_{t_0}^{T_f} \|\nabla a\|_{L^2(\Omega_s)}^2 ds + 2k_a \int_{t_0}^{T_f} \|a\|_{L^2(\Omega_s)}^2 ds \leq \\ C_2 + \int_{t_0}^{T_f} C_1(s) C_2 \exp\left(\int_s^{T_f} C_1(g) dg\right) ds, \end{aligned} \quad (\text{A.11})$$

where

$$C_2 = \|a(t_0)\|_{L^2(\Omega_{t_0})}^2 + 2k_a a_c \int_{t_0}^{T_f} \|a\|_{L^1(\Omega_s)} ds \quad \text{and} \quad C_1(t) = \|\nabla \cdot \boldsymbol{\beta}\|_{L^2(\Omega_t)}.$$

A.1. Stability analysis of the reaction-diffusion equation

From (A.11) we obtain the following estimate;

$$\begin{aligned} \|a(t)\|_{L^2(\Omega_t)}^2 + 2D_a \int_{t_0}^{T_f} \|\nabla a\|_{L^2(\Omega_s)}^2 ds + 2k_a \int_{t_0}^{T_f} \|a\|_{L^2(\Omega_s)}^2 ds \\ \leq C_2 \exp \left(\int_{t_0}^{T_f} C_1(s) ds \right). \end{aligned} \quad (\text{A.12})$$

Thus the stability estimate of the differential equation (A.3) is dependent on the flow velocity. The flow velocity β :

$$\beta = \frac{\partial \mathbf{u}}{\partial t} < \infty. \quad (\text{A.13})$$

Since \mathbf{u} are small displacements of the domain Ω_t . Hence the stability estimate of the differential equation (A.3) is bounded. We note that \mathbf{u} is the solution of the force balance equation and it determines the displacement (or velocity) of the domain Ω_t . By considering the cytomolecular model to be a reaction-diffusion equation that is coupled to a domain velocity β , we state that the stability estimate of the cytomolecular model is bounded.

Appendix B

Weak form and wellposedness

Definition B.0.1. (*Weak solution*) Let $\mathcal{G}_T := \bigcup_{t \in [t_0, T_f]} \Omega_t \times \{t\}$ be the union of $\Omega_t \times \{t\}$ for $t \in [t_0, T_f]$. We say that a function $a \in H^1(\mathcal{G}_T)$ is a weak solution of (4.15), if for almost every $t \in (t_0, T_f)$

$$\int_{\Omega_t} \varphi \left(\frac{Da}{Dt} + a(\nabla \cdot \boldsymbol{\beta}) \right) d\Omega_t + \int_{\Omega_t} (D\nabla a \cdot \nabla \varphi + k_a a \varphi) d\Omega_t = \int_{\Omega_t} k_a a_c \varphi d\Omega_t \quad (\text{B.1})$$

for every $\varphi(., t) \in H^1(\Omega_t)$.

Existence of unique weak solution

The existence of a weak solution for an advection-diffusion equation on an evolving surface is given in Dziuk and Elliott (2007). Following his work we show that there exist a weak solution of the differential equation (4.15). For this we require the following energy equations.

Lemma B.0.1. *Let a be a weak solution of (4.15). Then it can be shown that*

$$\begin{aligned} \frac{1}{2} \frac{d}{dt} \int_{\Omega_t} a^2 d\Omega_t + \int_{\Omega_t} \left(D|\nabla a|^2 + k_a a^2 \right) d\Omega_t + \frac{1}{2} \int_{\Omega_t} a^2 (\nabla \cdot \boldsymbol{\beta}) d\Omega_t \\ = \int_{\Omega_t} k_a a_c a d\Omega_t. \end{aligned} \quad (\text{B.2})$$

Proof. We choose $\varphi = a$ in

$$\frac{d}{dt} \int_{\Omega_t} a \varphi \, d\Omega_t + \int_{\Omega_t} (D\nabla a \cdot \nabla \varphi + k_a a \varphi) \, d\Omega_t = \int_{\Omega_t} k_a a_c \varphi \, d\Omega_t + \int_{\Omega_t} a \frac{D\varphi}{Dt} \, d\Omega_t. \quad (\text{B.3})$$

and we obtain that

$$\frac{d}{dt} \int_{\Omega_t} a^2 \, d\Omega_t + \int_{\Omega_t} (D|\nabla a|^2 + k_a a^2) \, d\Omega_t = \int_{\Omega_t} k_a a_c a \, d\Omega_t + \int_{\Omega_t} a \frac{Da}{Dt} \, d\Omega_t. \quad (\text{B.4})$$

Using product rule we can write that $a(Da/Dt) = 1/2(D(a^2)/Dt)$. Applying Reynolds transport theorem we obtain that

$$\frac{1}{2} \frac{D}{Dt} (a^2) \, d\Omega_t = \frac{1}{2} \frac{d}{dt} \int_{\Omega_t} a^2 \, d\Omega_t - \frac{1}{2} \int_{\Omega_t} a^2 \nabla \cdot (\boldsymbol{\beta}) \, d\Omega_t. \quad (\text{B.5})$$

We substitute (B.5) into (B.4) and we get

$$\begin{aligned} \frac{1}{2} \frac{d}{dt} \int_{\Omega_t} a^2 \, d\Omega_t + \int_{\Omega_t} (D|\nabla a|^2 + k_a a^2) \, d\Omega_t + \frac{1}{2} \int_{\Omega_t} a^2 (\nabla \cdot \boldsymbol{\beta}) \, d\Omega_t \\ = \int_{\Omega_t} k_a a_c a \, d\Omega_t, \end{aligned} \quad (\text{B.6})$$

which is (B.2). □

Lemma B.0.2. *Let a be a weak solution of (4.15). Then we have that*

$$\begin{aligned} \int_{\Omega_t} \left(\frac{Da}{Dt} \right)^2 \, d\Omega_t + \left(k_a \left(\frac{1}{2} - a_c \right) \right) \frac{d}{dt} \int_{\Omega_t} a^2 \, d\Omega_t + \int_{\Omega_t} (a \nabla \cdot \boldsymbol{\beta}) \frac{Da}{Dt} \, d\Omega_t \\ + \frac{D}{2} \frac{d}{dt} \int_{\Omega_t} |\nabla a|^2 \, d\Omega_t + k_a a_c \int_{\Omega_t} a \nabla \cdot \boldsymbol{\beta} \, d\Omega_t \\ = \frac{k_a}{2} \int_{\Omega_t} a^2 \nabla \cdot \boldsymbol{\beta} \, d\Omega_t + \frac{D}{2} \int_{\Omega_t} |\nabla a|^2 \nabla \cdot \boldsymbol{\beta} \, d\Omega_t. \end{aligned} \quad (\text{B.7})$$

Proof. To prove (B.7) we now choose $\varphi = \frac{Da}{Dt}$ in (B.1) and we obtain

$$\begin{aligned} \int_{\Omega_t} \left(\frac{Da}{Dt} \right)^2 \, d\Omega_t + \int_{\Omega_t} (a \nabla \cdot \boldsymbol{\beta}) \frac{Da}{Dt} \, d\Omega_t + \int_{\Omega_t} \left(D\nabla a \cdot \nabla \left(\frac{Da}{Dt} \right) \right) \, d\Omega_t \\ + \int_{\Omega_t} \left(k_a a \frac{Da}{Dt} \right) \, d\Omega_t = \int_{\Omega_t} k_a a_c \frac{Da}{Dt} \, d\Omega_t. \end{aligned} \quad (\text{B.8})$$

Here

$$\begin{aligned} \int_{\Omega_t} \left(D \nabla a \cdot \nabla \left(\frac{Da}{Dt} \right) \right) d\Omega_t &= \frac{D}{2} \int_{\Omega_t} \frac{D}{Dt} (|\nabla a|^2) d\Omega_t \\ &= \frac{D}{2} \frac{d}{dt} \int_{\Omega_t} |\nabla a|^2 d\Omega_t - \frac{D}{2} \int_{\Omega_t} |\nabla a|^2 \nabla \cdot \boldsymbol{\beta} d\Omega_t, \end{aligned} \quad (\text{B.9})$$

$$\begin{aligned} \int_{\Omega_t} \left(k_a a \frac{Da}{Dt} \right) d\Omega_t &= \frac{k_a}{2} \int_{\Omega_t} \left(\frac{D(a^2)}{Dt} \right) d\Omega_t \\ &= \frac{k_a}{2} \frac{d}{dt} \int_{\Omega_t} a^2 d\Omega_t - \frac{k_a}{2} \int_{\Omega_t} a^2 \nabla \cdot \boldsymbol{\beta} d\Omega_t, \end{aligned} \quad (\text{B.10})$$

and

$$\int_{\Omega_t} k_a a_c \frac{Da}{Dt} d\Omega_t = k_a a_c \int_{\Omega_t} \frac{Da}{Dt} d\Omega_t = k_a a_c \left[\frac{d}{dt} \int_{\Omega_t} a d\Omega_t - \int_{\Omega_t} a \nabla \cdot \boldsymbol{\beta} d\Omega_t \right]. \quad (\text{B.11})$$

We substitute (B.9) - (B.11) into (B.8) and we get

$$\begin{aligned} \int_{\Omega_t} \left(\frac{Da}{Dt} \right)^2 d\Omega_t &+ \int_{\Omega_t} (a \nabla \cdot \boldsymbol{\beta}) \frac{Da}{Dt} d\Omega_t + \frac{D}{2} \frac{d}{dt} \int_{\Omega_t} |\nabla a|^2 d\Omega_t - \frac{D}{2} \int_{\Omega_t} |\nabla a|^2 \nabla \cdot \boldsymbol{\beta} d\Omega_t \\ &+ \frac{k_a}{2} \frac{d}{dt} \int_{\Omega_t} a^2 d\Omega_t - \frac{k_a}{2} \int_{\Omega_t} a^2 \nabla \cdot \boldsymbol{\beta} d\Omega_t \\ &= k_a a_c \left[\frac{d}{dt} \int_{\Omega_t} a d\Omega_t - \int_{\Omega_t} a \nabla \cdot \boldsymbol{\beta} d\Omega_t \right]. \end{aligned} \quad (\text{B.12})$$

By factorizing some terms in the expression (B.12) we obtain

$$\begin{aligned} \int_{\Omega_t} \left(\frac{Da}{Dt} \right)^2 d\Omega_t &+ \left(k_a \left(\frac{1}{2} - a_c \right) \right) \frac{d}{dt} \int_{\Omega_t} a^2 d\Omega_t + \int_{\Omega_t} (a \nabla \cdot \boldsymbol{\beta}) \frac{Da}{Dt} d\Omega_t \\ &+ \frac{D}{2} \frac{d}{dt} \int_{\Omega_t} |\nabla a|^2 d\Omega_t + k_a a_c \int_{\Omega_t} a \nabla \cdot \boldsymbol{\beta} d\Omega_t \\ &= \frac{k_a}{2} \int_{\Omega_t} a^2 \nabla \cdot \boldsymbol{\beta} d\Omega_t + \frac{D}{2} \int_{\Omega_t} |\nabla a|^2 \nabla \cdot \boldsymbol{\beta} d\Omega_t, \end{aligned} \quad (\text{B.13})$$

which is (B.7) □

Theorem B.0.1. (Existence and uniqueness of weak solution) *There exist a unique weak*

solution of (A.4). And the following energy estimate holds

$$\begin{aligned} \sup_{t \in (0, T_f)} \int_{\Omega_t} a_N(\cdot, t)^2 d\Omega_t + \int_0^{T_f} \int_{\Omega_t} \left(D|\nabla a_N(\cdot, t)|^2 + k_a a_N(\cdot, t)^2 \right) d\Omega_t dt \\ \leq C_3. \end{aligned} \quad (\text{B.14})$$

$$\begin{aligned} \int_0^{T_f} \int_{\Omega_t} \left(\frac{D}{Dt} a_N(\cdot, t) \right)^2 d\Omega_t dt + \left(k_a \left(\frac{1}{2} - a_c \right) \right) \sup_{t \in (0, T_f)} \int_{\Omega_t} a_N(\cdot, t)^2 d\Omega_t \\ + \frac{D}{2} \sup_{t \in (0, T_f)} \int_{\Omega_t} |\nabla a_N(\cdot, t)|^2 d\Omega_t \leq C_4. \end{aligned} \quad (\text{B.15})$$

Proof. Our ansatz for a Galerkin solution of (B.1) from $X_N = \text{span} \{ \varphi_1(\cdot, t), \dots, \varphi_N(\cdot, t) \}$ is

$$a_N(\mathbf{x}, t) = \sum_{j=1}^N a_j(t) \varphi_j(\mathbf{x}, t).$$

The material derivative of a_N gives

$$\frac{D}{Dt} a_N(\mathbf{x}, t) = \sum_{j=1}^N \varphi_j(\mathbf{x}, t) \frac{D}{Dt} a_j(t)$$

as a consequence of the transport property of basis function (i.e. $\frac{D\varphi_j}{Dt} = 0$) (Dziuk and Elliott 2007). From linear ODE theory, it can be shown that a_N satisfies

$$\begin{aligned} \frac{d}{dt} \int_{\Omega_t} a_N \varphi d\Omega_t + \int_{\Omega_t} (D\nabla a_N \cdot \nabla \varphi + k_a a_N \varphi) d\Omega_t \\ = \int_{\Omega_t} k_a a_c \varphi d\Omega_t + \int_{\Omega_t} a_N \frac{D\varphi}{Dt} d\Omega_t. \end{aligned} \quad (\text{B.16})$$

for all $\varphi(\cdot, t) \in \text{span} \{ \varphi_1(\cdot, t), \dots, \varphi_N(\cdot, t) \}$. From Lemma B.0.1 we have the following energy equation

$$\begin{aligned} \frac{1}{2} \frac{d}{dt} \int_{\Omega_t} a_N^2 d\Omega_t + \int_{\Omega_t} \left(D|\nabla a_N|^2 + k_a a_N^2 \right) d\Omega_t + \frac{1}{2} \int_{\Omega_t} a_N^2 (\nabla \cdot \boldsymbol{\beta}) d\Omega_t \\ = \int_{\Omega_t} k_a a_c a_N d\Omega_t. \end{aligned} \quad (\text{B.17})$$

and a Gronwell argument yields the estimate

$$\begin{aligned} \sup_{t \in (0, T_f)} \int_{\Omega_t} a_N(\cdot, t)^2 d\Omega_t + \int_0^{T_f} \int_{\Omega_t} \left(D |\nabla a_N(\cdot, t)|^2 + k_a a_N(\cdot, t)^2 \right) d\Omega_t dt \\ \leq C_2 \exp \left(\int_{t_0}^{T_f} C_1(s) ds \right), \end{aligned} \quad (\text{B.18})$$

where

$$C_2 = \|a_N(t_0)\|_{L^2(\Omega_{t_0})}^2 + k_a a_c \int_{t_0}^{T_f} \|a_N(s)\|_{L^1(\Omega_s)}^2 ds \text{ and } C_1(t) = \|\nabla \cdot \boldsymbol{\beta}\|_{L^2(\Omega_t)}.$$

Let us define C_3 :

$$C_3 = C_2 \exp \left(\int_{t_0}^{T_f} C_1(s) ds \right).$$

then from (B.18), we obtain that

$$\begin{aligned} \sup_{t \in (0, T_f)} \int_{\Omega_t} a_N(\cdot, t)^2 d\Omega_t + \int_0^{T_f} \int_{\Omega_t} \left(D |\nabla a_N(\cdot, t)|^2 + k_a a_N(\cdot, t)^2 \right) d\Omega_t dt \\ \leq C_3. \end{aligned} \quad (\text{B.19})$$

which is (B.14). Similarly from Lemma B.0.2 we obtain the following energy equation

$$\begin{aligned} \int_{\Omega_t} \left(\frac{Da_N}{Dt} \right)^2 d\Omega_t + \left(k_a \left(\frac{1}{2} - a_c \right) \right) \frac{d}{dt} \int_{\Omega_t} a_N^2 d\Omega_t + \frac{D}{2} \frac{d}{dt} \int_{\Omega_t} |\nabla a_N|^2 d\Omega_t \\ = c \int_{\Omega_t} |a_N| \left| \frac{Da}{Dt} \right| d\Omega_t + c \int_{\Omega_t} a_N d\Omega_t \\ + c \int_{\Omega_t} a_N^2 d\Omega_t + c \int_{\Omega_t} |\nabla a_N|^2 d\Omega_t, \end{aligned} \quad (\text{B.20})$$

and a Gronwell argument yields the estimate

$$\begin{aligned} \int_0^{T_f} \int_{\Omega_t} \left(\frac{D}{Dt} a_N(\cdot, t) \right)^2 d\Omega_t dt + \left(k_a \left(\frac{1}{2} - a_c \right) \right) \sup_{t \in (0, T_f)} \int_{\Omega_t} a_N(\cdot, t)^2 d\Omega_t \\ + \frac{D}{2} \sup_{t \in (0, T_f)} \int_{\Omega_t} |\nabla a_N(\cdot, t)|^2 d\Omega_t \leq C_4. \end{aligned} \quad (\text{B.21})$$

which is (B.15). By combining the estimates (B.19) and (B.21) we obtain the bounded-

ness of the sequence $(a_N)_{N \in \mathbb{N}} \in H^1(\mathcal{G}_T)$. Thus there exist an $a = a(\mathbf{x}, t)$, $a \in H^1(\mathcal{G}_T)$ such that for a subsequence say $a_m \subset a_N$; $m, N \in \mathbb{N}$ ([Dziuk and Elliott 2007](#)),

$$a_m \rightharpoonup a \quad \text{as } m \rightarrow \infty \quad \text{in } H^1(\mathcal{G}_T). \quad (\text{B.22})$$

□

We do not show the existence of a unique solution of the force balance equation and of the coupled problem because this is more involved. The force balance equation has been well studied by [Lewis and Murray \(1991; 1992\)](#); [Murray \(1993\)](#) and numerous other authors. Their solutions are known to exist and are well-posed.